

University of Windsor

Scholarship at UWindor

Electronic Theses and Dissertations

Theses, Dissertations, and Major Papers

5-11-2018

Development of Optimal Material Extrusion Additive Manufacturing Tool Path Parameters for Minimizing Void Regions Using Contemporary Tool Path Solutions

Hasti Eiliat
University of Windsor

Follow this and additional works at: <https://scholar.uwindsor.ca/etd>



Part of the [Engineering Commons](#)

Recommended Citation

Eiliat, Hasti, "Development of Optimal Material Extrusion Additive Manufacturing Tool Path Parameters for Minimizing Void Regions Using Contemporary Tool Path Solutions" (2018). *Electronic Theses and Dissertations*. 7464.

<https://scholar.uwindsor.ca/etd/7464>

This online database contains the full-text of PhD dissertations and Masters' theses of University of Windsor students from 1954 forward. These documents are made available for personal study and research purposes only, in accordance with the Canadian Copyright Act and the Creative Commons license—CC BY-NC-ND (Attribution, Non-Commercial, No Derivative Works). Under this license, works must always be attributed to the copyright holder (original author), cannot be used for any commercial purposes, and may not be altered. Any other use would require the permission of the copyright holder. Students may inquire about withdrawing their dissertation and/or thesis from this database. For additional inquiries, please contact the repository administrator via email (scholarship@uwindsor.ca) or by telephone at 519-253-3000ext. 3208.

**Development of Optimal Material Extrusion Additive Manufacturing Tool Path
Parameters for Minimizing Void Regions Using Contemporary Tool Path Solutions**

By

Hasti Eiliat

A Dissertation
Submitted to the Faculty of Graduate Studies
through the Industrial and Manufacturing Systems Engineering Graduate Program
in Partial Fulfillment of the Requirements for
the Degree of Doctor of Philosophy
at the University of Windsor

Windsor, Ontario, Canada

2018

© 2018 Hasti Eiliat

**Development of Optimal Material Extrusion Additive Manufacturing Tool Path
Parameters for Minimizing Void Regions Using Contemporary Tool Path Solutions**

By

Hasti Eiliat

APPROVED BY:

C. Duty, External Examiner
University of Tennessee

R. Caron
Mathematics and Statistics

M. Wang
Mechanical, Automotive and Materials Engineering

G. Zhang
Mechanical, Automotive and Materials Engineering

J. Urbanic, Advisor
Mechanical, Automotive and Materials Engineering

May 08, 2018

DECLARATION OF CO-AUTHORSHIP / PREVIOUS PUBLICATION

I. Co-Authorship

I hereby declare that this dissertation incorporates material that is result of joint research, as follows:

Chapter 1 of the dissertation was co-authored with Luis Fernando Villalpando and Hasti Eiliat under the supervision of Professor Dr. Ruth Jill Urbanic. In all cases, the key ideas, primary contributions, experimental designs, data analysis, interpretation, and writing were performed by the author. The contribution of co-authors was primarily through the provision of relationship between parameters of material extrusion process and strength. Luis Fernando Villalpando contributed to the statistical analysis and graphing results; Hasti Eiliat provided feedback on refinement of ideas and editing of the manuscript.

I am aware of the University of Windsor Senate Policy on Authorship and I certify that I have properly acknowledged the contribution of other researchers to my dissertation, and have obtained written permission from each of the co-author(s) to include the above material(s) in my dissertation.

I certify that, with the above qualification, this dissertation, and the research to which it refers, is the product of my own work.

II. Previous Publication

This dissertation includes seven original papers that have been previously published/submitted for publication in peer reviewed journals, as follows:

Dissertation Chapter	Published title/full citation	Published status
Chapter 1	Using Genetic Algorithms to Optimize the Build Orientation for Fused Deposition Molded Components Containing Internal Reinforcement Structures. Hasti Eiliat and Ruth Jill Urbanic. 2014, ASME International Mechanical Engineering Congress and Exposition, Montreal, Quebec, Canada [1].	Published
Chapter 1	Experimental Evaluation of Light-weighting Design Options for the Fused Deposition Modelling Process. Hasti Eiliat, Ruth Jill Urbanic, and Luis Fernando Villalpando. 2015, 65th Annual Conference and Expo of the Institute of Industrial Engineers, Nashville, Tennessee, USA [2].	Published
Chapter 2	An Optimization Approach for Components Built by Fused Deposition Modeling with Parametric Internal Structures. Luis Fernando Villalpando, Hasti Eiliat, and Ruth Jill Urbanic. 2014, 47th CIRP International Conference on Manufacturing Systems, Vol. 17, pp. 800-805 [3].	Published
Chapter 3	Minimizing Voids with Using an Optimal Raster Orientation and Bead Width for a Material Extrusion Based Process. Hasti Eiliat and Ruth Jill Urbanic. 2016, ASME International Mechanical Engineering Conference and Exposition, Phoenix, Arizona, USA [4].	Published
Chapter 3	Minimizing Voids for a Material Extrusion Based Process. Hasti Eiliat and Ruth Jill Urbanic. 2018, Rapid Prototyping Journal, pp. 1-23 [5].	Published
Chapter 4	Visualizing, Analyzing, and Managing Voids in the Material Extrusion Process. Hasti Eiliat and Ruth Jill Urbanic. 2018, Advanced Manufacturing Technology Journal, pp. 1-15 [6].	Published
Chapter 5	Determining the Relationships between the Build Orientation and Voids in Additive Manufacturing Material Extrusion Processes. Hasti Eiliat and Ruth Jill Urbanic. 2018, Advanced Manufacturing Technology Journal	Submitted

I certify that I have obtained a written permission from the copyright owner(s) to include the above published material(s) in my dissertation in Appendix A. I certify that the above material describes work completed during my registration as a graduate student at the University of Windsor.

III. General

I declare that, to the best of my knowledge, my dissertation does not infringe upon anyone's copyright nor violate any proprietary rights and that any ideas, techniques, quotations, or any other material from the work of other people included in my dissertation, published or otherwise, are fully acknowledged in accordance with the standard referencing practices. Furthermore, to the extent that I have included copyrighted material that surpasses the bounds of fair dealing within the meaning of the Canada Copyright Act, I certify that I have obtained a written permission from the copyright owner(s) to include such material(s) in my dissertation.

I declare that this is a true copy of my dissertation, including any final revisions, as approved by my dissertation committee and the Graduate Studies office, and that this dissertation has not been submitted for a higher degree to any other University or Institution.

ABSTRACT

A problem with the planning solutions for the additive manufacturing material extrusion process is a lack of optimization strategies to improve upon the standard raster and contour toolpaths. After experimental testing, it was recognized that a component's strength relationship with respect to the volume of material usage is inconsistent and that failures occurred in regions of voids. From previous studies, it was found that a build orientation in the material extrusion process influences the support material requirements, processing time, surface finish, voids volume, etc. This dissertation aims to identify, minimize, and manage void regions during the toolpath generation, and studies the effects of build orientation on the amount and location of unwanted voids in the finished part. This includes comparing all possible build orientations to minimize voids in each layer, preventing void regions from being stacked in 3D, and avoiding creating an internal chimney. This approach is divided into three phases. Phase I is minimizing voids in each layer, phase II is identifying and managing voids between layers, and the third phase is comparing the total voids in all possible build orientations. Material extrusion processes, with a wide selection of nozzle sizes (0.4 mm to 21 mm), are considered suitable candidates for this solution. To carry out this study, a literature review was performed to understand the influence of the build parameters. Then, an analysis of valid parameter settings to be targeted was performed on a commercial system. The mathematical model is established based on the component geometry and the available build options for a given machine-material configuration. A C++ program has been developed to select a set of standard (available) toolpath parameters to determine the optimal output process variables (bead width, raster angle, and the overlap percentage), managing voids between layers, and compare total voids in all possible build orientations. Case studies are presented to show the merits of this approach. It is found that the entire void area is significantly reduced (~7%) with the phase I, by 5% with the second phase, at least 11% with phase III.

DEDICATION

This dissertation is dedicated to my family and my friends, especially ...

Charlie

ACKNOWLEDGEMENTS

I would like to thank my advisor, Dr. Urbanic, for sharing her wisdom and expertise with me throughout this research. Her guidance and supervision for establishing the project are appreciated. I also would like to thank Dr. Caron for reviewing the work throughout the process and for his suggestions on the mathematical model.

I would like to express my appreciation to my committee members, Dr. Wang and Dr. Zhang, for their time and consideration. I am thankful to CAMufacturing Solution, Inc., specifically Bob Hedrick for the support and patience during this initiative.

I could have never finished this task without the support and encouragements from Dr. Mary Anne Johnston. I am thankful for her guidance and her open arms and ears. I would like to thank my best friend, Hamed, who brings happiness and peace in my life

I thank my parents for their help and support. Also, I want to thank my angel sister, Dr. Hoda Eiliat, for her faithful friendship and encouragement.

Lastly, I wish to thank my colleagues, friends, and everyone who shared a part of their time and knowledge in the completion of this dissertation.

TABLE OF CONTENTS

DECLARATION OF CO-AUTHORSHIP / PREVIOUS PUBLICATION	iii
ABSTRACT	vi
DEDICATION	vii
ACKNOWLEDGEMENTS	viii
LIST OF TABLES	xi
LIST OF FIGURES	xiii
LIST OF APPENDICES	xviii
LIST OF ABBREVIATIONS	xix
NOMENCLATURE	xxi
CHAPTER 1 INTRODUCTION	1
Material Extrusion Process	1
Typical Materials	3
Process Planning	5
Classifications	10
Advantages and Disadvantages	15
Dissertation Objectives and Main Contribution	17
Dissertation Outline	25
CHAPTER 2 LITERATURE REVIEW	27
Toolpath Parameters	27
Build Orientation	27
Bead Height	30
Bead Width	33
Percent Overlap	35
Raster Angle	37
Toolpath and Strength	38

Toolpath on Surface Finish and Accuracy.....	42
Generating New Toolpath.....	43
CHAPTER 3 METHODOLOGY	45
Phase I _ Optimizing Voids Area	45
Determining Toolpath Parameters	48
Determining Voids Area.....	54
Phase II _ Optimizing Voids Position.....	60
Managing Nozzle Movements	62
Managing Voids Position.....	69
Covering Voids	75
Phase III _ Optimizing Build Orientation.....	77
CHAPTER 4 EXPERIMENTS FOR PHASE I AND II.....	82
Solid Shapes.....	83
Non-Solid Shapes	91
Combination of Solid and Non-Solid Shapes	96
CHAPTER 5 EXPERIMENTS FOR PHASE III	111
CHAPTER 6 CONCLUSIONS AND FUTURE RESEARCH	120
REFERENCES	126
APPENDICES	137
Appendix A.....	137
Appendix B.....	141
Appendix C.....	143
Appendix D.....	148
Appendix E	151
Appendix F	152
VITA AUCTORIS	154

LIST OF TABLES

Table 1. Example of some build materials for the material extrusion process [18] _____	4
Table 2. Characteristics of ABS and PC materials _____	5
Table 3. OEM software for material extrusion process [21] _____	8
Table 4. Characteristics of different material extrusion processes _____	11
Table 5. Control and fixed parameters for Fortus 400 machine [18] _____	12
Table 6. Stratasys machine series [18] _____	13
Table 7. Comparison of decision making for the FDM and RepRap machines _____	14
Table 8. Comparison between injection molding and material extrusion process for Figure 11 _____	16
Table 9. Comparison of time, build and support materials for open face up and down of Figure 19 _____	22
Table 10. Comparison of time, build and support materials for open face up and down of Figure 20 _____	23
Table 11. Comparison of time, build and support materials for optimal position _____	23
Table 12. Results of changing the part orientation _____	27
Table 13. The new height of the car seat with different bead height in the OEM software _____	31
Table 14. Different kinds of the air gap _____	36
Table 15. Literature review on toolpath parameters and strength _____	39
Table 16. The literature review of toolpath parameters and surface finish/accuracy _____	44
Table 17. The relationship between bead height and bead width for a Fortus 400 mc and the insight® software _____	46
Table 18. An optimal combination of bead heights to produce Figure 29 _____	49
Table 19. The relationship between raster angle, bead width and overlaps for Figure 43 (b and c) _____	52
Table 20. The relationship between toolpath parameters and the edge voids area _____	58
Table 21. Voids possibility matrices for some simple shapes _____	65
Table 22. Methods for dividing concave shapes _____	66
Table 23. Details of points and area of voids in the first layer of Figure 58 _____	70
Table 24. Details of points and area of voids in the first layer of Figure 59 _____	71
Table 25. Details of points and area of voids in the first layer of Figure 60 _____	72
Table 26. The formula of voids points _____	73
Table 27. Category of shapes _____	82
Table 28. Target applications for this dissertation _____	83
Table 29. Convex and concave shape examples _____	84
Table 30. Convert concave shape to convex shape _____	84
Table 31. Parameters of the solid hexagonal shape _____	85
Table 32. Cover and Uncover Voids _____	86
Table 33. Comparison voids for the solid hexagonal shape _____	87
Table 34. Information of new model for seven-side non-symmetric convex shape _____	89

Table 35. Comparison voids for seven-side non-symmetric convex shape	89
Table 36. Comparison voids for multiple 2D geometry extrusions examples	90
Table 37. Comparison voids for Figure 81(a)	92
Table 38. Comparison voids for Figure 82	94
Table 39. Comparison voids for Figure 83	96
Table 40. Calculating an optimal bead width and overlap for section 5 in Figure 85	97
Table 41. Comparison voids for Figure 82	97
Table 42. Details of each layer for each solid convex shape	98
Table 43. Comparison the OEM software with the first and second approaches of the new model with overlaps limit 50%	103
Table 44. Difference between the OEM software (for the seat orientation shown) and the new model with different overlaps limit	107
Table 45. Comparing voids in different rotation around X and Y axes	110
Table 46. Comparing cases parameters when the allowable overlaps are 0% and 50%	115
Table 47. ANOVA for car seat case study	116
Table 48. Voids volume with OEM software	116
Table 49. Pros and cons of the three phases	122
Table 50. (a to e) examples of dividing different concave shapes	143

LIST OF FIGURES

Figure 1. Seven categories of additive manufacturing processes: (a) Material Extrusion [9], (b) Powder Bed Fusion [10], (c) Vat Photo Polymerization [11], (d) Binder Jetting [12], (e) Material Jetting [13], (f) Sheet Lamination [10], and (g) Directed Energy Deposition [14]	2
Figure 2. Material extrusion process [16]	2
Figure 3. (a) A four-layer cylinder, (b) Top view of the cylinder	3
Figure 4. Build and support materials (*.stl file is from [17])	3
Figure 5. Process planning for the material extrusion process	5
Figure 6. Relationship of resolution and number of triangles for a sphere [11]	6
Figure 7. Closed volume model features [17]	7
Figure 8. (a) Watertight 3D model, (b) Set of triangles to convert the 3D model to a *.stl file, and (c) Slice the part to 33 layers with bead height 0.254 mm	8
Figure 9. Two classifications for the material extrusion process	10
Figure 10. A strength comparison of different types of processes [26] [27]	15
Figure 11. An example for comparison between injection molding and material extrusion process	16
Figure 12. Interior light weighting strategies inspired a primitive atomic crystal structure [29]	17
Figure 13. (a) Sample with strategically placed interior voids, (b) Comparison of the compressive strength of the material used	18
Figure 14. Tensile failure point with ABS and polycarbonate materials (adapted from [4])	18
Figure 15. (a) Direction parallel toolpath, (b) Contour parallel toolpath (adapted from [4])	18
Figure 16. Voids in the tensile specimen	19
Figure 17. Voids and discontinuity (a) Direction parallel toolpath and voids for one layer, and (b) Contour parallel toolpath and voids for one layer.	19
Figure 18. Different rotation of one part	20
Figure 19. Bottom vent cover geometry and time and material build estimates	21
Figure 20. Cover vent cover geometry and time and material build estimates	22
Figure 21. Different rotation and position of voids	24
Figure 22. Problem statement in the process planning of material extrusion process	25
Figure 23. The comparison of (a) The build and support materials (cm ³), (b) Number of layers and (c) Build times (min) for the 0°, 45° and 90° rotations about the X-axis	28
Figure 24. (a), (b) Part orientation influences the tensile strength of the sample (b) being weaker than sample (a) in the longitudinal direction	28
Figure 25. The relationship between part orientation and compressive strength on surface “A”	29
Figure 26. The relationship between build orientation and voids (a) 90° around the X-axis, and (b) 30° around the Y-axis	29
Figure 27. Available bead height	30

Figure 28. Compare the final height of part (a) and the height of the finished part after using available bead heights in Figure 27 (b to e)	30
Figure 29. Car seat example with height, 150.0086 mm	31
Figure 30. One part with different bead heights (a) 0.254 mm and (b) 0.127 mm	32
Figure 31. The relationship between bead height and voids in the first layers, (a) bead height 0.1270 mm (b) bead height 0.3302 mm	32
Figure 32. The relationship between feeding rate/ linear speed and bead width	33
Figure 33. Top view of one layer with bead width (a) 0.4016 mm and (b) 0.8314 mm	33
Figure 34. Comparison of voids between two different bead width sizes, (a) 3D model, (b) layer with 0.4064mm bead width, and (c) 0.8314 mm bead width	34
Figure 35. The relationship between the bead width with time and surface finish (the sample parts are from [41])	35
Figure 36. Zero air gaps, bead width, and bead height	36
Figure 37. One part with or without overlaps with two different bead width sizes	37
Figure 38. Compare three toolpath with raster angle (a) 0° , (b) 45° , and (c) 30°	38
Figure 39. Three phases for minimizing total voids in the material extrusion processes	45
Figure 40. Phase I process flow diagram	47
Figure 41. (a) Slicing the part to four layers with bead height S_j , (b) Points and lines in a layer	47
Figure 42. Compare the final height and number of layers with bead heights from Figure 27	49
Figure 43. The relationship between raster angle and the bounding rectangle, (a) $r=0^{\circ}$ and (b) $r=135^{\circ}$	50
Figure 44. W_r Of one layer when the raster angle is, (a) 0° and (b) 45°	51
Figure 45. (a) Optimal bead with and (b) Optimal overlaps per raster angle from 0° to 179° for one layer of Figure 43(a)	53
Figure 46. Three categories of voids – (a) corner, (b) edge, and (c) contour center	54
Figure 47. The relationship between corner void with (a) $g_l=50^{\circ}$, (b) $g_l=100^{\circ}$, and (c) $g_l=160^{\circ}$ with two bead width sizes: (left) 20 mm and (right) 40 mm	55
Figure 48. (a) Exact screenshot of a layer in the real OEM software, (b) Sorting Ψ_t for this layer	56
Figure 49. The relationship between raster angle and voids area for an optimized bead width with (a) 40° raster angle without overlaps, (b) 55° raster angle without overlaps, (c) 40° raster angle with a 15% overlap condition.	57
Figure 50. Steps of Phase I	60
Figure 51. Phase II diagram added to phase I diagram	61
Figure 52. Nozzle movements, (a) Shape of a layer, (b) Contour toolpath, (c) Position of rasters, (d) Stop and start points, (e) Nozzle path, and (f) Complete nozzle movements	63
Figure 53. Difference between convex (a) and concave (b) shapes.	64
Figure 54. Triangle example for voids place	65
Figure 55. Example of shapes with an internal hole	67

Figure 56. (a) 3D view, (b and c) First Layer (4 regions) and second Layer (5 regions) before connecting start points of some regions, (d) after connecting 0% overlaps, (e) 50% overlaps	68
Figure 57. (a) Layer with triangle shape example, (b) Relationship of raster angle and voids, (c) relationship of bead width, overlap, and raster angle	69
Figure 58. Void regions for the layer with 0° raster angles	70
Figure 59. Void regions for the layer with 30° raster angles	71
Figure 60. Void regions for the layer with 120° raster angles	72
Figure 61. Combination voids for the three layers, respectively and the black circles show the voids which are not covered by these three layers	72
Figure 62. Position of voids	73
Figure 63. The position of voids with points' illustration	74
Figure 64. (a) 3D view, (b) Logic of tracking voids between layers	75
Figure 65. Example for phase II, 22 layers for a specific build orientation of a box	76
Figure 66. Difference between voids when the start point of the nozzle is on the (a) left side or (b) right side	76
Figure 67. (a) The voids of the layer that need to be covered by next layer, (b) adding one more contour	77
Figure 68. Color code of Figure 39, Phase I (blue), phase II (green), and phase III (orange)	77
Figure 69. Rotation around X and Y axes	79
Figure 70. 3D example of rotation around X and Y axes	80
Figure 71. The position of voids of different rotations around X and Y axes	81
Figure 72. The position of voids around a dice	81
Figure 73. (a) Insight® software toolpath, (b) Voids in part after processing	85
Figure 74. Three optimal layers for the Table 31	86
Figure 75. (a to c) Optimal layers for the hexagonal shape, (d) finished part after processing	87
Figure 76. Infinite-side shape with twelve layers	88
Figure 77. Seven-side non-symmetric convex shape	88
Figure 78. Compare first (a) and second (b) layers in the existing OEM software	88
Figure 79. Covering voids between seven layers	90
Figure 80. Multiple 2D extruded shapes with their blueprints (mm) (adapted from [4])	91
Figure 81. (a) 3D example of the shape with internal holes (b) Blueprint (mm), (c) Optimal splitting (adapted from [4])	92
Figure 82. (a) Complex shapes with holes and its blueprint, (b) dividing complex shapes, and (c) connection rasters between the divided shapes	93
Figure 83. Examples of shapes with internal holes	94
Figure 84. Optimal splitting of Figure 83	95
Figure 85. Divided the complex shape to seventeen solid convex shapes	96
Figure 86. Producing the Figure 85 with Fortus 400 Machine	99

Figure 87. Cluster/grouping bead width for Figure 85	99
Figure 88. Cluster/grouping raster angle for Figure 85	100
Figure 89. Cluster/grouping overlap for Figure 85	100
Figure 90. Car seat example, (a) 3D model, 0° with X and Y axes, and (b) Slice it during Z-axis	101
Figure 91. (a) The first layer, (b) The second layer, (c) The third layer, and (d) Relationship between raster angle and voids area for layers 1, 2, and 3, with the 45°/-45° solution highlighted	102
Figure 92. Actual percentage overlap bins	103
Figure 93. Multiple layers of the car seat example	104
Figure 94. The relationship between Raster Angle and Voids Area for Layers 1 st , 6 th , and 8 th	105
Figure 95. The sensitivity of the new model with its constraints, the relationship between layers and (a) overlaps, (b) bead width, (c) voids area by changing maximum allowable overlaps	106
Figure 96. Different voids area in the first layer with part rotation with Z-axis (a) 90°, (b) 60°, and (c) 150° in the OEM software – note the standard raster angle is relative to the machine ‘world coordinates’	108
Figure 97. 3D view, support materials and the first layer when Figure 90, (a) 60° rotates around X-axis, (b) 60° rotates around Y-axis, and (c) 60° rotates around X and Y axes	109
Figure 98. Comparing voids, processing time, number of layers, and support materials in different rotation around X and Y axes	110
Figure 99. Three case studies with 0° rotations around X and Y axes(a) Toy car seat, (b) Valve cover I, and (c) Valve cover II	111
Figure 100. The rotation which has the minimum voids for each part	112
Figure 101. Bead width and overlaps per layer for (a) Car seat and (b) Valve cover I and II	113
Figure 102. Comparison of time and support material between two optimal orientations	113
Figure 103. Optimal rotation to minimize voids with overlap percent set to 0%	114
Figure 104. a) Voids per rotations and (b) Comparing voids in the small range of rotations	117
Figure 105. The frequency of voids with the new model for the car seat case with 50% allowable overlaps	118
Figure 106. The frequency of voids with the new model for the valve cover II study with 50% allowable overlaps	118
Figure 107. The worst rotation for car seat case study	119
Figure 108. Algorithm for minimizing and managing voids	121
Figure 109. Complex 3D parts	123
Figure 110. Toolpath with connection rasters (a) and no continuity between rasters (b)	123
Figure 111. Unwanted overlaps of start and stop points between layers	124
Figure 112. (a) 3D geometry and cross-section of the specimen with three overlapped beads. (b) Average hardness values in the bead and substrate for specimens [93]	124
Figure 113. Comparison between injection molding process and material extrusion process [94]	125

Figure 114. Voids volume (mm ³) per rotation around X and Y axes for a Car seat with allowable overlaps (a) 50% and (b) 0%	148
Figure 115. Voids volume (mm ³) per rotation around X and Y axes for Valve cover I with allowable overlaps (a) 50% and (b) 0%	149
Figure 116. Voids volume (mm ³) per rotation around X and Y axes for Valve cover II with allowable overlaps (a) 50% and (b) 0%	150
Figure 117. (a) 3D model, (b) Voids in the OEM software toolpath, (c) Expectation of the new model toolpath	152
Figure 118. (a) 3D model of tensile strength sample, (b) the view of 3D model from Z and X axis, and (c) Layers of the sample	153
Figure 119. Three examples with different internal structures	153

LIST OF APPENDICES

Appendix A: Published/submitted papers—Acceptance/Permission Letter _____	137
Appendix B: Additive Manufacturing Categories _____	141
Appendix C: Voids Possibility Matrix _____	143
Appendix D: Total Voids per Build Rotation _____	148
Appendix E: Mathematical Model Steps _____	151
Appendix F: Future Work _____	152

LIST OF ABBREVIATIONS

3DP™	3D Printing
3SP™	Scan, Spin, and Selectively Photo cure
ABS	Acrylonitrile Butadiene Styrene
AM	Additive Manufacturing
AM-ME	Additive Manufacturing Material Extrusion
ASTM	American Society for Testing and Materials
BAAM	Big Area Additive Manufacturing
CAD	Computer Aided Design
CLIP™	Continuous Liquid Interface Production
CNC	Computer Numerical Control
DED	Directed Energy Deposition
DLP™	Digital Light Processing
DMD™	Direct Metal Deposition (DM3D)
DMLS™	Direct Metal Laser Sintering
EBM™	Electron Beam Melting
FDM™	Fused Deposition Modeling
FFF	Fused Filament Fabrication
LENS™	Laser Engineered Net Shaping
LMD	Laser Metal Deposition
LOM	Laminated Object Manufacture
LSAM	Large Scale Additive Manufacturing
MAAM	Medium Area Additive Manufacturing
MJF™	Multi-Jet Fusion
MJM	Multi-Jet Modeling
OEM	Original Equipment Manufacturer
PBF	Powder Bed Fusion
PC	Polycarbonate

SAAM	Small Area Additive Manufacturing
SCP™	Smooth Curvatures Printing
SDL	Selective Deposition Lamination
SHS™	Selective Heat Sintering
SLA™	Stereolithography Apparatus
SLM™	Selective Laser Melting
SLS™	Selective Laser Sintering
UAM	Ultrasonic Additive Manufacturing

NOMENCLATURE

B_l^r	Binary voids possibility in edge l with raster angle r .
\hat{e}_l	Angle between the edge l and X axis.
ε	Tolerance of the part height (mm).
$f \in F$	New convex shapes after dividing a concave shape.
\hat{g}_l	Angle of corner l .
H	Height of the part (mm).
$i \in I$	Bead width.
$j \in J$	Bead height.
$l \in L$	Integer number of corners for layer q .
M_q^f	Voids possibility matrix of profile f in layer q .
m	Total number of raster angles which are studied for layer q .
N_j	Integer number layers with bead height j .
n	Total number of edges in layer q .
O_i	Percentage of overlap with bead width w_i^j .
O^*	Maximum allowable percentage of overlap.
$q \in Q$	Integer number of layers.
r	Raster angle.
R_i	Integer number of rasters with bead width w_i^j .
s_{l+1}^l	Slope of the edge between corner l and $l + 1$.
S_j	Bead height j (mm).

$T(N_j)$	Number of total layers.
v_q^c	Area of corner voids for layer q (mm^2).
v_q^E	Area of edge voids for layer q (mm^2).
w_i^j	Bead width i for bead height j (mm).
W_r	Length between lowest and highest Y-axis (mm).
Ψ_t	Distance between Y-axis of two continuous corners (mm).
(x_r^l, y_r^l)	Point of corner l in the layer q with raster angle r .
Y_{l+1}^l, X_{l+1}^l	Formula of the edge between corner l and $l + 1$.
y_r^{max}	Maximum Y-axis in the bounding rectangle (mm).
y_r^{min}	Minimum Y-axis in the bounding rectangle (mm).
$(\mathcal{X}^{(\theta_x, \theta_y)}, \mathcal{Y}^{(\theta_x, \theta_y)}, \mathcal{Z}^{(\theta_x, \theta_y)})$	Point of *.stl file with θ_x and θ_y angles with X and Y axes.

CHAPTER 1

INTRODUCTION

The material extrusion process is one of several additive manufacturing (or 3D printing) procedures employed to fabricate a component or assembly without using special tools, fixtures, or human intervention. The material extrusion process is used in various industries like automotive, aerospace, education, and medical, etc. The most previous researchers have focused on the build orientation targeted reducing support material requirements, optimizing surface finish, etc. However, research needs to be performed to develop methodologies while considering the fill conditions concerning an optimal build orientation. The goal of this dissertation is identifying, minimizing, and managing void regions during the toolpath generation and studies the effects of build orientation and the amount of unwanted voids in the finished part. This chapter will explain how the toolpath leaves voids and why it impacts the strength and performance of a finished product. This chapter summarizes the background of the material extrusion process and describes machines, materials, classifications, advantages, and disadvantages of the material extrusion process. In the end, the problem statement, motivation, and dissertation outline are explained, individually.

Material Extrusion Process

S. Scott Crump is the inventor of Fused Deposition Modeling (FDMTM) and co-founder of Stratasys, Ltd in 1989 [7]. In late 1980s Additive Manufacturing Material Extrusion (AM-ME) processes were identified as a part of rapid prototyping or fixtureless manufacturing. The AM-ME process is the one of Additive Manufacturing (AM) process. The AM process is the process of building products by layering a material directly from a Computer Aided Design (CAD) model in a structured manner to fabricate a component or assembly. In 2010, the American Society for Testing and Materials (ASTM) group formulated a set of standards that classify the range of AM processes into seven categories [8], Figure 1 (a to g) shows these processes.

As it shows in the figure, each of these processes uses specific materials and descriptions. This dissertation focuses on material extrusion process (AM-ME) which Figure 1(a) shows and Appendix B, explains all AM processes in detail.

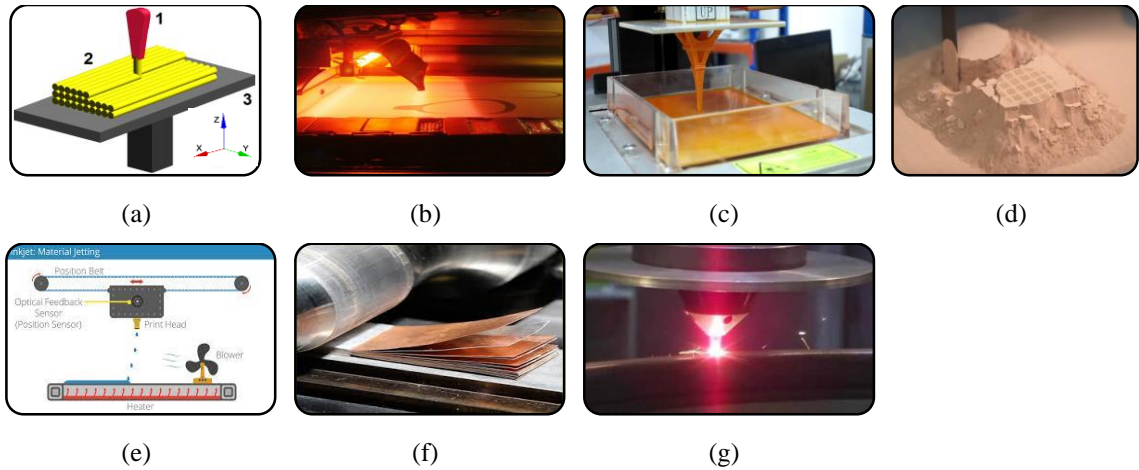


Figure 1. Seven categories of additive manufacturing processes: (a) Material Extrusion [9], (b) Powder Bed Fusion [10], (c) Vat Photo Polymerization [11], (d) Binder Jetting [12], (e) Material Jetting [13], (f) Sheet Lamination [10], and (g) Directed Energy Deposition [14]

As Figure 2 shows, the AM-ME process is a layering technology where each layer is built from extruded beads of material – typically a thermoplastic. In the AM-ME process, the material is extruded through a nozzle, where it is heated and then deposited in beads placed side by side. The component or assembly is built incrementally, layer by layer. The nozzle can move along the X and Y axes horizontally, and a platform (or deposition head) moves up or down vertically after each new layer is deposited [15].

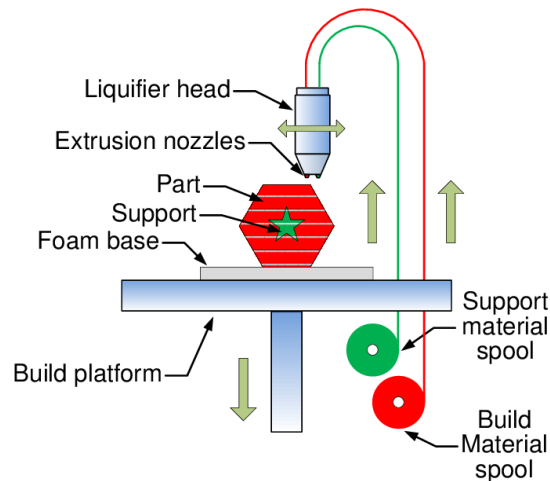


Figure 2. Material extrusion process [16]

The layers are positioned from bottom to top in AM-ME process. For example, the first layer in Figure 3 (a) is built as nozzle deposits material where required onto the cross-sectional area of the cylinder. The following layers are added on top of previous layers. Layers are fused together upon

deposition as the material is in a melted state. Figure 3 (b) shows a top view of the last layer which is layer 4. The top view shows how the nozzle had moved during the process, and how the toolpath creates voids. This process is independent of material in AM-ME. The next section explains types of material in AM-ME and names some of them in industry.

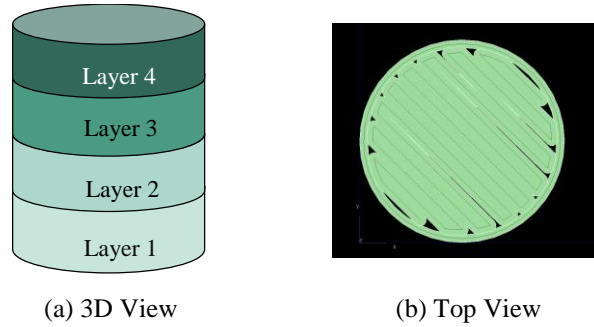


Figure 3. (a) A four-layer cylinder, (b) Top view of the cylinder

Typical Materials

There are two types of material in the AM-ME process which are the build material and support material. As it shows, for producing Figure 4 (a), the build material, red part of Figure 4 (b), and the support material, gray part of Figure 4 (c), are used during the process. In the end, the support material is needed to remove from Figure 4 (c) to get Figure 4 (a).

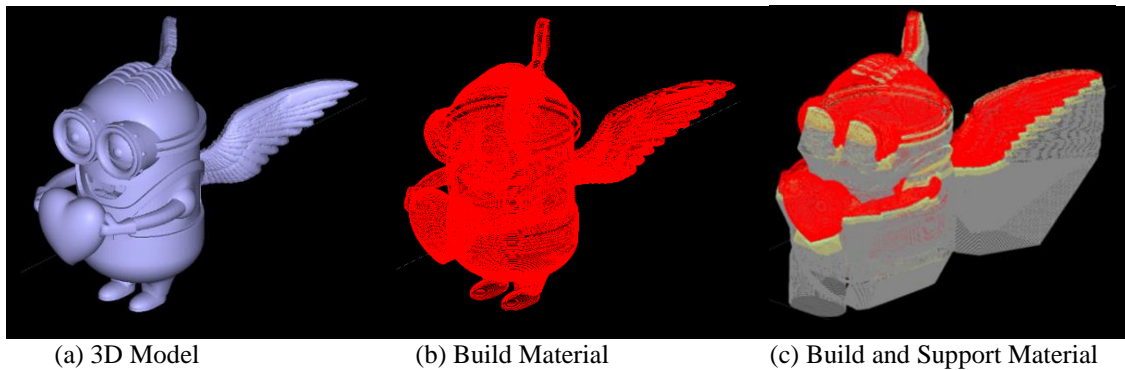














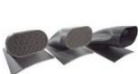


Figure 4. Build and support materials (*.stl file is from [17])

Table 1 shows the categories for some of the thermoplastic materials that are used in industry as the build material. The build material is divided into four groups; standard thermoplastics, engineering thermoplastics, high-performance thermoplastics, and sacrificial tooling material thermoplastics [18]. Table 1 describes the features and product examples for each kind of materials.

Table 1. Example of some build materials for the material extrusion process [18]

	Build Material	Feature	Product Example
Standard Thermoplastics	ABS-ESD7	Static dissipation	
	ABS plus	In 9 colors and has option for custom colors	
	ABSi	Translucence	
	ABS-M30	In six colors for high tensile, impact and flexural strength	
	ABS-M30i	Biocompatibility	
	ASA	In 10 colors for high mechanical strength, UV stability, and the best aesthetics	
Engineering Thermoplastics	FDM Nylon 6	Ductile engineering plastic	
	FDM Nylon 12	Maximum toughness	
	PC	Superior mechanical properties and heat resistance	
	PC-ABS	The highest impact strength, plus the mechanical properties and heat resistance of PC and the surface appeal of ABS	
	PC-ISO	Biocompatibility and superior strength	
High-Performance Thermoplastics	PPSF/PPSU	Highest heat and chemical resistance	
	ULTEM 1010	The highest heat resistance, chemical resistance and tensile strength of any FDM thermoplastic	
	ULTEM 9085	Best mix of mechanical, chemical and thermal properties	
Sacrificial Tooling Material	ST-130	Sacrificial cores that withstand the heat and pressure of composite lay-up and dissolve easily from hollow part interiors	

In this dissertation, Acrylonitrile Butadiene Styrene (ABS-M30) and Polycarbonate (PC) are used as the build materials, which are in the standard thermoplastics and engineering thermoplastics groups, respectively. Table 2 compares the characteristic of these two materials.

Table 2. Characteristics of ABS and PC materials

Characteristic	ABS	PC
Heat Deflection	96 °C	138 °C
Support Material	Dissolving	Breakaway
Price per m ³ [19]	~ \$27,500	~ \$50.000

The support material in the AM-ME process is Acrylonitrile Butadiene Styrene (ABS), Polycarbonate (PC), PPSF, ULTEM 1010, ULTEM 9085, or ST130. In this dissertation, ABS and PC are used as the support materials. The removal process for these two materials are dissolving and breakaway, respectively (Table 2).

Process Planning

The process planning of AM-ME is same for all materials. The AM-ME process is separated into six steps. The steps are categorized into three main groups; pre-processing, processing, and post-processing (Figure 5).

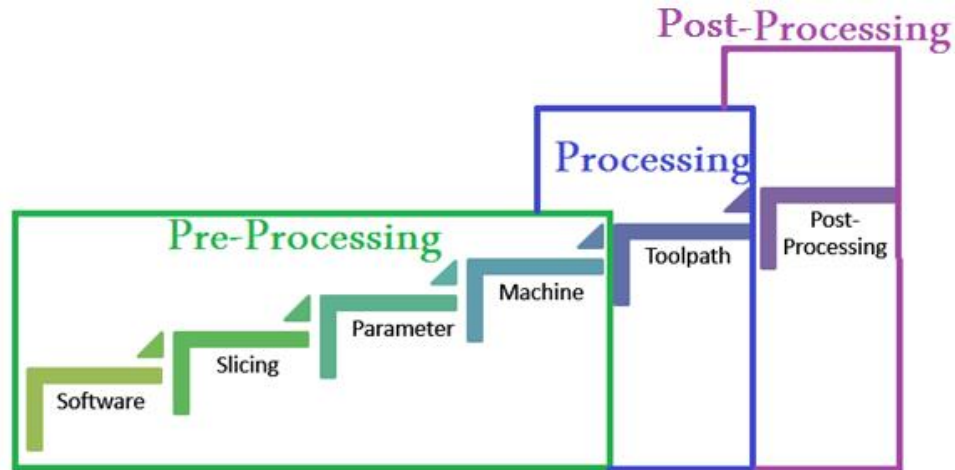


Figure 5. Process planning for the material extrusion process

Software, slicing, parameter, machine steps are in the pre-processing group. Below, these steps are explained deeply.

Software Step: The process planning is started by a 3D model which is developed by CAD software. The CAD software can be Autodesk Inventor, Catia, IronCAD, McNeel Rhino, ProEngineering, Solid Edge, SolidWorks, and UGS NX. SolidWorks is used as the CAD software in this dissertation. The CAD model needs to be a watertight or closed volume model (Figure 8 (a)). The reason is the closed volume 3D model can convert to a *.stl file. A *.stl file uses triangular facets to represent a shape, where each facet is defined regarding the coordinates of its three vertices [20]. The number of triangles is related to the size and resolution of the surface. As it shows in Figure 6 by increasing numbers of the triangles, the resolution of the sphere is improved.

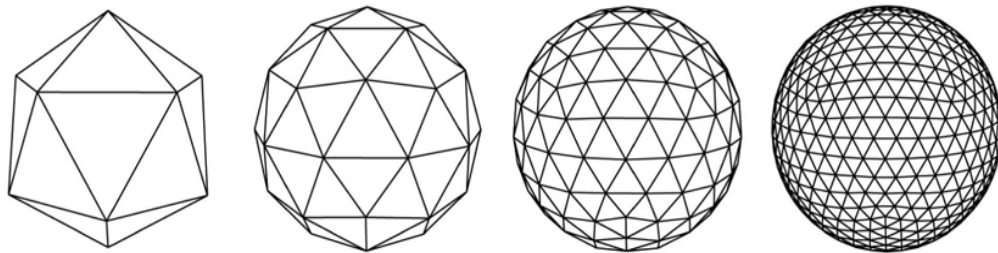


Figure 6. Relationship of resolution and number of triangles for a sphere [11]

The *.stl file is readable by the Original Equipment Manufacturer (OEM) software, i.e., Insight® or Catalyst® software. Thus, the 3D model needs to be comprised a set of triangles that are connected by their common edges or corners to be ready for the AM-ME machine. It means the 3D model needs to be a closed volume model. The features of the closed volume model are listed below

- (a) Every triangle edge has exactly two neighbors. It implies that there are no holes or non-manifold edges. (Figure 7 (a)).
- (b) Every node in the triangle is connected to only one "fan" of triangles around it. That is, for a given node, every triangle that shares that node must be accessible from any other triangle that shares the same node by moving across triangle edges (Figure 7 (b)).
- (c) There are no geometric overlaps or intersections in the model (Figure 7 (c, d)).

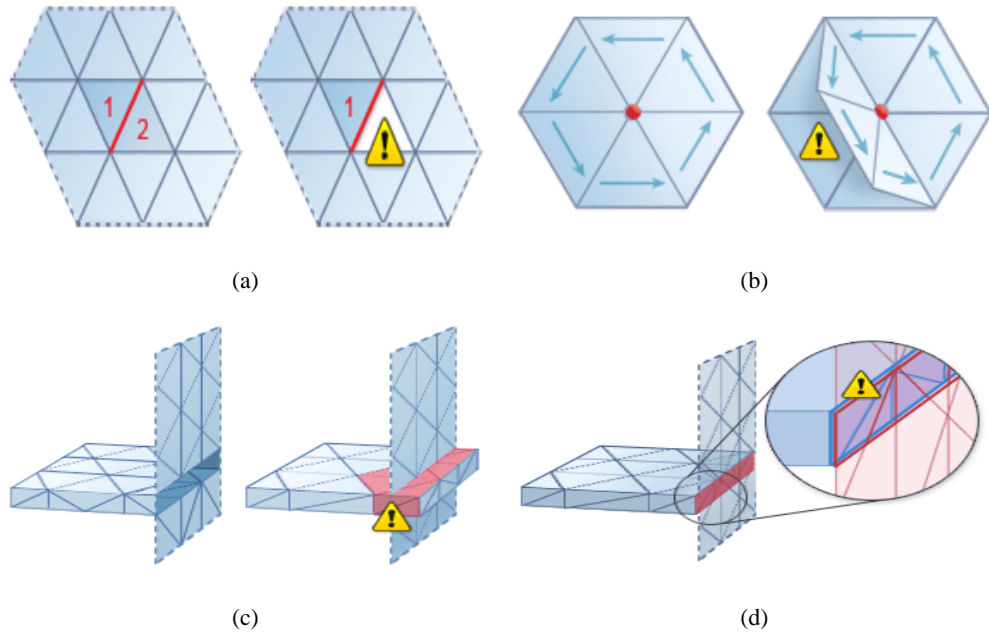


Figure 7. Closed volume model features [17]

Slicing Step: The OEM software is a type of control machine software to develop a build file from the *.stl file. Table 3 gives some examples of OEM software in the market. This dissertation uses Insight® software as an OEM software. This table describes the functions for each software. The slicer function for the OEM software, such as the Cura software, prepares the selected model and generates the G-code for a machine. The 3D printer host function allows users to control and monitor all activities from the web browser and handheld machines. The 3D design and CAD function enable users to change the 3D model before sending the model to machines. The STL checker, STL repair, and STL editor functions let users check, repair, and edit a *.stl file during printing the model, respectively.

Table 3. OEM software for material extrusion process [21]

Software	Function
Cura	Slicer, 3D Printer Host
CraftWare	Slicer, 3D Printer Host
Insight	Slicer, 3D Printer Host
Catalyst	Slicer, 3D Printer Host
123D Catch	3D Design, CAD
3D Slash	3D Design, CAD
TinkerCAD	3D Design, CAD
3DTin	3D Design, CAD
Sculptris	3D Design, CAD
ViewSTL	STL viewer
Netfabb Basic	Slicer, STL Checker, STL Repair
Repetier	Slicer, 3D Printer Host
FreeCAD	3D Design, CAD
Sketch Up	3D Design, CAD
3D-Tool Free Viewer	STL Viewer, STL Checker
Meshfix	STL Checker, STL Repair
Simplify3D	Slicer, 3D Printer Host
Slic3r	Slicer
Blender	3D Design, CAD
Mesh Lab	STL Editor, STL Repair
Meshmixer	STL Checker, STL Repair, STL Editor
OctoPrint	3D Printer Host

Figure 8 (b) shows the *.stl file of the 3D model (Figure 8 (a)) with a set of triangles. These triangles help the OEM software to slice the 3D model to different layers like Figure 8 (c). The next step in the AM-ME process is choosing process parameters.

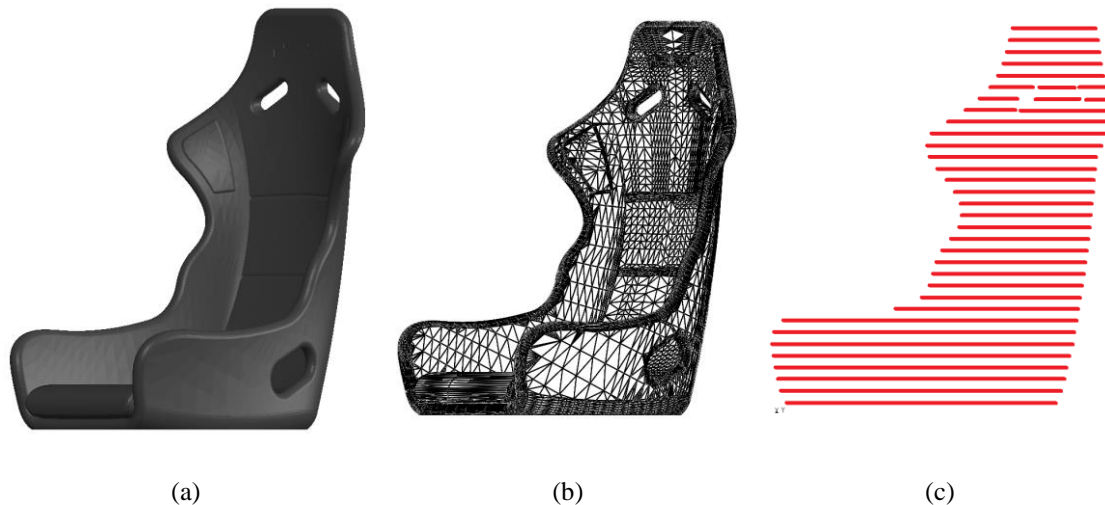


Figure 8. (a) Watertight 3D model, (b) Set of triangles to convert the 3D model to a *.stl file, and (c) Slice the part to 33 layers with bead height 0.254 mm

Parameter Step: The commercial OEM software employed to develop a process plan typically requires the user to input a material type, a fill strategy, and a slice height. The component position, orientation, and scale can also be altered. Depending on the software solution, the bead width may be changed from a default value, and tool path editing can be performed. The process parameter configuration for a material-bead geometry is highly coupled (i.e., changing the travel speed will change the bead height and width), but this is opaque to the user. Some software solutions have pre-set process parameter settings; other software tools require the user to establish the heating conditions, travel speed, material feed rate, and so forth. These software tools may help users to select parameters to improve the features of a finished part such as the surface quality, minimizing the support material, or choosing an orientation to fit the component in the build envelope.

Machine Step: This step is sending the build file (proprietary or open source format) to the machine. The build file contains information to tell the machine to move to the various points (X, Y and, Z) at the desired speed (toolpath). G-Code is a control language for AM-ME machine typically used for open source machines. The next section explains these type of machines. This step is the last step of the pre-processing group.

Toolpath Step: This step is AM-ME process, it starts with feeding the plastic filament through a heated nozzle where the material is melted and deposited onto a build platform. As layers are deposited onto the platform, each layer deposits on top of the other until the part is completed.

Post Processing Step: After finishing producing the part, post-processing needs to be done such as smoothing a rough surface finish, polishing, cleaning a part, or removing support material, etc.

As Figure 9 shows, there are two types of classifications based on process planning of AM-ME. These two classifications are classification based on nozzle size and classification based on the source machine. These two classifications will be described below, respectively.

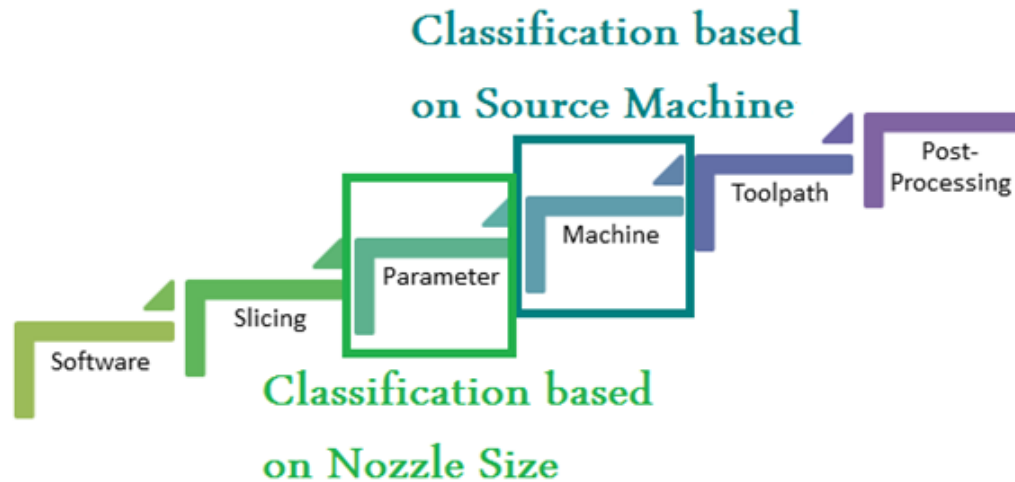


Figure 9. Two classifications for the material extrusion process

Classifications

In the market, there are different types of AM-ME process. This section will be described the two strategies for categorizing the AM-ME process. One is classified based on nozzle sizes, and the other one is based on process machines.

(a) Classification of Material Extrusion Based on Nozzle Size

The AM-ME process family includes systems with a wide variety of nozzle and available bead sizes, such as the Large Scale Additive Manufacturing (LSAM), Big Area Additive Manufacturing (BAAM), Medium Area Additive Manufacturing (MAAM), Small Area Additive Manufacturing (SAAM), and Fused Deposition Modeling (FDM). Table 4 presents a partial set of different achievable bead sizes for these AM-ME processes. This classification proves that the AM-ME are used for a wide variety of applications in the schools, automotive, aerospace, and medical domains with different sizes and qualities for both prototype and functional components. Consequently, there are extreme variants with the surface finish, build time, and the final component size for these AM-ME. The FDM and other small bead systems are ideal for components that fit within a 0.2 to 1 mm build envelop, as the bead widths vary from 0.13 to 1 mm. BAAM and LSAM processes are additive machines that produce beads with a 6 to 21 mm bead width and a 4 to 5 mm bead height. These systems are designed to allow AM-ME to be utilized for large scale (physical dimensions) production manufacturing, such as a car body. The size and speed of these systems enable large parts to be made quickly.

Table 4. Characteristics of different material extrusion processes

Process	Nozzle Diameter (mm)	Bead Width (mm)	Bead Height (mm)
LSAM [20] [4] 	15	5 - 21.08	5.08
BAAM [19] [20] 	7.6	6 - 10	4
MAAM [4] 	0.5-2.5	0.5 – 1.5	0.5 – 1.5
SAAM [23] 	0.4064	0.2032	0.1778 - 0.3048
FDM [24] 	0.4	0.4064 - 0.7112	0.127 - 0.33

(b) Classification of Material Extrusion Based on Source Machines

Closed (proprietary formats, limited process planning control) and open source machines are two kinds of machines for the AM-ME. These machines are described partially, below.







Closed Source Machine: Stratasys in Eden Prairie, Minnesota developed a closed source machine or the Fused Deposition Modelling (FDM) [18]. FDM machines have two semi-melted thermoplastics; the build material and support material. Both materials are extruded through two separate nozzles that trace the part cross sectional geometry layer by layer. The semi-melted thermoplastic hardens immediately after flowing from the nozzles and bonds to the layer below. Once a layer is built, the platform lowers, and the extrusion nozzles deposit another layer, it will shift 90° between each layer to maximize the strength between layers. Once the processing is completed for a layer, the Z-axis increments the appropriate amount, and the process is repeated. Then all support material needs to be removed after finishing the process. Most of the decision making parameters for the FDM process is determined automatically, which makes the process inflexible. The OEM software for this kind of machines automatically slice and generates the toolpath. This dissertation uses the Fortus 400 as a closed source machine. The maximum build size for the machine is 406 x 356 x 406 mm and parts are produced within an accuracy of +/- 0.127 mm. This machine is flexible to build complex 3D components. Table 5 shows the control and fixed parameters for the Fortus 400 machine.

Table 5. Control and fixed parameters for Fortus 400 machine [18]

Control Parameters		Fixed Parameters	
Bead width (mm)	0.4064 to 0.7112.	Maximum Part Dimensions (cm)	35.56 deep, 40.64 wide, 40.64 tall
XY Dimensional Tolerance (mm)	± 0.0015 or ± 0.127	Minimum “safe” wall thickness (mm)	3.175
Slip fit for shaft	0.254 larger than the shaft	Minimum wall thickness (mm)	0.9144
Press fit for the shaft (mm)	0.127 larger than the shaft	Minimum clearance between surfaces (mm)	0.1778
Air gap (mm)	(-0.0254) – (+2,54) Can safely be increased to 250% of the default	Minimum “safe” clearance between surfaces (mm)	0.3302
Part Orientation	0°- 90°	Model build temperature	367° F
Bead Height / Slice Height (mm)	0.127, 0.178, 0.254, 0.330	Raster Orientation	XYZ

FDM is created in 1989 by Scott Crump. It was one of the first commercially viable rapid prototyping technologies, now a part of Stratasys Inc. [18]. Table 6 shows different Stratasys machine series in the market.

Table 6. Stratasys machine series [18]

Machine		OEM Software	Build Envelope Size	Layer Thicknesses	Achievable Accuracy
Fortus 380mc		Insight	355 x 305 x 305 mm	0.330 mm 0.254 mm 0.178 mm 0.127 mm	± .127 mm or ± .0015 mm/mm
Fortus 450mc		Insight	406 x 355 x 406 mm	0.330 mm 0.254 mm 0.178 mm 0.127 mm	± .127 mm or ± .0015 mm/mm
Fortus 900mc		Insight	914.4 x 609.6 x 914.4 mm	0.508 mm 0.330 mm 0.254 mm 0.178 mm	+/- .089 mm or +/- .0015 mm/ mm
Conne3 Systems		Objet Studio	340 × 340 × 200 mm	0.01524 mm	20-85 micron for features below 50 mm; up to 200 microns for full model size
Object1000 plus		Objet Studio	1000 x 800 x 500 mm	0.01524 mm	Up to 85 microns for features smaller than 50mm; Up to 600 microns for full model size
Stratasys J750		Polyjet Studio	490 x 390 x 200 mm	14 microns (0.00055 in)	20-85 microns for features below 50 mm; up to 200 microns for full model size

Open Source Machine: An open source machine, such as the RepRap, work the same as a printer, but rather than ink, it puts down thin layers of material. The RepRap machine requires all decision-making parameters such as the travel speed, material feed rate, melting temperature or power requirements to be identified manually. The tool paths also need to be generated using appropriate software tools. Thus, working with a RepRap system, users need more knowledge of CNC machines and the control software. Determining the calibration configuration for a material-bead geometry set may take time because of the coupled relationships between the different variables.

Table 7 summarizes the difference between these two source machines. As the OEM software for the FDM process will automatically slice the STL file and generate the tool paths for both the build and support materials, is easier to use than the RepRap machine. In the RepRap machines, all parameters for the slicing, and generating a toolpath for the build and support materials need to be manually coded by the users. In below table, the multiple choice for closed source machine means advanced editing required to adjust the parameters.

Table 7. Comparison of decision making for the FDM and RepRap machines

	Close Source Machine	Open Source Machine
Type of Material	Multiple choices	Controlled by User
Type of Support Material	Multiple choices	Controlled by User
Slice Height	Multiple choices	Controlled by User
Bead Width	Multiple choices	Controlled by User
Air Gap	Multiple choices	Controlled by User
Raster Orientation	Multiple choice	Controlled by User
Part Orientation	Controlled by User	Controlled by User
Toolpath	Fixed	Controlled by User
Bed Size	Fixed	Fixed
Extrusion Temperature	Fixed	Controlled by User
Nozzle Diameter	Fixed	Fixed
Material Feed rate	Fixed	Controlled by User
Travel Speed	Fixed	Controlled by User

As same as other manufacturing processes, the AM-ME method has advantages and disadvantages. The below section explains pros and cons of the AM-ME process.

Advantages and Disadvantages

The AM-ME process is becoming more common [22] [23] [24] as this process uses reduced materials and energy to fabricate a component or assembly, and can be used to produce light, optimized products with minimal production operations [25]. However, the reasons why the AM-ME is becoming one of the essential manufacturing processes are

- This process uses less material, reusing material and producing lighter products with eliminating production steps in the other manufacturing processes.
- Products are built layer by layer instead of machining part from stock.
- Products can be fabricated as soon as the CAD model has been created.
- This process enables fabrication of designs with complex geometries that would be impossible to achieve using other procedures [25].
- It provides the ability to design products with more complex parts instead of many simpler parts [25].
- It enables rapid response to markets and creates new production options outside of factories.

However, same as other processes there are disadvantages. These disadvantages of the AM-ME process are

- The inherent problem with the AM-ME process is that the final fabricated product is weaker when compared AM-ME built component to other traditional manufacturing processes when using the same materials. It is due to the limited bonding between the layers, and between the side-to-side beads. Figure 10 shows a process comparison for strength between different manufacturing processes. It shows that the AM-ME process, compared to injection molding and plastic forming, is weaker.



Figure 10. A strength comparison of different types of processes [26] [27]

- The average speed of producing is around one to five cubic per inches per hour.
- The building time, high-quality machines and price of material are higher than other processes. For example, for producing Figure 11 with the AM-ME process with Fortus 400 machine, the total time is 1010 minutes, the build material is 583.08 cm³, and the support

material is 19.58 cm³. The bead height, bead width, and raster angle for this process are 0.254 mm, 0.6096 mm, and 45⁰, respectively.

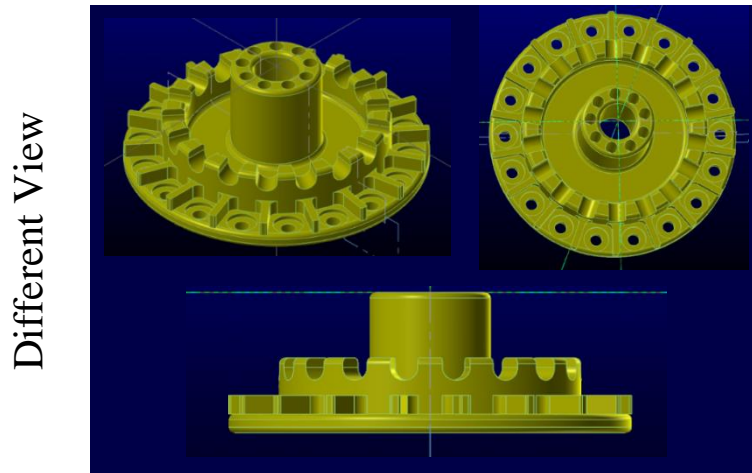


Figure 11. An example for comparison between injection molding and material extrusion process

Table 8 compares the total time process and cost of materials of the CNC machining process and AM-ME process for this product. The time and cost of the AM-ME process are seven times and three times more than the CNC machining process, respectively.

Table 8. Comparison between injection molding and material extrusion process for Figure 11

Process	Time of Process (min)	Cost of Total Material
CNC Machining	150	~ \$3
Material Extrusion	1010	~ \$17

- This process needs extensive knowledge of CAD design.
- The process has component size and materials options limitation.
- Layering and multiple interfaces cause defects in the product such taller and shorter product due to the slice height, discontinuities or voids.
- Parts are built one at a time. Thus it is preventing economies of scale.
- Not having variety toolpath for processing as compared to Computer Numerical Controlled (CNC) machining toolpath [2] [28].

Next section describes the dissertation objectives and main contribution.

Dissertation Objectives and Main Contribution

As it was explained before, one conventional material employed in the AM-ME process is ABS plastic. As the ABS, thermoplastic material costs are high compared to the other material (Table 8), preliminary research focused on balancing mechanical strength and material usage using a parametric interior light weighting strategy [29]. After testing some tensile and compression samples with strategically placed interior voids (Figure 12), unexpected repeatable results occurred, which are explained below.

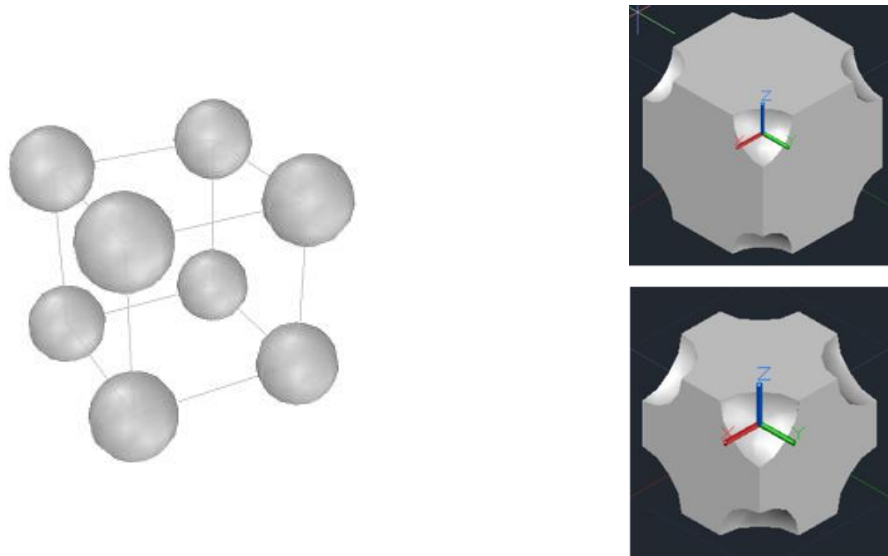


Figure 12. Interior light weighting strategies inspired a primitive atomic crystal structure [29]

In selected cases ((Figure 13 (a)), the compressive strength is weak for the volume material used (encircled value in Figure 13 (b)). Thus, unexpectedly, the build strength had an inverse relationship concerning the volume material usage in this case. For some components that exhibited this failure, the estimated volume of the build material to be utilized was approximately 12% less than the theoretical volume of the element but was in-line with other samples with similar material volumes. When performing compressive tests for specimens with differently designed interior pockets, the observed compressive forces varied between 19 and 30.5 kN for specimens with 52 cm³ (3.17 inch³) of material [4]. The experimental deviations between three test specimens for each compressive specimen's configuration are less than 1%.

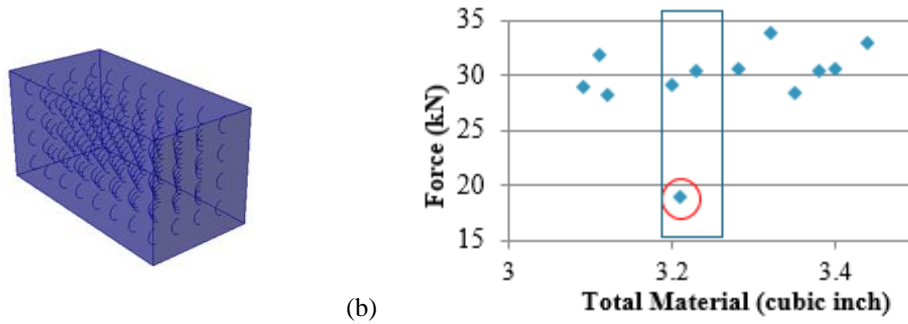


Figure 13. (a) Sample with strategically placed interior voids, (b) Comparison of the compressive strength of the material used

The other unexpected result is illustrated with the tensile test. The failure points are not in the center for several (most) cases. The cases are experiments with diverse internal raster fill angle orientations [20]. Figure 14 shows tensile specimens with different materials.

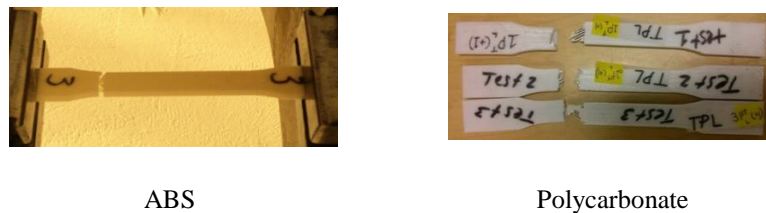


Figure 14. Tensile failure point with ABS and polycarbonate materials (adapted from [4])

The reason for these unusual tensile and compressive test results is due to the presence of unexpected voids created by the tool path deposition pattern. The toolpath in the AM-ME process is the trajectory of the nozzle or print head during the manufacturing process to fill the interior of each layer [30]. There are two kinds of toolpaths typically employed for the AM-ME process. The first one is a direction parallel toolpath for the interior area of the layer. The raster fill angle or the fill direction varies 90° between layers [31] and the second one is a contour parallel toolpath for the boundary of the layer [32]. Figure 15 shows these two toolpaths, respectively.



Figure 15. (a) Direction parallel toolpath, (b) Contour parallel toolpath (adapted from [4])

As Figure 16 shows, there are unwanted voids (which are the regions not covered with the material during the build process) between the contour tool path and the raster fill tool path for a tensile sample. In this figure, the raster angle, raster, contour, and bead width are shown, respectively.

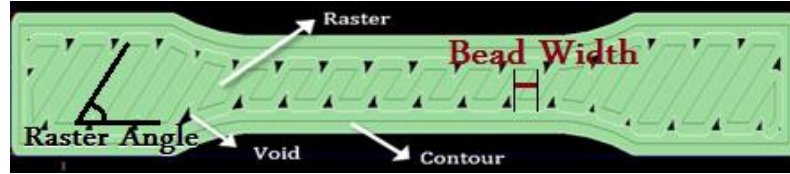


Figure 16. Voids in the tensile specimen

An additional issue is related to the start and stop points in the tool path. These introduce discontinuities, which reduces the strength, and typically occur near to the unwanted void regions (Figure 17 (a)). Having voids, discontinuities, and 3D voids that are interconnected through multiple layers (chimneys) will introduce internal failure points for a product. Therefore, this dissertation aims to identify voids region in a toolpath to minimize them in each layer, and to manage available build solutions to avoid creating an internal chimney condition. Figure 17 (a and b) illustrates two toolpath types, direction parallel, and contour parallel toolpath, respectively. The figure shows unwanted voids with both toolpaths, but the number, sizes, and locations vary. If this information can be captured, then these resultant voids can be reduced, or managed (i.e., repositioned).

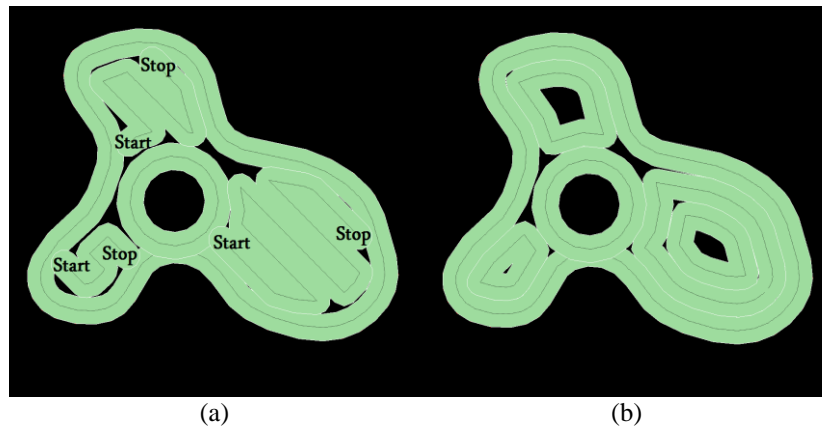
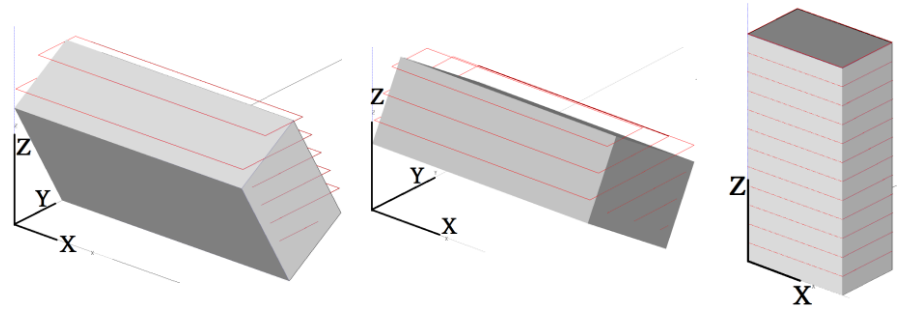


Figure 17. Voids and discontinuity (a) Direction parallel toolpath and voids for one layer, and (b) Contour parallel toolpath and voids for one layer.

The other issue is the component orientation in the build envelope influences the positions and areas for the voids. By changing the build orientation of the part, the number of slices and the cross-

sectional areas to be filled, along with the void regions within a component, will be different. Figure 18 shows the three different rotations for one part around the X and Y axes.

The figure shows the number of layers, the area of each layer, the volume of support materials, etc. are different between these build orientations. The bead height, bead width and raster angle for this example are 0.254 mm, 0.5064 mm, and 45°.



# of Layers	47	41	80
Support Material (cm ³)	0.926	1.558	0.203
Build Material (cm ³)	1.929	2.317	1.475
Average Volume per Layer	0.041	0.057	0.018
Time (min)	13	18	9
	(a)	(b)	(c)

Figure 18. Different rotation of one part

The next example shows the relationship between the build orientation and total materials. For example, the thin covers, with vent holes, are utilized to illustrate the positive and negative characteristics of the AM-ME processes. The cover in Figure 19 has a large surface volume, and wall thicknesses that vary between 1.2 - 2.0 mm. The vent holes or slots have a 0.4 mm radius. The cover has a bounding box of 394 x 166 x 81 mm and 370 vent holes.

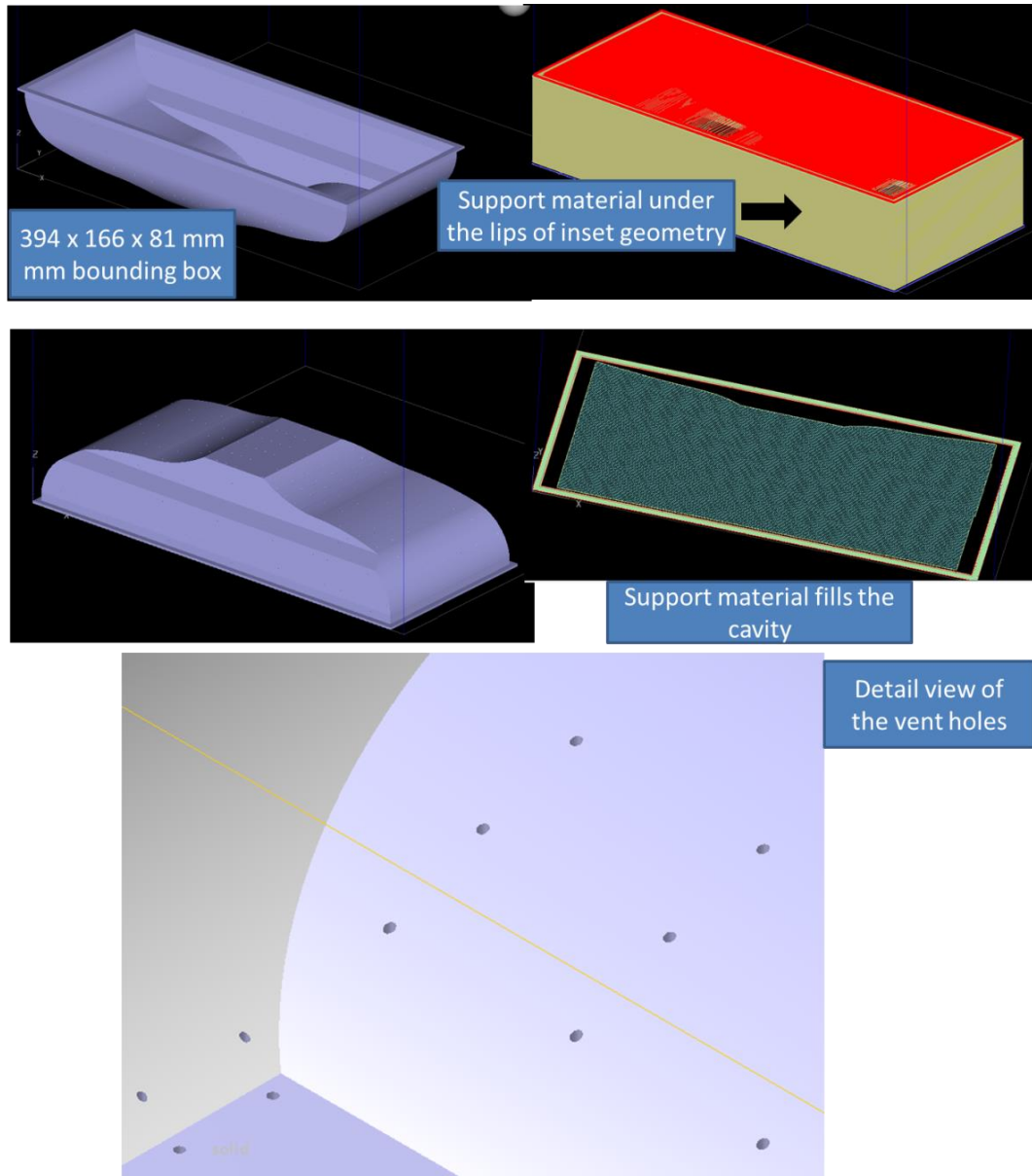


Figure 19. Bottom vent cover geometry and time and material build estimates

The build times are long for any build orientation, and there is support material required for overhanging structures (Table 9). The critical decisive characteristic for the AM-ME process family is that complex components such as this part can be readily manufactured using an AM-ME machine for a moderately low cost and reduced material waste compared to a machining solution; however, support material (here approximately $380 - 1010 \text{ cm}^3$) may be required. Consequently, support structure optimization has been designed to minimize support material requirements, and the standard build orientation optimization is linked with reducing support material requirements.

Table 9. Comparison of time, build and support materials for open face up and down of Figure 19

0.178 mm slice thickness, 2:1 ratio bead thickness: bead height

	Open face UP		Open face DOWN	
	Solid, Basic Supports	Solid Build & Sparse Support Material	Solid, Basic Supports	Solid Build & Sparse Support Material
Time	39hr 9 m	32 hrs. 3 m	58 hrs. 44 m	34 hrs. 59 m
Build (cm ³)	189.0	188.9	228.2	208.3
Support (cm ³)	646.8	384.4	1013.1	403.7
Total material	835.8	573.3	1241.3	612.0

A complementary venting cover (Figure 20 and Table 10) has an optimal build orientation, as there is one build orientation that minimizes support material and the total build time (Table 11).

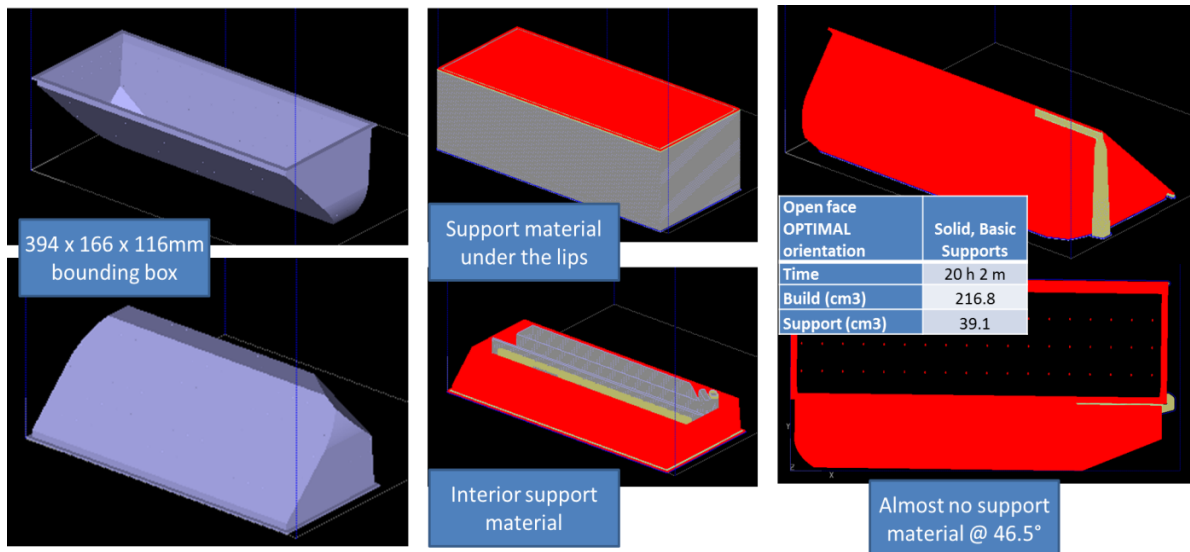


Figure 20. Cover vent cover geometry and time and material build estimates

Table 10 compares the time, build material, and support material for two positions shown in Figure 20.

Table 10. Comparison of time, build and support materials for open face up and down of Figure 20

0.178 mm slice thickness, 2:1 ratio bead thickness: bead height

	Open face UP		Open face DOWN	
	Solid, Basic Supports	Solid Build & Sparse Support Material	Solid, Basic Supports	Solid Build & Sparse Support Material
Time	43 h 47 m	36 hrs. 43 m	48 hrs. 33 m	37 hrs. 12 m
Build (cm ³)	264.5	252.6	278.7	251.1
Support (cm ³)	391.3	281.5	576.6	304.3
Total material	655.8	534.1	855.3	555.4

For the cover in Figure 19, the four build options were generated in less than 10 minutes. The generated tool path and the build parameters for the process are opaque to the user.

Table 11. Comparison of time, build and support materials for optimal position

Open face Optimal	Solid, Basic Supports
Time	20 h 2 min
Build (cm ³)	216.8
Support (cm ³)	39.1
Total material	255.9

As Figure 19 and Figure 20 show, the build orientation effects on time, build support materials. In the AM-ME process, by changing build orientation (XY plane versus the XZ plane), the volume of voids are adjusted, too. Figure 21 compares two build orientation and size of voids of one part. The green color shows the toolpath for the specific layer and the red color illustrates the voids in that layer. It can be seen that there are numerous interior voids during the process.

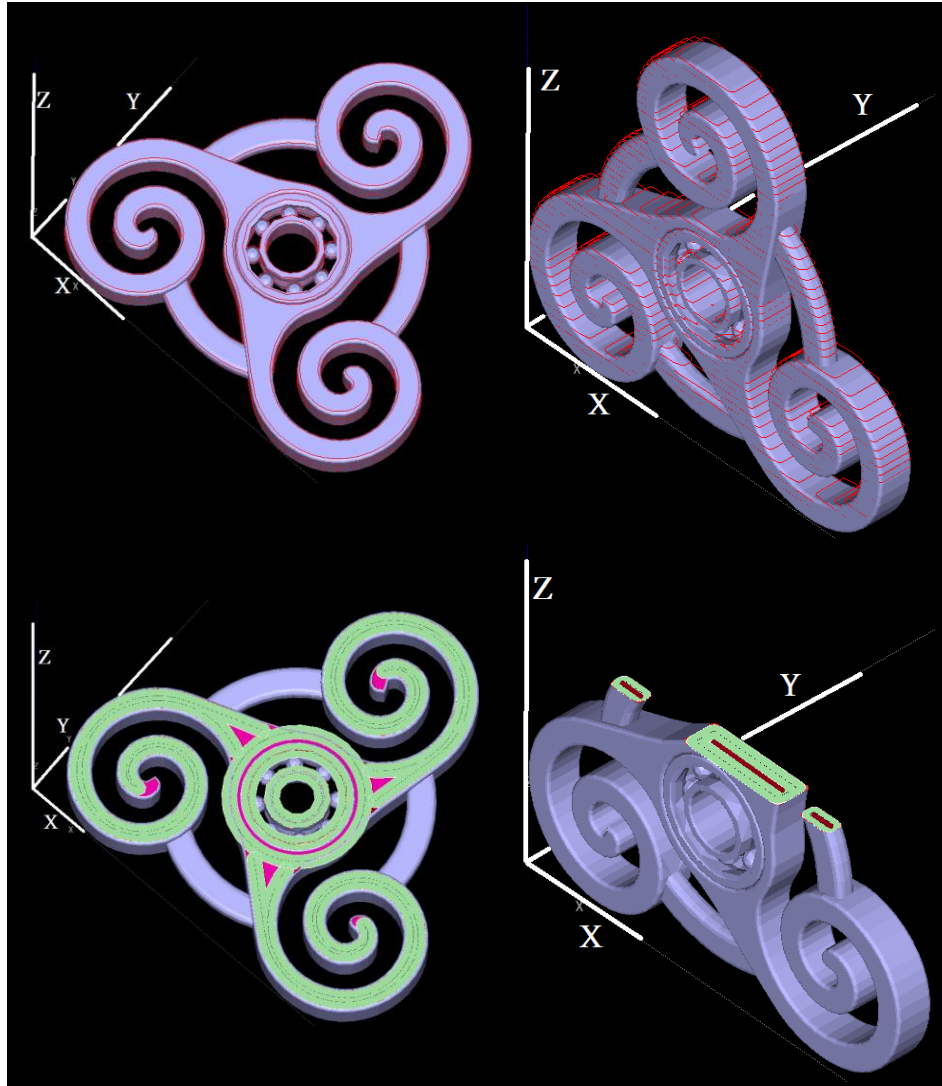


Figure 21. Different rotation and position of voids

In the process planning of AM-ME process, the voids regions have occurred during the toolpath step of the AM-ME process (Figure 22). As it was discussed before in this section, the deposition toolpath leaves voids, which impacts the strength and performance of the finished product. There is a lack of methodologies to optimize available the standard raster and contour toolpath strategies in the existing process planning software. Contemporary solutions cause unwanted voids, which in turn creates a set of potential failure points within the finished product. The goal is to minimize voids in each layer, and to prevent void regions being stacked in 3D, i.e., avoid creating an internal chimney by using available machine/process settings. Also, the build orientation is studied to choosing the best build orientation to minimize the volume of voids.

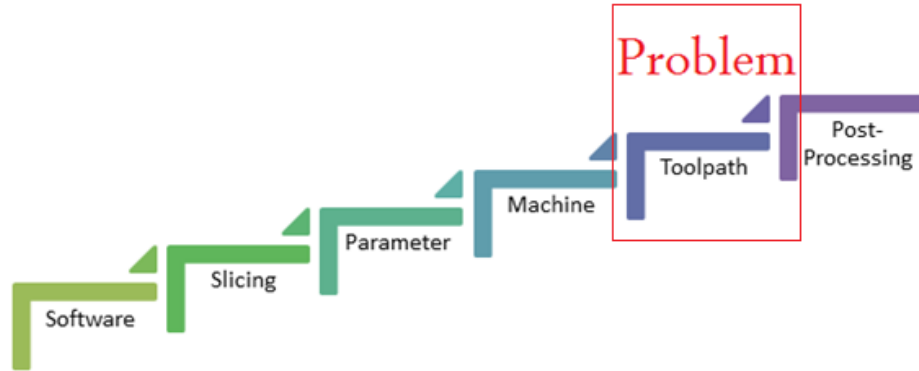


Figure 22. Problem statement in the process planning of material extrusion process

Dissertation Outline

In this dissertation, the derived mathematical model, which establishes a build solution based on the component geometry and the available build options for a given AM-ME process is novel. A C++ program has been developed to select a set of standard (available) toolpath parameters to determine the optimal output process variables (bead width, raster angle, and the overlap percentage) for a layer, and for the stacked layers. This optimization strategy has not been proposed before.

Chapter 2 reviews the background on optimization strategies in the AM-ME process. A collection of significant studies done on toolpath solutions is presented. The five parameters, the orientation of the part, bead height, bead width, overlaps, and raster angle, which influence the toolpath are explained by details. The relationship between toolpath and strength, surface finish, and accuracy are studied.

Chapter 3 presents the mathematical model to minimize voids and its conditions. Variables and parameters involved in the mathematical model are defined and explained. Optimal relationships are established based on the geometry and available machine build configurations. The component geometry is analyzed and decomposed into build regions. The mathematical model is used to determine a standard (available) toolpath with optimal variables (bead height, bead width, raster angle, part orientation and the air gap) to minimize voids for each layer and build region. The relationship between build orientation and volume of voids is studied, and the algorithm for choosing the best build orientation to minimize voids is demonstrated.

Chapter 4 gathers the results and discusses the effect of different variables on the toolpath. It was found that the new model decreases unwanted voids. The final component will contain multiple

bead widths and overlap conditions, but all are feasible as the available machine solutions are employed to seed the model. The total voids are compared before and after when the voids are managed and covered between layers. The experiments are categorized into three main groups which are solid shapes, non-solid shapes, and the combination of solid and non-solid shapes. This chapter is shown that the new model is independent of the form of the part and layers.

Chapter 5 compares the build orientation of some case studied. The difference of volume of voids in each build orientation is discussed. In the end, the best and worst build orientation of the case studies are compared.

Chapter 6 highlights the contributions arising from the current dissertation and summarizes the conclusions. Also, the recent research trends and potential future work on toolpath are discussed.

CHAPTER 2

LITERATURE REVIEW

In this chapter, the previous researches on the AM-ME process, the toolpath parameters, and the relationship between the toolpath and strength, surface finish, and accuracy will be reviewed. In the end, the researchers who were working on creating a new toolpath for the AM-ME process will be mentioned.

Toolpath Parameters

There are five parameters which influence the toolpath, and the resulting voids. These parameters are the build orientation, the bead height, the bead width, the percent overlaps, and the raster angle. These parameters influence the toolpath, potential voids follow, strength and the surface finish. Each of these parameters is explained individually, below.

Build Orientation

The part build orientation affects strength, build time and the appearance of the product. Table 12 and Figure 23 present the differences for the build material (cm³), support material (cm³), number of layers and build time (min) for the 0⁰, 45⁰ and 90⁰ rotation about the X-axis. As it shows, the 90⁰ has the maximum build and support materials and the smallest number of layers.

Table 12. Results of changing the part orientation

Slice Height (mm)	Orientation												
	0 ⁰ Rotation about X					45 ⁰ Rotation about X					90 ⁰ Rotation about X		
	Build Material	Support Material	# Layers	Build Time	Build Material	Support Material	# Layers	Build Time	Build Material	Support Material	# Layers	Build Time	
0.1270	1.69	1.79	88	23	1.69	1.79	109	23	3.25	4.92	73	48	

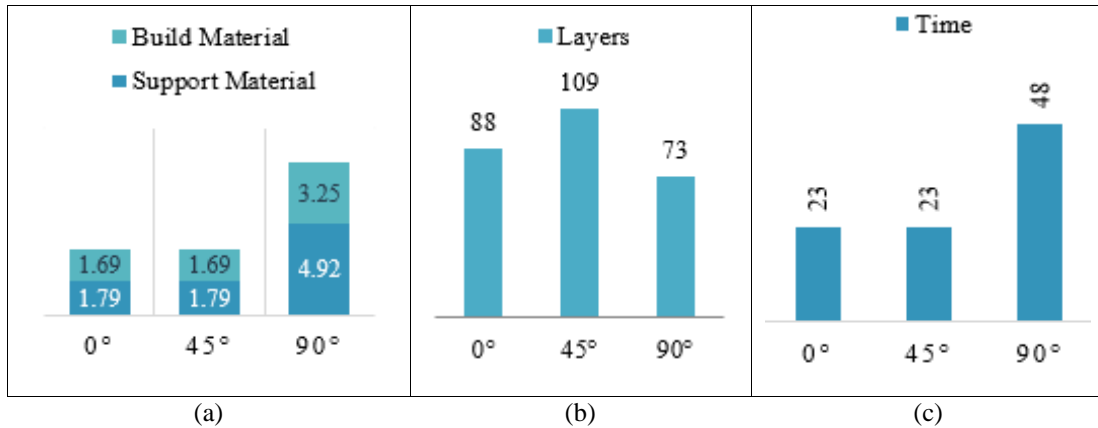


Figure 23. The comparison of (a) The build and support materials (cm³), (b) Number of layers and (c) Build times (min) for the 0°, 45° and 90° rotations about the X-axis

It is well known that the AM-ME processes have anisotropic properties, which are influenced by the build orientation [33] [34]. For example, after comparing two build orientations for the part presented in Figure 24, it has been experimentally shown that build orientation in Figure 24 (a) has a higher tensile strength than that shown in Figure 24 (b). Consequently, understanding the possible mechanical properties for a material-machine-process set is an ongoing area of research. However, as it was described before (Figure 14), for the higher strength orientation configuration (Figure 24 (a)), the tensile testing failure points are not in the center for several experiments with varying internal raster fill angle orientations [20].

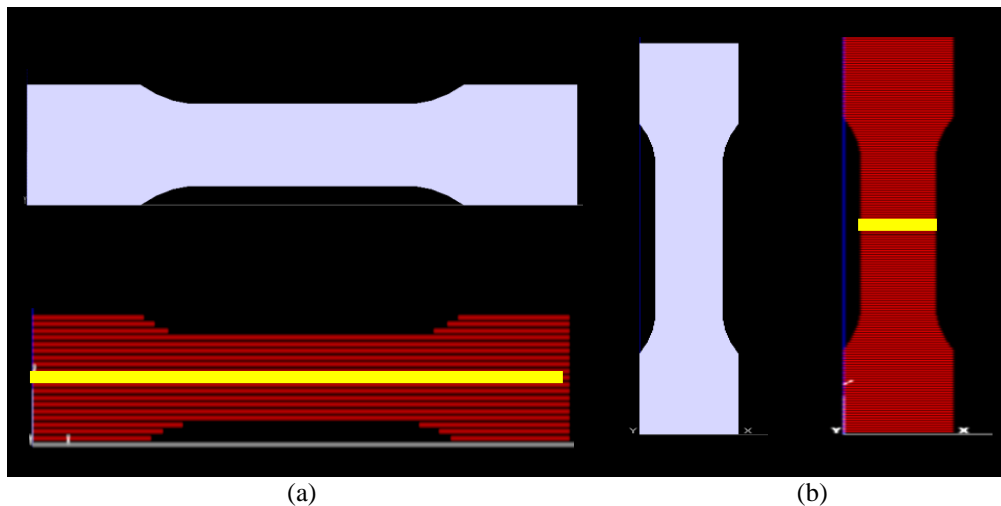


Figure 24. (a), (b) Part orientation influences the tensile strength of the sample (b) being weaker than sample (a) in the longitudinal direction

For compressive strength on surface “A” in Figure 25. The maximum compressive strength is for Figure 25 (b) rather than Figure 25 (a).

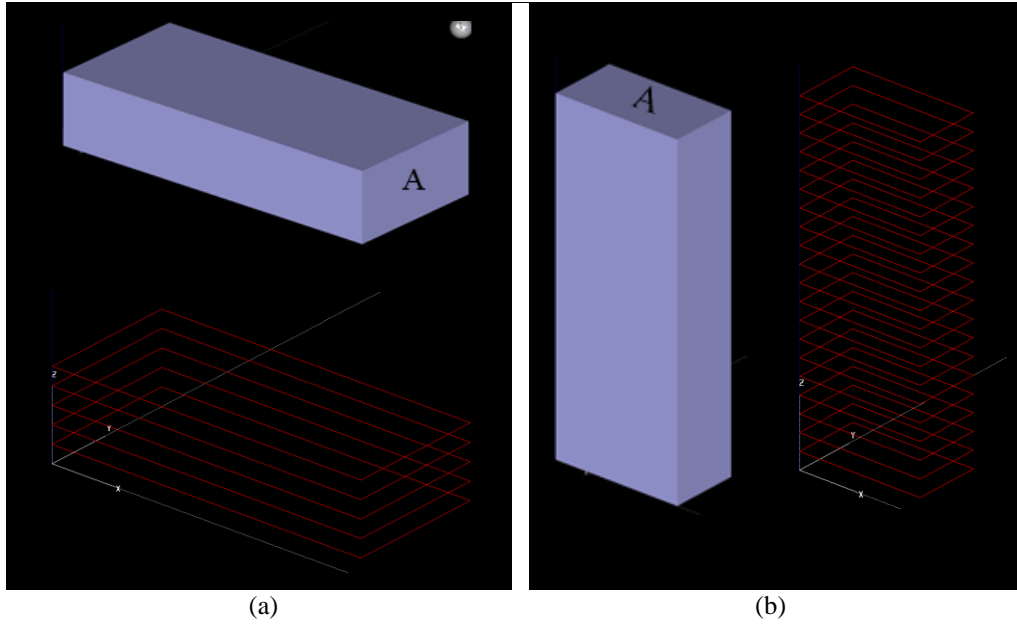


Figure 25. The relationship between part orientation and compressive strength on surface “A”

The build parameters and the resulting characteristics are interlinked. The build orientation also influences these results. Figure 26 shows voids in the 32nd layer for both cases, (a) 90° around the X-axis and (b) 30° around the Y-axis. The volume of voids, position of voids, and shape of voids are depended on the build orientation.

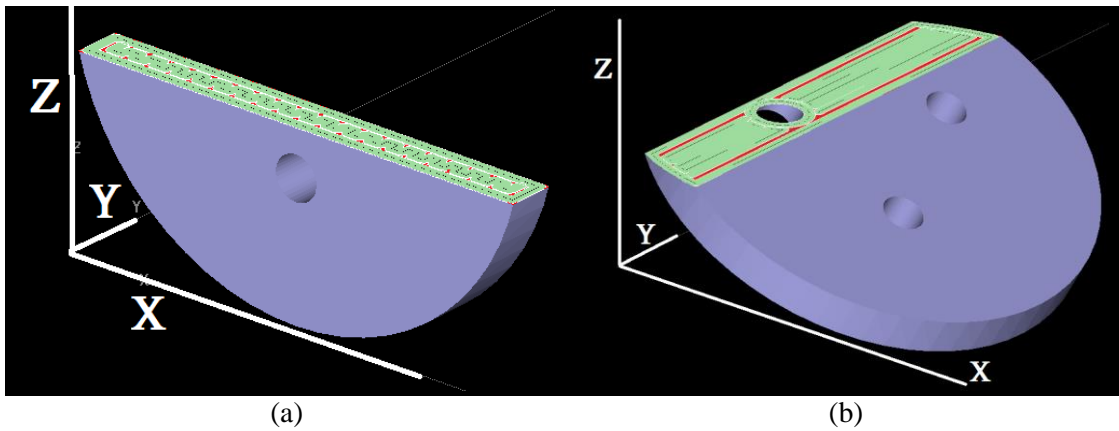


Figure 26. The relationship between build orientation and voids (a) 90° around the X-axis, and (b) 30° around the Y-axis

Bead Height

The bead height or slice height is the vertical thickness of each layer. Typically, the available process planning software utilizes a ‘ceiling’ value to determine the number of layers. The bead height is related to a velocity of nozzle, temperature, and types of material. Thus, it is a discrete variable which can be chosen from the range of available variables in the OEM software. In the OEM software, the bead height selected will be fixed during the whole process. Using just one bead height for the build process increases possibility in having a shorter or taller finished product (depending on the round off strategy). Employing a combination of available bead heights will help in achieving an accurate finished product in the Z-direction. In this dissertation, the assumption issuing a combination of convenient bead height in the process.

Consider the possible build solutions for the part that shown in Figure 28 (a) which has a height of 7 mm, and the available bead heights are 1.5, 2, 3, and 4.5 mm (Figure 27). Note: these bead heights are typical for the BAAM process [35] [36] which was described in Table 4 before.

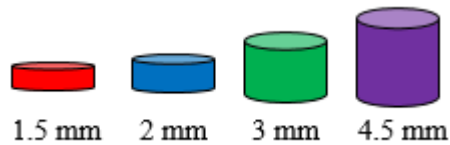
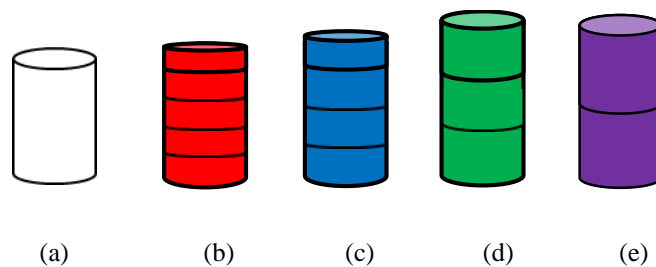


Figure 27. Available bead height

Figure 28 (b to e) shows the difference between the height of the part and the height of the finished part when utilizing uniform bead heights.



Height				
7 mm	7.5 mm	8 mm	9 mm	9 mm

Figure 28. Compare the final height of part (a) and the height of the finished part after using available bead heights in Figure 27 (b to e)

The other example is for producing the car seat (Figure 29) with the OEM software; users are limited to four bead height sizes if the OEM software such as Insight® software with Fortus 400

machine is used. For this example, the available bead heights are {0.127 mm, 0.1778 mm, 0.254 mm, and 0.3302 mm}.



Figure 29. Car seat example with height, 150.0086 mm

Table 13 shows the difference between the actual height of the car seat which is shown in Figure 29 and its new height when the OEM software produces it. It shows with none of the available bead heights in the OEM software, the height of the car seat would be as same as Figure 29.

Table 13. The new height of the car seat with different bead height in the OEM software

Bead Height (mm)	Number of Layers	New Height = Bead Height * Number of Layers (mm)	Difference between Actual Height and New Height (mm)
0.1270	1182	150.114	0.0254
0.1778	845	150.241	0.1524
0.254	591	150.114	0.0254
0.3302	455	150.241	0.1524

The relationship between bead height and the strength is by increasing thickness of layers, the strength of the part decreases [37, 38, 39]. For example, Figure 30 (a) with bead height, 0.254 mm has less strength than Figure 30 (b) with bead height 0.127 mm. The numbers of the layers with these two bead heights in this example are 25 layers and 50 layers, respectively. Although, Figure

30 (b) is stronger than Figure 30 (a), the build time of Figure 30 (b) is much more than Figure 30 (a).

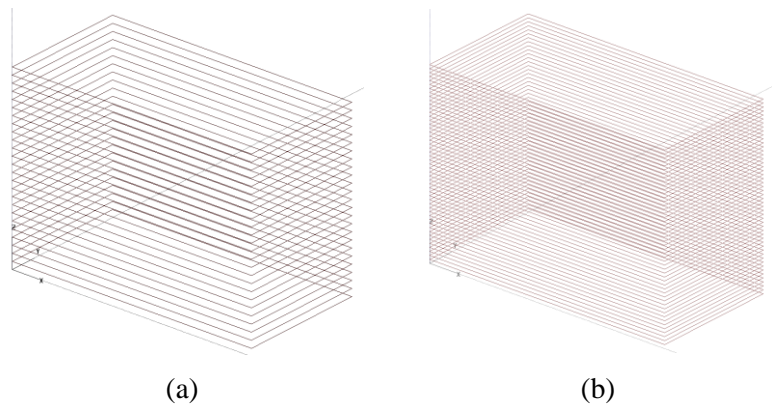


Figure 30. One part with different bead heights (a) 0.254 mm and (b) 0.127 mm

Researchers have shown that the strength of the part decreases with increasing layer thicknesses. In other words, a minimum viable bead height improves strength [38] [39] [37]. However, by minimizing bead height, all voids are not covered, even though usually a reduced bead width occurs with a smaller bead height (Figure 31).

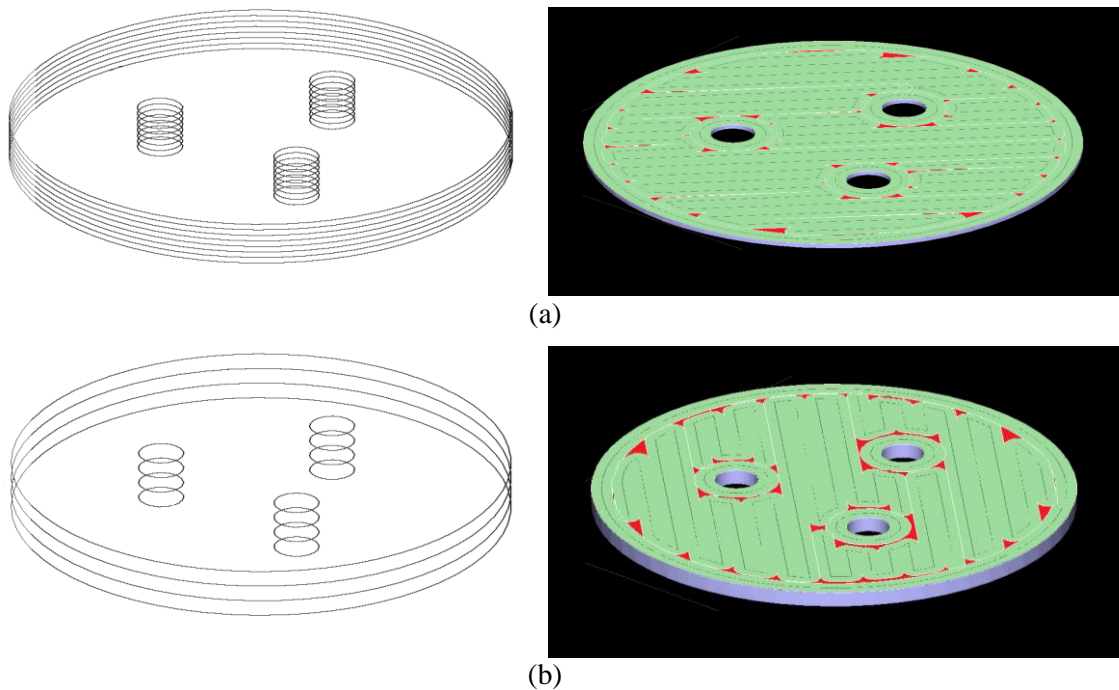


Figure 31. The relationship between bead height and voids in the first layers, (a) bead height 0.1270 mm (b) bead height 0.3302 mm

Bead Width

The road track or bead width is the horizontal thickness of a single bead during direction parallel toolpath. This parameter depends on the feeding rate of the machine and linear movement speed of the nozzle [40]. As Figure 32 shows, an increase in the feeding rate or a decrease in the linear movement speed leads to the rise of the bead width for the same bead height (S_j) [40].

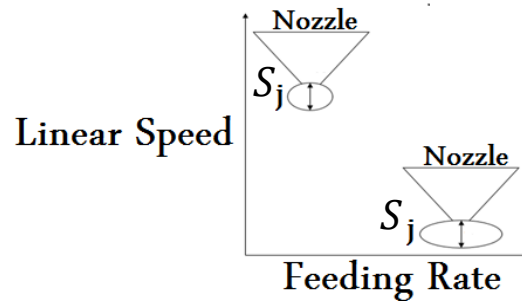


Figure 32. The relationship between feeding rate/ linear speed and bead width

Two kinds of bead width are raster bead width and contour bead width. In this dissertation, raster bead width is named as bead width. A small bead width increases build time significantly, but it improves surface quality as it reduces the staircase effect [28]. It has been reported in the literature that a minimum bead width also enhances strength [39]. Figure 33 compares two different sizes for bead width. Figure 33(a) is with the smallest bead width, 0.4064 mm and Figure 33(b) is with the most significant bead width 0.8314 mm in the OEM software (Insight software). The contour bead width for these two figures are same, and it is 0.5 mm.

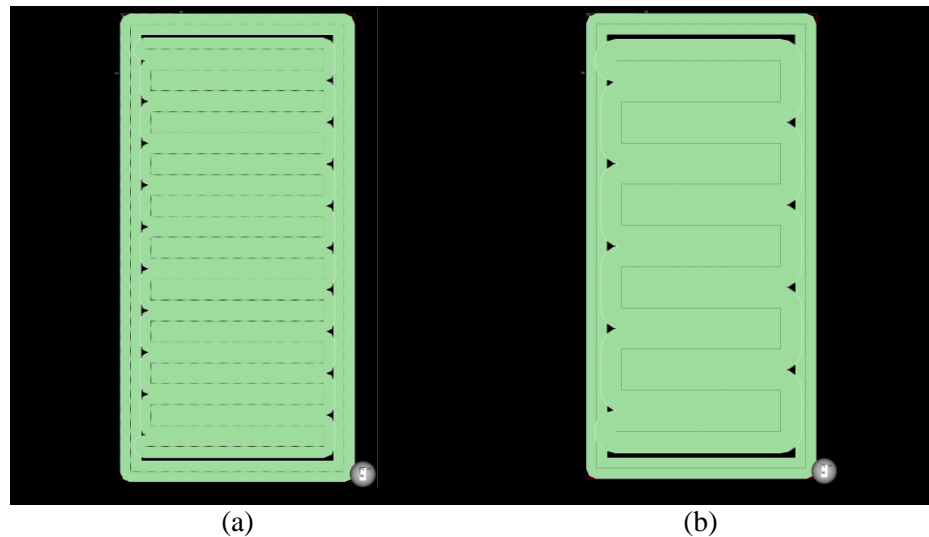


Figure 33. Top view of one layer with bead width (a) 0.4016 mm and (b) 0.8314 mm

A small bead width increases the build time significantly (Figure 18), but it improves surface quality as it reduces the staircase effect [28]. It has been reported in the literature that a minimum bead width also enhances strength [39]; however, this research does not consider the influence of a partial fill condition. For example, Figure 34 (a) shows the cylinder with three holes, Figure 34 (b and c) show the filling condition with 0.4064 mm and 0.8314mm bead width, respectively. As seen here, in both cases there are unwanted voids; consequently, both scenarios will have reduced mechanical properties.

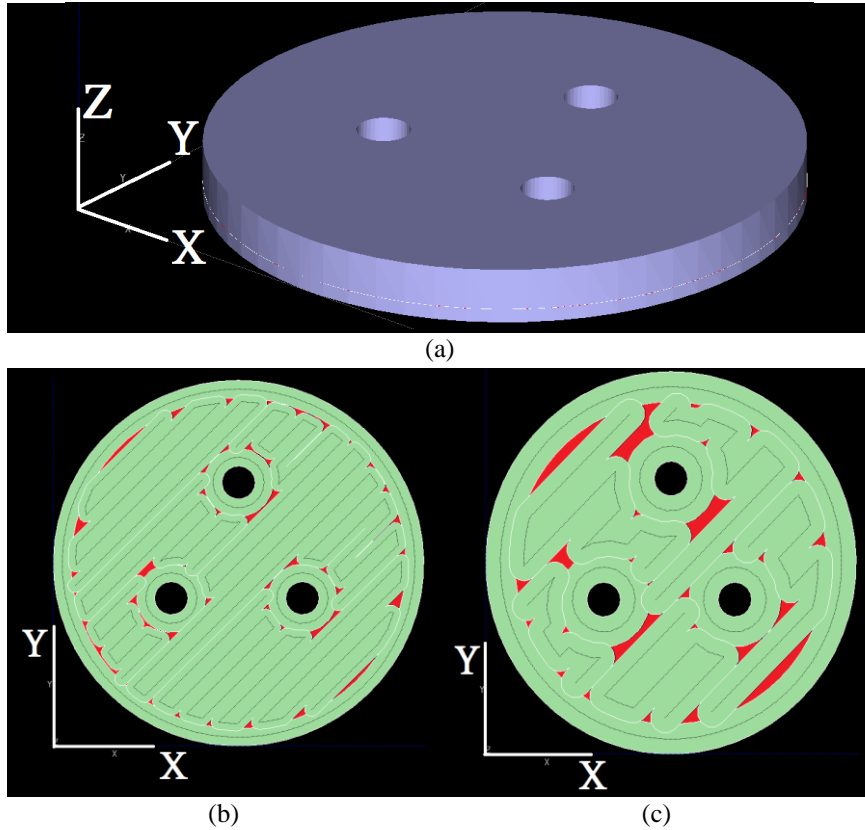
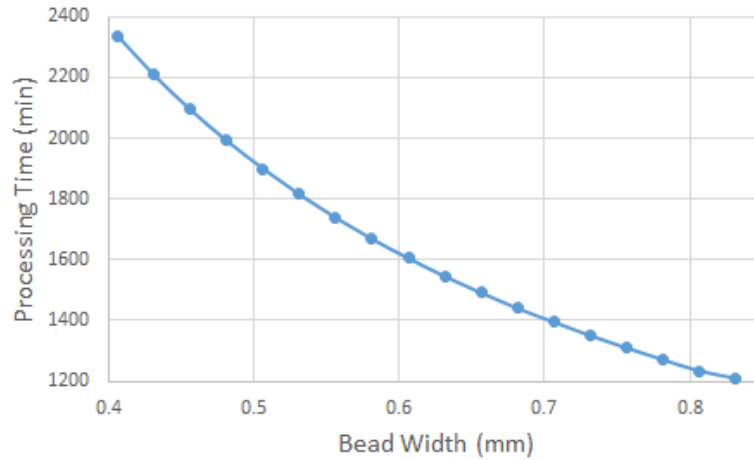
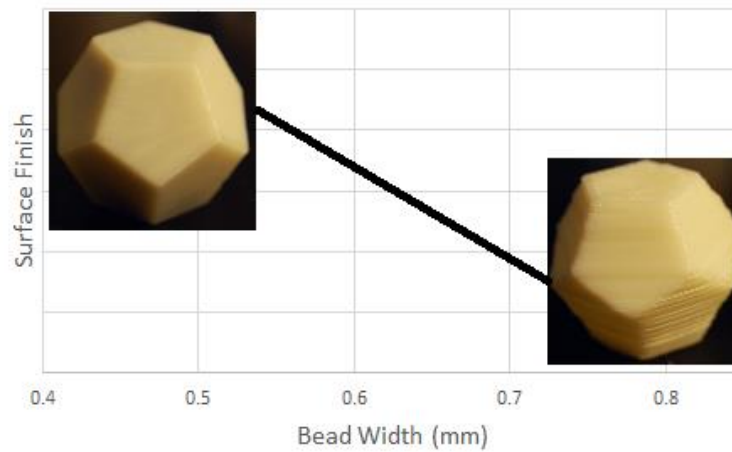


Figure 34. Comparison of voids between two different bead width sizes, (a) 3D model, (b) layer with 0.4064mm bead width, and (c) 0.8314 mm bead width

The relationship between bead width (for a set bead height) with time and surface finish are in Figure 35, respectively. Therefore, not only the time, strength, and surface finish conditions should be considered when selecting bead widths. The void locations and areas should be found.



(a)



(b)

Figure 35. The relationship between the bead width with time and surface finish (the sample parts are from [41])

Percent Overlap

The air gap is the space between the beads or rasters. It can be positive, zero and negative. A zero air gap means the beads touch. A positive air gap means two beads do not touch and negative air gap means two beads overlap, with the bead having a more ‘rectangular’ shape. In this dissertation, the negative air gap is named as overlaps. Figure 36 illustrates a zero-air gap condition between two beads with the same bead height and bead width.

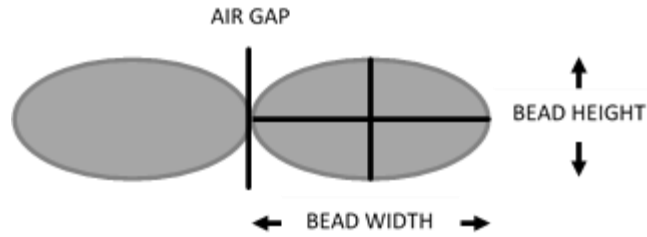
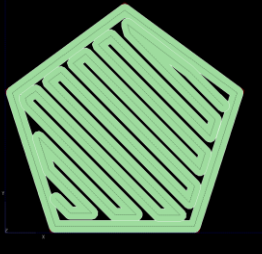
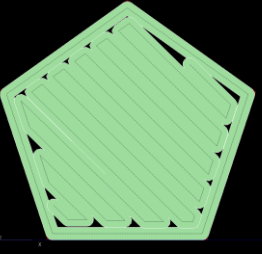
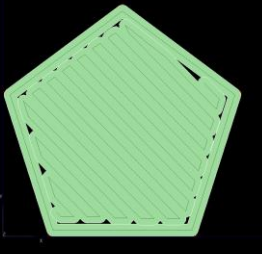

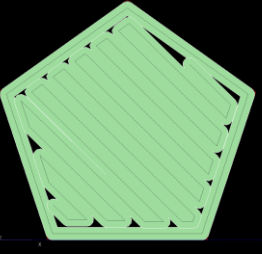
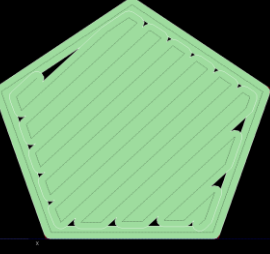


Figure 36. Zero air gaps, bead width, and bead height

In Table 14 the air gap influences can be visualized. Two kinds of air gaps are existed in the AM-ME process, internal raster air gap and contour to raster air gap. Overlaps in the AM-ME process significantly improves strength and stiffness [42, 28, 39, 38, 33, 29].

Table 14. Different kinds of the air gap

Air gap	Positive (Voids)	Zero (Voids)	Negative (Voids)
Internal Raster			
Contour to raster			

This dissertation, the overlaps between internal rasters is studied. Figure 37 shows differences between before and after existing overlaps between rasters. As it shows, the layer with overlaps between rasters has fewer voids than the layer without overlaps.

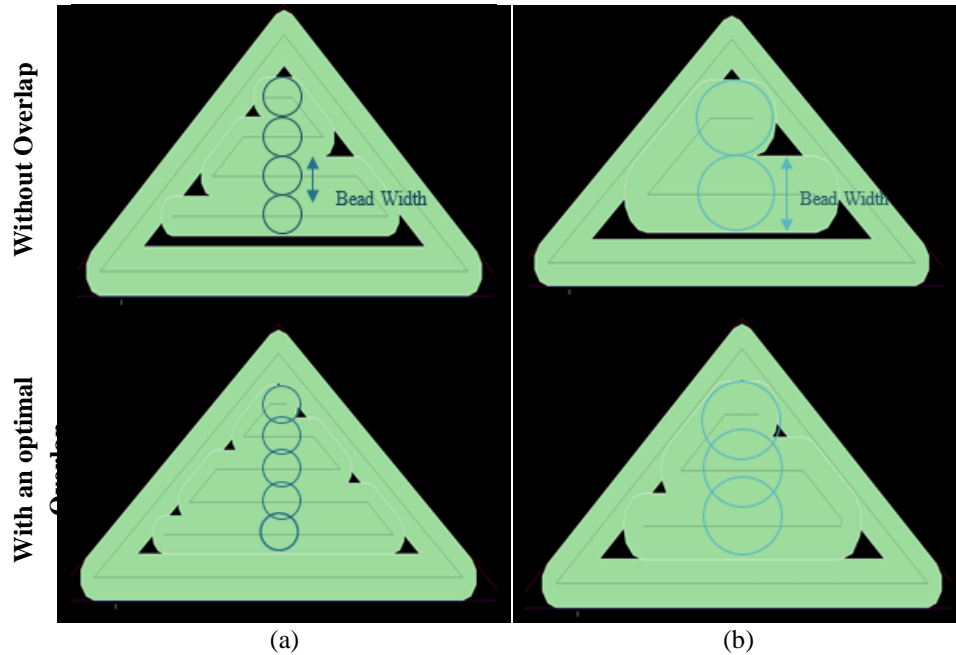


Figure 37. One part with or without overlaps with two different bead width sizes

For the overlap condition, conservation of mass must be considered – 100% overlap is a ‘bead stacking’ condition. A limited or controlled overlap solution will be utilized in this research. The allowable overlap percentage values need to be defined for known for a bead shape, which could be modeled as an ellipse or an ‘obround’ shape.

Raster Angle

The raster angle or raster orientation is the direction of the beads of material relative to the loading of the part. Figure 38 compares three different raster angles, with 0° , 45° , and 30° , respectively. A raster angle aligned with the load direction improves tensile strength [39] [33].

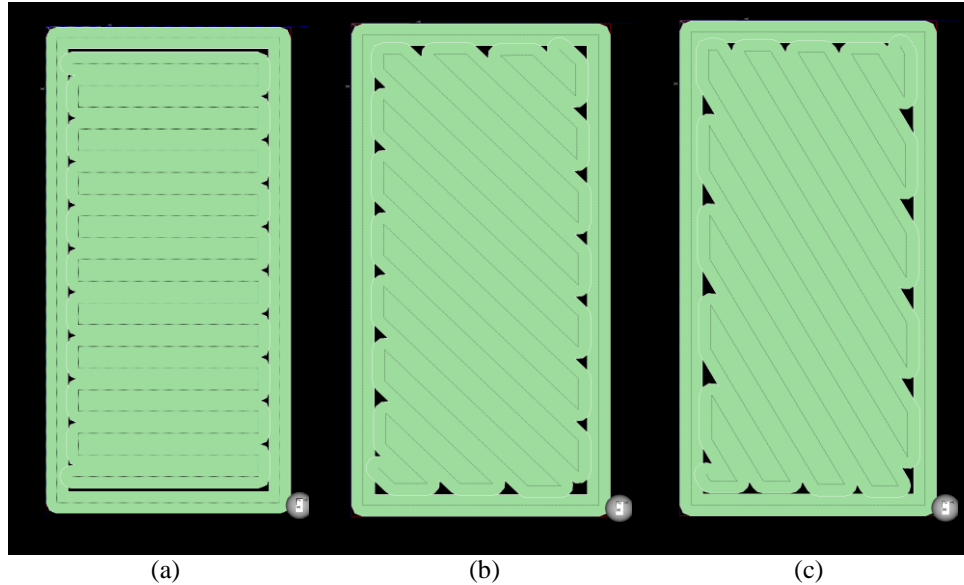


Figure 38. Compare three toolpath with raster angle (a) 0° , (b) 45° , and (c) 30°

The raster angle is related to the world coordinate system of the machine. If the raster angle for the component build is aligned with the load direction, there is an improvement in tensile strength [39] [33]. However, when considering the build conditions in Figure 34 (b) and (c), it is reasonable to expect lower mechanical strength characteristics for a raster-fill aligned loading condition due to the interspersed voids.

Toolpath and Strength

Researchers have been aiming to maximize the strength of a finished part by controlling the toolpath parameters. It can be found that some work has been done to study all five parameters simultaneously, and their combined influence on the component strength. Other researchers have studied the toolpath parameters concerning final surface finish and strength. Table 15 summarizes research activities related to investigating the importance of the bead height, bead width, part orientation, raster angle, and overlap on strength. Table 15 shows the types of materials, machines and the toolpath of these researchers. It shows 6 of researchers out of 26 studies all parameters with the same OEM software (Insight® software). 73% researchers studied the relationship between part orientation and strength and 54% used the Insight® software as an OEM software.

Table 15. Literature review on toolpath parameters and strength

#	Author	Parameters					Material		Source Machine		OEM Software		
		Bead Height	Bead Width	Part Orientation	Raster Angle	Air gap	ABS	Others	Closed Source	Open Source	Insight®	Catalyst™	Others
1	[28]		✓	✓	✓	✓	✓		✓				✓
2	[39]	✓	✓	✓	✓	✓	✓		✓		✓		
3	[25]		✓	✓	✓	✓	✓		✓				✓
4	[43]	✓		✓			✓		✓		✓		
5	[44]	✓	✓	✓	✓	✓	✓		✓		✓		
6	[42]	✓	✓	✓	✓	✓	✓		✓		✓		
7	[45]	✓	✓	✓	✓	✓	✓		✓		✓		
8	[46]	✓	✓	✓	✓	✓	✓		✓		✓		
9	[33]		✓	✓	✓	✓	✓		✓		✓		
10	[47]		✓	✓	✓	✓	✓		✓		✓		
11	[38]	✓	✓	✓	✓	✓	-	-	✓		✓		
12	[48]	✓	✓				✓		✓	✓	✓		
13	[49]				✓		✓		✓				✓
14	[50]	✓			✓	✓	✓		✓		✓		
15	[40]	✓		✓	✓			✓		✓			✓
16	[51]				✓		✓		✓		✓		
17	[52]	✓			✓		✓		✓			✓	
18	[53]				✓	✓	✓		✓		✓		
19	[39]		✓	✓	✓		✓		✓		✓		
20	[37]	✓					✓		✓			✓	
21	[54]	✓		✓			✓		✓		✓		
22	[55]	✓		✓			✓	✓	✓			✓	
23	[56]			✓				✓		✓	✓		
24	[57]			✓			✓		✓			✓	
25	[58]	✓		✓				✓		✓	✓		
26	[59]			✓			✓		✓			✓	

Below, some research activities are explained by details, and they are sorted by year.

Es-Said et al. [49] in 2000, found the layers which their raster orientation is parallel to the length of the samples have superior tensile strength. Sung-Hoon Ahn et al. [28] in 2002, showed that the air gap and raster orientation affect the tensile strength but not the compressive strength of FDM parts. Also, they found that bead width, model temperature, and ABS color have little effect on both strengths. In 2005, B. H. Lee et al. [50] concluded that layer thickness, raster angle, and air gap affects the elastic performance of FDM build part.

In 2007, C S. Lee et al. [25] focused on the compressive strength. It was confirmed that the build direction was an essential parameter than raster orientation, air gap, bead width, color, and model temperature for compressive strength. In 2009, Panda et al. [43] showed by increasing the layer thickness and part orientation, the diffusion between adjacent rasters increases and strength improves. Daekeon Ahn et al. [54] presented a new approach for formulating the surface roughness of FDM parts. They analyzed and evaluated, the effects of surface angle, layer thickness, a cross-sectional shape of the filament, and overlap interval on surface roughness.

In 2010, Sood et al. [44] studied the functional relationship between process parameters and strength. The settings are layer thickness, orientation, raster angle, raster width, and air gap. They realized that increasing the number of layers and using zero air gap, reduced the strength. Choosing a small raster angle and thick raster width improve the strength. But growing number of layers increases high-temperature gradient, residual stress accumulation, distortion, interlayer cracking, part delamination, and fabrication failure. In 2011, Sood et al. [42] continuing examining the same five parameters on the tensile strength and in 2012, they studied the same settings on the compressive strength. They showed that fiber-to-fiber bond strength is strong by controlling the distortions arising during part build stage [46]. They also determined a functional relationship between the five parameters and wore with using the response surface methodology [45]. In 2013, Smith and Dean [56] studied the relationship between tensile strength and orientation. Their results show 36%-63% of the strength depends on the orientation of the part.

In 2014, Farzad Rayegani et al. [33] and Onwubolu et al. [39] tested the part orientation and raster angle variations, and how these parameters influence the tensile strength. They also found that a negative air gap, minimum raster width and layer thickness, zero-part orientation with the direction of tensile loading and maximum raster angle improved tensile strength. Hergel et al. [60] analyzed the defects and the behavior of the extruders on improving surface finish. They used multiple color prints to hide the surface finish issues. Raut et al. [57] concluded that about Y-axis at 0° built up

orientation FDM parts has an excellent tensile strength and minimum cost. And about X-axis 0° built up orientation FDM parts has a good flexural strength and average price. Boschetto and Bottini [55] developed a geometrical model of the filament, dependent upon the raster angle and layer thickness, to predict the obtainable part dimensions. Hossain et al. [47] focused on how modifying process parameters such as build orientation, raster angle, contour width, raster width, and the raster-to-raster air gap can improve tensile strength.

In 2015, Ziemian et al. [51] found that the raster orientation influences the fatigue performance. Rezayat et al. [53] showed increasing the air gap, or raster angle reduces the strength of the single layer. Vijayaraghavan et al. [38] found that the wear strength decreases with an increase in layer thickness and raster width and increases with increase in the air gap. Carneiro et al. [40] studied part orientation, bead height and raster angle for RepRap machine. The relationship between these parameters and strength in the RepRap machine is exactly same as in an FDM machine. Bochmann et al. [59] determined the sources of imprecision in FDM like rough surface finish. Vidakis et al. [37] found that ABS parts build with larger layer thickness had lower compressive strength. They compared ABS and ABS plus parts and determined that ABS plus specimens on average had about double the compressive strength of the ABS specimens and lowered compressive strength than the stock ABS material. Beniak et al. [58] presented the relationship between the production time and settings of a production process. Galantucci et al. [48] proved that reducing the path speed improves the dimension accuracy, but increases the building model time. In 2016, Boschetto and Bottini [52] studied the relationship between surface quality and the process parameters like layer thickness and deposition angle. Steuben et al. [61] in 2016 introduced a new slicing algorithm to address the loss of non-geometric information.

In conclusion, they proved that

1. A small bead width increases build time significantly, but it improves surface quality as it reduces the staircase effect [28]. It has been reported in the literature that a minimum bead width also improves strength [39]. However, none of the researchers studied the relationship between bead width and creating voids during the toolpath. In this research, the relationship between bead width and volume of the voids will be examined.
2. A raster angle aligned with the load direction improves tensile strength [39] [33]. Loading conditions are not considered for this work. This dissertation shows the influence of raster angle on optimal bead width and percentage overlap to minimize the total voids area in each layer.

3. An overlap significantly improves strength and stiffness [42] [33] [39] [38] [28]. For the overlap condition, conservation of mass must be considered. The maximum overlap distance needs to be defined as known for a bead shape, which could be modeled as an ellipse or an ‘obround’ shape. It is defined by the percentage of the bead area concerning the width-height rectangular bounding box.
4. The strength of the part decreases with increasing layer thicknesses. In other words, a minimum viable bead height improves strength [38] [39] [37]. This dissertation optimizes bead height to produce the part with its exact height.

Although these researchers studied the relationships between strength and toolpath parameters, they did not evaluate the influence of the toolpath parameters on the interior void regions for the AM-
ME process. Researchers have noted that voids and discontinuities are sites for crack propagation. No one has shown the influence of the toolpath parameters on voids, fill strategy, or internal chimneys. However, as researchers have presented results where the failure points are not in the sample centre, it is reasonable to assume that voids and discontinuities influence these reported results as well.

Toolpath on Surface Finish and Accuracy

Table 16 shows the researchers who studied the relationship between toolpath with surface finish and accuracy. 31% of these researchers explored the relationship between bead height and surface finish. However, no researchers examined the relationship between raster angle and accuracy or surface finish. In this dissertation, the effect of all five process parameters on accuracy (height of the part) and surface finish (volume of voids) is studied.

Considering surface roughness for FDM, some researchers have been conducted to analyze process-independent geometric parameters such as the volume [62] and the height of surface asperities for surface finish quantification [54]. Other researchers have relied upon roughness measurements for samples built with different orientations, layer thicknesses and combinations of process variables [54] [55]. The dependency of surface finish upon the part surface angles was highlighted, too [63]. Statistical models, such as analysis of variance, Taguchi methods, and artificial neural network, were also applied for the quality modeling and improvements [50] [36] [37] [38] [64] [65] [66] [67].

Roughness data have been collected to demonstrate the feasibility of improving surface finishing through machining [68], barrel finishing [69], and chemical treatments [70] [71]. Geometrical

models were also studied for surface roughness characterization based on process setting variables [72] [73].

In literature, the accuracy of FDM parts has been widely studied [74]. The dimensional accuracy of the finished parts are dependent upon the process and product design parameters, as well as the properties of the feedstock filament, travel speed, extrusion temperature, etc. [74]. Some researchers studied geometry for FDM built parts [55], form and position errors, and the poor flatness of the layering plane [75].

Causes of geometric errors have been studied for the FDM process, usually for compensation purposes. Positioning errors due to machine feed drives have been calculated [76] and measured to decompose them into translational, rotational and scale errors on individual axes [77]. Other experimental investigations have focused on systematic deviations due to slicing [78] and propagation of flatness errors from the lowermost support layers [74]. Table 16 summarized the researchers who studied AM-ME toolpath with accuracy and surface finish.

Generating New Toolpath

This section explains some papers which are focused on creating new toolpath. Most of them studied the toolpath for complex shapes such as curve shapes, hollow structures, or non-geometric shapes, for example, Singamneni et al. [79] in 2010, described an FDM method for curved shapes. They showed with the new algorithm; it is possible to deposit the support material as conventional flat layers and then deposit build material over the support material following the curves of the part to minimize weakness between the laminations. In 2014, Ozbolat et al. [80] proposed a new continuous path planning approach for functionally graded material printing in porous hollow structures. The new toolpath follows material bending direction. Although this research optimizes the continuous path for AM process toolpath, it does not minimize voids in all layers. Muller et al. [81] presented the evaluation of toolpath incorporated into a global methodology to manufacture Functionally Graded Materials (FGM) parts. Although, their results showed a good correlation between the simulated and the deposited material distributions. They did not optimize the AM toolpath, automatically. Steuben et al. [61] in 2016 introduced a new slicing algorithm to address the loss of non-geometric information for slicer software instead of creating a new toolpath.

Although these researchers may help users to select parameters to improve the features of a finished part such as the surface quality, minimizing the support material, or choosing an orientation to fit the component in the build envelope. None of them allows a designer to visualize and manage 3D void placements in the fabrication process.

In conclusion, there is a lack of methodologies to visualize and quantify void regions and optimize the available standard raster and contour toolpath strategies in the existing process planning software. Contemporary solutions create unexpected and unwanted voids, which in turn creates a set of potential failure points within the finished product. The next chapter describes the mathematical model for minimizing and managing voids in the AM-ME process.

Table 16. The literature review of toolpath parameters and surface finish/accuracy

#	Author	Process Parameters					Other Parameters		Accuracy	Surface Finish
		Bead Height	Bead Width	Part Orientation	Raster Angle	Air gap	Temperature	Smoothing Process		
1	[62]			✓					✓	✓
2	[64]						✓		✓	
3	[82]	✓	✓							✓
4	[74]	✓							✓	✓
5	[83]							✓	✓	✓
6	[71]			✓			✓		✓	✓
7	[84]		✓	✓					✓	✓
8	[70]	✓	✓							✓
9	[85]							✓	✓	✓
10	[86]							✓	✓	✓
11	[87]							✓	✓	✓
12	[88]							✓	✓	
13	[89]	✓				✓			✓	✓

CHAPTER 3

METHODOLOGY

In this chapter, the approach to determine an optimal build orientation, along with an optimal set of layer-based settings to have the least total amount of voids in all layers is described. Figure 39 shows this solution approach consists of three phases. Phase I is an optimizing voids area in each layer for one build orientation, Phase II is an optimizing voids position between layers to avoid creating an internal chimney, and the last phase is the phase III which is choosing an optimal build orientation for a part to minimize total voids. Each of these phases will be explained below, in detail.

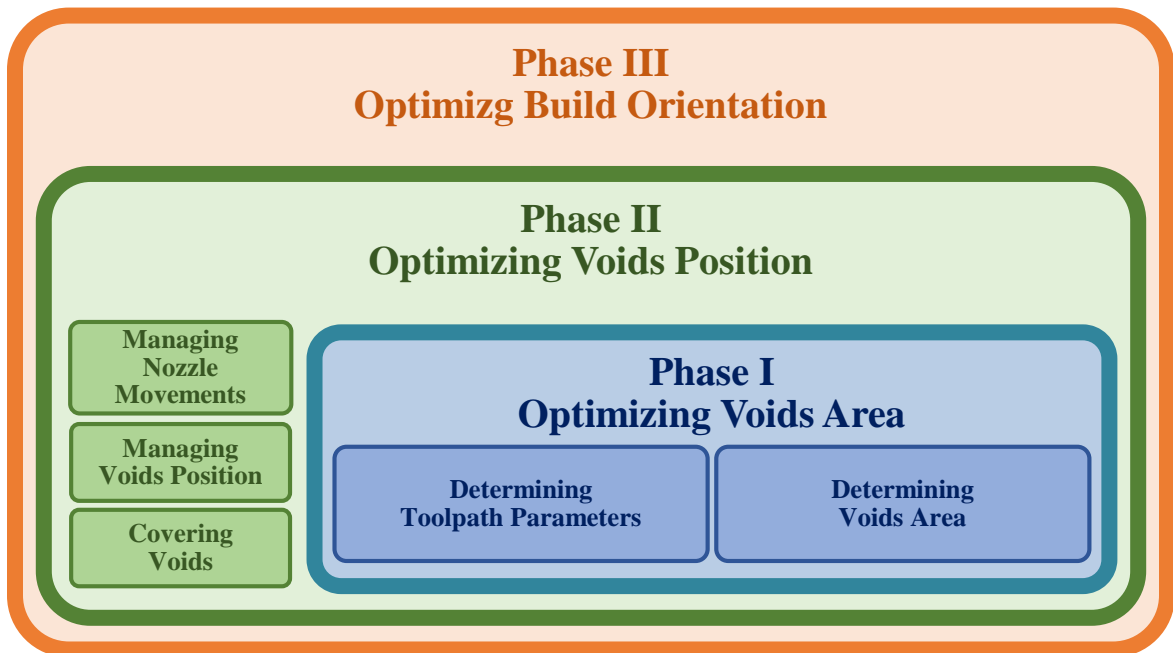


Figure 39. Three phases for minimizing total voids in the material extrusion processes

Phase I _ Optimizing Voids Area

The assumption in this dissertation is the process parameters that are used for optimization the toolpath, are the existing process parameter configurations for an AM-ME machine and material set. These process parameters are related to each other. For example, the available bead width and bead height for a Fortus 400 machine with ABS material, which was developed by Stratasys in Eden Prairie, Minnesota [18] are fixed and presented in Table 17. This table illustrates that each bead height has the fixed range of bead width. For example, if the optimal bead height is 0.1778 mm then the available bead width (mm) is between {0.3048, 0.3298, 0.3548, 0.3798, 0.4048,

0.4298, 0.4548, 0.4798, 0.5048, 0.5298, 0.5548, 0.5798, 0.6048, 0.6298, 0.6548, 0.6798, 0.7048, or 0.7298}.

Table 17. The relationship between bead height and bead width for a Fortus 400 mc and the insight® software

Bead Height, $S_j; j \in J$ (mm)	Bead width, $i \in I$ (mm) $w_{i+1}^j = w_i^j + 0.025$		
0.1270	0.2032	...	0.5782
0.1778	0.3048	...	0.7298
0.254	0.4064	...	0.8314
0.3302	0.4572	...	0.9822

From these available and known process configurations, optimal process parameters such as the bead height, bead width, raster angle, and overlap percentages are calculated. The phase I is divided into two steps, which are determining toolpath parameters and determining voids area (Figure 39).

Figure 40 shows the phase I process flow diagram. The step starts with uploading the *.stl file to the OEM software [90]. The *.stl file decomposed 3D model to points and lines. All of the formula in this chapter are depended on these points and lines. Thus, the edges and curves shape seen as a multifaceted shape in the process [91]. This format is sliced into a series of parallel cross-sections using simple line and plane intersection routines, which along with the specific process settings, is transparent to the user. The *.stl file decomposed to points and lines. The first position of the *.stl file in OEM software is assumed to have 0° rotation around X-axis and 0° rotation around Y-axis.

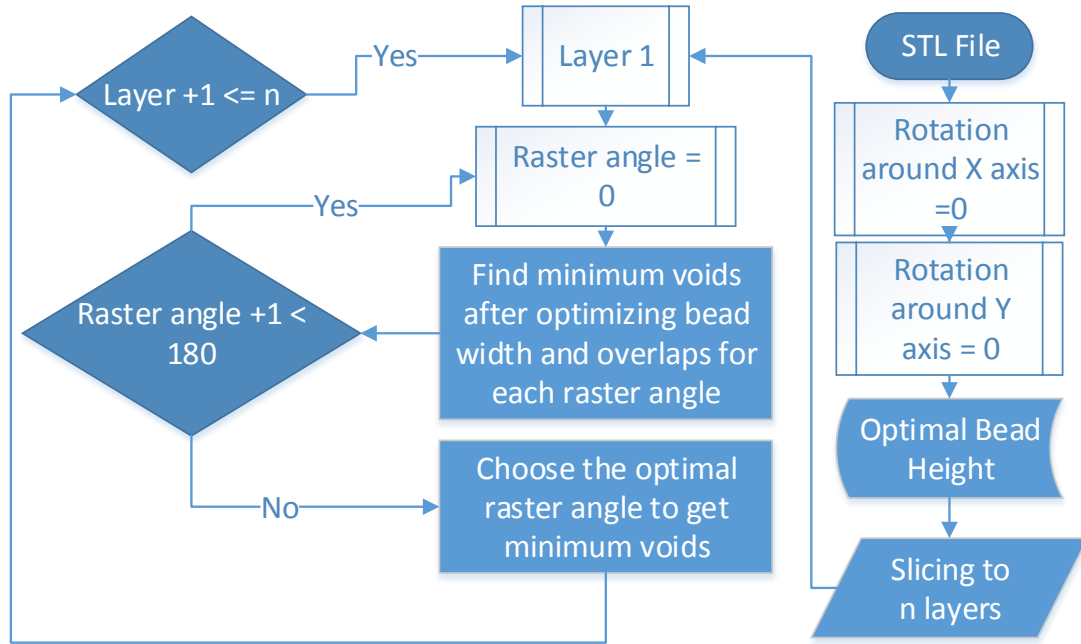


Figure 40. Phase I process flow diagram

After slicing a *.stl file with an optimal bead height S_j , (Figure 41 (a)), each layer $q \in Q$ is decomposed to points and lines (Figure 41 (b)). Let $l \in L$ be an integer number of corners in a layer $q \in Q$. Figure 41 (b) shows 76 corners of one layer. The edge between two corners l and $l + 1$ is the edge $l \in L$ and will be used in the mathematical model described in this chapter.

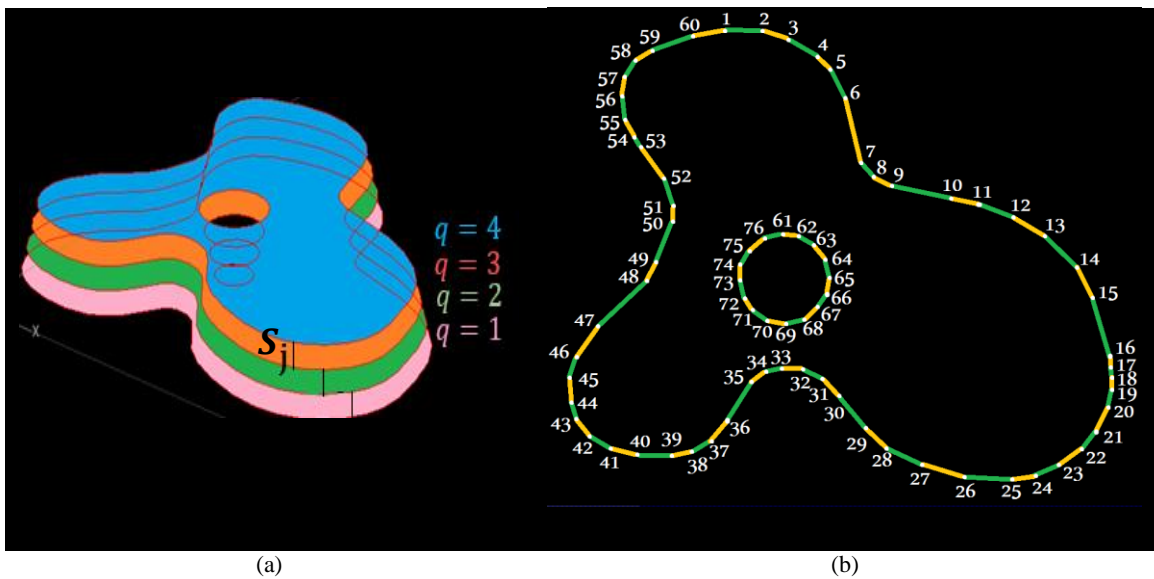


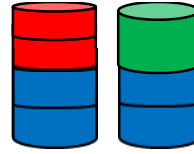
Figure 41. (a) Slicing the part to four layers with bead height S_j , (b) Points and lines in a layer

Determining Toolpath Parameters

Phase I determines optimal toolpath parameters. The first parameter that needs to be resolved is the bead height. The bead height is related to a velocity of nozzle, temperature, and types of material. Thus, it is a discrete variable which can be chosen from the range of available variables in the OEM software. In the OEM software, the chosen bead height will be fixed during the whole process. Using just one bead height for the build process increases possibility in having a shorter or taller finished product (depending on the round off strategy). Employing a combination of available bead heights will help in achieving an accurate finished product in the Z direction. Let S_j be the bead height j , and N_j be an integer number layers with the bead height S_j when the height of 3D model (during Z-axis) is H . If ε be the allowable part height tolerance, then for finding optimal bead height, the formula below is used.

$$\begin{aligned}
 &\text{Maximize} && T(N_j) = \sum_{\forall j} N_j \\
 &\text{Subject to} && \sum_{\forall j} S_j N_j \leq H + \varepsilon \\
 &&& N_j \leq \left\lceil \frac{H + \varepsilon}{S_j} \right\rceil; \forall j \\
 &&& N_j \in \mathbb{N}^0; \forall j.
 \end{aligned} \tag{1}$$

The above formulation denotes that the height of the part needs to be less or equal than the allowable part height tolerance. Also, a minimum bead height is preferred based on the assumption that a maximum strength condition is preferred, as explained in the Chapter 2/Toolpath Parameters/Bead Height section. This formulation is a type of the bounded knapsack problem. Thus, there exists a considerable amount of theoretical, algorithmic and computational results for solving this problem [92]. If the example which was illustrated in Figure 28, is optimized by above equation, then, by combining bead heights which were shown in Figure 27, it would be possible to get exact required height (7 mm). Figure 42 (a and b) shows the combination of different bead height to get the exact height. As it was explained before, a smaller bead height or more layers will generate a higher strength [37] [38] [39]; consequently. Thus, for this case, Figure 42 (a) would be preferred.



(a) (b)

Constraints	Height	
	7 mm	7 mm
$7 \leq \sum_{j \in J} S_j N_j \leq 7 + 0.1$	✓	✓
Total layers, $\sum_{j \in J} N_j$	4	3

Figure 42. Compare the final height and number of layers with bead heights from Figure 27

Figure 29 illustrates the car seat example. When producing this part with the OEM software (Insight® software), there are four available bead height sizes which are {0.1270, 0.1778, 0.254, and 0.3302 mm}. As it was discussed before, by using one bead height size during the process, is not possible to get the exact wanted height. However, by using Equation 1, by combining 666 layers of bead height 0.127 mm, 179 layers of bead height 0.1778 mm, and 102 layers of bead height 0.3302mm, is possible to get the exact height which is 150.0886 mm. Table 18 shows the combination of the number of layers with different bead heights for this example. In this dissertation, it is assumed that the first layer has the lowest optimal bead height. Thus, in this example, the bead heights of layers first to 666th are 0.127 mm, layers 667th to 845th have 0.1778 mm bead height, and from layer 846th to the last layer have 0.3302 mm bead height.

Table 18. An optimal combination of bead heights to produce Figure 29

Bead Height (mm)	Number of Layers
0.1270	666
0.1778	179
0.3302	102
Total	947

The next parameter that needs to be optimized is the bead width. For calculating an optimal bead width for layer $q \in Q$, the following steps are required. Note: this algorithm leverages the *.stl file characteristics, as the triangular facets are readily decomposed into points and lines for each slice layer.

1. Let (x_r^l, y_r^l) be a point of corner $l \in L$ in the layer $q \in Q$.
2. Add a bounding rectangle around the part. Figure 43 shows one layer with its seven corners (l) and the difference between the contour borders of the part with two different raster angles (0° and 135°). If the raster angle for layer $q \in Q$ is changed from r to r' then the point (x_r^l, y_r^l) is changed to $(x_{r'}^l, y_{r'}^l)$ which is

$$\begin{bmatrix} x_{r'}^l \\ y_{r'}^l \end{bmatrix} = \begin{bmatrix} \cos(r' - r) & -\sin(r' - r) \\ \sin(r' - r) & \cos(r' - r) \end{bmatrix} * \begin{bmatrix} x_r^l \\ y_r^l \end{bmatrix}; \forall l, r, \text{ and } r'. \quad [2]$$

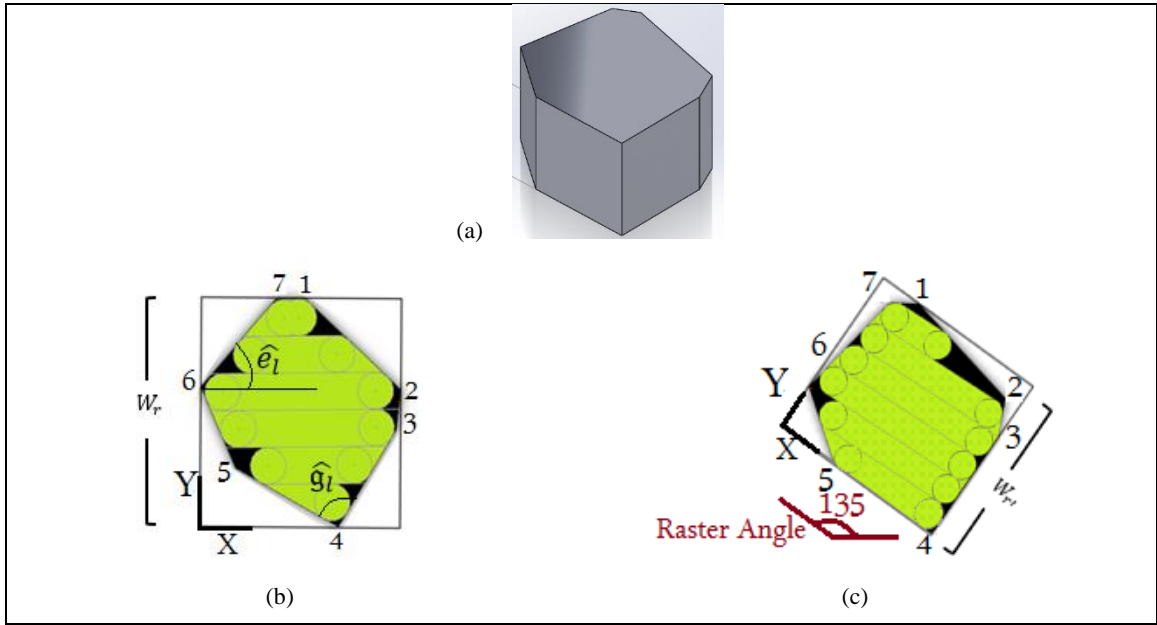


Figure 43. The relationship between raster angle and the bounding rectangle, (a) $\hat{r}=0^\circ$ and (b) $\hat{r}=135^\circ$

3. Let W_r be the length between the lowest and highest points of the bounding rectangle around one layer with the raster angle, r . Then

$$W_r = y_r^{max} - y_r^{min}; \forall r.$$

$$y_r^{max} = \max_{\forall l \in L} y_r^l; \forall r.$$

$$y_r^{min} = \min_{\forall l \in L} y_r^l; \forall r.$$

[3]

Figure 44 (a and b) show the difference of W_r when the raster angle is 0° and 45° . In these two cases, the size of optimal bead width is different due to the fact that W_r is depended on raster angle (r). The line spacing in Figure 44 is uneven to show the difference between optimal bead widths in two cases.

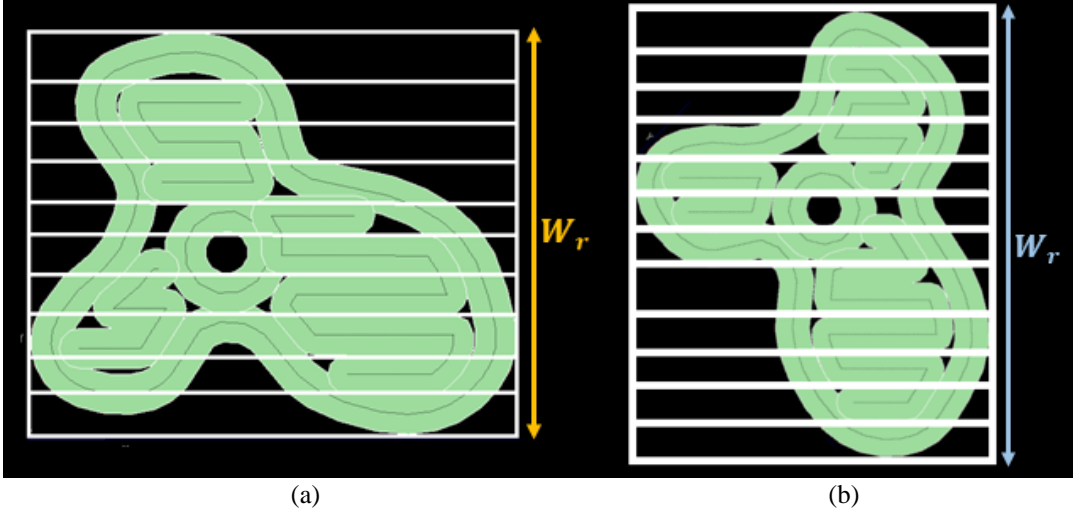


Figure 44. W_r Of one layer when the raster angle is, (a) 0° and (b) 45°

4. Let w_i^j be the bead width $i \in I$ for the optimal bead height S_j ; $j \in J$. As it was presented in Table 17, the bead height S_j ; $j \in J$, has a range of discrete available bead widths, $i \in I$. Let O_i be the percentage of overlap with a bead width w_i^j . If $R_i = \left\lceil \frac{W_r}{w_i^j} \right\rceil$; $\forall r, i, j$ is integer number of rasters with a bead width w_i^j and O^* be the maximum allowable overlap, then the optimal overlap percentages for each allowable bead width is calculated by

$$O_i = \frac{R_i w_i^j - W_r}{w_i^j (R_i - 1)} * 100 ; \forall i, j, r.$$

When

$$w_i^j \leq W_r ; \forall i, j, r.$$

$$R_i = \left\lceil \frac{W_r}{w_i^j} \right\rceil ; \forall i, j, r.$$

$$0 \leq O_i \leq O^*, \forall i.$$

[4]

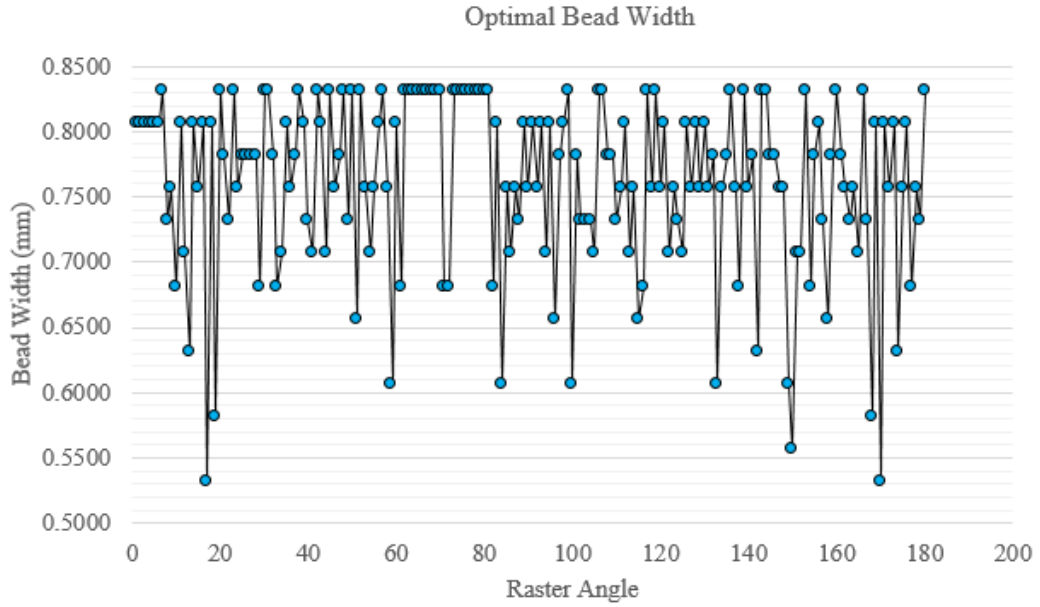
If O^* is the maximum allowable overlap in the process, then an optimal overlap need to be $O_i \leq O^*$. Thus, for one layer by changing the raster angle from 0° to 179° , there are 180 different W_r , and if the number of allowable bead width with bead height j is n , then for each raster angle there are n optimal bead width and n optimal overlaps with Equation 4.

Figure 45 (a) and (b) show the optimal bead width and overlap per raster angle for the layer Figure 43(a), respectively. The figures indicate each raster angle, has specific optimal bead width and overlaps.

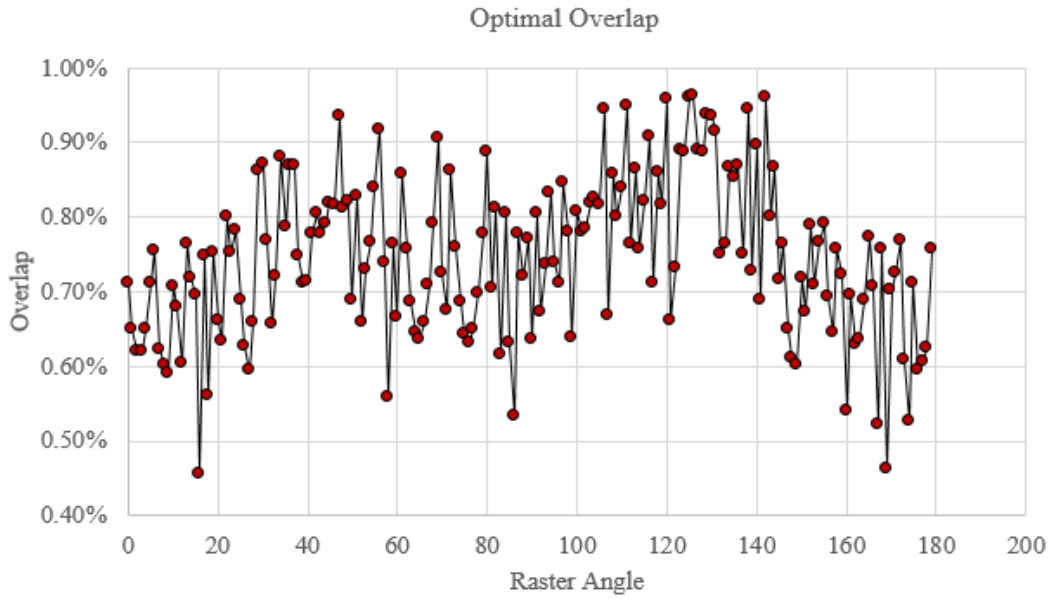
For example, for Figure 43(b and c) the optimal bead width and overlap percentages are shown in Table 19. As it shows, because of changing the length between the lowest and highest points of the bounding rectangle (W_r) with raster angle, r , there are different optimal bead width and overlaps percentages. This cause changes voids area with a different situation. The next part of this section illustrates visualizing and analyzing voids area in each layer with different raster angles.

Table 19. The relationship between raster angle, bead width and overlaps for Figure 43 (b and c)

r Raster Angle	W_r (mm) the length between the lowest and highest points	w_i^j (mm) Optimal Bead Width	O_i Optimal Overlaps
0°	104.8922	0.8064	0.71%
135°	80.79	0.8314	0.85%



(a)



(b)

Figure 45. (a) Optimal bead width and (b) Optimal overlaps per raster angle from 0° to 179° for one layer of Figure 43(a)

Determining Voids Area

After calculating optimal bead width and overlap percentages for each raster angle, the area of voids for each raster angle in one layer needs to be calculated. The minimum voids choose the optimal raster angle for each layer. The voids that are generated using the AM-ME process classifies into three groups, which Figure 46 show. The toolpath is shown as a green color, and the specific void type is labeled with the voids shown as the black color. Each of these void groups is explained below by details.

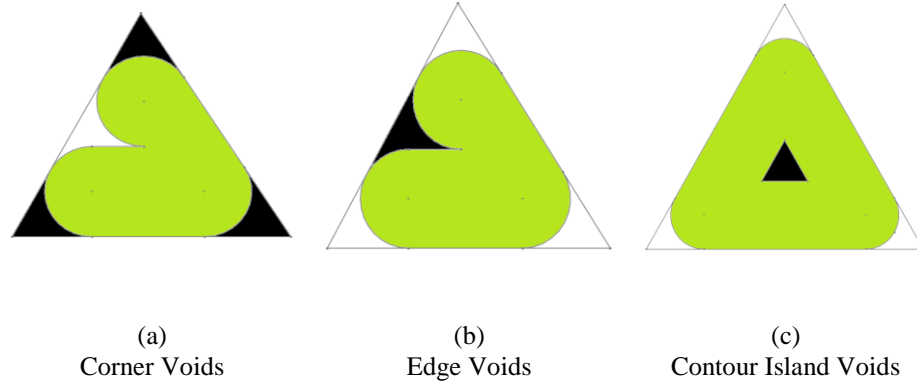


Figure 46. Three categories of voids – (a) corner, (b) edge, and (c) contour center

Having voids in a corner condition is an inherent characteristic of the AM-ME processes. As Figure 46 (a) shows, by minimizing the bead width, the area of the corner voids is reduced, but they cannot be eliminated. Consequently, the focus of this research targets the edge and contour island void conditions that are illustrated in Figure 46 (b) and (c), respectively.

Let $\hat{g}_l, \forall l \in L$ be the angle of corner $l \in L$ for the layer $q \in Q$ and w_i^j be the bead width $i \in I$ for bead height j . Then the formula for calculating the corner voids area for layer q, v_q^c , is

$$v_q^c = \sum_{l \in L} \left(\frac{w_i^j}{2}\right)^2 \left(\left| \cot \frac{\hat{g}_l}{2} \right| - \left(\frac{\pi - \hat{g}_l}{2}\right) \right); \forall i, j, q. \quad [5]$$

As Equation 5 shows, the relationship between the corner voids (v_q^c) and the bead width (w_i^j) is a direct relationship. This means that by decreasing the bead width, the corner void areas will be decreased, which is an obvious conclusion. As Figure 47 compares the corner voids area with different corner angles and two different bead width sizes, the smallest edge (corner with 50°) has the biggest voids area and by increasing bead width from 20 mm to 40 mm, the voids area is maximized from 101 mm² to 404 mm².

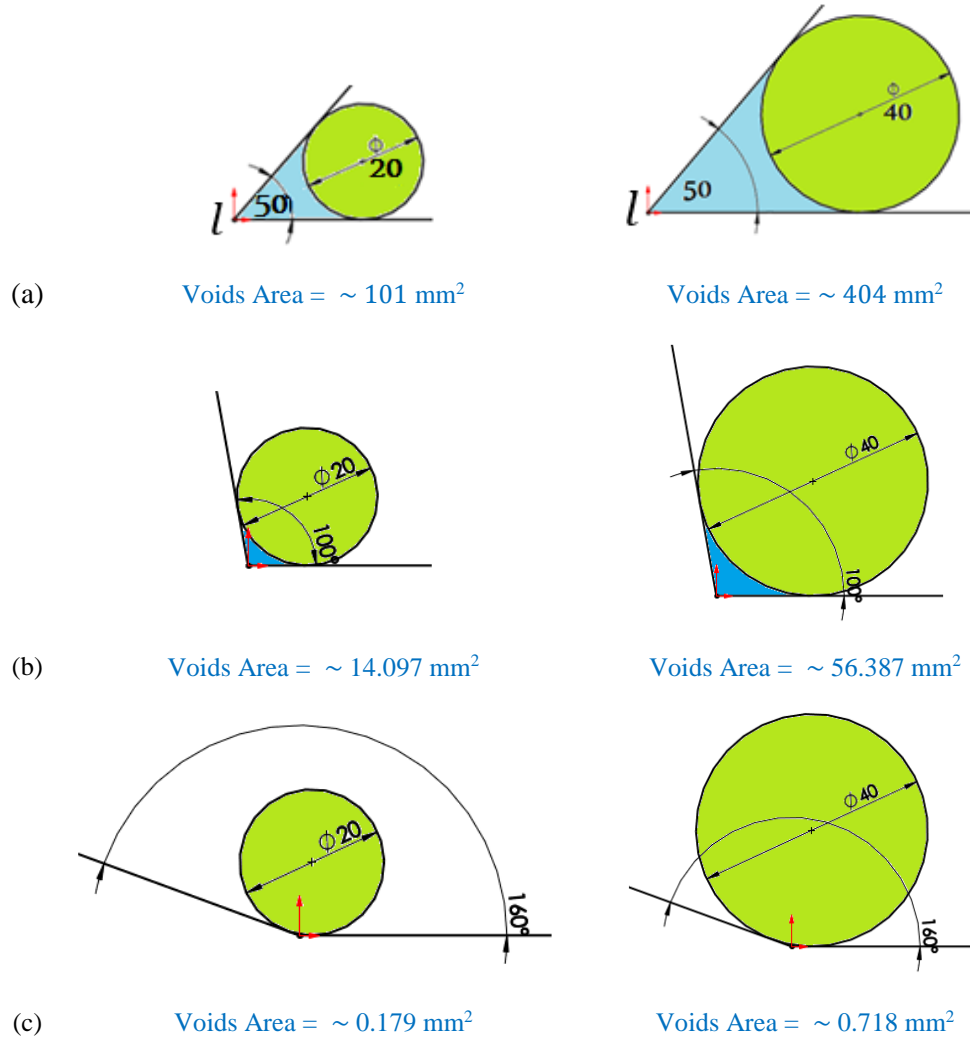


Figure 47. The relationship between corner void with (a) $\hat{g}_l=50^\circ$, (b) $\hat{g}_l=100^\circ$, and (c) $\hat{g}_l=160^\circ$ with two bead width sizes: (left) 20 mm and (right) 40 mm

The second type of voids is the edge voids, v_q^E , which is shown in Figure 46 (b). The edge voids are dependent on the raster angle, the bead width, and the percentage overlap. Let Ψ_t be the distance between Y-axis (y_l and y_{l+1}) of two continuous corners (l and $l + 1$) in the layer q . $t \geq 1$ is for the corners which have $x_r^l > x_r^{max}$ and $t \leq -1$ for $x_r^l < x_r^{max}$ with raster angle r . Figure 48 (b) shows this parameter for all points for Figure 48 (a).

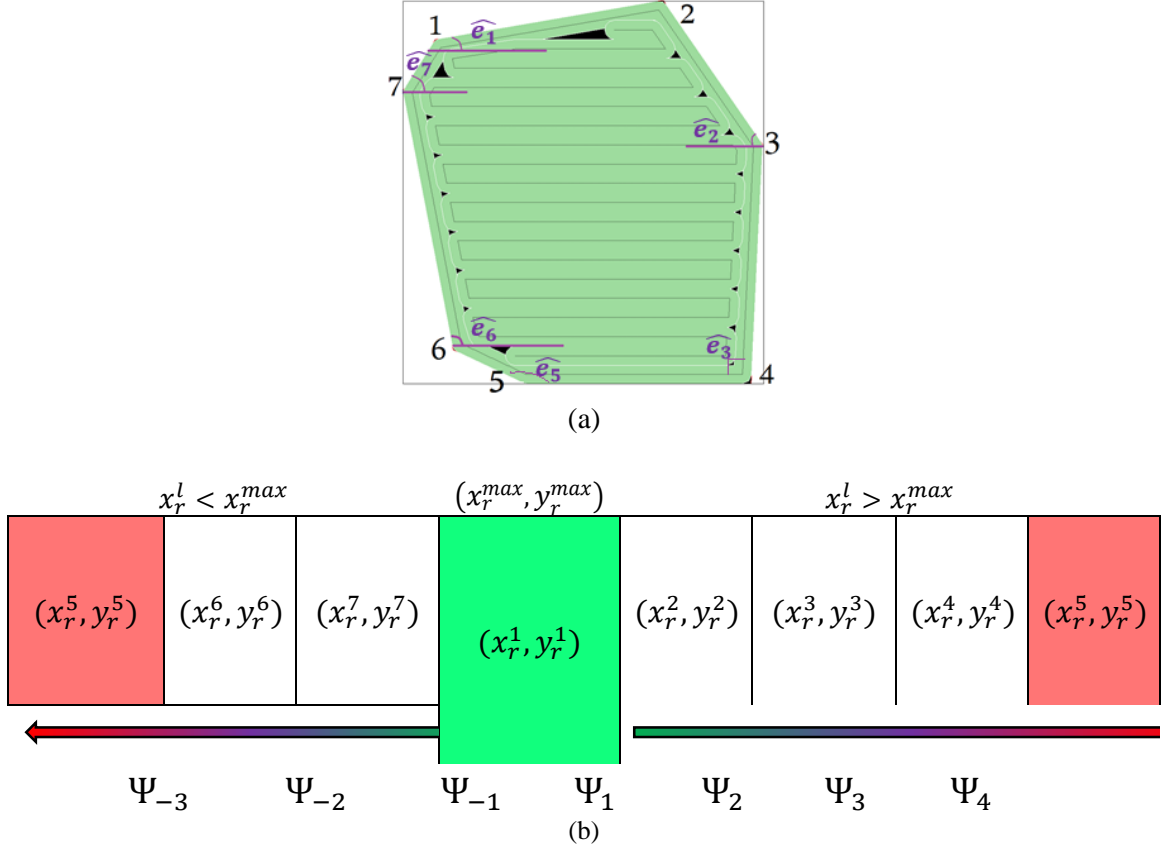


Figure 48. (a) Exact screenshot of a layer in the real OEM software, (b) Sorting Ψ_t for this layer

Let \hat{e}_l be the angle between the edge l and the Y-axis and O_i is optimal overlap. Edge l is the side between two corners of Ψ_t . Then the edge void, v_q^E , is calculated by

$$v_q^E = (1 - O_i) \frac{w_i^{j2}}{4} \sum_{\forall l} \left[\frac{\Psi_t}{w_i^j} \right] \left(\frac{2}{|\sin \hat{e}_l|} - \frac{\pi}{2} \right); \forall i, j, \hat{e}_l \in \{0, \pi\}. \quad [6]$$

Assume that a triangle with 80° , 51° and 49° internal angles exists, and the range of bead widths that are usable is $\{9.85, 10.52, 14.08, \text{ and } 16.30 \text{ mm}\}$. If the raster angle in Figure 49 (a) is increased from 40° to 55° , and the allowable overlap is 0%, the optimal bead width will be changed from 14.08 to 9.85 mm. The reason is that by the changing raster angle, W_r is changed from $W_r = 154.88$ mm to 128.05 mm. The edge voids which are calculated by Equation 6, and the voids area increases from 67 mm^2 to 74 mm^2 (Figure 49 (b)). If Figure 49 (a) has 15% overlap with the same raster angle, the optimal bead width will be changed from 14.08 to 16.30 mm and, the edge voids decrease from 67 mm^2 to 26 mm^2 (Figure 49 (c)). When increasing the overlap percentages, the edge voids

decrease dramatically. However, there are physical constraints related to the process type and bead shapes.

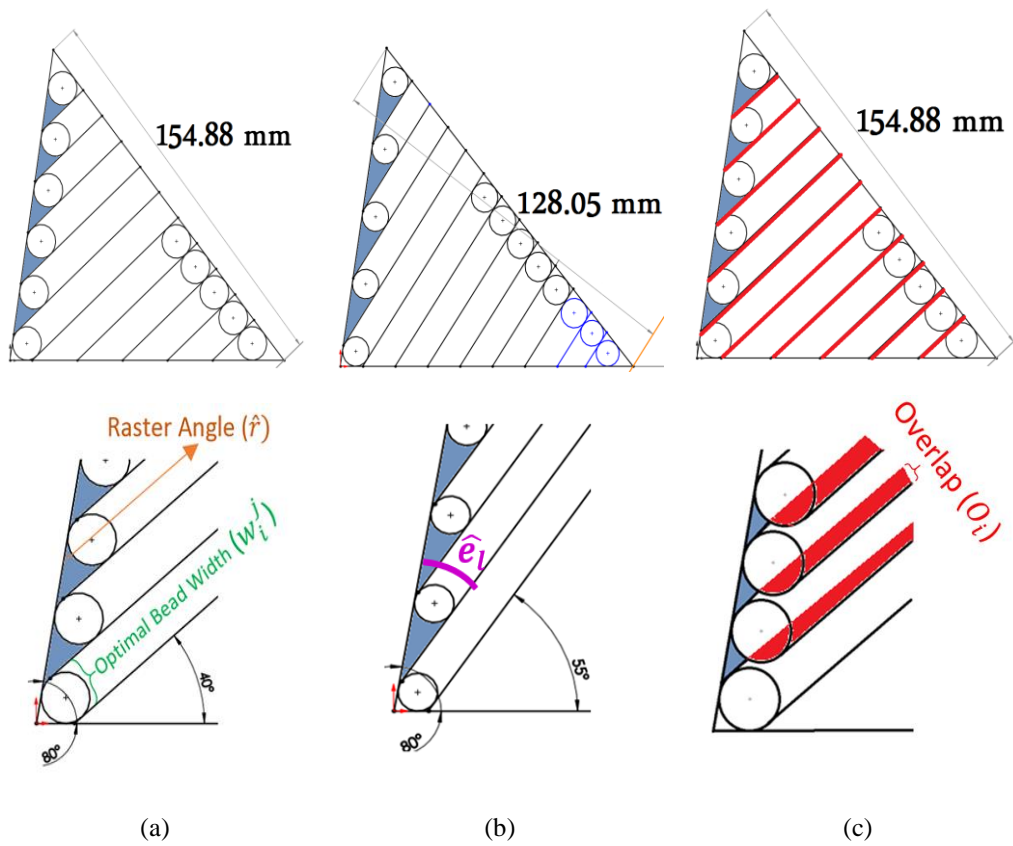


Figure 49. The relationship between raster angle and voids area for an optimized bead width with (a) 40° raster angle without overlaps, (b) 55° raster angle without overlaps, (c) 40° raster angle with a 15% overlap condition.

Table 20 summarizes the toolpath parameters for the example of Figure 49. It shows the edge voids has the relationship with raster angle, bead width and overlaps.

Table 20. The relationship between toolpath parameters and the edge voids area

Figure 49	(a)	(b)	(c)
Raster Angle (r)	40^0	55^0	40^0
Bead width (w_i^j)	14.08 mm	9.85 mm	16.30 mm
Number of Rasters (R_i)	11	13	11
Overlap (O_i)	0%	0%	15%
Edge Voids Area (v_q^E)	$\sim 67 \text{ mm}^2$	$\sim 74 \text{ mm}^2$	$\sim 26 \text{ mm}^2$

The other constraint for each edge void is that each edge void should be less than one bead. If the cross-sectional area of one bead is $\frac{\pi w_i^j^2}{8}$, (assuming a circular cross-section as the height is irrelevant for this analysis) then

$$\frac{w_i^j^2}{4} \left(\frac{2}{|\sin \hat{e}_l|} - \frac{\pi}{2} \right) < \frac{\pi w_i^j^2}{8} ; \forall i, j, \hat{e}_l - \{0, \pi\}. \quad [7]$$

The third type of void is the ‘contour center’ void (Figure 46 (c)). These voids occur when the contour toolpath is the only toolpath in the process like Figure 17 (b), and the contour geometry collapses upon itself. In this dissertation, it is assumed that there is one contour toolpath for each layer.

The total void area of layer $q \in Q$ with a raster angle r bead width w_i^j , and optimal overlap O_i , will be

$$v_q^C + v_q^E; \forall q \in Q. \quad [8]$$

For minimizing the total voids area of layer $q \in Q$ with an optimal bead height j , the mathematical model is:

$$\min_{\forall r} \min_{\forall i} \left(\frac{w_i^j}{2} \right)^2 \sum_{\forall l} \left| \cot \frac{\hat{g}_l}{2} \right| - \left(\frac{\pi - \hat{g}_l}{2} \right) + \left[\frac{\left[\frac{\Psi_t}{w_i^j} \right]}{2} \right] \left(1 - \frac{100 \left(\left[\frac{W_r}{w_i^j} \right] w_i^j - W_r \right)}{w_i^j \left(\left[\frac{W_r}{w_i^j} \right] - 1 \right)} \right) \left(\frac{2}{|\sin \hat{e}_l|} - \frac{\pi}{2} \right); \forall j.$$

Subject to

$$w_i^j < W_r; \forall i, j, r$$

$$0 \leq O_i \leq O^*; \forall i$$

$$\sin \hat{e}_l > \frac{2}{\pi}; \forall l.$$

[9]

After comparing total voids with n bead width and overlaps (n is a number of allowable bead width for bead height j) for each raster angle, and then comparing 180 raster angles in each layer, the optimal bead width, overlap, and raster angle for each layer are determined. Thus, an exhaustive search methodology is employed with this mathematical model for all layers. Figure 50 summarized phase I for the rectangular cube example. The rasters that are shown as an example of the layer; are 0° , 45° , 135° , and 90° . For this specific example, the optimal raster angle to minimize voids is 0° .

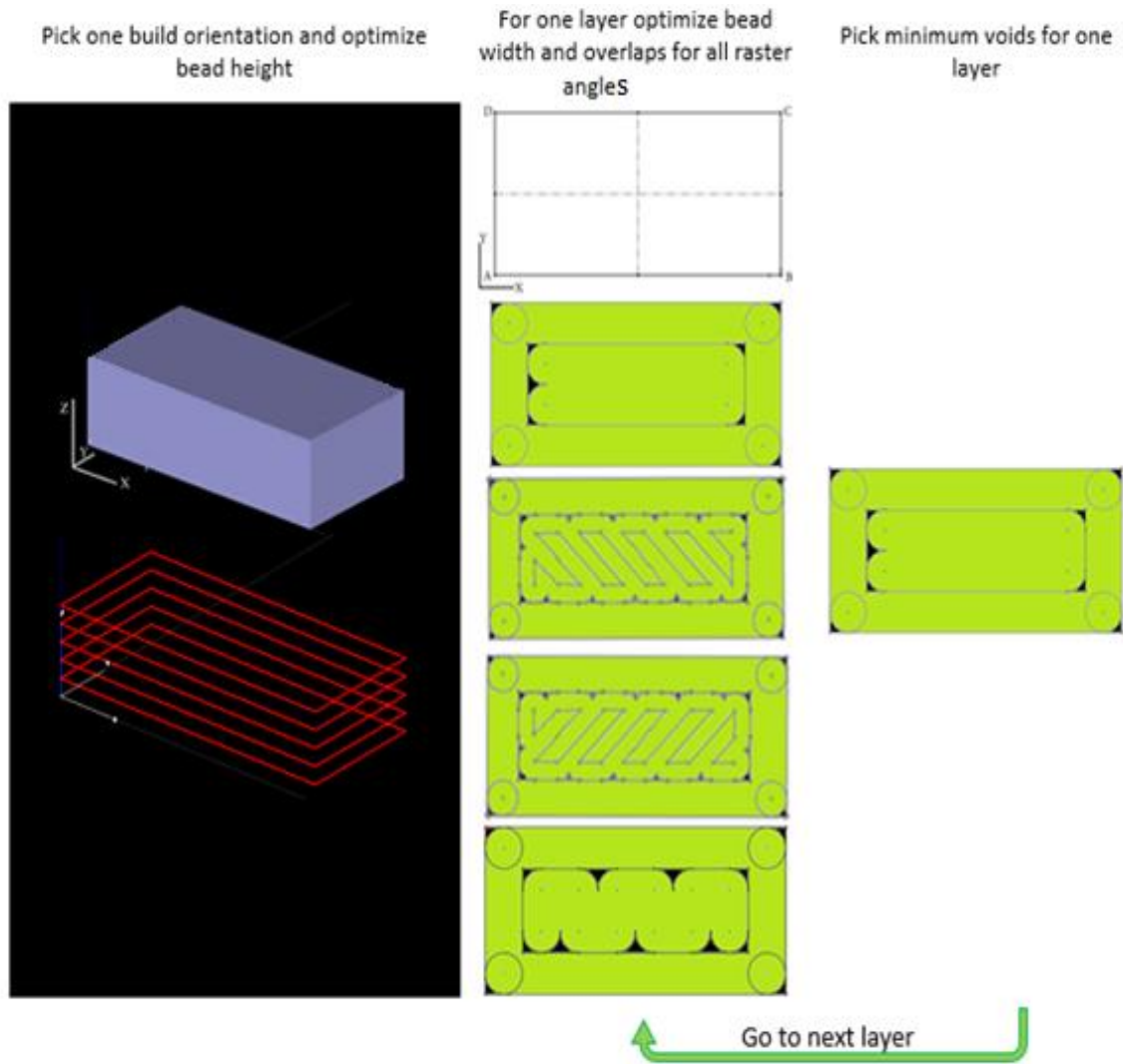


Figure 50. Steps of Phase I

This mathematical model minimizes corner voids and edge voids in each layer. However, this mathematical model does not follow voids between layers. The next section describes evaluating voids position to manage them between layers to cover all voids during the process.

Phase II _ Optimizing Voids Position

In this section, the nozzle movements during the toolpath and the ways of optimizing the nozzle movements in each layer during the process are explained at the beginning. Then the splitting the complex shape to simple shape is explained, and at the end, the optimization of the positions of voids to avoid creating chimneys is illustrated.

The second phase targets determining the positions of the voids, and selecting a ‘suboptimal’ process parameter configuration needed to prevent void regions being stacked contiguously between layers (Figure 51). Thus, an exhaustive search and sort methodology is employed in this phase as same as phase I. The below figure shows phase I and II together. Phase II starts since phase I has been finished for all layers.

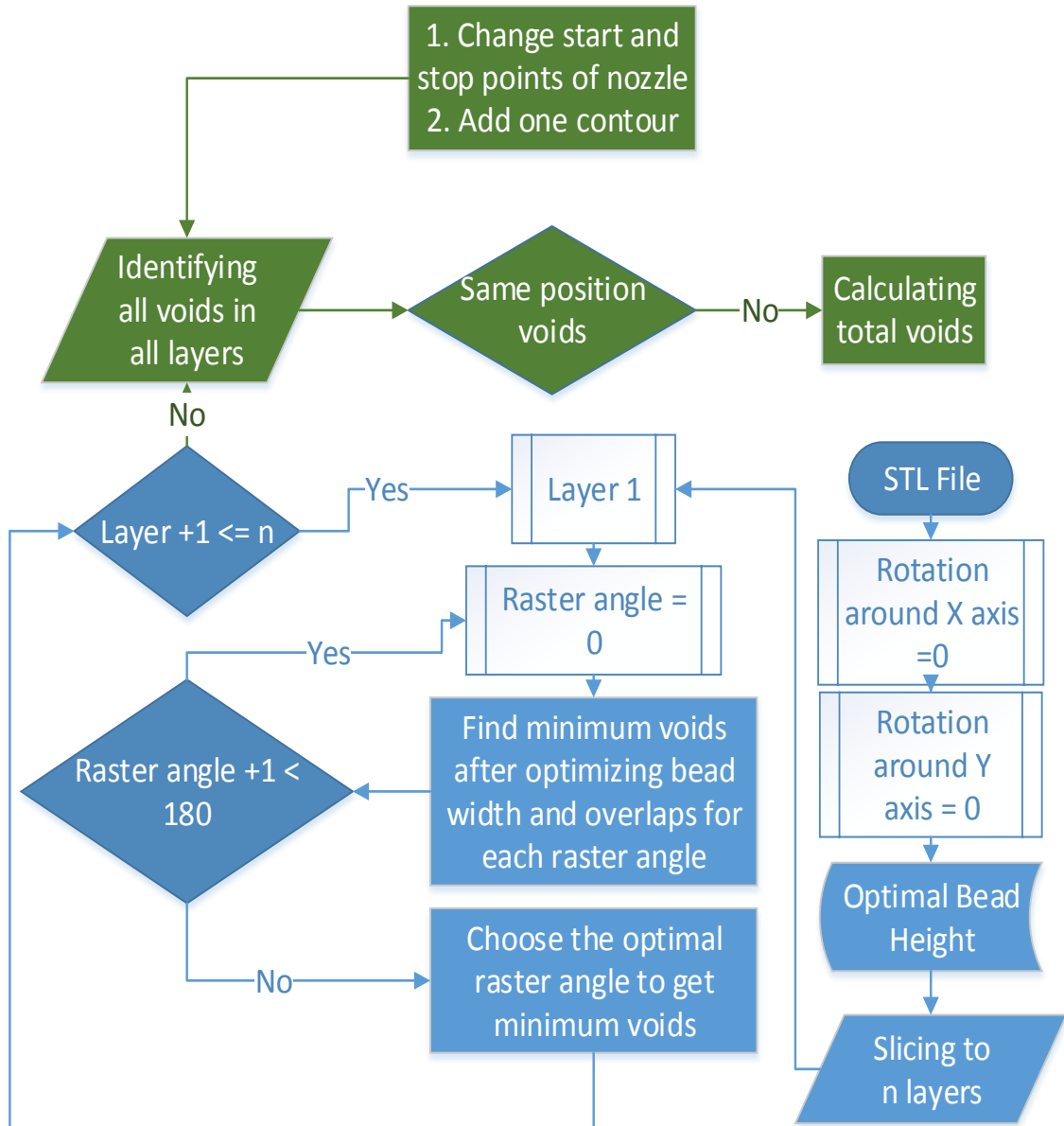


Figure 51. Phase II diagram added to phase I diagram

Managing Nozzle Movements

As it was discussed before, the toolpath is the trajectory of the nozzle during the manufacturing process to fill the interior of each layer [30]. The movement speed of the nozzle is determined bead width and bead height. By optimizing the bead width and bead height, the user will manage the movement speed of the nozzle. By optimizing the stop and start points of the nozzle, the toolpath is controlled during the process. This helps minimize voids in all complex shapes. For example, the optimal bead width, and overlap, for one raster angle of the layer Figure 52 (a) are found. The next step is visualizing the nozzle movement during the toolpath with these parameters. The contour offsets inside by half of the optimal bead width. All points and lines of the contour will be offset and defined. Figure 52 (b) illustrates the nozzle movement during the contour toolpath. With optimal bead width and overlaps, the position of rasters are defined which are parallel to X-axis (Figure 52 (c)). All start and stop points of rasters are determined as well as Figure 52 (d). In this figure, the blue beads are start points and the orange ones are stop points. The nozzle has traced these point during the toolpath. Figure 52 (e) shows the connection between the stop and start points between rasters. In the end, the nozzle movement is specified as Figure 52 (f) is shown.

However, in some cases, after visualizing the toolpath, the movement of nozzle needs to be optimized to remove the unwanted start and stop points. For example, if the layer Figure 53 (a) rotates 90^0 , there is the new layer which is shown in Figure 53 (b). For Figure 53 (a) there is no gap for any raster deposition path, but for Figure 53 (b) there is a gap between rasters. As Figure 53 (a and b) show, if the intersection between the line generated by a tool path and the edges of a layer is more than two, there are gaps during one raster deposition track. For example, in Figure 53 (b), the raster number 3 stops at point number 2 and restarts at point number 3.

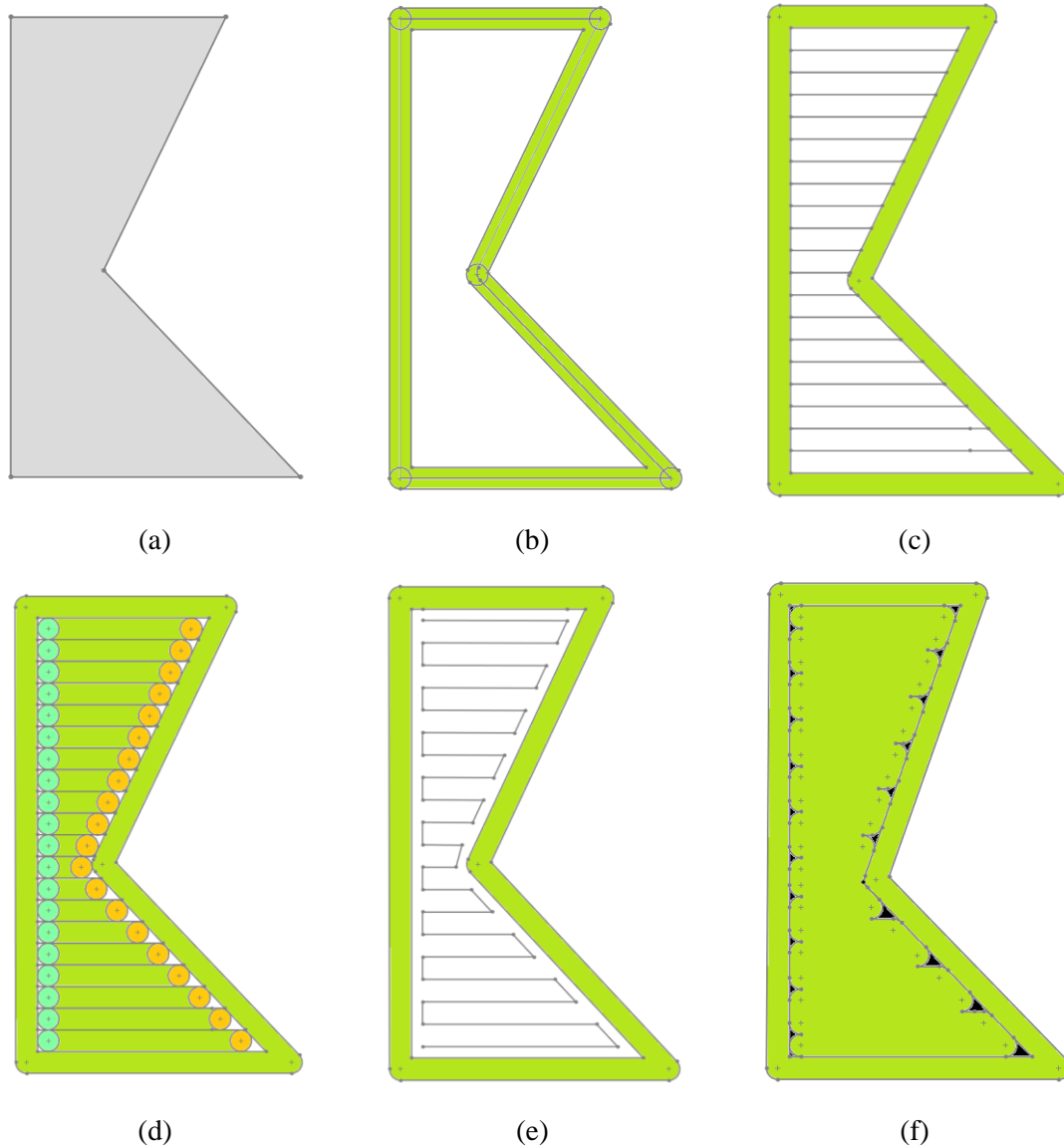


Figure 52. Nozzle movements, (a) Shape of a layer, (b) Contour toolpath, (c) Position of rasters, (d) Stop and start points, (e) Nozzle path, and (f) Complete nozzle movements

In this dissertation, a condition shown in Figure 53 (a) (i.e. no steps or start and stop points for a deposition path) are implicitly concave; therefore, they are identified as convex shapes (for the context of tool path generation); whereas, the other orientation is ‘classically’ concave shapes (Figure 53(b)). Here, the convex shapes are preferred than concave shapes as this reduces discontinues and potential void conditions. If the total void area in both cases is the same, Figure 53(a) is chosen as an optimal raster angle because it is a convex shape.

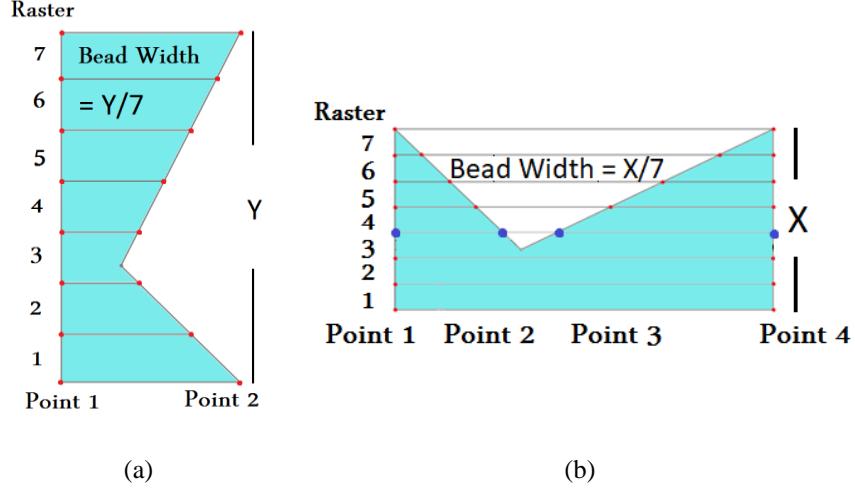


Figure 53. Difference between convex (a) and concave (b) shapes.

However, not all shapes can be rotated to result in a “convex” shape solution. The best strategy for the complex shapes is dividing a concave shape into multiple convex shapes. If a new convex shape is $f \in F$, and n is a total number of edges and m is a total number of rasters. Then the voids possibility matrix, M_q^f , of layer q is

$$M_q^f = \begin{bmatrix} B_1^1 & \dots & B_n^1 \\ \vdots & \ddots & \vdots \\ B_1^m & \dots & B_n^m \end{bmatrix}, \forall f, q, n, \text{ and } m. \quad [10]$$

$$B_l^r = \begin{cases} 0, & \text{Raster Angle, } r, \text{ is Parallel to Side } l \\ 1, & \text{Otherwise} \end{cases}$$

The above equation means there is a binary function for having edge voids in side l . If the raster angle is parallel to the side, the function is $B_l^r=0$, otherwise is equal to one. In the layer, q , after dividing the concave shape to $f \in F$ new shapes with n edges, there is the matrix for each new shape f . The summation of all B_l^r in M_q^f results in the total possibilities of having edge voids. This helps choose the optimal division before calculating voids area. For example for triangle shape, six options are existed for having voids in Figure 54.

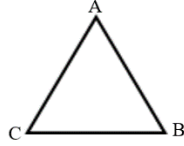
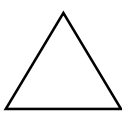
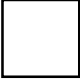

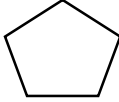
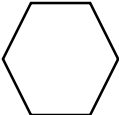


Figure 54. Triangle example for voids place

The Matrix for having voids in each edge is $M_q^f = \begin{matrix} & AB & BC & CA \\ AB & 0 & 1 & 1 \\ BC & 1 & 0 & 1 \\ CA & 1 & 1 & 0 \end{matrix}$.

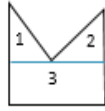
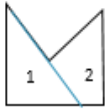


It means that if the raster angle is a parallel of edge AB, on the edge of AB has no voids but on the other edges like BC and CA, there are voids. Table 21 illustrates voids possibility matrix for some simple shapes.

Table 21. Voids possibility matrices for some simple shapes

					
Voids Possibility	$\begin{matrix} 0 & 1 & 1 \\ 1 & 0 & 1 \\ 1 & 1 & 0 \end{matrix}$	$\begin{matrix} 0 & 1 & 0 & 1 \\ 1 & 0 & 1 & 0 \\ 0 & 1 & 0 & 1 \\ 1 & 0 & 1 & 0 \end{matrix}$	$\begin{matrix} 0 & 1 & 1 & 1 \\ 1 & 0 & 1 & 0 \\ 1 & 1 & 0 & 1 \\ 1 & 0 & 1 & 0 \end{matrix}$	$\begin{matrix} 0 & 1 & 1 & 1 & 1 \\ 1 & 0 & 1 & 1 & 1 \\ 1 & 1 & 0 & 1 & 1 \\ 1 & 1 & 1 & 0 & 1 \\ 1 & 1 & 1 & 1 & 0 \end{matrix}$	$\begin{matrix} 0 & 1 & 1 & 0 & 1 & 1 \\ 1 & 0 & 1 & 1 & 0 & 1 \\ 1 & 1 & 0 & 1 & 1 & 0 \\ 0 & 1 & 1 & 0 & 1 & 1 \\ 1 & 0 & 1 & 1 & 0 & 1 \\ 1 & 1 & 0 & 1 & 1 & 0 \end{matrix}$
Total Voids Possibility	6	8	10	20	24

For dividing the concave shape into convex shapes, there are multiple alternative solutions. As Table 22 shows, there are multiple alternatives to divide Figure 53 (b) into a set of convex shapes. The total voids area for each case listed in the table is calculated. As shown, column c of Table 22 has the minimum total voids area and the number of void possibilities. The results in Table 22 show that instead of calculating void areas, the possibilities can generate the same answer. For example, shape 1 in Column c of Table 22 has 6 possibilities to create edge voids for each sub-divided shape, and the total voids possibilities sums to 12. This scenario introduces the minimum void possibilities, which is less than the other decomposition cases, as well as having a lesser predicted void area.

Table 22. Methods for dividing concave shapes

# Profile $f \in F$									
	1	2	3	1	2	1	2	1	2
Voids Area (mm ²)	5.47	12.13	2.91	6.88	13.18	6.34	4.77	4.82	12.50
Total Voids Area (mm ²)	20.51			20.06		11.11		17.32	
Voids Possibility	0 1 1 1 0 1 1 1 0	0 1 1 1 0 1 1 1 0	0 1 0 1 1 0 1 0 0 1 0 1 1 0 1 0	0 1 1 1 0 1 1 1 0	0 1 1 1 1 0 1 1 1 1 0 1 1 1 1 0	0 1 1 1 0 1 1 1 0	0 1 1 1 0 1 1 1 0	0 1 1 1 1 0 1 0 1 1 0 1 1 0 1 0	0 1 1 1 1 0 1 0 1 1 0 1 1 0 1 0
	6	6	8	6	12	6	6	10	10
Total Voids Possibility	20			18		12		20	

(a)

(b)

(c)

(d)

For finding an optimal solution for splitting a concave shape into convex shapes without calculating voids possibilities or void areas, the new geometry needs to satisfy the following constraints, in the order presented:

- Minimize the number of convex shapes, as this will limit the computational time, and limit the boundary curve-raster fill conditions. Voids occur in the boundary-fill junctions.
- Minimize the difference between areas of new convex shapes, as this will reduce the chances of having a small, unfillable region enclosed by a boundary.
- Minimize the number of sides in the new convex shapes, as this will reduce computation time for the general problem. Appendix C summaries multiple examples of different concave shapes and the optimal solution.

Also, this method is used for complex shapes like a solid cuboid with an internal rectangular hole (Figure 55(a)), there are several alternative ways to split the surface to generate multiple solid convex shapes without any internal holes. Figure 55 (b to e) shows alternatives of breaking the part. For the partitioning in this dissertation, the following constraints are employed:

The surface areas of the new partitioned convex shapes need to be same or nearly same to each other, as this will reduce the chances of a ‘no-fill’ scenario. Figure 55 (b, e) does not have this constraint. For example, in Figure 55 (b) the area of section 4 is much bigger than the other three areas. The partitioning line needs to be parallel to outside shape (contour) or inside the shape (hole). Figure 55(c) does not have this constraint. In this example, Figure 55 (d) has all constraints, and it is the best way to split the cuboid shape.

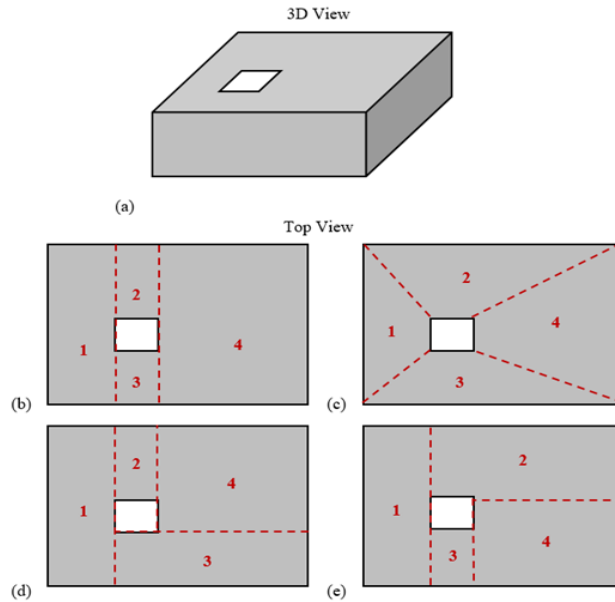
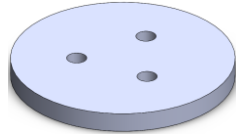
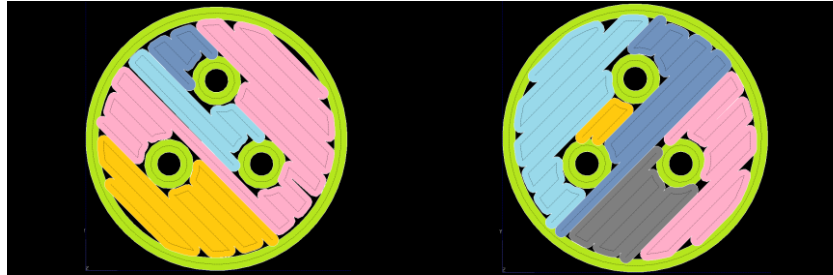


Figure 55. Example of shapes with an internal hole

It was found that there are unwanted voids within the toolpath and, there are discontinuities at the start and stop points during the direction parallel toolpath for complex shapes. Figure 56 (b and c) show unwanted voids in the layers during the process for the component Figure 56 (a). The Figure 56 (b and c) show voids for the first layer and the second layer, which are repeated throughout the component. Note that a ‘chimney’ throughout the component is inadvertently created. Each region of the toolpath has one stop and one start points. For example, the first layer has four regions. Thus, eight stop and start points are in this later. For solving this example, by dividing the shape to 4 regions and optimized bead width and raster angle with overlaps 0%, the voids area is minimized around 4%. Figure 56 (d) illustrates these four regions by the different colors. In this example, if the maximum allowable overlap changes to 50% then the voids area is minimized around 35%. Figure 56 (e) shows the optimal toolpath with 50% overlaps.

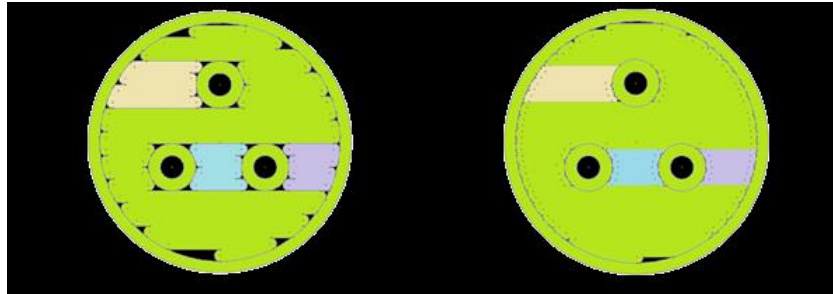


(a)



(b)

(c)



(d)

(e)

Figure 56. (a) 3D view, (b and c) First Layer (4 regions) and second Layer (5 regions) before connecting start points of some regions, (d) after connecting 0% overlaps, (e) 50% overlaps

Managing Voids Position

From Equation 9, for minimizing voids in a layer like a Figure 57 (a), there is a range of void areas, bead widths, and overlaps per raster angle which is illustrated in Figure 57 (b and c). As it shows, by changing raster angle for this layer the voids area is changed, dramatically. As it shows in three raster angles which are 0° , 30° , and 120° , the voids area are the minimum that other raster angles. The reason is with these raster angles; the rasters are parallel to edges.

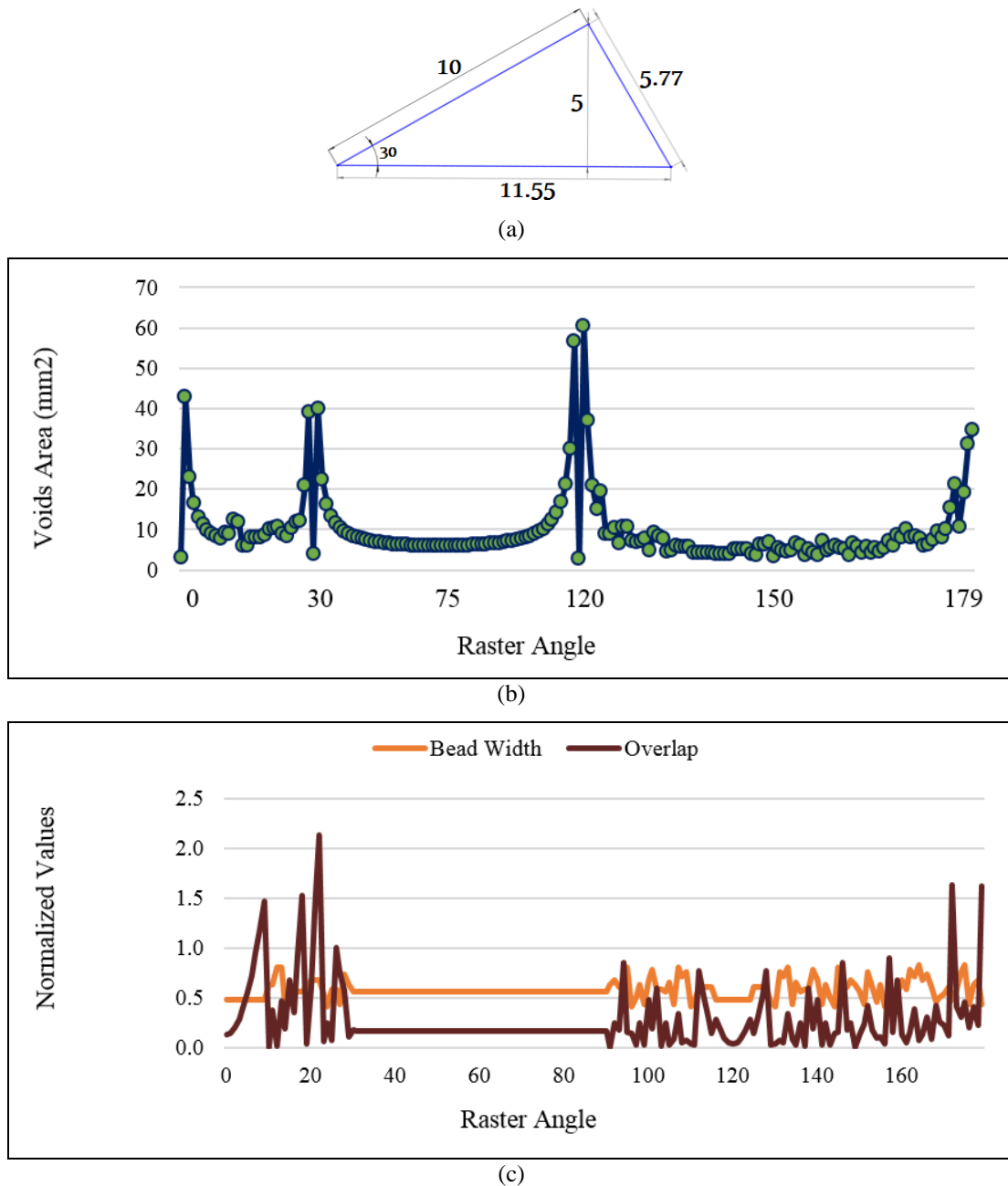


Figure 57. (a) Layer with triangle shape example, (b) Relationship of raster angle and voids, (c) relationship of bead width, overlap, and raster angle

After comparing the total void areas for all raster angles between 0° and 179° , it was found that for raster angles, 0° , 30° , and 120° , the whole void areas are less than others. These three raster angles are exactly parallel to each edge of Figure 57 (a). The voids' positions for the three optimal layers are shown below, respectively. As these figures show, all layers are in the same position, and raster angles are different.

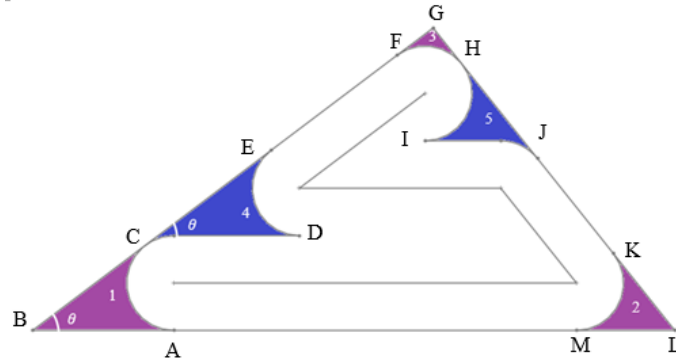


Figure 58. Void regions for the layer with 0° raster angles

Table 23. Details of points and area of voids in the first layer of Figure 58

Voids	ABC			CDE			FGH			HIJ			KLM		
Points	A	B	C	C	D	E	F	G	H	H	I	J	K	L	M
X	0	-1.89	-0.38	-0.38	1.6	1.3	2.98	3.47	3.85	3.85	3.36	4.86	5.88	6.7	5.39
Y	0	0	1.13	1.13	1.26	2.4	3.65	4.02	3.65	3.65	2.52	2.28	1.02	0	0
Area (mm ²)	0.695			1.946			0.079			1.642			0.382		
Total Voids	4.745														

The area of the layer of Figure 58 is 17.27 mm^2 and the area of the toolpath (material usage) is 12.525 mm^2 , which means around 27% voids occur during the toolpath. For the second layer, the optimal bead width is 0.3956 mm with raster angle 30° . The details of voids and points are in Figure 59 and Table 24.

The percentage of voids in this layer (second layer) is around 16%. For calculating the total void, there is

$$V_2^{ABCA} + V_2^{T'HS'T'} + V_2^{P'Q'LP'} + 8 * W_2^{CDEC} + 7 W_2^{B'C'U'B'} =$$

$$0.069 + 0.008 + 0.038 + 8 * 0.192 + 7 * 0.162 = 2.782 \text{ mm}^2.$$

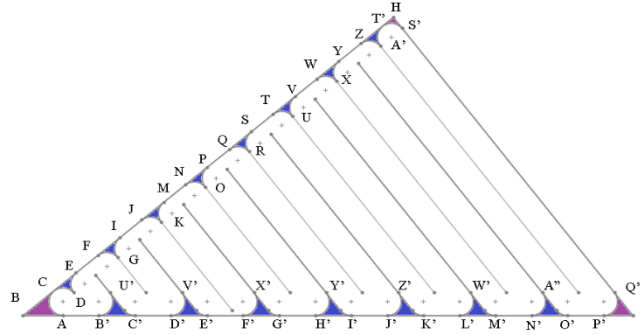


Figure 59. Void regions for the layer with 30° raster angles

Table 24. Details of points and area of voids in the first layer of Figure 59

Points	A	B	C	D	E	F	G	H	I	J	K	L	M
X	-1.89	-1.89	-1.42	-1.09	-0.94	-0.62	-0.30	3.47	-0.15	0.17	0.49	6.70	0.64
Y	0.00	0.00	0.36	0.36	0.71	0.95	0.95	4.02	1.31	1.54	1.54	0.00	1.90
Points	N	O	P	Q	R	S	T	U	V	W	X	Y	Z
X	0.96	1.29	1.43	1.75	2.08	2.22	2.54	2.87	3.02	3.33	3.66	3.81	4.12
Y	2.14	2.14	2.49	2.73	2.73	3.09	3.32	3.32	3.68	3.92	3.92	4.01	4.01
Points	A'	B'	C'	D'	E'	F'	G'	H'	I'	J'	K'	L'	M'
X	3.56	-1.49	-1.10	-0.70	-0.31	0.09	0.48	0.88	1.27	1.67	2.07	2.46	2.86
Y	4.01	0.00	0.00	0.00	0.00	0.00	0.00	0.00	0.00	0.00	0.00	0.00	0.00
Points	N'	O'	P'	Q'	S'	T'	U'	V'	W'	X'	Y'	Z'	A''
X	3.25	3.65	6.29	6.44	3.62	3.32	-1.36	-0.57	2.60	0.22	1.02	1.81	3.39
Y	0.00	0.00	0.00	0.32	3.88	3.88	0.32	0.32	0.32	0.32	0.32	0.32	0.32

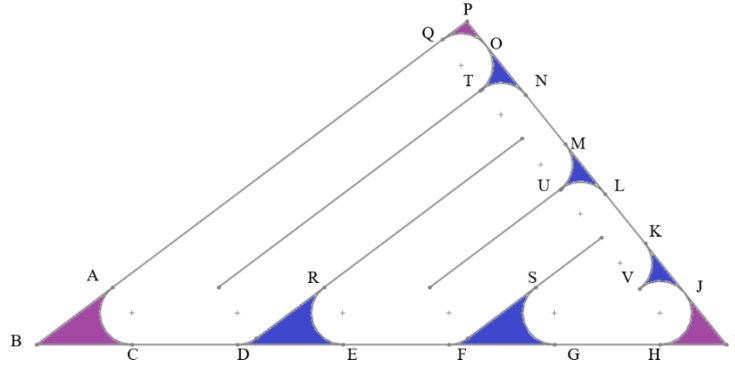


Figure 60. Void regions for the layer with 120° raster angles

Table 25. Details of points and area of voids in the first layer of Figure 60

A	B	C	D	E	F	G	H	I	J	K	L	M	N	O	P	Q	R	S	T	U	V
-0.94	-1.89	-0.70	0.61	1.93	3.25	4.56	2.48	6.70	6.14	5.69	5.19	4.70	4.20	3.66	3.47	3.16	1.69	4.32	3.64	4.63	5.62
0.71	0.00	0.00	0.00	0.00	0.00	0.00	4.17	0.00	0.69	1.26	1.87	2.49	3.11	3.78	4.02	3.79	0.71	0.71	3.16	1.93	0.69

The next step is evaluating void stacking for all layers to avoid creating an internal chimney. Figure 61 shows the combination of voids for the three layers and the black circles indicate the voids which are not covered between these three layers. These essentially void regions essentially create an unexpected internal channel.

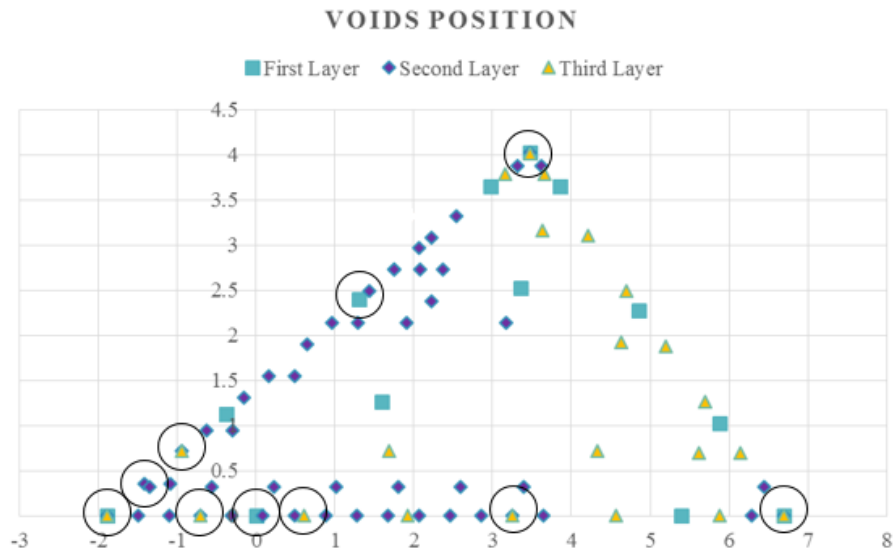


Figure 61. Combination voids for the three layers, respectively and the black circles show the voids which are not covered by these three layers

For finding the position of voids in a layer, the points between rasters and edges of the layers need to be determined.

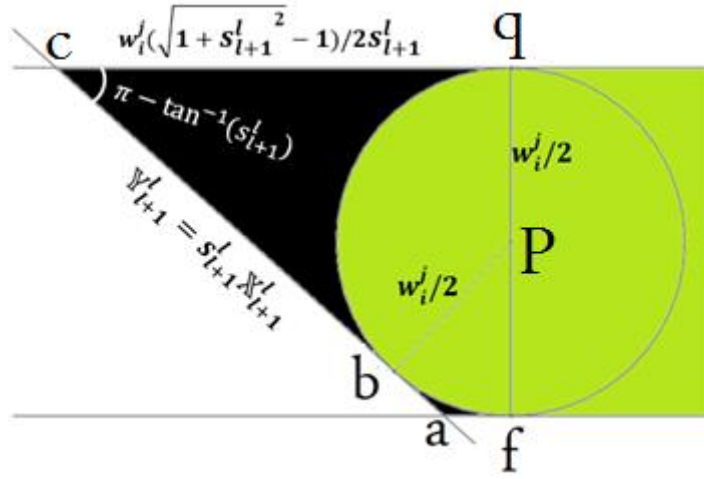


Figure 62. Position of voids

For example, if the edge formula between point a to b in the above figure is $Y_{l+1}^l = s_{l+1}^l X_{l+1}^l$. If points a and c are (U^3, V^3) and (U^4, V^4) , respectively, then the formula of points q, p, and b are in Table 26. In this dissertation, the area of voids is “fabcqf” (black area in Figure 62).

Table 26. The formula of voids points

q	p
$(U^4 + \frac{w_i^j(\sqrt{1+s_{l+1}^l{}^2}-1)}{2s_{l+1}^l}, V^4)$	$(U^4 + \frac{w_i^j(\sqrt{1+s_{l+1}^l{}^2}-1)}{2s_{l+1}^l}, V^4 - w_i^j/2)$
b	
$(U^3 + \frac{w_i^j(\sqrt{1+s_{l+1}^l{}^2}+1)}{2s_{l+1}^l\sqrt{1+s_{l+1}^l{}^2}}, V^3 + \frac{w_i^j(\sqrt{1+s_{l+1}^l{}^2}+1)}{2\sqrt{1+s_{l+1}^l{}^2}})$	

[11]

The below figure, emphasizes points of voids with different raster angles for a simple shape. For example, in layer (a) which its color is blue, the points ‘k’ and ‘p’ are the center of the beads (start

points), the voids which is created in this edge is “dcgqbafd” (black area). With above equation, all these points are calculated to avoid creating chimneys between layers. The position of points of Figure 63 (a and b) are same, except the angles are $\hat{a}' = \pi - \hat{a} = -\tan^{-1} s_{l+1}'$.

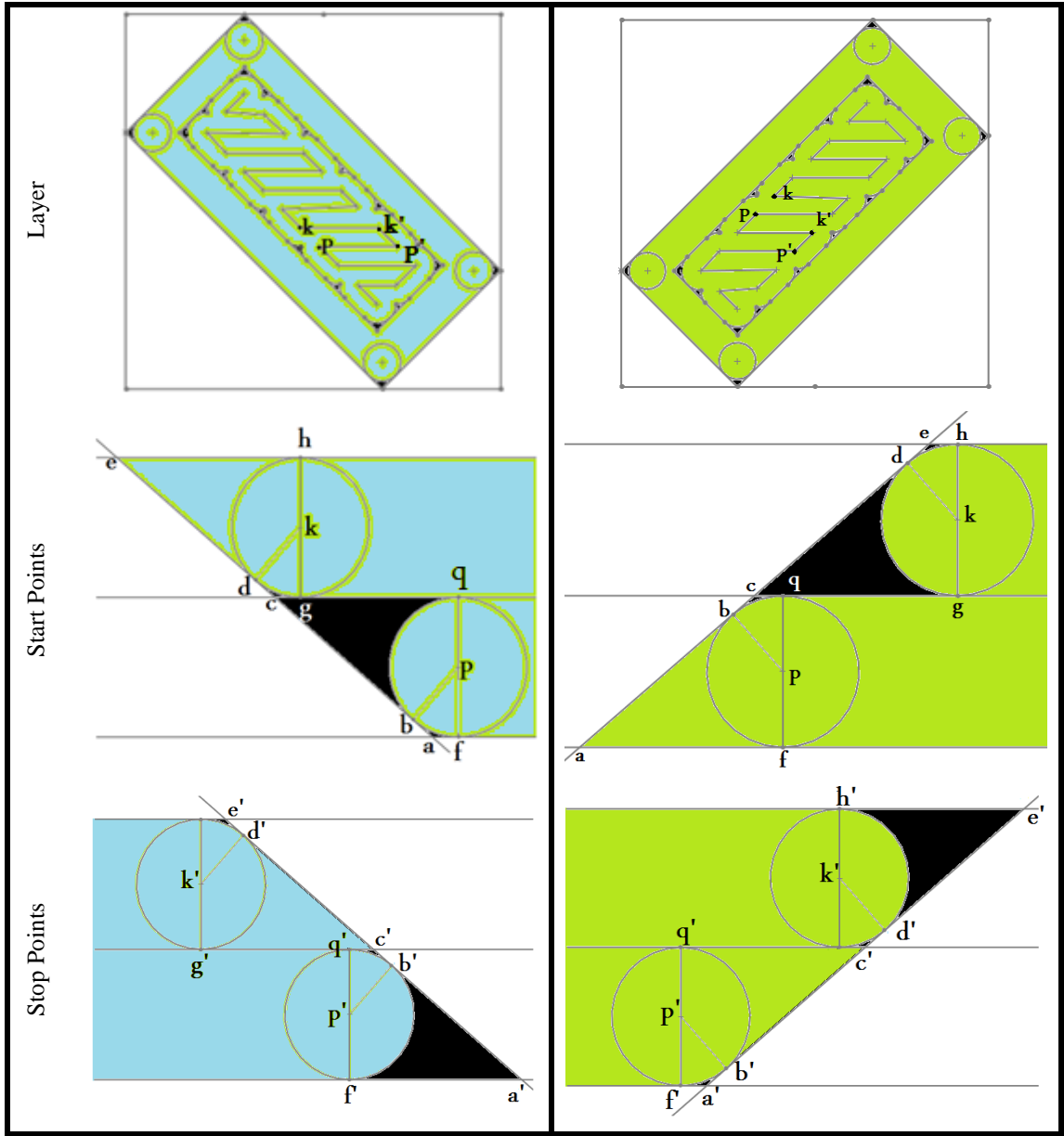


Figure 63. The position of voids with points' illustration

For understanding how to manage voids between layers, assume that all voids should be covered at least one time during the process. Figure 64 (b) shows the logic related to tracking the voids for Figure 64 (a). For example, if layer 1 has seven voids and layer 2 has six voids, then, the combination of these two layers is layer 1&2, which has three voids. These resultant voids are void

number 4 of layer 1 and void numbers 1' and 5' for layer 2, which are not covered between these two layers. This process repeats for all layers to become sure all voids are covered during the process. The next build optimization step targets are reducing or eliminating the void stacking issue by selecting a suboptimal raster angle-bead width-overlap condition that will result in a build condition that will cover void regions generated in a previous layer. For example, voids 1' and 5' in layer two are never covered within all layers when using the void minimization solution. The raster angle of layer 2 needs to be changed to cover these voids.

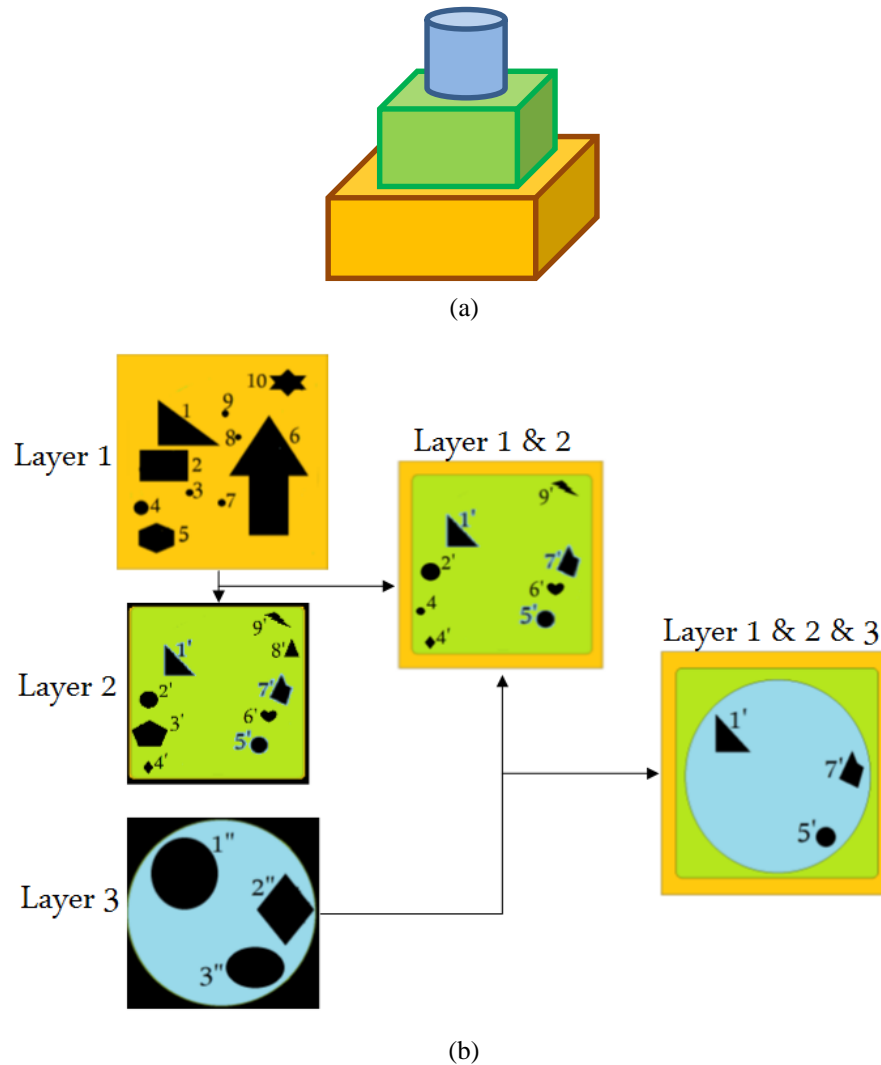


Figure 64. (a) 3D view, (b) Logic of tracking voids between layers

Covering Voids

A simple example for a box rotated at a random orientation is used to illustrate this algorithm is presented in Figure 65. For the optimal bead height in this scenario, the box is sliced into 22 layers.

The voids in each layer are identified in this figure. It can be seen that there are regions where there will be a 3D chimney, which is circled in this figure.

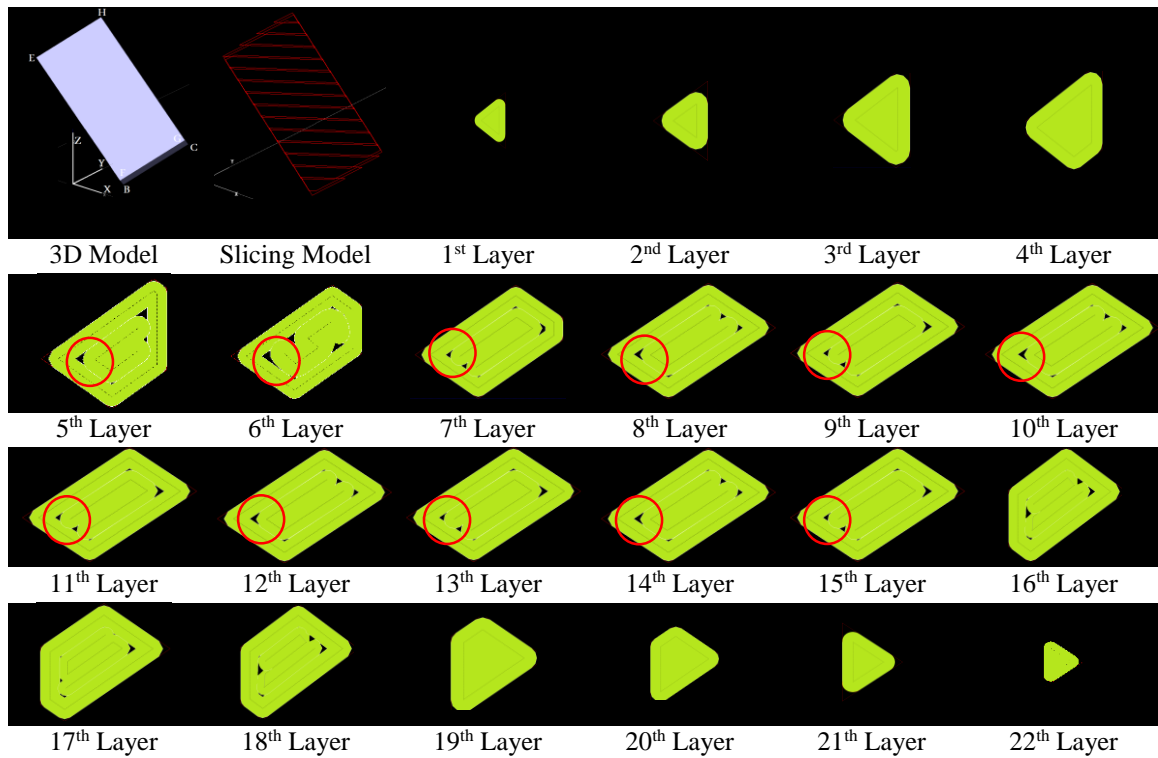


Figure 65. Example for phase II, 22 layers for a specific build orientation of a box

Multiple approaches can be taken to cover the voids between layers. Choosing the optimal strategy is dependent on the shape of the part. If the part is 2D extruded shape, then by changing the position of the start point of the nozzle from left to right between each layer all voids will be covered. For example, if the optimal layer for the 2D extruded rectangular box in Figure 66 (a), the next layer on top of the previous layer should be Figure 66 (b) to cover voids during the last layer.

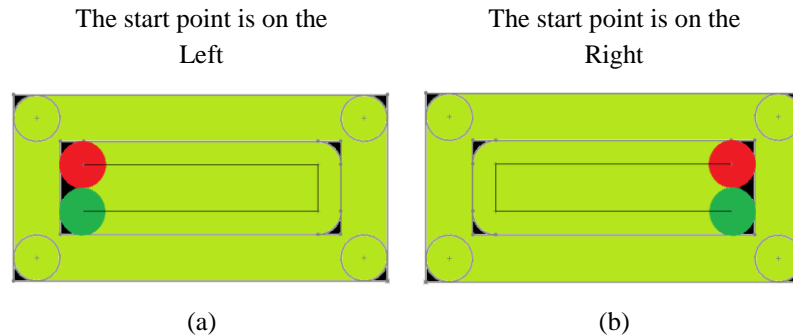


Figure 66. Difference between voids when the start point of the nozzle is on the (a) left side or (b) right side

However, in some 2D extruded cases or the other complex shapes, changing the start point of the nozzle does not address this issue. In these cases, one or more contours will be added to the specific layer-contour set to cover the voids in the previous layer. For example, for covering the voids in the layer that is shown in Figure 67 (a), by adding one more contour to the next layer, all voids will be covered.

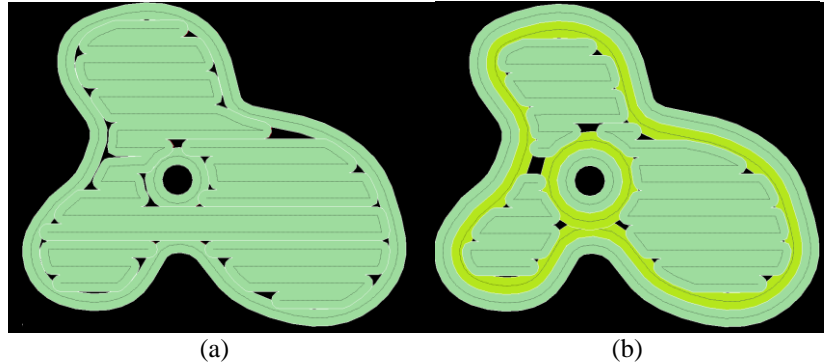


Figure 67. (a) The voids of the layer that need to be covered by next layer, (b) adding one more contour

Phase III _ Optimizing Build Orientation

The process flow diagram related to determining an optimal orientation set (Phase III) is shown in Figure 68.

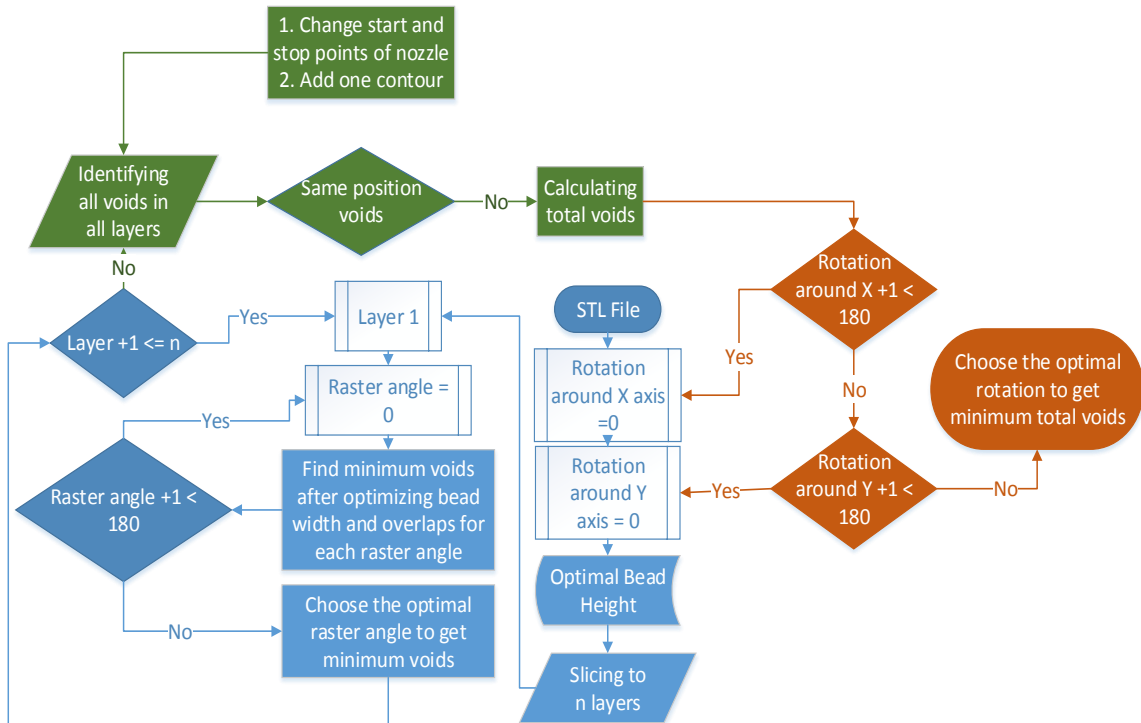


Figure 68. Color code of Figure 39, Phase I (blue), phase II (green), and phase III (orange)

In this third phase, the part is rotated around X and Y axes, and the optimal build conditions determined. The total amount of rotations is 180²: there are 0° to 179° rotations around the X-axis and 0° to 179° rotations around the Y-axis. If the *.stl file has θ_x angle about the X-axis and θ_y angle about Y-axis then points in a *.stl file is described as $(\mathcal{X}^{(\theta_x, \theta_y)}, \mathcal{Y}^{(\theta_x, \theta_y)}, \mathcal{Z}^{(\theta_x, \theta_y)})$. The rotation matrices rotate vectors by an angle θ_x and θ_z about the X and Y-axes are

$$\begin{array}{cc}
 \text{Rotate X-axis} & \text{Rotate Y-axis} \\
 \begin{bmatrix} 1 & 0 & 0 \\ 0 & \cos \theta_x & -\sin \theta_x \\ 0 & \sin \theta_x & \cos \theta_x \end{bmatrix} & \begin{bmatrix} \cos \theta_y & -\sin \theta_y & 0 \\ \sin \theta_y & \cos \theta_y & 0 \\ 0 & 0 & 1 \end{bmatrix}
 \end{array} \quad [12]$$

Thus, if the *.stl file with points $(\mathcal{X}^{(\theta_x, \theta_y)}, \mathcal{Y}^{(\theta_x, \theta_y)}, \mathcal{Z}^{(\theta_x, \theta_y)})$ rotates $(\theta'_x - \theta_x)$ about X-axis and $(\theta'_y - \theta_y)$ about Y-axis, then the new point, will be changed to

$$\begin{bmatrix} \mathcal{X}^{(\theta_{x'}, \theta_{y'})} \\ \mathcal{Y}^{(\theta_{x'}, \theta_{y'})} \\ \mathcal{Z}^{(\theta_{x'}, \theta_{y'})} \end{bmatrix} = \begin{bmatrix} \cos(\theta'_y - \theta_y) & -\sin(\theta'_y - \theta_y) & 0 \\ \cos(\theta'_x - \theta_x) * \sin(\theta'_y - \theta_y) & \cos(\theta'_x - \theta_x) * \cos(\theta'_y - \theta_y) & -\sin(\theta'_x - \theta_x) \\ \sin(\theta'_x - \theta_x) * \sin(\theta'_y - \theta_y) & \sin(\theta'_x - \theta_x) * \cos(\theta'_y - \theta_y) & \cos(\theta'_x - \theta_x) \end{bmatrix} * \begin{bmatrix} \mathcal{X}^{(\theta_x, \theta_y)} \\ \mathcal{Y}^{(\theta_x, \theta_y)} \\ \mathcal{Z}^{(\theta_x, \theta_y)} \end{bmatrix}; \quad [13]$$

$\forall \theta_x, \theta_y, \theta'_x, \text{ and } \theta'_y$.

Thus, with the above equation all points, lines, and curves are defined in each rotation, as shown in Figure 69. The algorithm for these phases is written in C++ and run for different cases studies and the results.

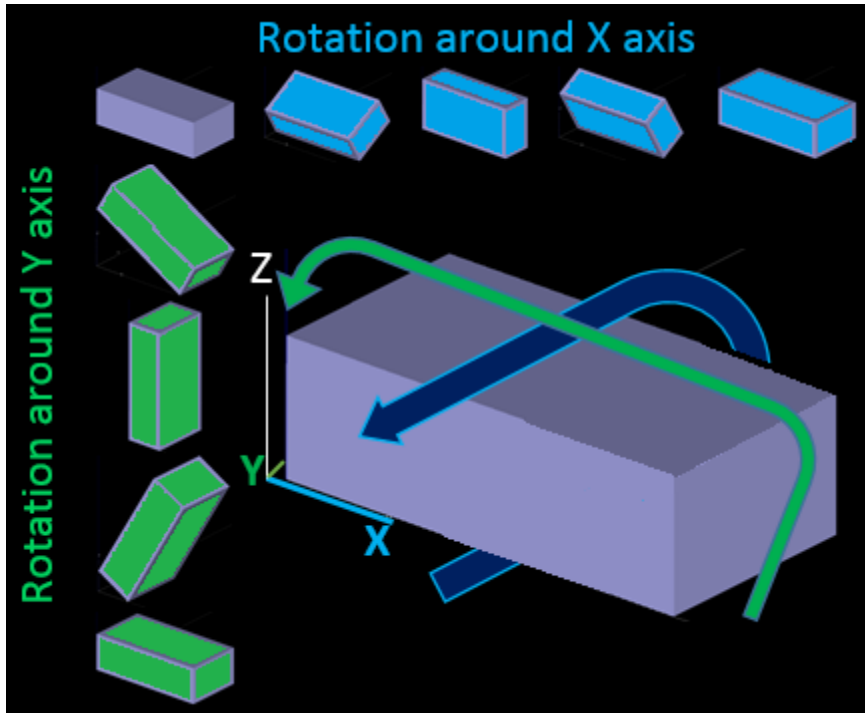
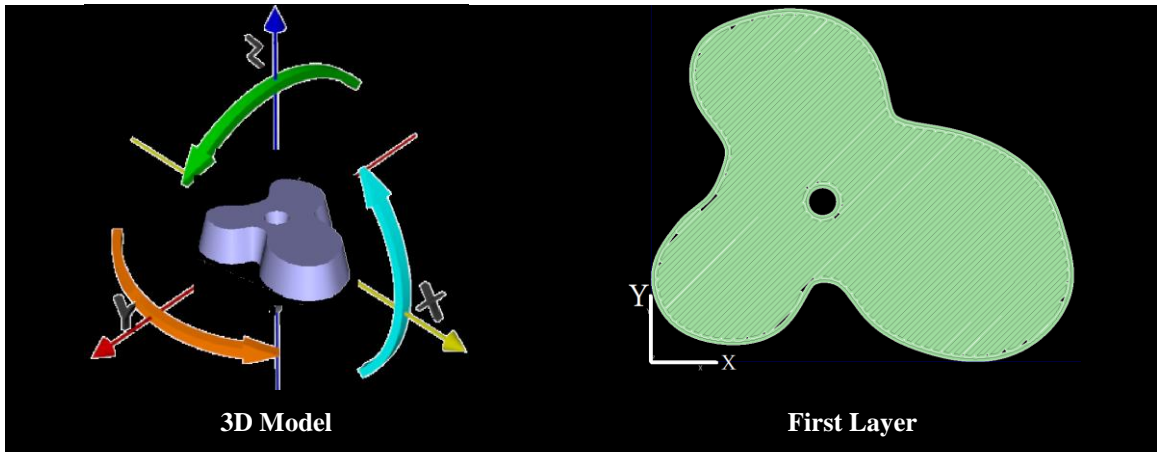
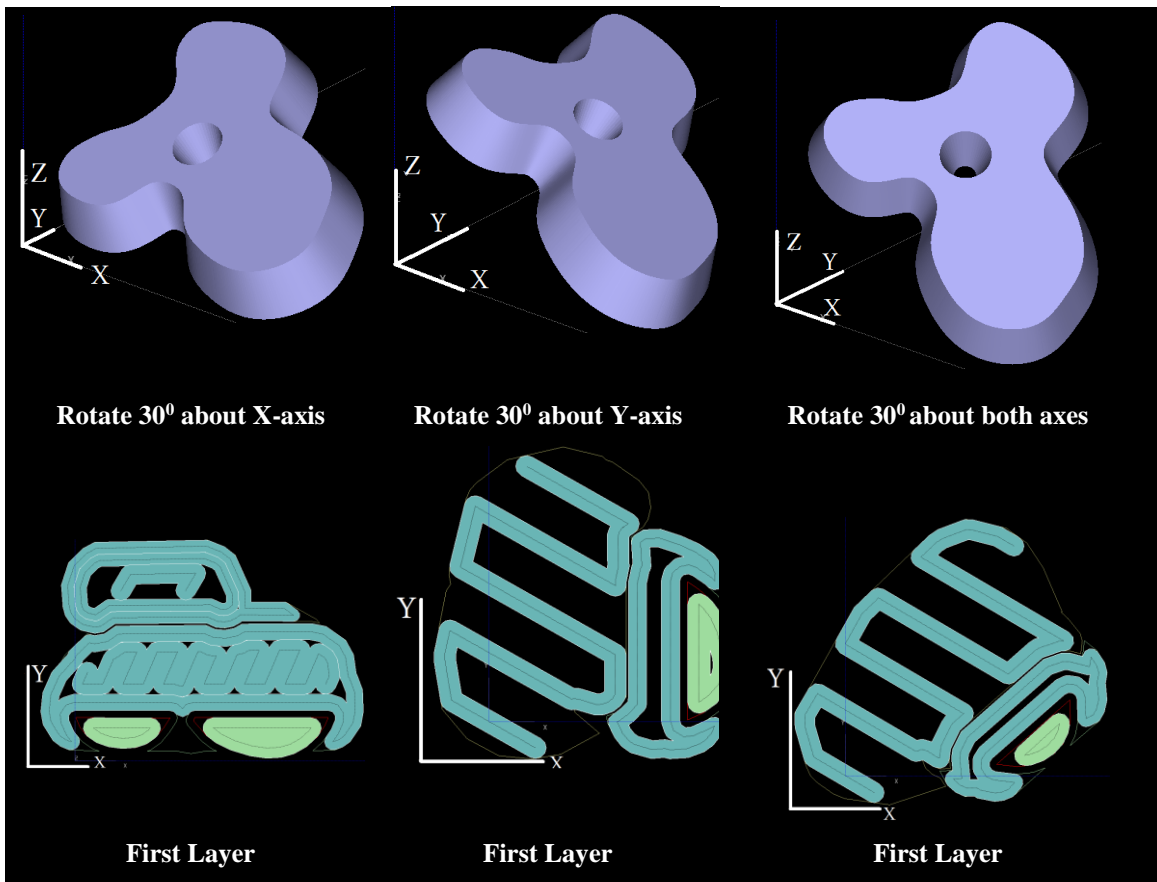


Figure 69. Rotation around X and Y axes

For example, Figure 70 (a) rotates 30° about X, Y, and both axes then after slicing, the new first layer is changed to Figure 70 (b) to (d), respectively. The blue toolpath in these figures is the support material toolpath. Thus, the processing time will be extended because of adding the support material in the process and removing them in the post-process steps. Although the rotation of this cases is not optimal for minimizing time and price, they may be an optimal solution to minimize voids.



(a)



(b)

(c)

(d)

Figure 70. 3D example of rotation around X and Y axes

By rotating the part around X and Y axes, the position of voids is able to be managed. For example, for previous examples, the position of voids are around Z-axis that shows in Figure 71 (a to d).

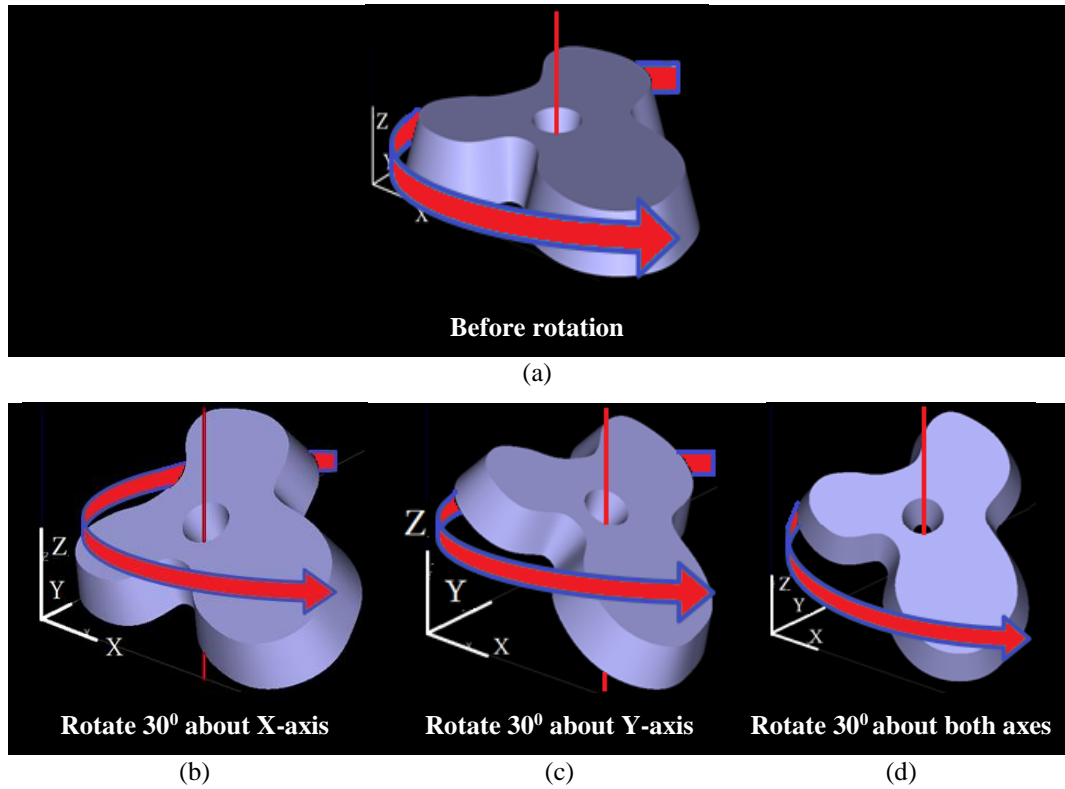


Figure 71. The position of voids of different rotations around X and Y axes

This parameter helps users to identify surfaces which the voids occur on them. For example, if the voids should not be on surface number 1 of the dice then between Figure 72 (a to c), the position of Figure 72 (a) is chosen. This parameter will be explained more in the next chapters with real case studies.

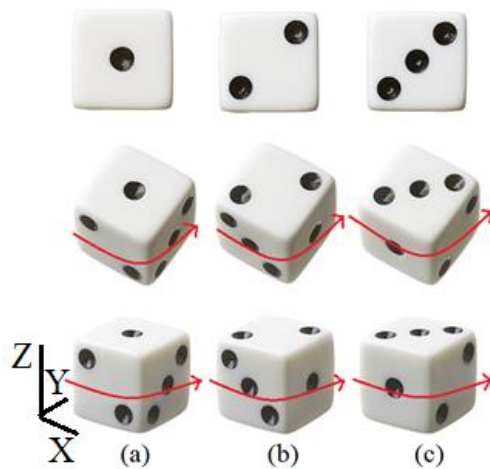


Figure 72. The position of voids around a dice

CHAPTER 4
EXPERIMENTS FOR PHASE I AND II




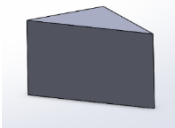

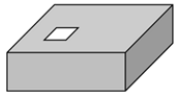
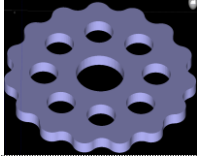



This chapter illustrates multiple examples to prove the new model is independent on the geometrical shape of the part on phase I and II (Figure 39). In this chapter, the geometrical shapes for generic slice geometries are categorized, and different case studies for components designed for mechanism analyses are employed to compare fabrication solutions and to highlight areas of concern to be addressed. The geometrical shapes for generic slice geometries are categorized in Table 27. As it shows, the two main categories are solid shapes and shapes with internal holes. Solid shapes categorized to N-side, arc, and a combination of these two. Shapes with internal holes separated to internal N-side, internal arc, and the internal combination of them. In this chapter, each of these main shapes studies individually to prove the mathematical model gives an optimal answer not depending on the shape of the part.

Table 27. Category of shapes

Solid	N-side	Convex
		Concave
	Arc	Convex
		Concave
	Combination (N-side & Arc)	Convex
		Concave
Internal Hole Non-Solid	Internal N-side	External N-side
		External Arc
		External Combination
	Internal Arc	External N-side
		External Arc
		External Combination
	Internal Combination	External N-side
		External Arc
		External Combination

In Table 28, the kinds of voids for standard toolpath generated by the OEM software (Insight® software) are presented for the identified categories, and it shows the target applications for this chapter.

Table 28. Target applications for this dissertation

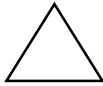
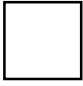
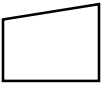
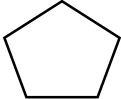
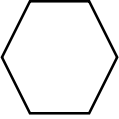
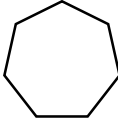
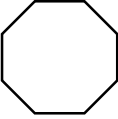
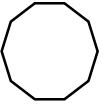
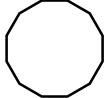
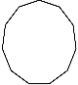

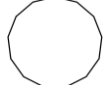


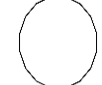
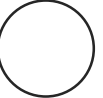


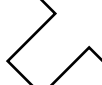

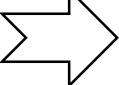


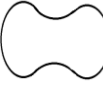
Example		Kinds of Voids		
		Corner	Edge	Contour Island
				
Solid	 Convex	✓	✓	
	 Concave	✓	✓	✓
Internal Hole	 Internal Convex External	✓	✓	✓
	 Internal Convex External	✓	✓	✓
	 Internal Concave External	✓	✓	✓
	 Internal Concave External	✓	✓	✓
	 Internal Concave External	✓	✓	✓

The two main groups which are studied in this chapter are solid shapes and shapes with internal holes. Below these groups are described by details.

Solid Shapes




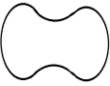
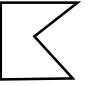
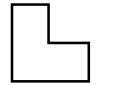
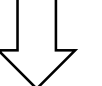
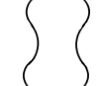
As it was discussed before, the solid shapes are categorized into two groups, convex and concave shapes. Table 29 shows some example of convex and concave cases, for shapes with a different number of sides.

Table 29. Convex and concave shape examples

Convex								
	3 Sides	4 Sides	4 Sides	5 Sides	6 Sides	7 Sides	8 Sides	9 Sides
	Triangle	Square	Quadrilateral	Pentagon	Hexagon	Heptagon	Octagon	Enneagon
								
	10 Sides	11 Sides	12 Sides	13 Sides	14 Sides	15 Sides	16 Sides	Infinite Sides
	Decagon	Hendecagon	Dodecagon	Tridecagon	Tetradecagon	Pentadecagon	Hexadecagon	Circle
Concave								
	5 Sides	6 Sides	7 Sides	8 Sides	9 Sides	10 Sides	14 Sides	Infinite Side
	Pentagon	Hexagon	Heptagon	Octagon	Nonagon	Decagon	Tetradecagon	

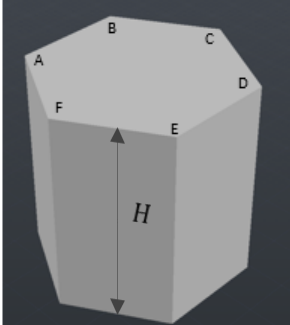
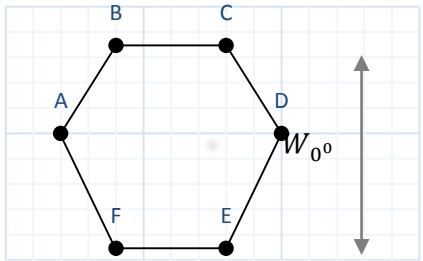
As it was discussed before, in this dissertation, the shapes with no steps or start and stop points for a deposition path are identified as convex shapes; whereas, the other orientation is ‘classically’ concave shapes. Here, the convex shapes are preferred than concave shapes as this reduces discontinues and potential void conditions. For example Table 30 shows some example of concave shapes. By rotation these shapes, they are converted to convex shapes. If the total voids area of these shapes when they are concave or convex shapes are the same, then the convex shapes are preferred. In this section, some solid convex shapes are studied to compare voids area between the OEM software and the new model.

Table 30. Convert concave shape to convex shape

Concave				
Convex				

This section starts with the simple hexagonal case study. Table 31 contains the details of the solid hexagonal shape with $H = 25.4$ mm and $W_{0^0} = 40.5\sqrt{3}$ mm.

Table 31. Parameters of the solid hexagonal shape

3D Model	Chart Scatter	Points = (x , y)
		A = (2 , 50)
		B = (22 , 85)
		C = (63 , 85)
		D = (83 , 50)
		E = (63 , 4)
		F = (22 , 4)

If the OEM software, Insight® software, is used for producing this shape with 0.254mm bead height, 0.5064 mm bead width, and 45^0 raster angle, then there are voids between the contour and raster toolpath as Figure 73 (a) shows. Since these voids are not covered during the process with the OEM software, there are visible unwanted voids in the finished part as Figure 73 (b) shows.

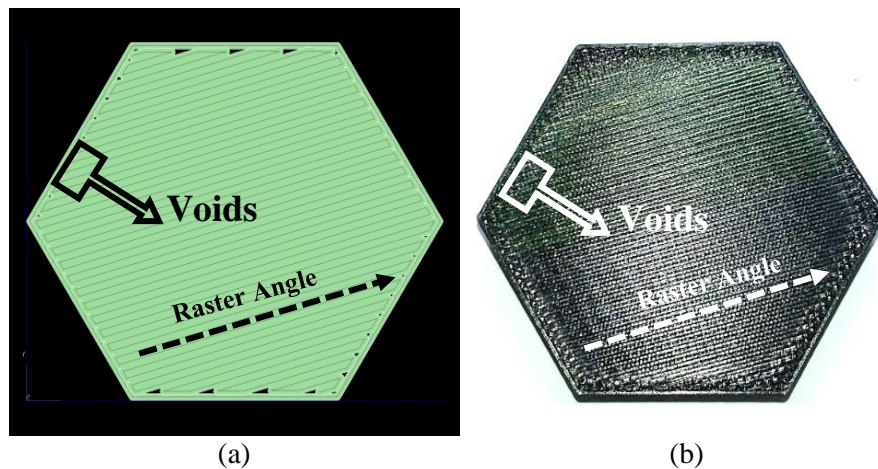


Figure 73. (a) Insight® software toolpath, (b) Voids in part after processing

By equation 9, the minimum voids are for the layer with 0.5064 mm bead width by 19% overlaps which their raster angles are 0^0 , 60^0 , and 120^0 . The reason for having three same optimal layers for this example is the asymmetric shape of the hexagonal shape. For managing voids during the process, these three layers need to be on top of each other to cover all voids. Figure 74 shows these three optimal layers with voids and their position.

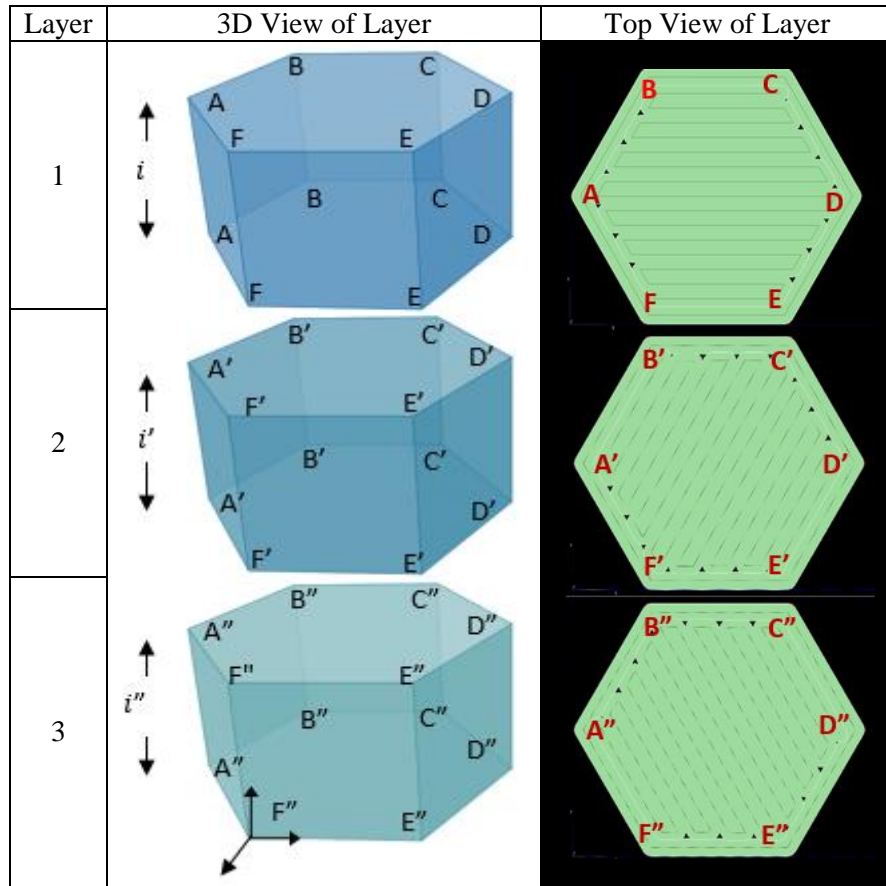


Figure 74. Three optimal layers for the Table 31

Table 32 shows covered (✓) and uncovered (✗) voids in Figure 74. The table indicates with these three layers the voids are covered once during the process.

Table 32. Cover and Uncover Voids

		Position of Voids					
		AB	BC	CD	DE	EF	FA
Layers	1	✗	✓	✗	✗	✓	✗
	2	✓	✗	✗	✓	✗	✗
	3	✗	✗	✓	✗	✗	✓

Figure 75 (a to c) shows optimal three layers with the raster angles which are parallel to the edges. Figure 75(d) is the finished product after producing by AM-ME, and it shows the finished part does not have any uncovered voids.

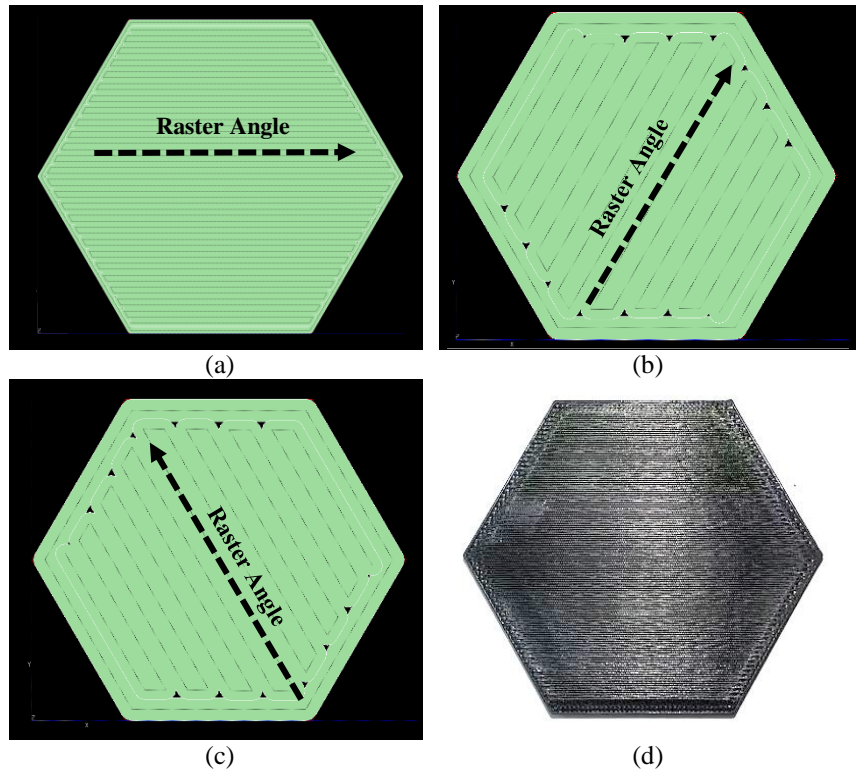


Figure 75. (a to c) Optimal layers for the hexagonal shape, (d) finished part after processing

As Table 33 shows, the percentage of fill improvement for this approach is approximately 12% [4].

Table 33. Comparison voids for the solid hexagonal shape

Volume (cm ³)	OEM Software				Optimal Answer			
	Build material (cm ³)	Support material (cm ³)	Voids (cm ³)	% voids	Build Material (cm ³)	Support Material (cm ³)	Voids (cm ³)	% voids
1089.91	957.52	65.92	132.39	12.15	1088.25	65.91	1.66	0.15

The other example which is same as the hexagonal example is from individual cases for polygons with infinite sides. For optimizing these symmetric shapes, first the raster angle needs to be established, and at present, this is determined by the number of build layers. For example, for producing a cylinder with 12 edges (Figure 76), an optimized raster angle calculated by $\frac{2\pi}{\text{Number of Edges}}$. For this scenario, an optimized raster angle is $\frac{2\pi}{12} = 30^\circ$. This means that the raster angle shifts 30° between each layer. In these case, the assumption is the number of layers is more or equal to the number of edges. If the number of edges is more than the number of layers the

optimal raster angle formula will be changed to $\frac{2\pi}{\text{Number of layers}}$. The next example is the solid convex shape but it is a non-symmetric shape.

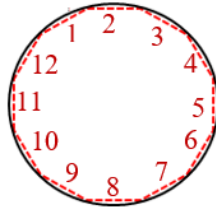


Figure 76. Infinite-side shape with twelve layers

This section is illustrated optimization of non-symmetric solid shapes. One of an example of this kind of shape is shown in Figure 77. With existing OEM software like Insight®, the build material for producing this component (non-symmetric seven-side convex shape) with the commercial software is 276.42 cm³. The slice height is 0.254 mm, and a non-standard (but available) 0.6096 mm bead width was chosen to ensure that there was no air gap between the contour and the 45° raster angle.

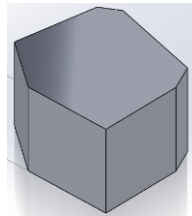


Figure 77. Seven-side non-symmetric convex shape

The percentage of voids with above parameters is around %5. As Figure 78 shows, some voids (red circles) are not covered with the existing OEM software. Thus, there could be weak regions at the component boundary and potential leak paths within this component.

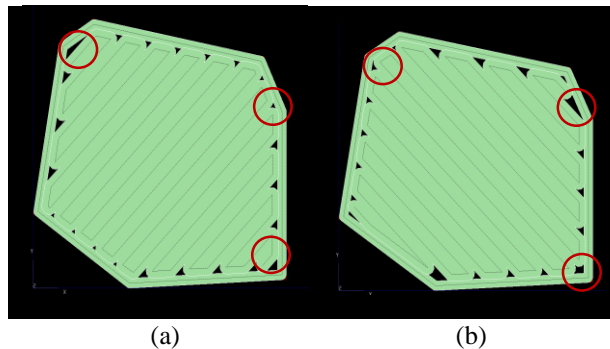
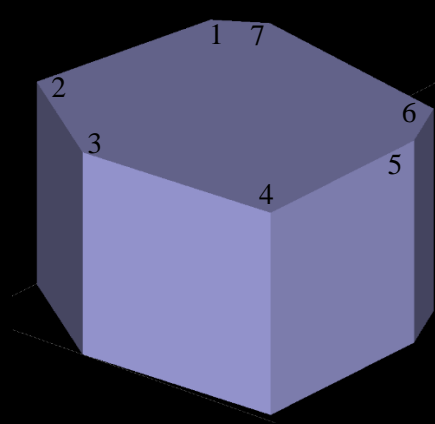


Figure 78. Compare first (a) and second (b) layers in the existing OEM software

The optimized solution for this example is generating seven different layers as summarized in Table 11.

Table 34. Information of new model for seven-side non-symmetric convex shape

Layer	3D View	Optimal Layers			
		Bead Height (mm)	Bead Width (mm)	Raster Angle	Overlaps
1		0.2540	0.5064	43.22 ⁰	0%
2		0.2540	0.5314	47.95 ⁰	0%
3		0.2540	0.5564	37.35 ⁰	0%
4		0.2540	0.4064	0 ⁰	9%
5		0.2540	0.4314	87.25 ⁰	0%
6		0.2540	0.4564	25.32 ⁰	0%
7		0.2540	0.4814	53.48 ⁰	0%

As it was discussed before the layers with the raster angle is parallel to edges, have minimum total edge voids. Figure 79 shows these seven layers, and the voids in layer (a) are circled, these voids will be covered with the next (top) layers.

There are 1% voids with this solution, as shown in Table 35, but a significant feature to be considered is that there are no ‘chimneys’ in the finished part.

Table 35. Comparison voids for seven-side non-symmetric convex shape

Volume (cm ³)	OEM Software				Optimal Answer			
	Build material (cm ³)	Support material (cm ³)	Voids (cm ³)	% voids	Build Material (cm ³)	Support Material (cm ³)	Voids (cm ³)	% voids
291.03	276.42	3.13	14.61	5.02	286.11	3.13	4.92	1.69

The last member of the solid shape category is for components with multiple 2D geometry extrusions; the first step consists of repartitioning the component into its elemental 2D shapes and solving these sub-features separately. In Figure 80, two multiple extruded shapes are shown. Figure 80(a) contains three sub-component features, and Figure 80 (b) includes ten subcomponent features.

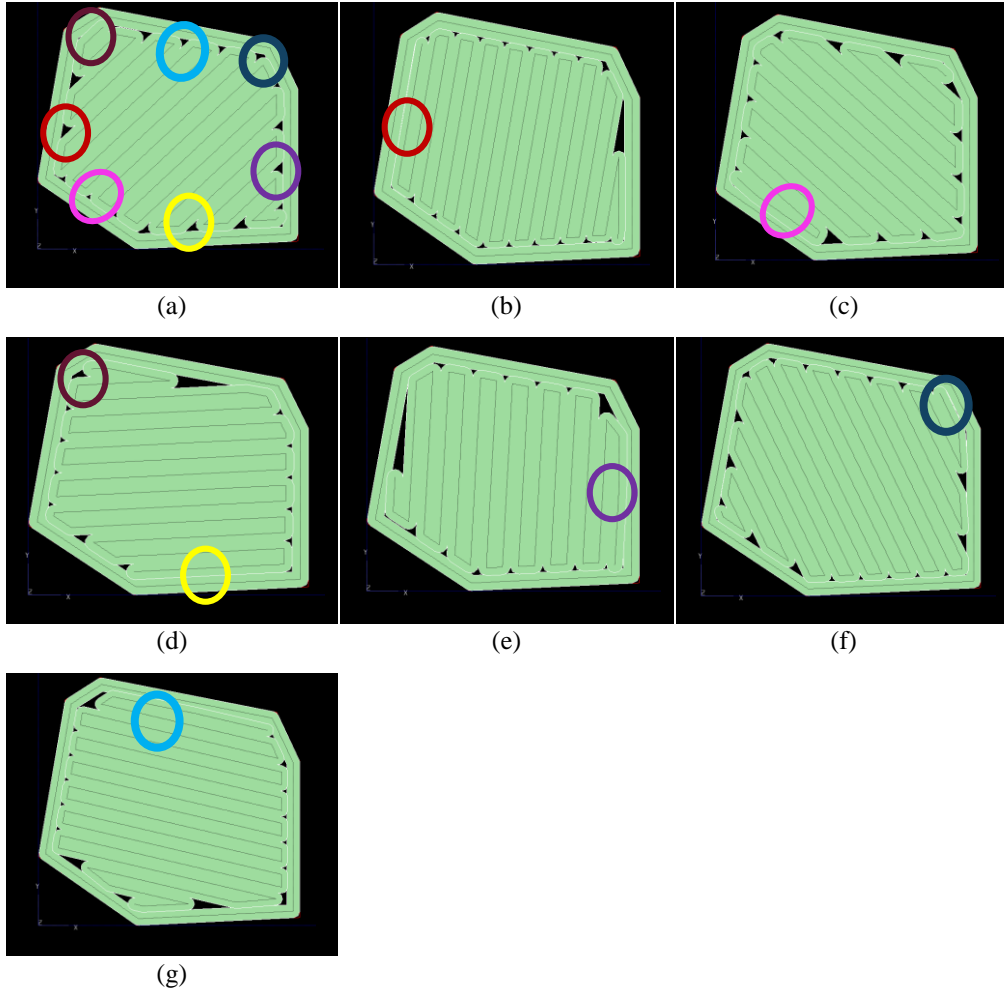
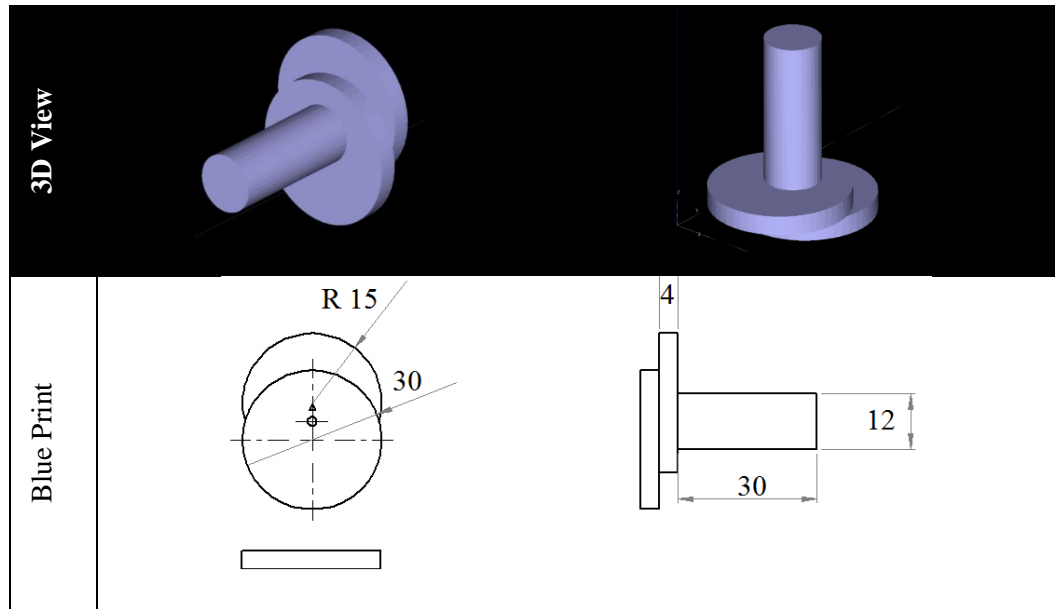


Figure 79. Covering voids between seven layers

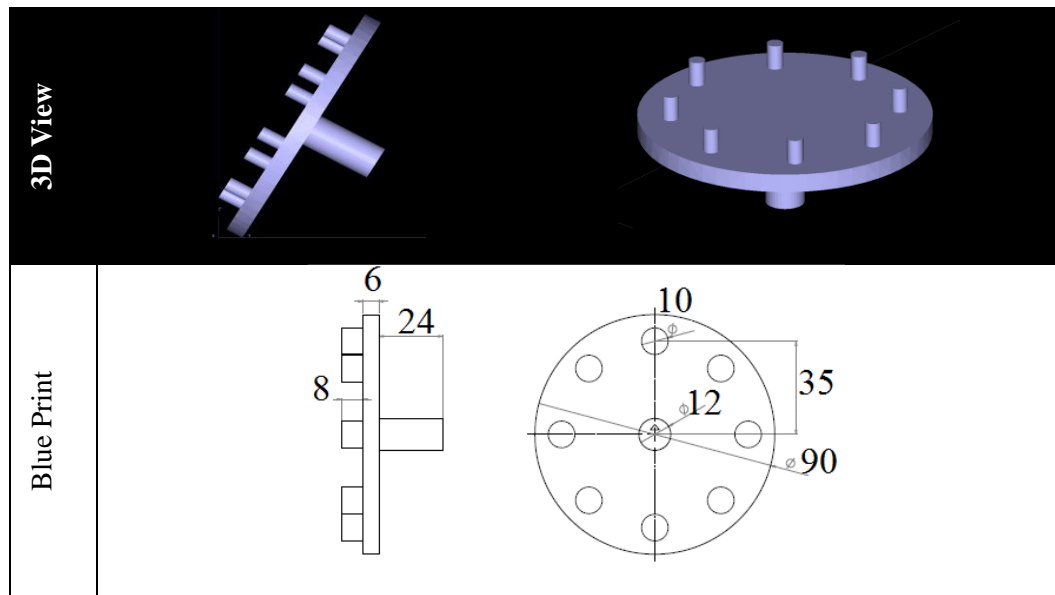
The voids for two examples are compared in Table 36. For the Figure 80 (b) components, the new model decreases the voids around 8%. For Figure 80 (a) component, the existing OEM software used more material than the volume due to having an integer number of layers. With the new model, the real voids decrease approximately 3%, and it has an exact height for each subcomponent feature for the Figure 80 (a) component.

Table 36. Comparison voids for multiple 2D geometry extrusions examples

Example	Volume (cm ³)	OEM Software				Optimal Answer			
		Build material (cm ³)	Support material (cm ³)	Voids (cm ³)	% voids	Build Material (cm ³)	Support Material (cm ³)	Voids (cm ³)	% voids
(a)	9.04	9.51	2.16	-0.47	-5.2	8.98	2.16	0.06	0.66
(b)	45.91	42.17	28.16	3.74	8.15	45.88	28.16	0.03	0.07



(a)



(b)

Figure 80. Multiple 2D extruded shapes with their blueprints (mm)

(adapted from [4])

Non-Solid Shapes

For shapes with internal holes, the first step is splitting the shape into multiple simple convex shapes. Figure 81(a) shows an example of this kind of shapes.

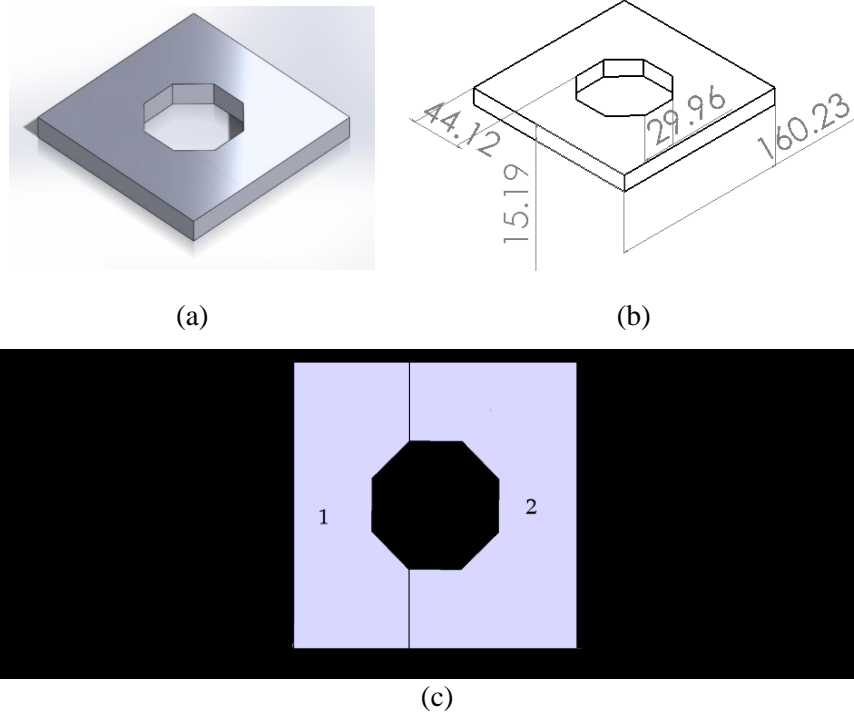


Figure 81. (a) 3D example of the shape with internal holes (b) Blueprint (mm), (c) Optimal splitting (adapted from [4])

For splitting Figure 81(a), the shape is divided into two simple convex shapes. The extruded height for this example is 15.19 mm, but with the OEM (Insight®) software, the height is changed to 15.29 mm. When using a bead height of 0.1778 mm, 85.43 layers are needed. But as the number of layers must be an integer number, the total number of layers is set to 86 layers. The build material which is used with the OEM software is 316.67 cm³, and the void percentage is 4%. With the new model, the bead height is optimized, and consists of 64 layers and uses two bead heights. For this example, 50 layers with bead height 0.254 mm and 14 layers with bead height 0.1778 mm are used to have an exact 15.19 mm height for the finished product. In Table 37 the percentage of voids in the existing OEM software is 2% but because of an extra layer, the real percentage of voids is approximately 4%, and with the new model, the voids are decreased to 0.52%.

Table 37. Comparison voids for Figure 81(a)

Volume (cm ³)	OEM Software				Optimal Answer			
	Build material (cm ³)	Support material (cm ³)	Voids (cm ³)	%voids	Build Material (cm ³)	Support Material (cm ³)	Voids (cm ³)	%voids
324.14	316.67	7.75	7.47	2.30	322.45	7.75	1.69	0.52

Figure 82 (a) is the example with internal or external infinite-side shapes; it shows 3D and its blueprint (left to right). The raster angles related to the infinite side shapes are determined from the heuristic described before in this chapter. Each section has its bead width, overlap, and raster fill angle generated based on the boundary geometry and the tool path optimization rules, with the ‘infinite side’ shapes having the raster angle variants pre-selected. For shapes like Figure 82 (a), the division method is complex and has many solutions due to the mixing of convex and concave boundaries. In addition to segmenting the component, the toolpath needs to be optimized with blending between these new divided shapes (Figure 82 (b and c)).

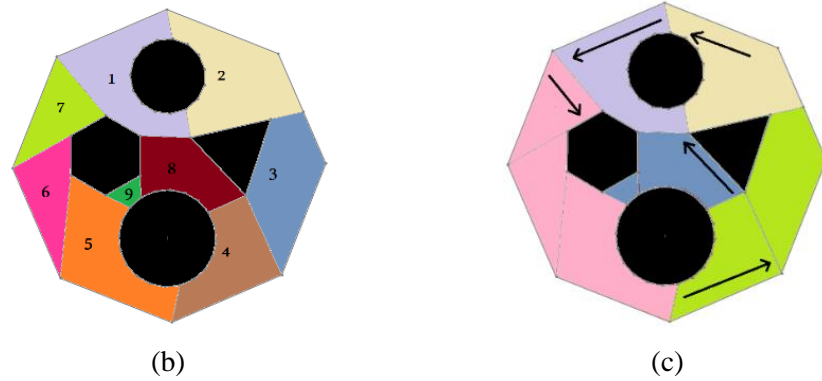
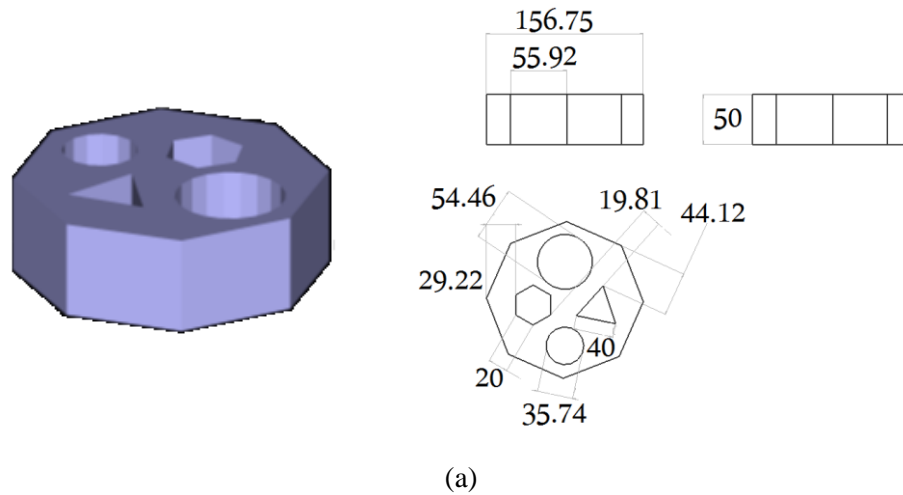


Figure 82. (a) Complex shapes with holes and its blueprint, (b) dividing complex shapes, and (c) connection rasters between the divided shapes

For this components after splitting it, the new model decreases the voids around 3%.

Table 38. Comparison voids for Figure 82

Volume (cm ³)	OEM Software				Optimal Answer			
	Build material (cm ³)	Support material (cm ³)	Voids (cm ³)	% voids	Build Material (cm ³)	Support Material (cm ³)	Voids (cm ³)	% voids
610.64	577.53	5.32	33.11	5.42	595.80	5.32	14.84	2.43

Figure 83 (a to c) are the other examples of shapes with internal holes.

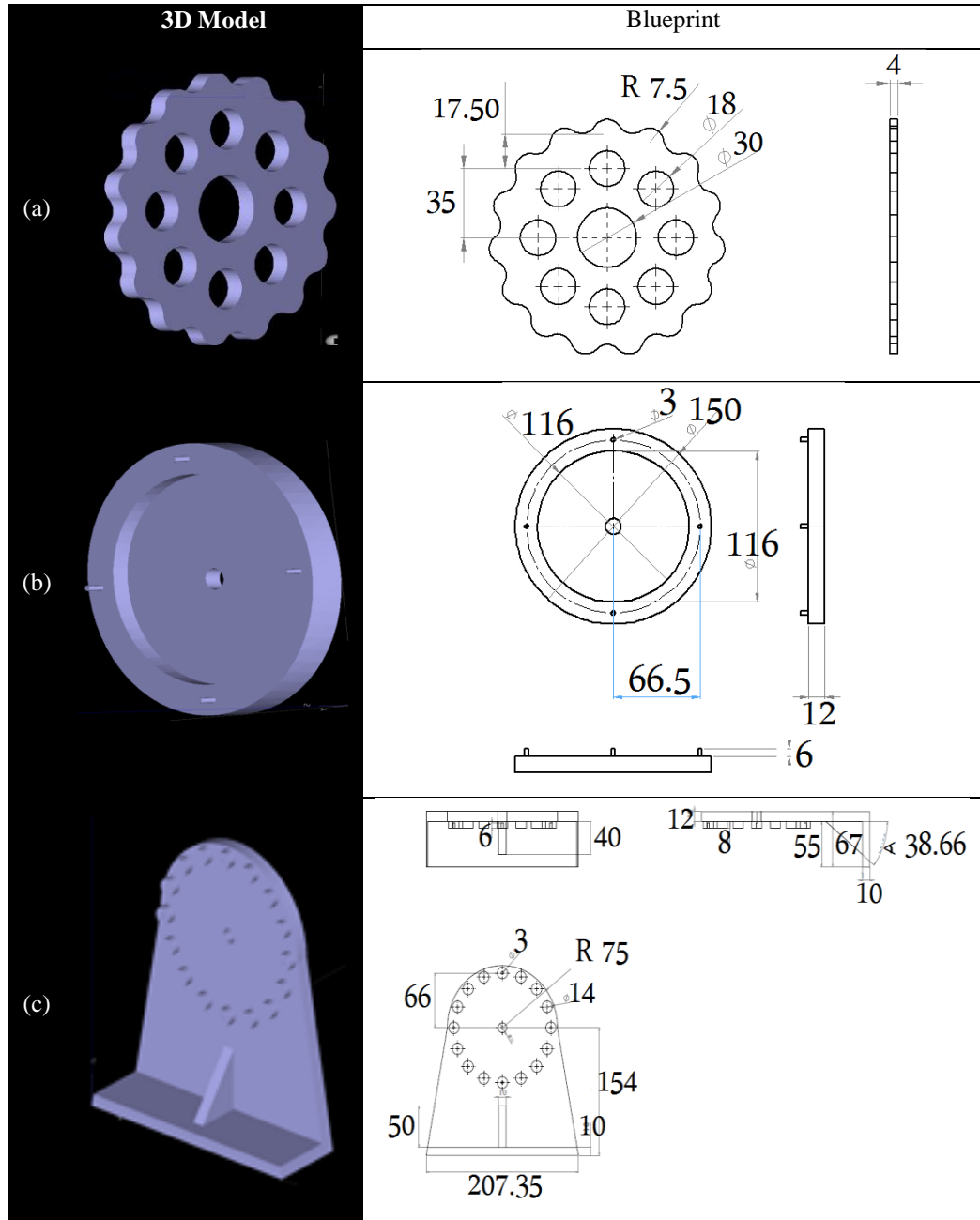


Figure 83. Examples of shapes with internal holes

The optimized splitting solutions for this example is shown in Figure 84. In this three examples, the optimal raster angles are parallel to the contour of the shapes. In Figure 84 (a) the path of the nozzle is shown by black arrows.

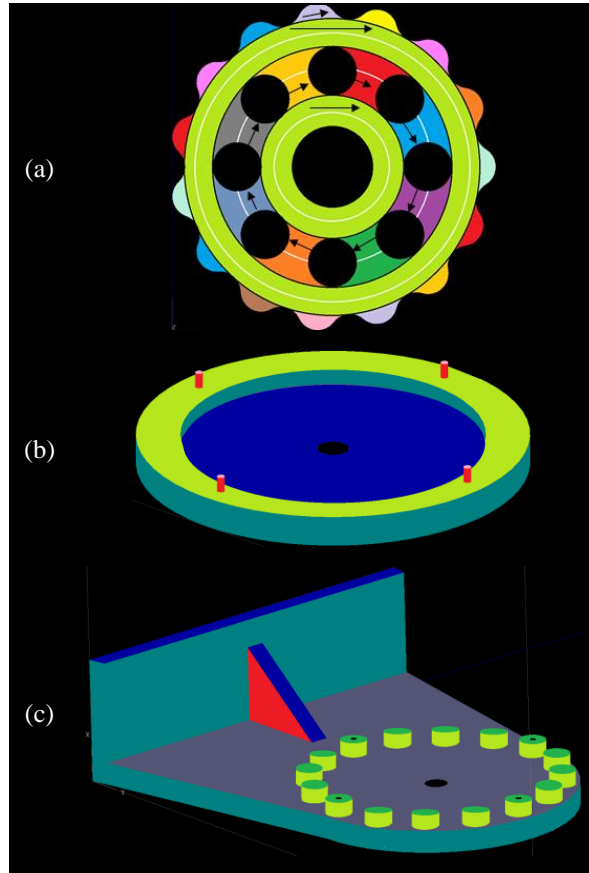


Figure 84. Optimal splitting of Figure 83

In Table 39 the voids for above examples are compared. For example (a) which is Figure 84 (a), the height is 4.0 mm, but in the OEM software is 4.29 mm because an additional layer is needed to fabricate the component. Theoretically, each layer requires 2.6 cm^2 build material; however, the commercial algorithm employs 2.5 cm^2 build material. Therefore, although the OEM solution contains more build material, the void difference is approximately 4%. For other examples (b and c) components, the new model decreases the voids around 2% and 4%, respectively.

Table 39. Comparison voids for Figure 83

Example	Volume (cm ³)	OEM Software				Optimal Answer			
		Build material (cm ³)	Support material (cm ³)	Voids (cm ³)	% voids	Build Material (cm ³)	Support Material (cm ³)	Voids (cm ³)	% voids
(a)	30.11	33.92	8.52	-3.81	-12.65	29.3	8.52	0.81	2.69
(b)	148.14	142.57	14.55	5.57	3.76	144.67	14.55	3.47	2.34
(c)	577.4	545.04	29.54	32.36	5.60	569.84	29.54	7.56	1.31

Combination of Solid and Non-Solid Shapes

Figure 85 presents a solution for dividing a more complex product into seventeen simple solid shapes. For producing this product, it is noted that support material is needed during the process of creating the hole which is between shape 1 to 4 (side view). Thus, the product is same as a set of 2D extruded shapes, which is divided into thirteen simple solid shapes (5 to 17).

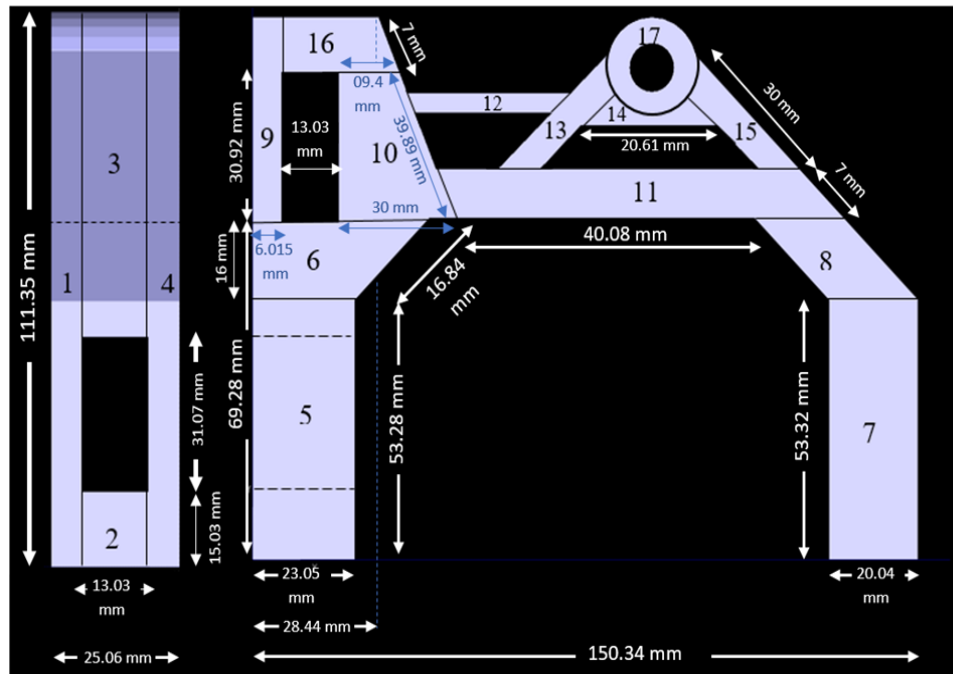


Figure 85. Divided the complex shape to seventeen solid convex shapes

The solid convex shape number 5 is rectangular with size 23.05 mm * 53.28 mm. For calculating optimal bead width and overlaps, the Equation 4 is used. First for $W_{00} = 23.05$ mm and 50% allowable overlaps Table 40 is calculated with Equation 4, with this table an optimal bead width is 0.2032 mm with an overlaps 44%.

Table 40. Calculating an optimal bead width and overlap for section 5 in Figure 85

Bead width (mm)	0.2032	0.2282	0.2532	0.2782	0.3032	0.3282	0.3532	0.3782	0.4032	0.4282	0.4532	0.4782	0.5032	0.5282	0.5532	0.5782
Number of Rasters	113	101	91	82	76	70	65	60	57	53	50	48	45	43	41	39
Overlaps	44%	1%	3%	85%	2%	23%	26%	95%	17%	83%	86%	20%	81%	64%	67%	87%

Table 42 shows all details of each layer for this example.

For producing the model illustrated in Figure 85 with the existing OEM software, 127.89 cm³ build material is used. With the new model, the build material is increased to 138.95 cm³ or 8% increase. It means the voids decreased around 8% in the new model.

Table 41. Comparison voids for Figure 82

Volume (cm ³)	OEM Software				Optimal Answer			
	Build material (cm ³)	Support material (cm ³)	Voids (cm ³)	% voids	Build Material (cm ³)	Support Material (cm ³)	Voids (cm ³)	% voids
140.20	127.89	10.83	12.31	8.78	138.95	10.83	1.25	0.89

Table 42. Details of each layer for each solid convex shape

Cluster	Section	Bead Height	Bead Width	Raster Angle	Overlaps
1	5	0.127	0.2032	0	44%
2		0.127	0.2032	90	20%
3	6	0.127	0.2782	0	23%
4		0.127	0.2282	90	11%
5		0.127	0.4532	45.73	16%
6	7	0.127	0.2782	0	3%
7		0.127	0.2032	90	40%
8	8	0.127	0.2782	0	3%
9		0.127	0.4532	67.39	16%
10	9	0.127	0.3532	0	3%
11		0.127	0.2532	90	12%
12	10	0.127	0.4532	0	2%
13		0.127	0.2532	90	12%
14		0.127	0.4282	45.73	6%
15	11	0.127	0.2782	0	10%
16		0.127	0.3032	45	9%
17	12	0.127	0.2282	0	28%
18		0.127	0.4282	45	1%
19		0.127	0.4282	-45	1%
20	13	0.127	0.3032	0	1%
21		0.127	0.4282	45	6%
22		0.127	0.3282	Contour	6%
23	14	0.127	0.2282	0	28%
24		0.127	0.4532	45	7%
25		0.127	0.4532	-45	7%
26		0.127	0.5282	Contour	2%
27	15	0.127	0.3032	0	1%
28		0.127	0.4282	-45	6%
29		0.127	0.3282	Contour	6%
30	16	0.127	0.2282	0	27%
31		0.127	0.2532	90	4%
32		0.127	0.3032	45.73	9%
33	17	0.127	0.3782	Contour	0%

Figure 86 shows the finished part with the Insight software and Fortus 400 machine. As it shows, the voids and 45° raster angle are visible on the surface of the part. The reasons for reducing voids with the new model for this example are

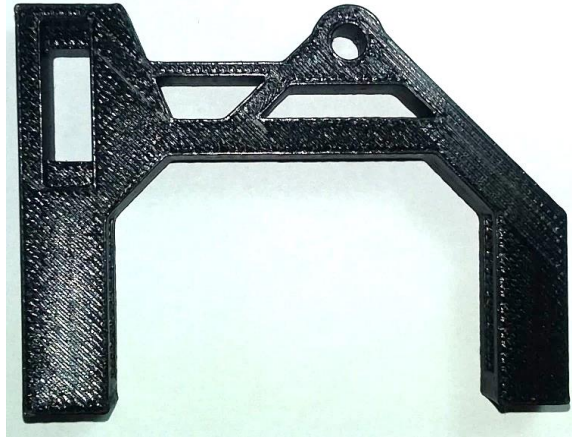


Figure 86. Producing the Figure 85 with Fortus 400 Machine

1. The bead width of each layer can be different in the new model, based on the geometric shape. However, in the existing OEM software, the bead width is fixed during the whole build process. Figure 87 shows the different bead width for each part of Figure 85 shows all bead heights for the component.

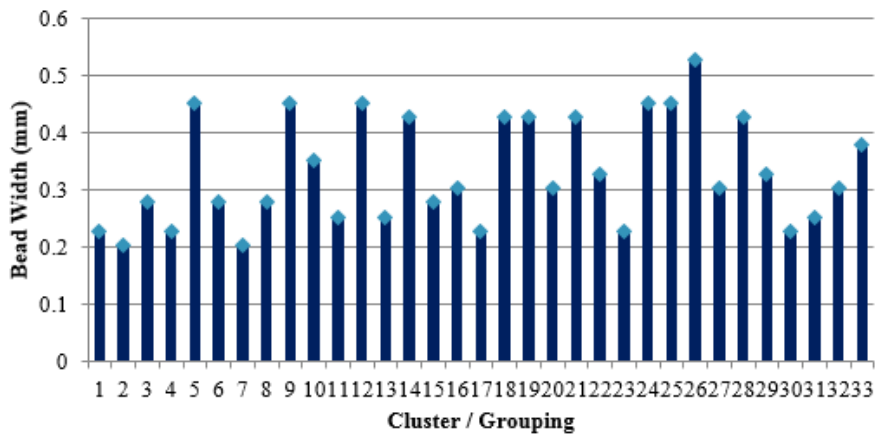


Figure 87. Cluster/grouping bead width for Figure 85

2. In the existing OEM software, the raster angle rotates 90° between each layer. In the new model, the raster angle will be changed between each layer based on the component geometry. The order is selected to cover unwanted voids such that there are no leak paths or chimneys. Figure 88

shows the different raster angles while producing the component. The red bars in Figure 88 are the raster angle for arc shapes, and in each layer, the raster angle will be turned clockwise.

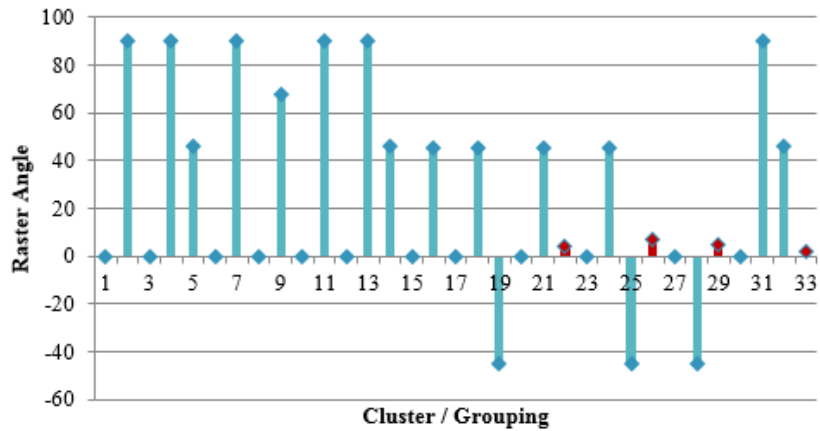


Figure 88. Cluster/grouping raster angle for Figure 85

3. The overlap is fixed in the existing OEM software, and the default for the overlap is zero. Thus, it causes unwanted voids between direction parallel toolpath. In the new model, overlap can be flexible to cover all voids. Figure 89 shows all overlaps for the above example.

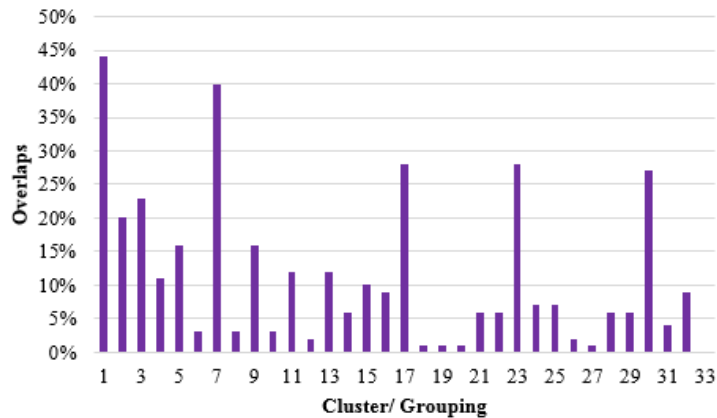


Figure 89. Cluster/grouping overlap for Figure 85

These optimal parameters help to get rid of unwanted voids in the AM-ME process using the available OEM process configurations.

The other example is for shapes which all layers are different with each other. Figure 90 (a) shows a sports car seat which has 83 layers for a 0.254 mm bead height when it sliced along the Z-axis, Figure 90 (b). The maximum allowable overlap percentage scenarios (for each layer) between

rasters is $O^*=0\%$, 15%, and 50% for this case study. The first analysis is performed using a 50% overlap percentage limit. There are two approaches for optimizing the problem in this case study. The first approach focuses on minimizing voids in each layer individually. The second approach compares the void locations between layers, to ensure that voids are covered from one layer to the next.

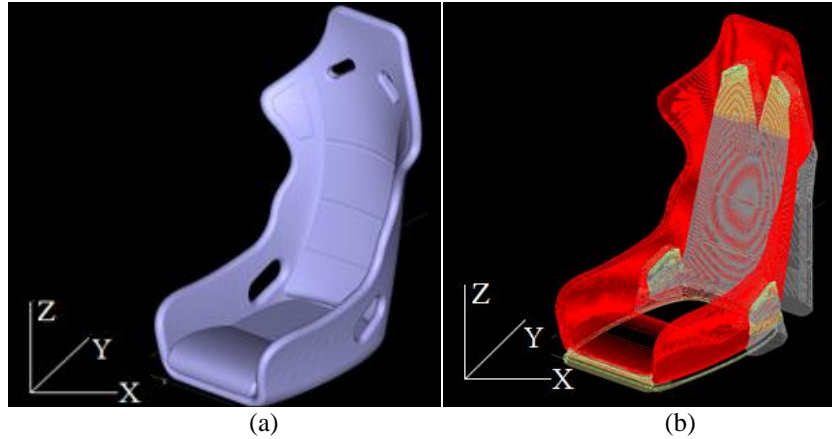


Figure 90. Car seat example, (a) 3D model, 0° with X and Y axes, and (b) Slice it during Z-axis

Figure 91 (a to c) shows the 1st, 2nd, and 3rd layers, respectively. Figure 91 (d) illustrates the relationship between the void area (mm^2) and the raster angle for these three layers. The raster angles 45° and 135° (as same as -45°) are highlighted because these two angles are the default angles for the chosen OEM software (Insight® software) for this research. It can be seen that if an alternative initial orientation for the seat were different, the total void area could be greater than 5 mm^2 when using a ‘world’ coordinate raster fill approach, which is a standard strategy in commercial systems.

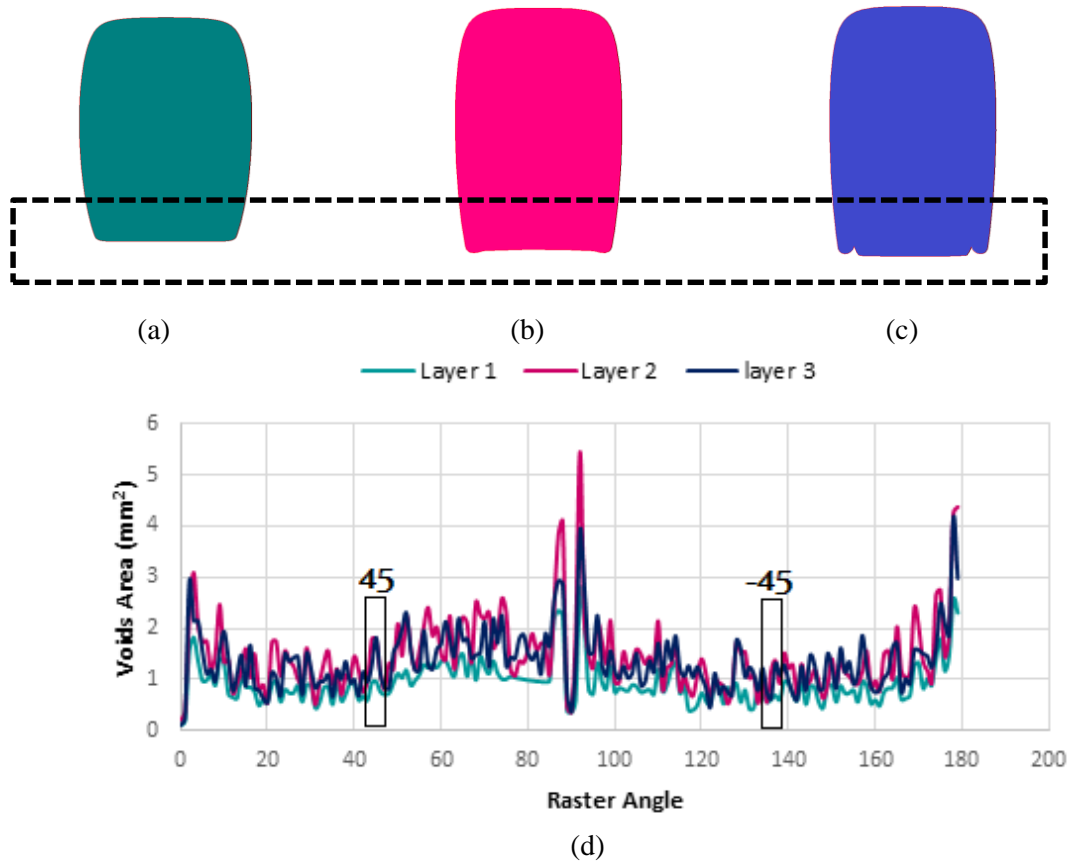


Figure 91. (a) The first layer, (b) The second layer, (c) The third layer, and (d) Relationship between raster angle and voids area for layers 1, 2, and 3, with the 45°/-45° solution highlighted

The range of overlap percentages for this solution is shown in Figure 92. It can be seen that the majority of the overlap percentage values are less than 25%, with the most common overlap percentage being between 10 – 20%.

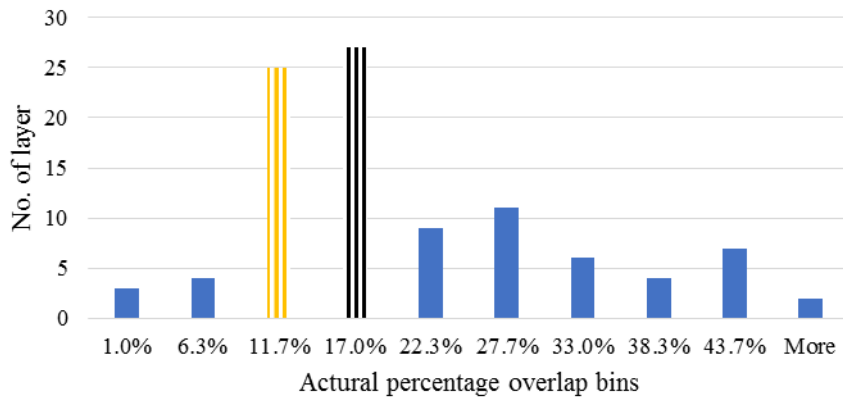


Figure 92. Actual percentage overlap bins

The next build optimization step targets are reducing or eliminating the void stacking issue by selecting a suboptimal raster angle-bead width-overlap condition that will result in a build condition that will cover void regions generated in a previous layer. In this case study, 20% of the layers need to be reselected to manage voids. Table 43 compares the optimal answer of the new model and the OEM software for the first three layers with first and second approaches. As it is shown, the total void area of the second layer is minimized by 3% with the new model-first approach (before managing voids), but after applying the void management strategy, it is minimized by 2.8%. Although with the first approach the void area minimization is higher than the second approach, the voids are completely covered within the car seat using the second approach, reducing crack propagation regions.

Table 43. Comparison the OEM software with the first and second approaches of the new model with overlaps limit 50%

Approach	Layer	Bead Width (mm)		Raster Angle		Overlap (%)		Voids Area (mm ²)		Improvement (%)
		OEM Software	New Model	OEM Software	New Model	OEM Software	New Model	OEM Software	New Model	
First	1st	0.5064	0.5064	45 ⁰	0 ⁰	0	7	0.1456	0.1125	2
	2nd	0.5064	0.4814	45 ⁰	0 ⁰	0	20	0.1398	0.0860	3
	3rd	0.5064	0.4814	45 ⁰	0 ⁰	0	15	0.1343	0.0727	4
Second	1st	0.5064	0.5064	45 ⁰	0 ⁰	0	7	0.1456	0.1125	2
	2nd	0.5064	0.4564	45 ⁰	89 ⁰	0	13	0.1398	0.0910	2.8
	3rd	0.5064	0.4814	45 ⁰	0 ⁰	0	15	0.1343	0.0727	4

The other layers of this example are shown in Figure 93. Some layers like layer 8th (Figure 93 (c)) have at least two specific contour shapes (profile). For these kinds of layers, optimal raster angle is chosen individually for each profile.

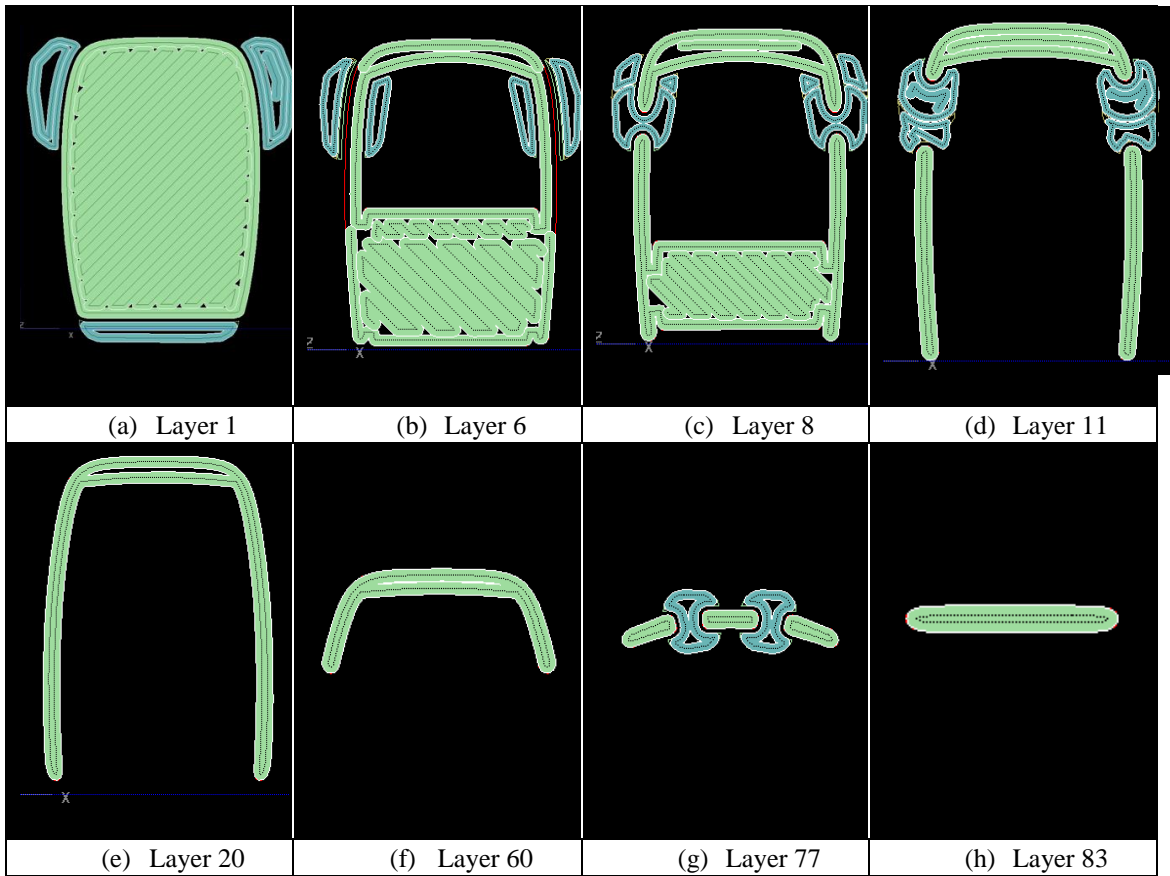


Figure 93. Multiple layers of the car seat example

Some of layers or profiles are filled just with contour rasters like layer 60 in Figure 93 (f). The other layers like 11, 20, 77, and 83 are filled with contour rasters, too. In these cases, the area of voids is zero. Figure 95 shows the relationship between raster angle and voids area for layers 1, 2, 3, 6 and 8. As it shows, the best raster angle for each layer is the raster angle parallel to one of the sides of the layer.

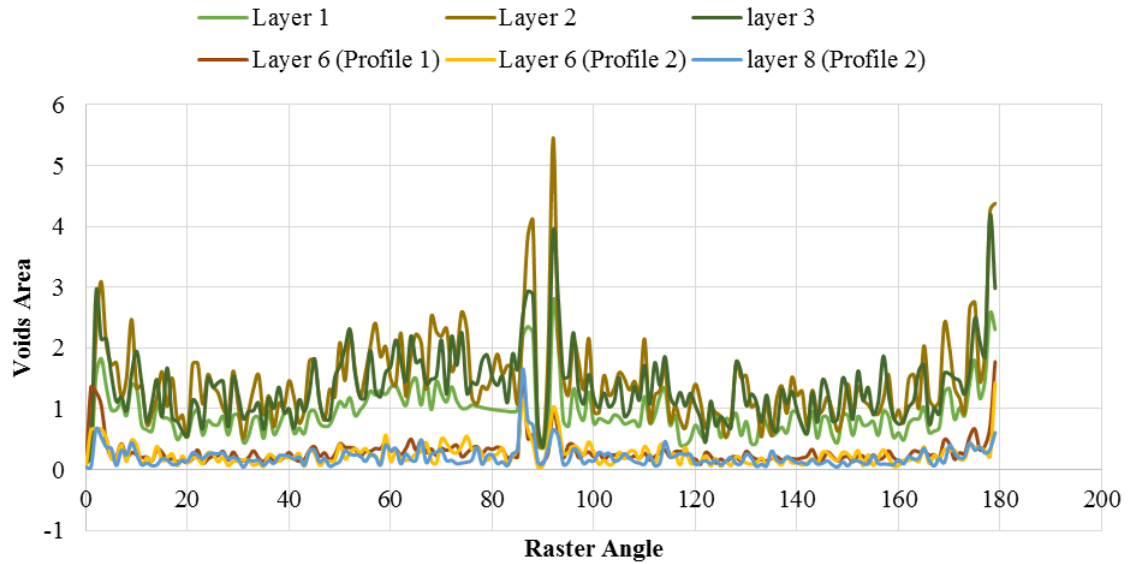
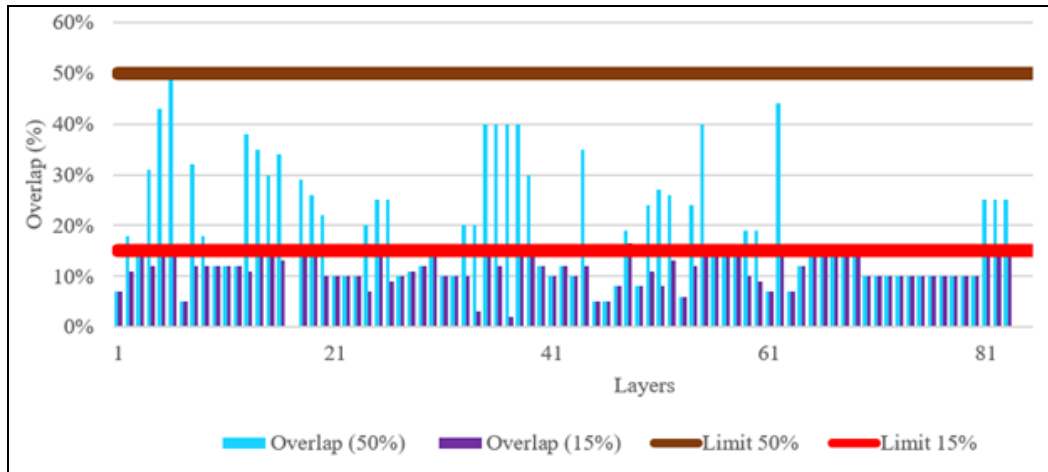
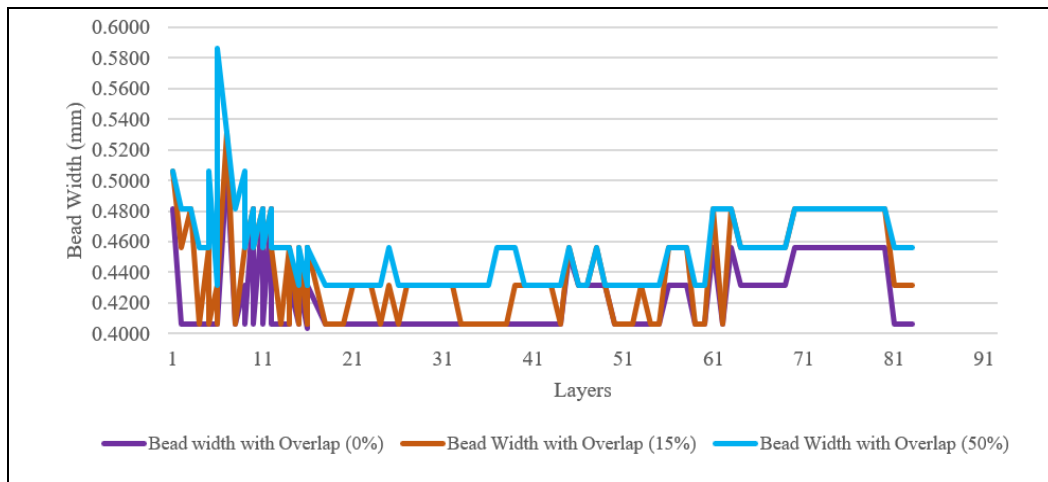


Figure 94. The relationship between Raster Angle and Voids Area for Layers 1st, 6th, and 8th

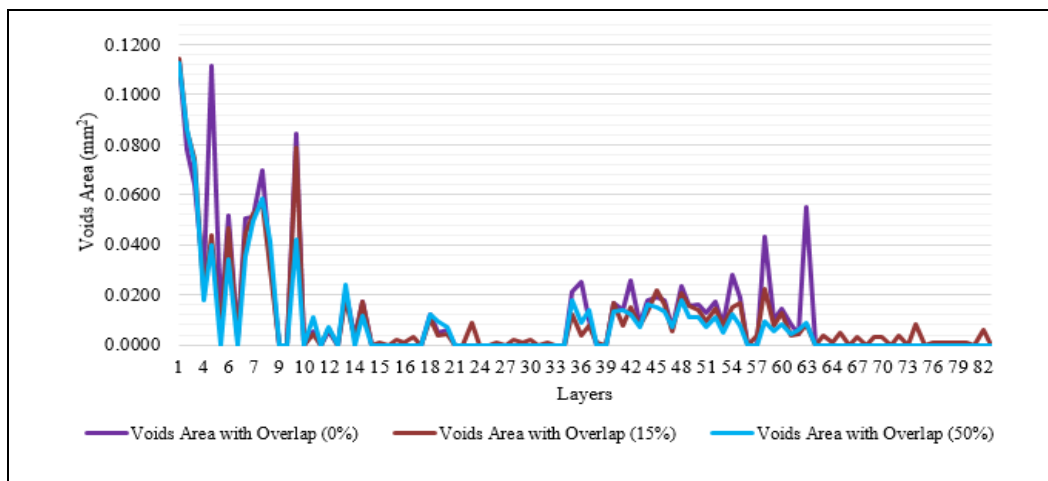
For sensitivity testing of the new model, the maximum allowable overlap percentage is changed to 0% and 15%. As Figure 95 shows by changing the maximum overlap maximum limit, the selected overlap percentage, bead width, and voids area are changed. There are overlap percentage and width oscillations when assessing the results on a layer by layer basis. The regions where the width changes generally correlate for these three overlap percentage limits. It is interesting to note that larger beads are selected with a higher acceptable overlap percentage limit.



(a)



(b)



(c)

Figure 95. The sensitivity of the new model with its constraints, the relationship between layers and (a) overlaps, (b) bead width, (c) voids area by changing maximum allowable overlaps

The comparison between the new model and the OEM software is shown in Table 44. It compares the voids with different overlap percentage limits. For the first approach (2D optimization only), the total void area is decreased by 9% with the overlap limit $\leq 50\%$, but with the second approach, the total void area is decreased by 8%. The reason for the difference is due to choosing a suboptimal set of process parameters for a layer such that the voids in the previous layer are covered.

Table 44. Difference between the OEM software (for the seat orientation shown) and the new model with different overlaps limit

Overlaps (%)	OEM Software	New Model-First Approach			New Model-Second Approach		
	0%	0%	15%	50%	0%	15%	50%
Total Voids Area (mm ²)	1.6400	1.2836	1.0953	0.9359	1.7829	1.2462	1.0023
Percentage of voids	21%	17%	14%	12%	23%	16%	13%

As many optimal overlap percentages are between 10% and 20%, an overlap limit $\leq 15\%$ is explored. It can be seen that the total void area was significantly reduced ($\sim 7\%$) with the first approach, and is reduced by 5% with the second approach.

It is interesting to note the 0% overlap condition results. When considering each layer individually, selecting an optimal set of raster angles and bead widths reduce the void area by 4%. However, when considering a 3D solution where the goal is to eliminate void stacking, there is a 2% increase in the total void area.

This process is computationally expensive. For this specific example which the size of the *.stl file is 1.62 MB size, the algorithm takes around 15 h with processor i7-3770, CPU 3.40 GHz, and 64-bit operating system.

The optimized answer with the new model is independent of the build orientation or the angle of the *.stl file around the Z-axis. As Figure 96 (a to c) shows, by changing the rotation about the Z-axis in the OEM software (90° , 60° , and 150°), the area of the voids in the first layer is changed from 0.14 mm^2 , 0.17 mm^2 , and 0.19 mm^2 respectively.

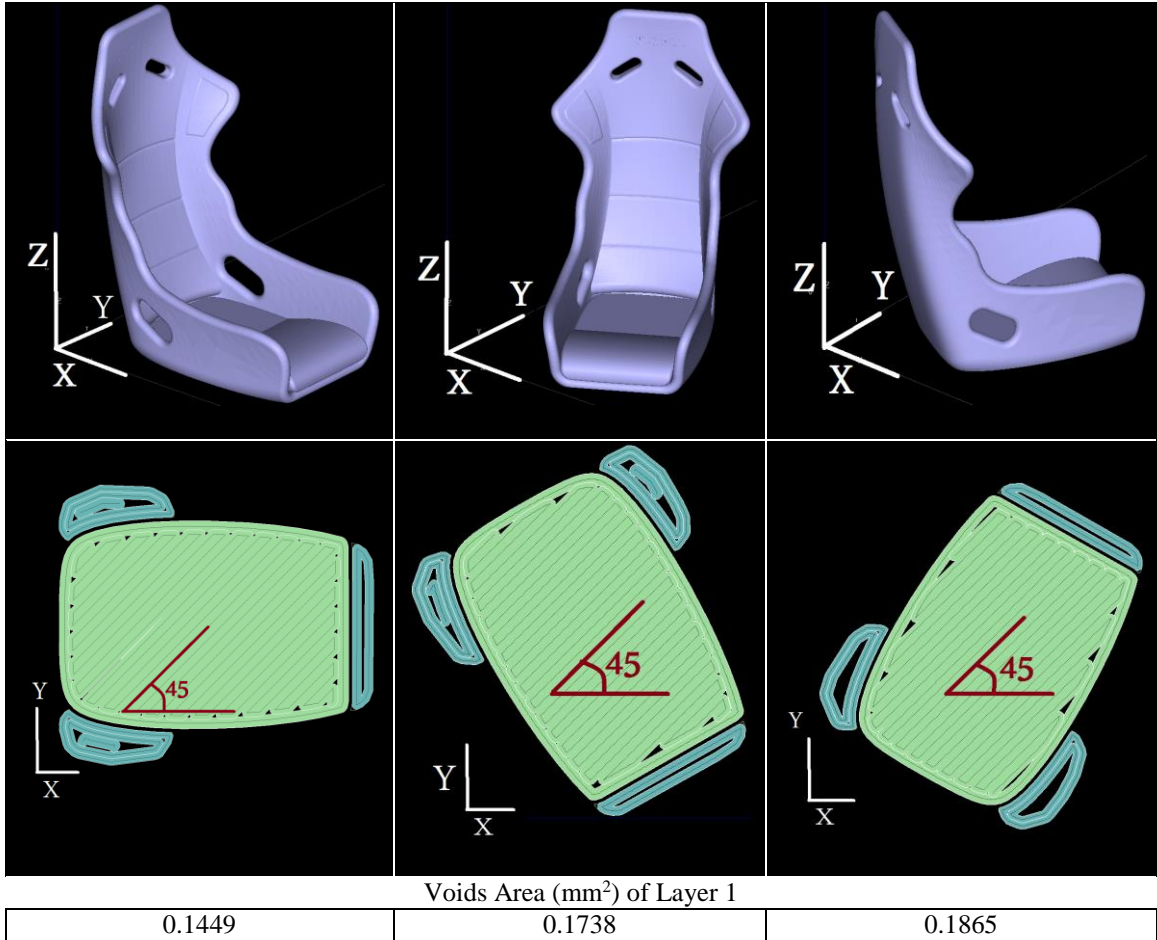


Figure 96. Different voids area in the first layer with part rotation with Z-axis (a) 90°, (b) 60°, and (c) 150° in the OEM software – note the standard raster angle is relative to the machine ‘world coordinates’

The next step is extended the research to another level; it focuses on comparing the total void area and regions for different rotations of the *.stl file around X and Y axes. Figure 97 compares when Figure 90 is rotated 60° around X-axis, 60° around Y-axis, and 60° around X and Y axes. As it shows, the volume of the support material is dependent on the rotation of the part. After slicing the part based on the rotation, the shapes of layers are changed. In this figure, the only first layer of these rotations is compared.

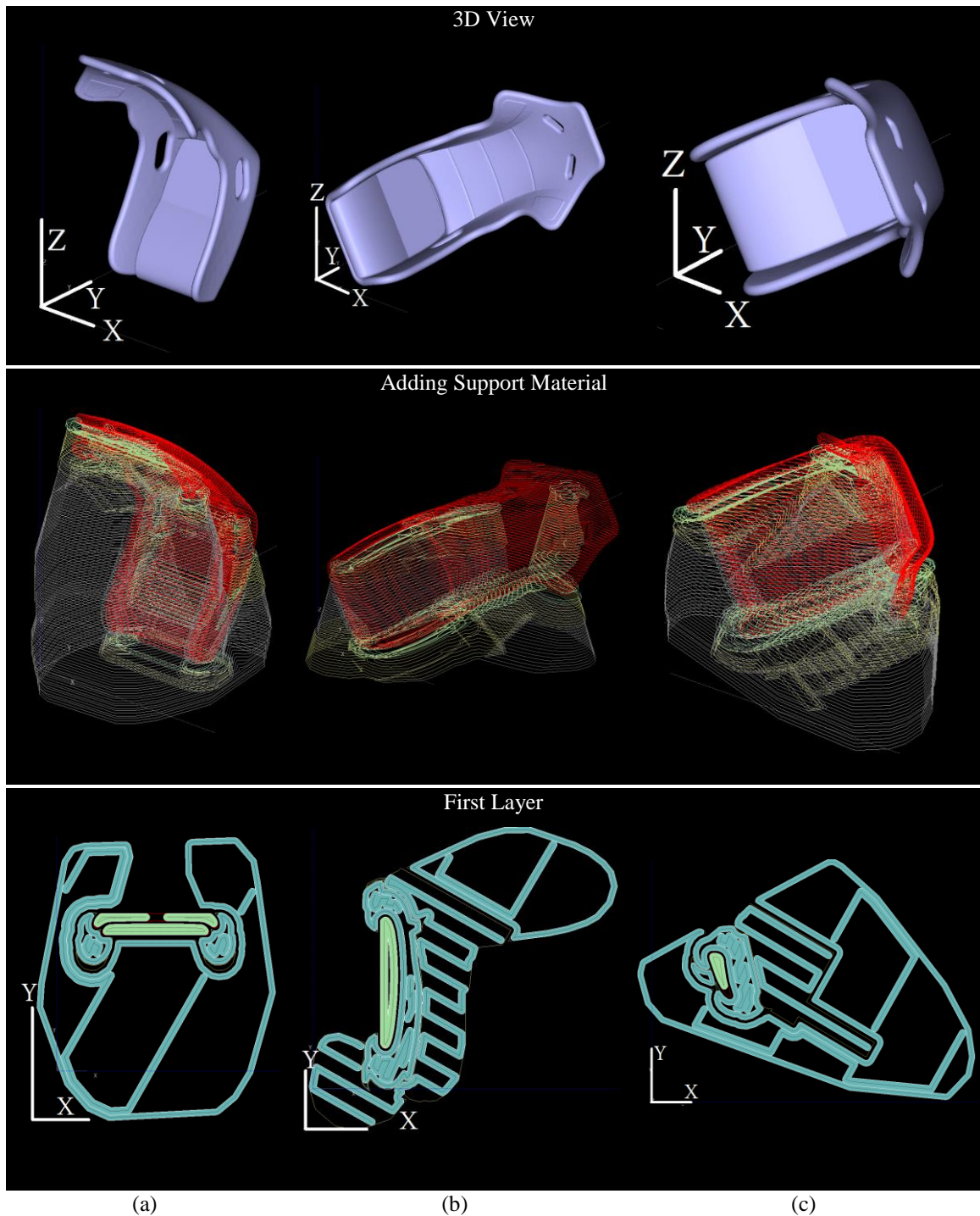


Figure 97. 3D view, support materials and the first layer when Figure 90, (a) 60° rotates around X-axis, (b) 60° rotates around Y-axis, and (c) 60° rotates around X and Y axes

After optimizing voids with allowable 50% overlaps in these rotations (the second approach), it is found that the voids minimization is not related to the rotations (Table 45)

Table 45. Comparing voids in different rotation around X and Y axes

Rotations around		OEM		New Model First Approach		Volume of Support (cm ³)	Process Time (min)	Number of layers
X-axis	Y-axis	Voids mm ²	Voids Percentage	Voids (mm ²)	Voids Percentage			
0	0	1.64	21%	0.9371	12%	1.788	23	83
60	0	5.43	26%	2.0887	10%	7.12	71	101
0	60	3.37	24%	1.2643	9%	4.18	45	73
60	60	3.89	25%	1.4016	9%	5.18	53	79

Figure 98 shows the comparison of four rotations around X and Y axes.

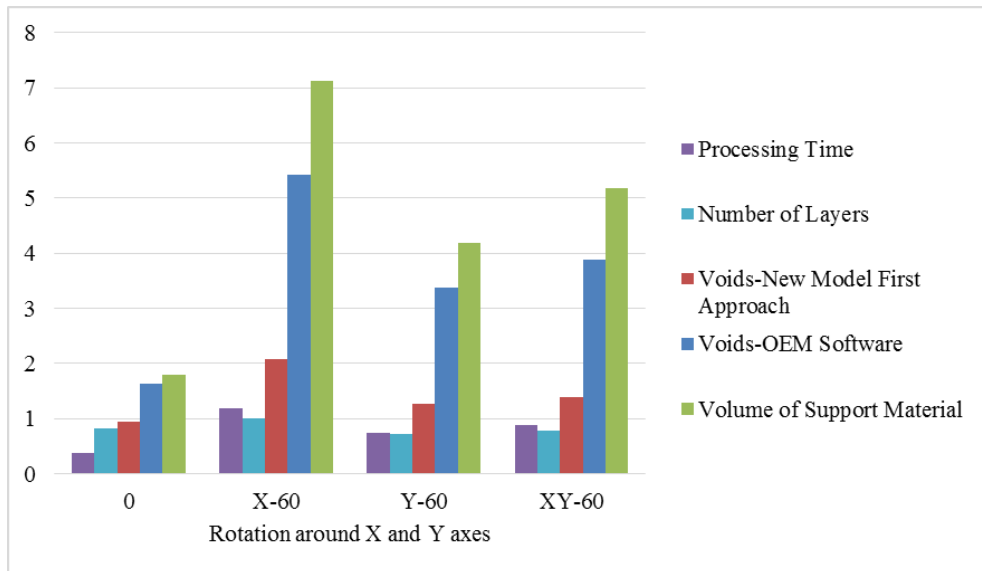


Figure 98. Comparing voids, processing time, number of layers, and support materials in different rotation around X and Y axes

CHAPTER 5

EXPERIMENTS FOR PHASE III

This chapter illustrates two different case studies. The first case study is a toy car seat [8] and is an extension of previous work that discussed on page 96 (car seat). The other case study targets developing an optimal build condition for a valve cover pattern set to be used as patterns for sand casting. This is a ‘rapid tooling’ application, and the achievable production volumes will be linked to the durability of the patterns. Consequently, determining optimal build conditions and a minimum void orientation is important. The difference of their sizes and the key features are shown in Figure 99.

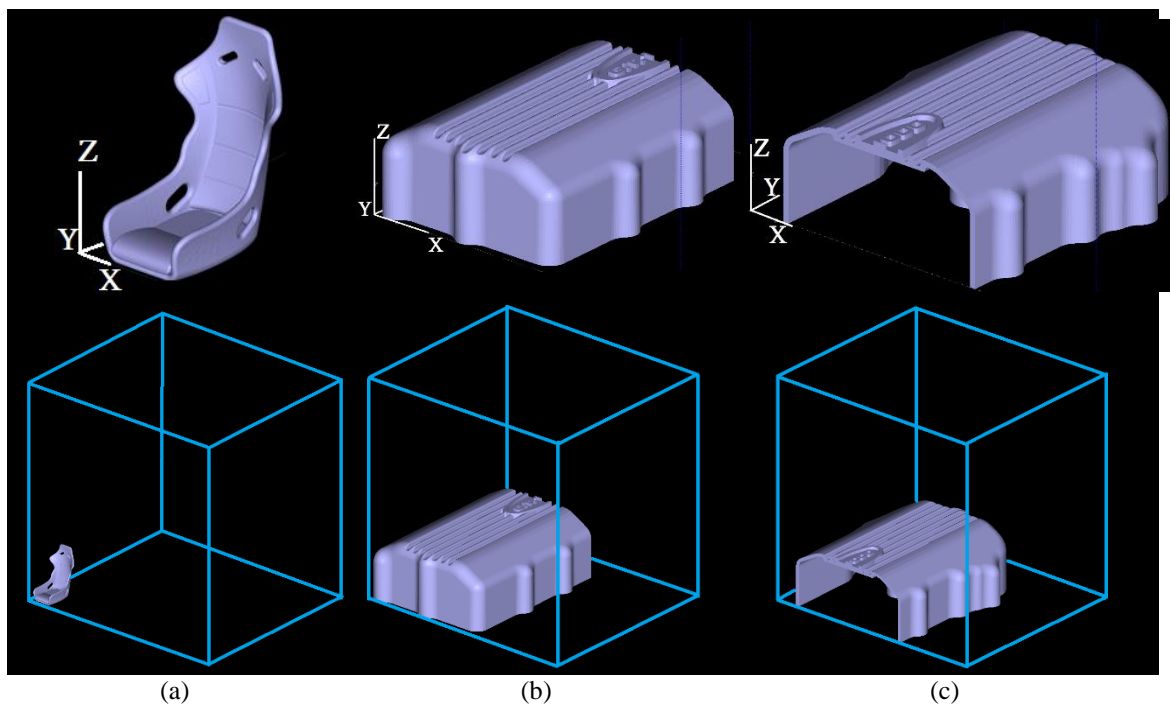


Figure 99. Three case studies with 0° rotations around X and Y axes (a) Toy car seat, (b) Valve cover I, and (c) Valve cover II

The car seat is mm 13.59 x 17.24 x 21.26 cm, it has 4 non-planar slots, is symmetric in the along the Z-axis at the mid value along the X-axis, and has no flat surfaces. The valve cover pattern is large: 237.26 x 600 x 113.59 cm, and has internal features, which will result in multiple contours per layer, depending on the build orientation. The part sections are non-symmetric, but there are regions where the 2D extrusion geometry is consistent. There is surface detail, and it should have the best surface finish possible to be aesthetically pleasing. The valve cover part is divided into two separate parts with 237.26 x 300 x 113.59 cm sizes. Figure 99 shows these case studies when they have 0° rotation about X and Y axes.

After performing the analyses, the optimal rotations for the case studies are shown in Figure 100. The maximum allowable overlaps for these cases are 50%, and the bead widths and bead heights are from Table 17.

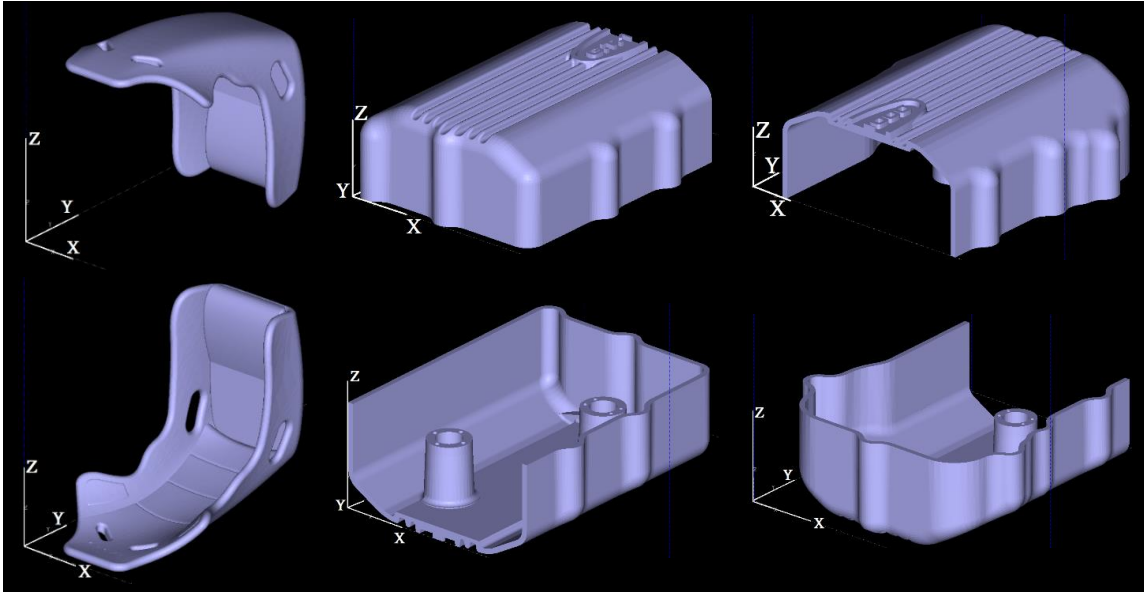


Figure 100. The rotation which has the minimum voids for each part

Each of the optimal rotations for Figure 100 has a specific optimal process parameter set for each layer. The toy car seat, Figure 101 (a), in the optimal orientation has 68 layers with 0.1778 mm bead height. The optimal bead widths are between 0.3 mm to 0.5 mm. The valve cover, Figure 101 (b and c), has 453 layers with a 0.254 mm bead height and the optimal bead widths are between 0.4 mm and 0.46 mm. Although the maximum allowable overlap percentages for all cases is 50%, the optimal overlaps in these cases do not exceed 25%. The reason for this result is that the model prefers to use the minimum bead width rather than a maximum overlap percentage.

For each specific case, there are two optimal rotations, as the results can be mirrored. The factors like the surface finish or the required support material, would need to be considered to choose the build orientation.

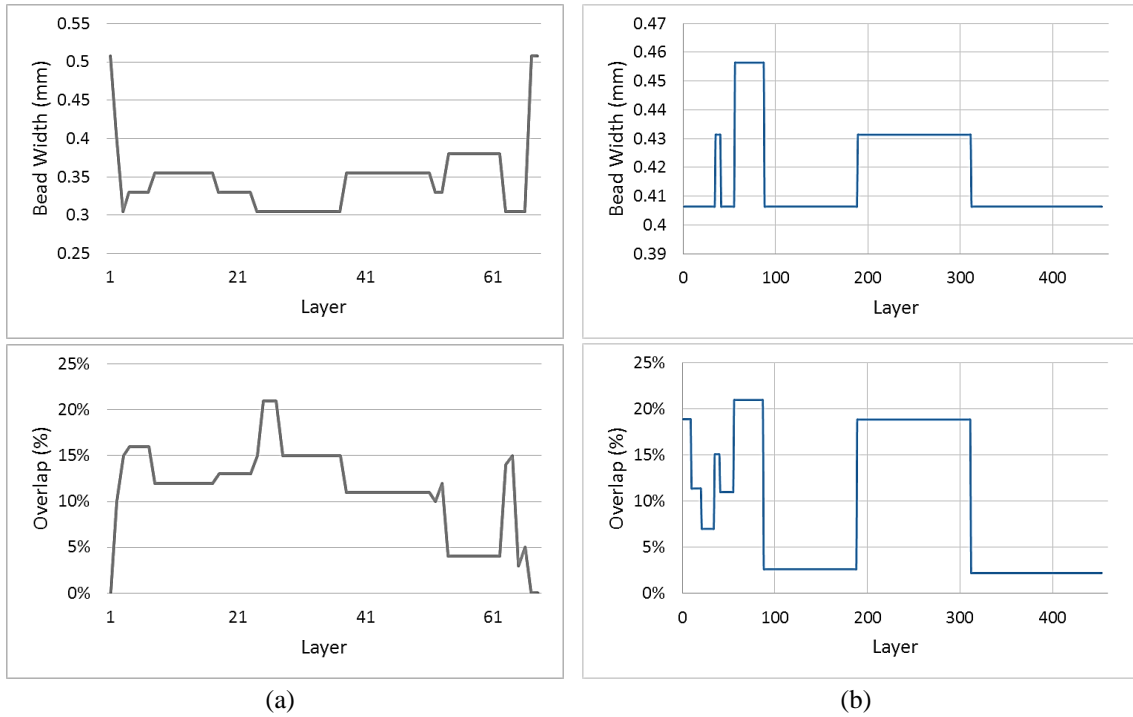
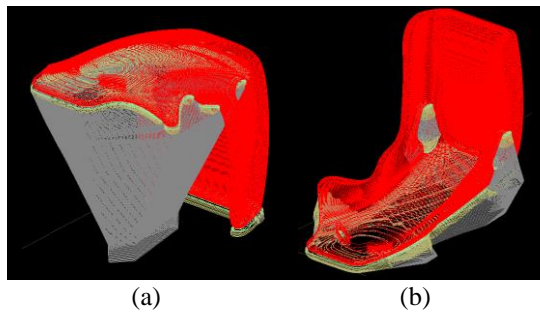


Figure 101. Bead width and overlaps per layer for (a) Car seat and (b) Valve cover I and II

Figure 102 shows the difference between time and support material for two optimal build orientations for the car seat. In both rotations, the total void results are the same. As it can be seen, for producing Figure 102 (a), the support material is approximately three times more than the amount required in Figure 102 (b). By using more support material, the building time and the time for removing the support material will be dramatically increased. The total processing time for Figure 102 (a) is around twice more than Figure 102 (b). The other parameter for choosing between these two optimal rotations is surface finish. If the user needs to have the best surface finish on the seat depth and back of the seat, Figure 102 (b) will be preferred. However, if the surface finish of the seat back is to be considered, then Figure 102 (a) is the best choice.



Building time	4 hrs. 24 min	2 hrs. 43 min
Support material (cm ³)	31.212	12.892
Removing support material time	1 hr.	10 min

Figure 102. Comparison of time and support material between two optimal orientations

For testing the solution variations generated by this new model, the allowable overlap percentage in the previous cases is changed from 50% to 0% (the standard build condition for commercial systems). The new optimal rotations, number of layers, and the range of bead widths for these cases are illustrated in Figure 103. The assumption of these cases is the optimal bead height is constant during the process. The regions where the planar slices are approximately the same (highlighted) result in constant bead widths (bold line in Figure 103 (b)) for the available build options.

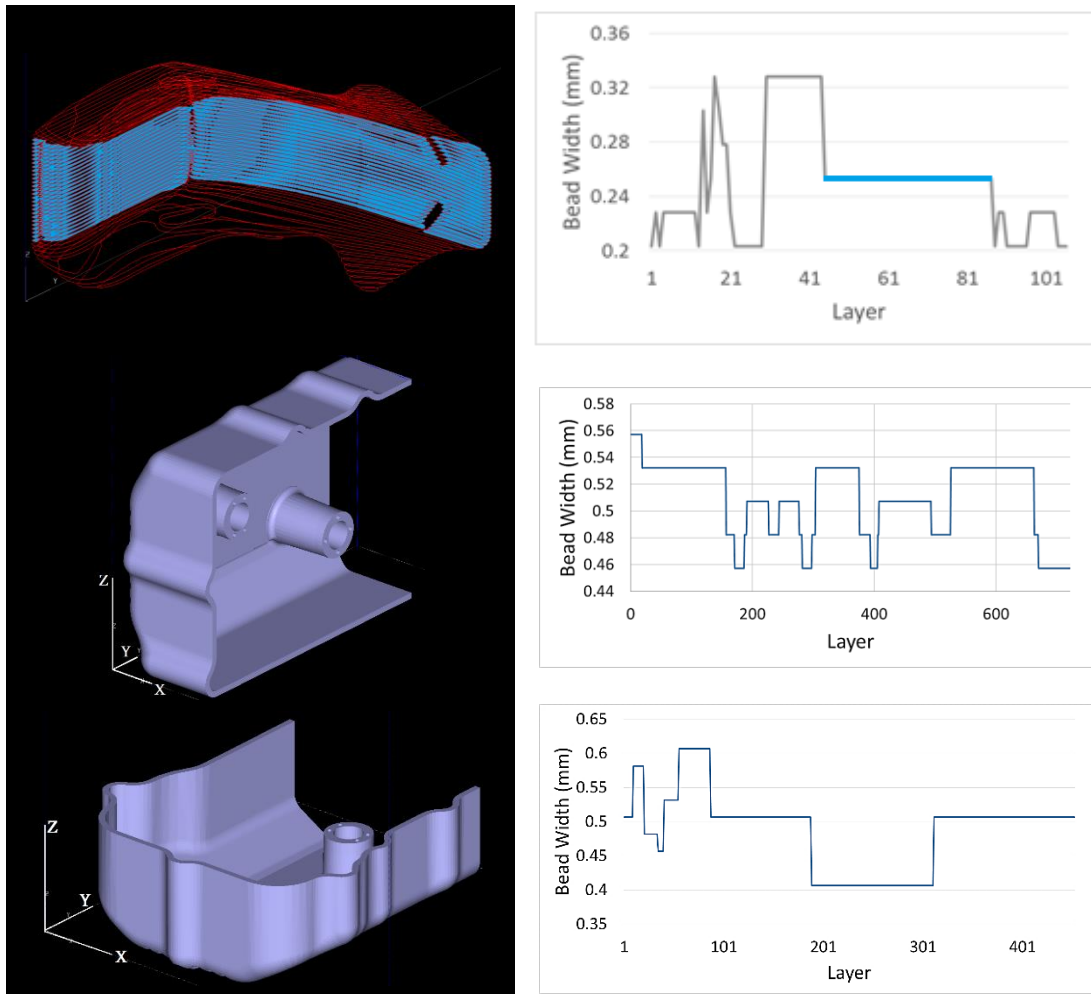


Figure 103. Optimal rotation to minimize voids with overlap percent set to 0%

Table 46 compares the case studies with two different allowable overlaps 0% and 50%. In this table, the volume of the part varies as there are different overlap percentages. Thus, the optimal bead height is changed, and the area of each layer is changed as well. The below table shows when the overlap is 50% the percentage of voids is less than when the allowable overlap is 0%.

Table 46. Comparing cases parameters when the allowable overlaps are 0% and 50%

Overlap	Car Seat		Valve Cover I		Valve Cover II	
	0%	50%	0%	50%	0%	50%
Rotations (θ_x, θ_y)	(0°,90°)	(90°,0°)	(0°,90°)	(0°,0°)	(0°,0°)	(0°,0°)
Number of layers	106	68	721	453	453	453
Optimal Bead Height (mm)	0.127	0.1778	0.3302	0.254	0.254	0.254
Volume of Voids (mm ³)	1.48	0.79	98.52	50.22	90.10	47.93
Volume of Part (mm ³)	7.79	7.71	1005.33	1004.42	958.55	958.55
Percentage of Voids	19%	13%	9.8%	4.9%	9.4%	5%

In Appendix D, Figure 114 (a and b) to Figure 116 (a and b) compares the total voids per build rotation for the car seat, valve cover I, and valve cover II, respectively, when the allowable overlaps are 50% (a) and 0% (b). As these Figs show, the voids where the allowable overlap percentage is 0%, have more fluctuation than the solution that allows for the 50% overlap condition. The reason is the optimal bead widths, and overlap percentages in these cases are not global optimal (phase I algorithm). Show the impact of symmetry for the car seat, discuss not completely symmetric due to the void stack elimination (phase II). The reason is in phase II algorithm, the toolpath of the top layer needs to cover voids on the previous layer. For example, phase II of Figure 102 (a) starts with the second layer to cover voids on the first layer, then the third layer covers voids on the second layer and so on. Figure 102 (b) also starts with the second layer but this layers in Figure 102 (a), is layer 67th. Thus, the toolpath of these two build orientations is not same and symmetric.

The voids with the 0% allowable overlaps are bigger than with the 50% allowable overlaps. In all cases, the range of voids is increased when the allowable overlaps are decreased. For example, for the valve cover I with 50% allowable overlap, the range of voids is between 49.5 mm³ and 52 mm³. However, with 0% allowable overlaps, the range of voids is changed to 52.5 mm³ and 55 mm³ (Figure 115).

For valve cover II with 50% allowable overlap, the range of voids is between 45 mm³ and 52 mm³. However, with 0% allowable overlap, the range of voids is changed to 88 mm³ and 95 mm³. This is a significant increase - 1.5 times more than when allowable overlap percentage is 50%. Figure 116 shows this differences.

The ANOVA results for the car seat case study with both allowable overlap percentages (0% and 50%) is summarized in Table 47. Small P-values indicate that the total void areas are dependent on the build rotation. The big F value in the table proves that the total voids between rotations are different and build orientations influence voids in the finished part.

Table 47. ANOVA for car seat case study

Allowable Overlaps	Source of Variation	SS	df	MS	F	P-value	F
50%	Rotation around X	172.25	359	0.48	84922.63	0	1.12
	Rotation around Y	57.67	359	0.16	28432.33		
	Error	0.73	128881	5.64987E-06			
0%	Rotation around X	5.13	359	0.01	67267.36	0	1.13
	Rotation around Y	1.81	359	0.005	23787.45		
	Error	0.03	128881	2.12E-07			

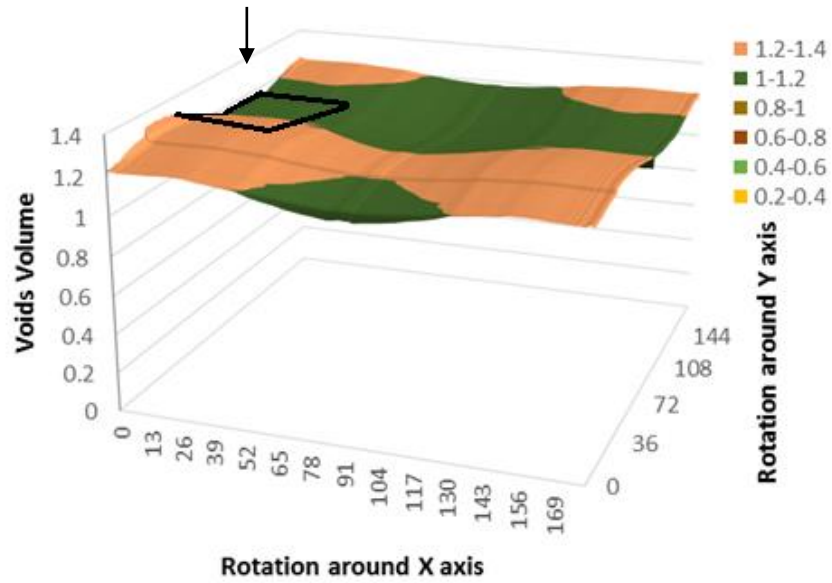
Although the small P values in Table 47 statistically confirms the relationship between voids and rotations, methods to determine an optimum global set of solutions is challenging. A heuristic search approach cannot be readily implemented as the bead width, raster angle, and percentage overlap are calculated for each input orientation.

In Figure 104 (a), the bounded region in Figure 114 (a) is expanded. This magnified region illustrates that localized ripples in the void-rotation angle solution surface are apparent. Comparing all voids is computationally expensive. For this specific car seat example, which has a file size of *.stl of 1.62 MB, the algorithm takes approximately 15 hours with processor i7-3770, CPU 3.40 GHz, and a 64-bit operating system [6].

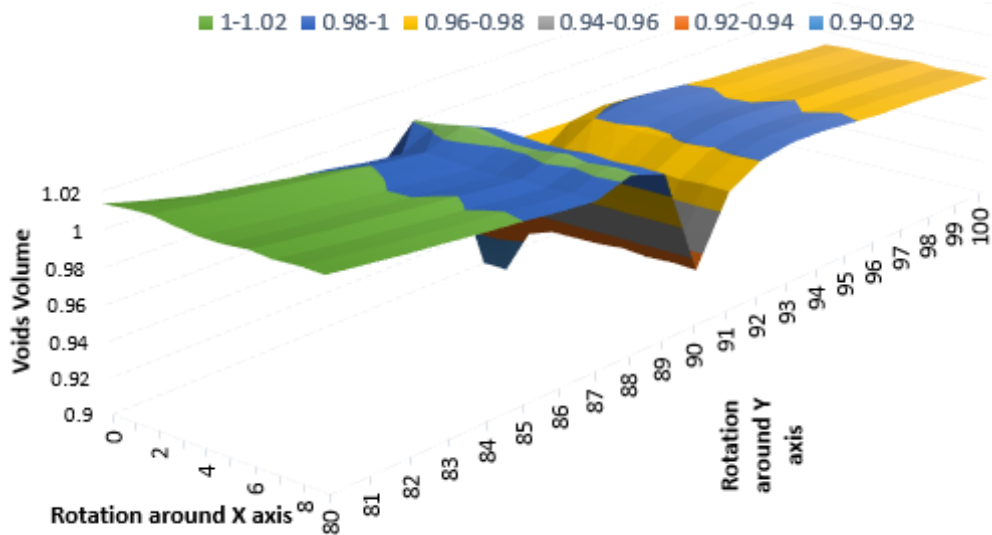
Table 48 shows the total voids with the default toolpath using the Insight® software used for the Fortus 400 MC. The selected build orientations in this table are the same as the build orientations presented in Table 46, which are the optimal rotations when the allowable overlaps are 0% and 50%. The default parameters in the OEM software are bead height with 0.254 mm, bead width with 0.5080 mm, 45° raster angle, and 0% overlaps. The comparison between Table 46 and Table 48 proves that the new model minimizes voids between 3% and 10%. However, the new model avoids contiguous void chimneys. If this condition (phase II) were not implemented, the void area reduction would be higher [8].

Table 48. Voids volume with OEM software

Rotations (θ_x, θ_y)	Car Seat		Valve Cover I		Valve Cover II
	(0°,90°)	(90°,0°)	(0°,90°)	(0°,0°)	(0°,0°)
Volume of Voids (mm ³)	1.67	1.63	147.78	143.63	138.99
Percentage of Voids	21.4%	21.1%	14.7%	14.3%	14.5%



(a)



(b)

Figure 104. a) Voids per rotations and (b) Comparing voids in the small range of rotations

To explore the solution space options, a frequency analysis comparing the void volumes (void areas multiplied by the slice height) for all rotation variations for the car seat is presented in Figure 105 when the allowable overlap percentage is limited to 50%. There are 360*360 possible solutions for integer values of rotation. For this example, less than 4% of the build rotations have volume for the voids less than 0.91 mm³. Approximately 19% of the solution would generate void volumes between 0.95-0.97 mm³, and 9% of the solutions will result in void volumes between 1.05 - 1.13 mm³. This worst case condition is 1.5 times less than the default OEM toolpath.

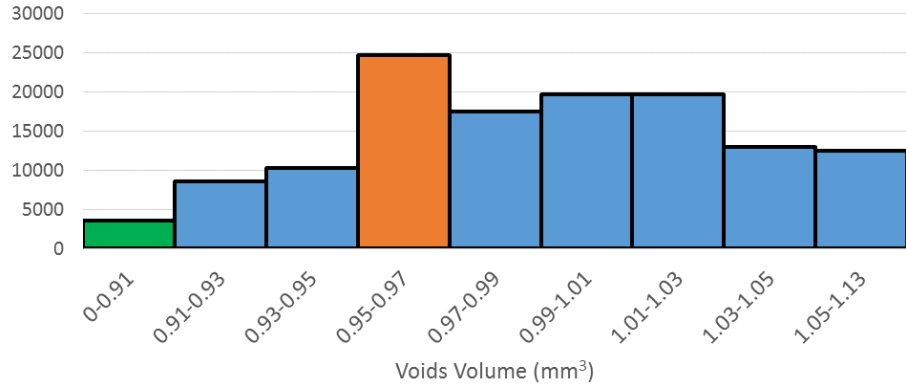


Figure 105. The frequency of voids with the new model for the car seat case with 50% allowable overlaps

For the car seat, the maximum void volume is 1.1296 mm³ which occurs for a rotation 39° around the X-axis and 0° around the Y-axis (Figure 104). For this rotation, there are 106 layers with 0.254 mm bead height. The optimal bead width and overlaps for this rotation are illustrated in Figure 107 (b) and (c). It can be seen that both the bead width and percentage overlaps are noticeably higher than the best case (Figure 100).

Figure 106 shows a frequency analysis comparing the void volumes for all rotation variations for the valve cover II. For this example, less than 4% of the build rotations have volume for the voids less than 48.29 mm³. Approximately 40% of the solution would generate void volumes between 48.65-49.01 mm³, and 4% of the solutions will result in void volumes between 50.1-50.46 mm³.

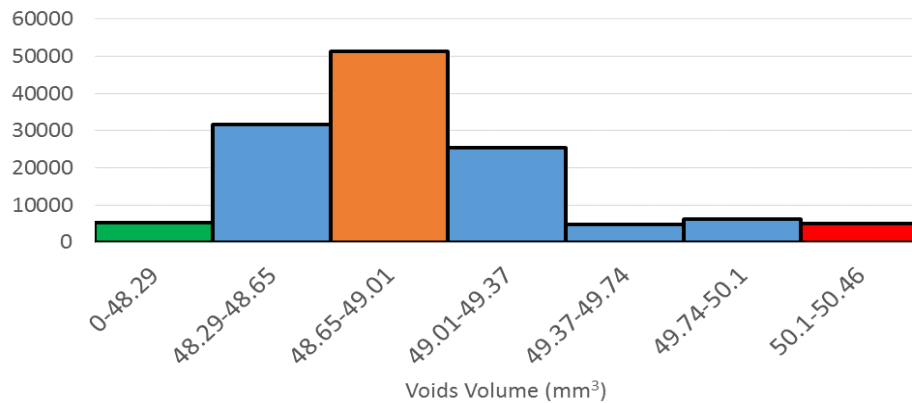
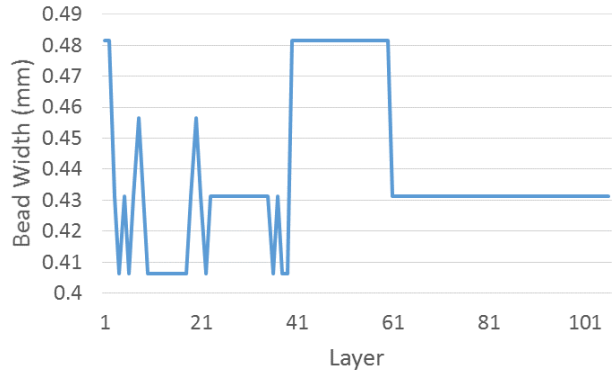
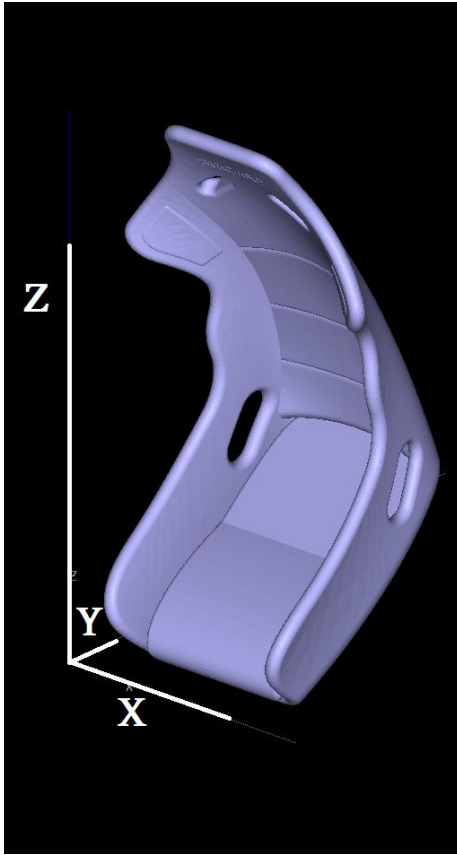
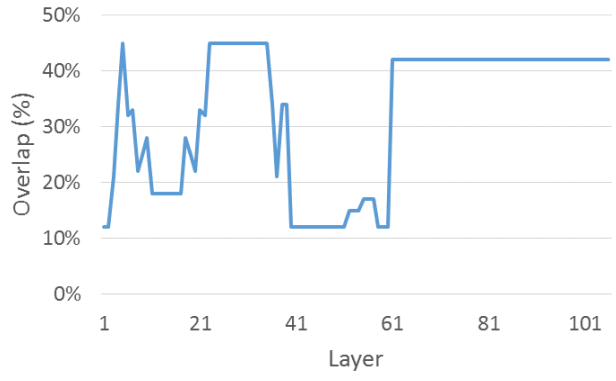


Figure 106. The frequency of voids with the new model for the valve cover II study with 50% allowable overlaps



(b)



(c)

Figure 107. The worst rotation for car seat case study

CHAPTER 6

CONCLUSIONS AND FUTURE RESEARCH

As it was discussed in the introduction, after experimental testing, it was recognized that a component's strength relationship with respect to the volume material usage is inconsistent and that failures occurred in regions of voids in the AM-ME process. Related to the characterization of mechanical properties for samples built with various AM-ME processes, there is now an understanding of the anisotropic problems with AM-ME processes. However, there is no comprehensive appreciation of the issues associated with the numerous interior voids inherent in the AM-ME processes contained in each possible build orientation. Previous researchers have focused on the build orientation targeted reducing support material requirements, surface finish, etc. However, research needs to be performed to develop methodologies while considering the fill conditions with respect to an optimal orientation.

This dissertation explores the influence of the build parameters, includes the build orientation on interior void regions generated by the AM-ME tool paths, and aims to identify, minimize, and manage void regions during the toolpath generation. In addition, it studies the effects of build orientation and the amount of unwanted voids in the finished part and finds optimal build candidates to minimize the voids in tandem with eliminating contiguous void stack regions. An exhaustive search and sort methodology is employed. Available machine-process settings are utilized in this dissertation. The process flow of this algorithm illustrates in Figure 108.

As Figure 108 shows, the algorithm starts with slicing the *.stl file with the desired bead height, and then for each layer, the raster angle, the optimal bead width, overlap percentages, and total void area is calculated using a set of valid bead widths to seed the model. Then, the set of conditions which generates the minimum entire void area chooses for each layer (phase I). The final stage, which is highlighted in Figure 108, focuses on managing voids between layers to ensure void coverage during the build process (phase II). This process is repeated for all possible build orientations and at the end by comparing the total voids volumes, the best build orientation to have the minimum voids volume is chosen (phase III).

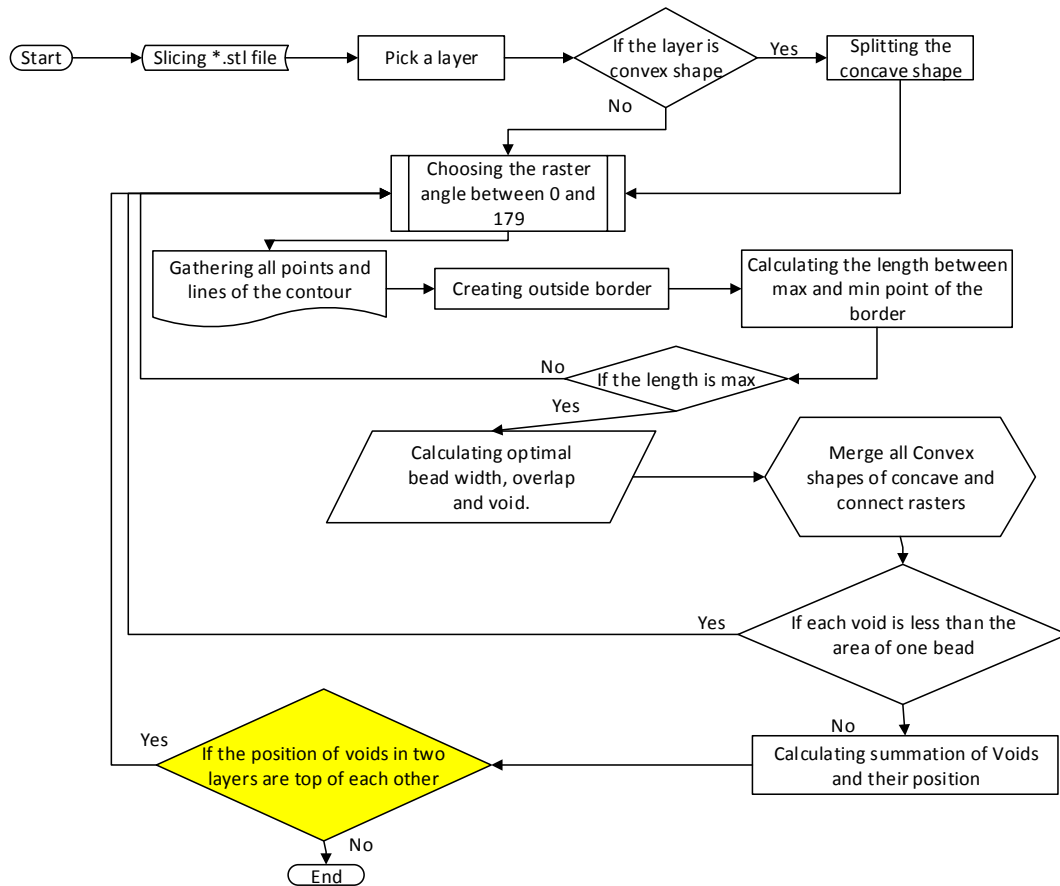


Figure 108. Algorithm for minimizing and managing voids

The algorithm is divided into three phases. Phase I is a 2D optimization and does not guarantee that voids are covered. Phase II is a 3D optimization and covers voids between layers. In addition to the search and sort approach, void location comparisons are performed. It was found that the unwanted voids are decreased by up to 8 per cent with the new model in these phases. The final component will contain multiple bead widths and overlap conditions, but all are feasible as the available machine solutions are used to seed the model.

In phase III, it is clearly shown that the build orientation influences the voids that are generated. The generated surface graphs show the influence of the build rotation on the generated voids, even when variable build settings per layer of a component are implemented.

By comparing the algorithm with the previous researchers, some of the results are complemented. For example, Chapter 2 discusses that a small bead width improves strength. As Equation 9 shows, there is a direct relationship between the bead width and void areas. Thus, by minimizing a bead width, the void area is decreased, and consequently, the strength is improved as there is more

material within a unit volume. Another critical parameter is the overlap percentage. An overlap significantly enhances strength. Equation 9 shows the relationship between the voids area and the overlap is an indirect relationship. Which means by increasing the overlap, the volume of the voids decreases, and the strength increases.

The novelty of this dissertation is an optimization strategy that targets minimizing the voids within a component is industrially relevant for both software developers, providers, and the end users. The research solutions presented in this dissertation can be readily implemented by the software solution providers listed in Table 3, as existing settings and tool path strategies are being used, but in a strategically manner to reduce potential internal failure points. This is important to the end users because they expect the performance characteristics of an injection molded part. Table 49 summarises the pros and cons of each phase. The timeline that is provided in this table is for the *.stl file with 1.62 MB size with processor i7-3770, CPU 3.40 GHz, and 64-bit operating system like Figure 90.

Table 49. Pros and cons of the three phases

Phase	I	II	III
Time	~2 min	~12 min	~15 hours
Optimization	2D	3D	3D
Covering voids		√	√
Independent of the build envelope	√	√	√
Best build orientation			√

Table 49 shows the processing time is the only disadvantage of phase III. Thus, heuristics to reduce the processing time need to be explored. Once heuristics are developed to facilitate processing time, another future work project will be establishing a global optimization model that considers filling criteria along with surface finish, and support material. It can help optimize the process time, strength, surface finish, accuracy, and support material usage.

When exploring case studies, it was found that the rotation of the part in the cases like Figure 109 (a to c), does not affect on the number, shape, and voids area in layers, significantly. Geometry based heuristics need to be developed for cases like these. It is recognized that strategically adjusting the number of boundary contours could position voids in areas determined to be less sensitive, but this is outside the scope of this research.

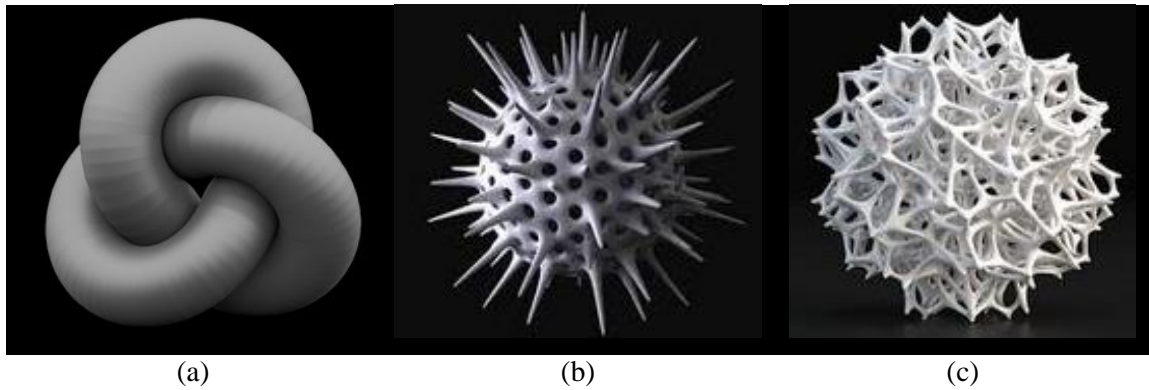


Figure 109. Complex 3D parts

This research can be continued by rearranging the bead height between layers. As it was discussed in chapter 3, the minimum optimal bead height is for the first layer, and the maximum is for the last layer. By adding additional algorithm, the users can control bead heights between layers in phase II. This may help find the best arrangement between layers to cover and manage voids.

The other field that this research can be continued is, after dividing the complex shape, introducing internal boundaries from any segmentation solution will introduce voids due to these new boundary-edge conditions. The rasters between edges of the new convex shapes need to be connected to avoid creating new voids. Figure 110 (b) shows Figure 110 (a) after connecting the raster toolpath between the new shapes. The connection with two new convex shapes is as same as the connection between the start and stop points of rasters that was described in Figure 52 (e). Figure 110 (b) illustrates a blending condition where the toolpath raster angle is dynamically changed. This need the expert knowledge on G-Code to control the nozzle movement, however, it will be improve the filling condition dramatically and help create the new toolpath generation.

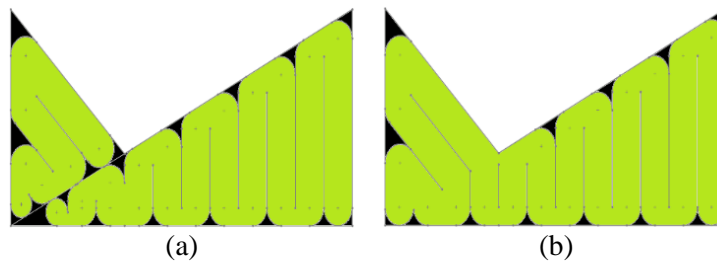


Figure 110. Toolpath with connection rasters (a) and no continuity between rasters (b)

Another problem in solid shapes with the OEM software is the start and stop points are located at the same point between layers (Figure 111(a)). For solving this problem, the stop and start points between layers need to be shifting between layers in the new model. The equation $\frac{360^0}{T(N_j)}$ is the

angle of shifting start and stop points between layers (Figure 111(b)). The influence of this rotation needs to be studied in the future work.

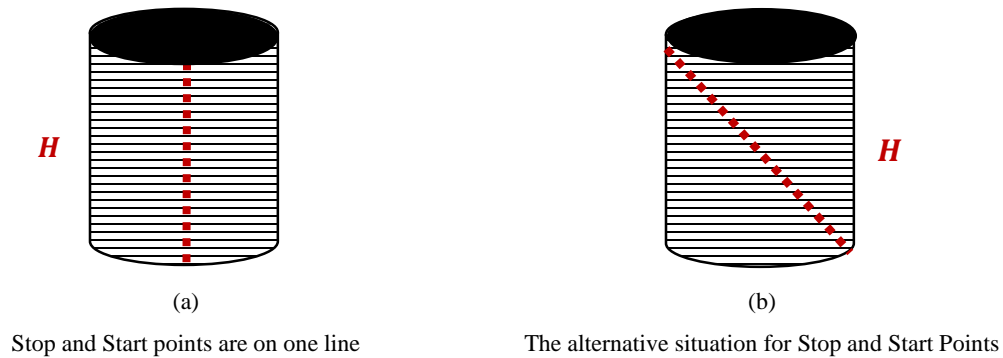


Figure 111. Unwanted overlaps of start and stop points between layers

Reducing the processing time is another future work research activity. This research can be continued by reducing the number and amount of input variable via heuristics, and adding more constraints such as processing time limits.

This mathematical model can be employed with metal based systems. The overlaps and raster angles affect the hardness and residual stress on the part in metal additive manufacturing methods (Figure 112). Consequently, void regions highlighted in this research correlate to regions with variable mechanical and physical properties for the metal deposition processes, and this research needs to be continued.

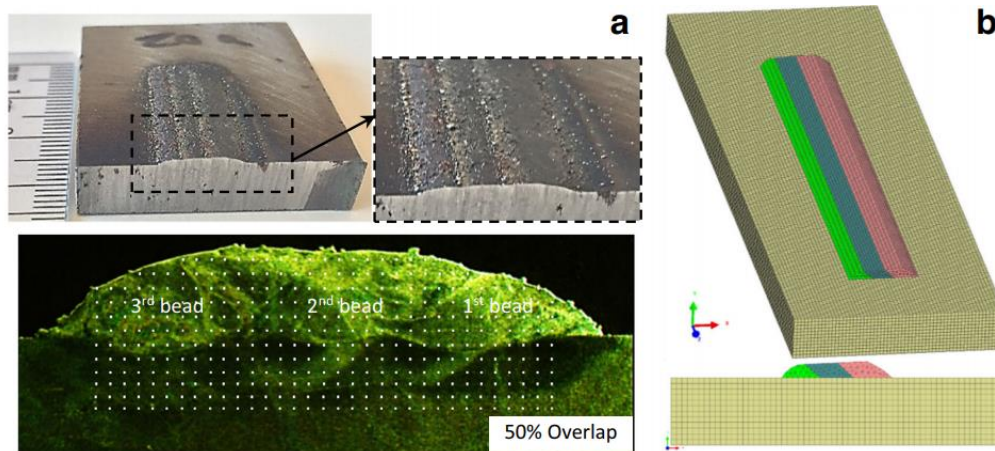


Figure 112. (a) 3D geometry and cross-section of the specimen with three overlapped beads. (b) Average hardness values in the bead and substrate for specimens [93]

In addition, experimental tests need to be examined to validate the relationship between voids and processing factors like strength in each phase and then compare to the OEM software. Also void

coverage methods which are illustrated in Chapter 3 need to be compared with each other. Appendix shows suggestions for experimental test samples. Figure 113 shows the other important factors like permeability, material usage, and surface finish between two processes; injection molding and AM-ME.

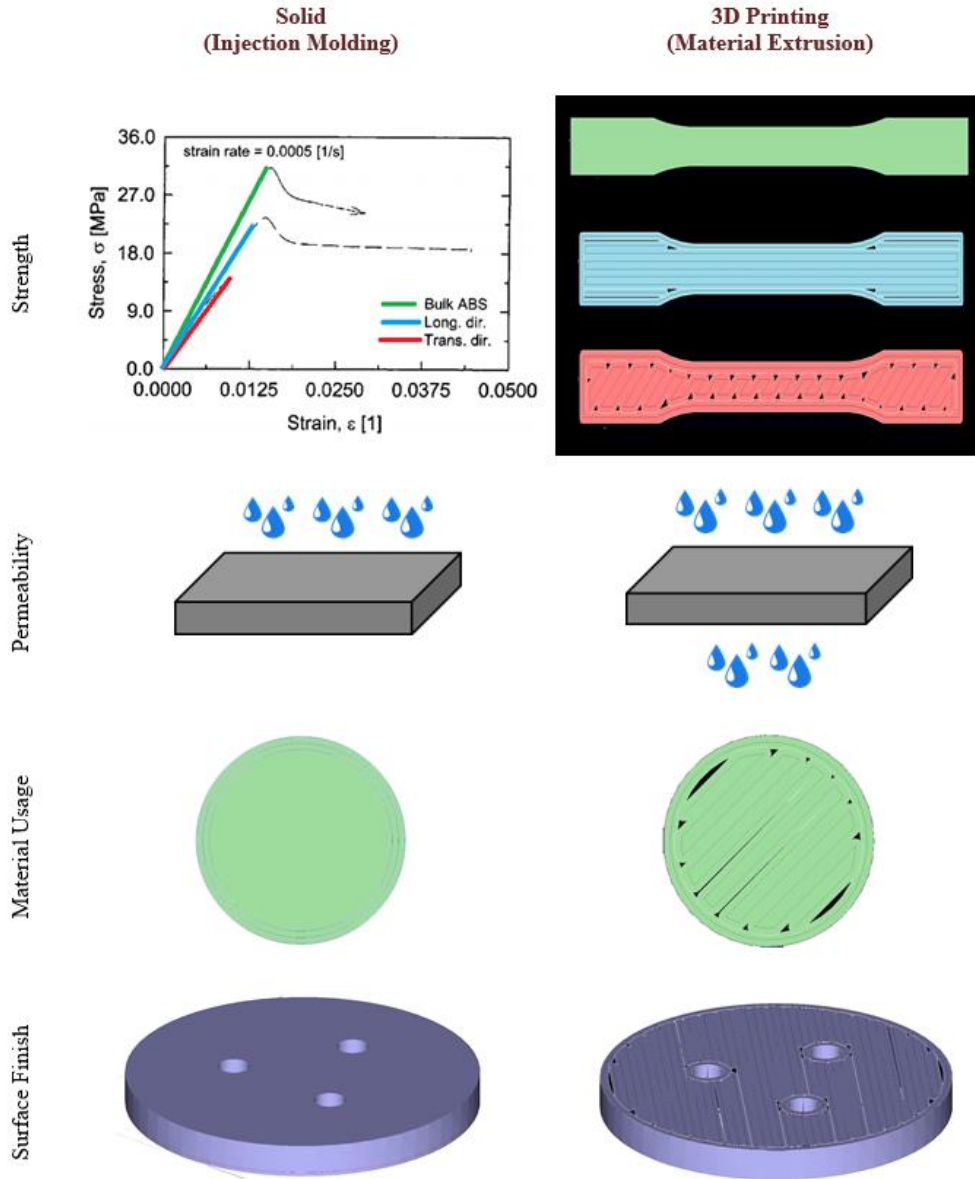


Figure 113. Comparison between injection molding process and material extrusion process [94]

REFERENCES

- [1] Hasti Eiliat and Ruth Jill Urbanic, "Using Genetic Algorithm to Optimize the Build Orientation for Fused Deposition Molded Components Containing Internal Reinforcement Structures," in *ASME International Mechanical Engineering Congress and Exposition*, Montreal, Quebec, Canada, 2014.
- [2] Hasti Eiliat, Ruth Jill Urbanic, and Luis Fernando Villalpando, "Experimental Evaluation of Light-weighting Design Options for the Fused Deposition Modelling Process," in *65th Annual Conference and Expo of the Institute of Industrial Engineers*, Nashville, Tennessee, USA, 2015.
- [3] Luis Fernando Villalpando, Hasti Eiliat, and Ruth Jill Urbanic, "An Optimization Approach for Components Built by Fused Deposition Modeling with Parametric Internal Structures," *47th CIRP International Conference on Manufacturing Systems*, vol. 17, pp. 800-805, 2014.
- [4] Hasti Eiliat and Ruth Jill Urbanic, "Minimizing Voids with Using an Optimal Raster Orientation and Bead Width for a Material Extrusion Based Process," in *ASME International Mechanical Engineering Congress and Exposition*, Phoenix, Arizona, USA, 2016.
- [5] Hasti Eiliat and Ruth Jill Urbanic, "Minimizing Voids for a Material Extrusion Based Process," *Rapid Prototyping Journal*, pp. 1-23, 2018.
- [6] Hasti Eiliat and Ruth Jill Urbanic, "Visualizing, Analyzing, and Managing Voids in the Material Extrusion Process," *The International Journal of Advanced Manufacturing Technology*, pp. 1-15, 2018.
- [7] S. S. Crump, "Apparatus and Method for Creating Three-Dimensional Objects". USA/Minnesota Patent 5,121,329, 30 10 1989.
- [8] ASTM, "The ASTM International committee F42 on Additive Manufacturing Technologies," 2016. [Online]. Available: www.astm.org/COMMITTEE/F42.htm. [Accessed 30 01 2016].

- [9] Zureks, "FDM," Based on drawing in: Duc Truong Pham, Stefan Dimov, Rapid manufacturing, Springer-Verlag, 2001, 2008. [Online]. Available: https://commons.wikimedia.org/wiki/File:FDM_by_Zureks.png. [Accessed 2017].
- [10] Additive Manufacturing Research Group, "About Additive Manufacturing," Loughborough University, [Online]. Available: <http://www.lboro.ac.uk/research/amrg/about/the7categoriesofadditivemanufacturing/powderbedfusion/>. [Accessed 2017].
- [11] "Stereo Lithography (SLA)," MKS Technologies Pvt Ltd., 2015. [Online]. Available: <http://www.mkstechgroup.com/stereolithography-sla/>. [Accessed 2017].
- [12] Steven Schmid, "Additive Manufacturing: 3-D Printing Beyond Plastic - Science Nation," National Science Foundation, 18 12 2012. [Online]. Available: https://www.nsf.gov/awardsearch/showAward?AWD_ID=1254287&HistoricalAwards=false.
- [13] Blog, "Material Jetting 3D Printing Technology," threeding, 25 10 2016. [Online]. Available: <https://www.threeding.com/blog/%E2%80%8Bmaterial-jetting-3d-printing-technology>. [Accessed 2017].
- [14] Craig Bratt, "Center for Laser Applications," Fraunhofer CLA, [Online]. Available: http://www.cla.fraunhofer.org/content/dam/ccl-laser/en/documents/CLA_Overview_web.pdf. [Accessed 2017].
- [15] W. Associates, "Wohlers Report 2014 – 3D Printing and Additive Manufacturing State of the Industry," Annual Worldwide Progress Report, 2014.
- [16] Fu-da Ning, Weilong Cong, Junhua Wei, Shiren Wang, and Meng Zhang, "Additive Manufacturing of CFRP Composites Using Fused Deposition Modeling: Effects of Carbon Fiber Content and Length," in *Proceedings of the ASME 2015 International Manufacturing Science and Engineering Conference*, Charlotte, North Carolina, USA, 2015.
- [17] 3daddfab, "3D Additive Fabrication," STL File, 2016. [Online]. Available: <http://3daddfab.com/>. [Accessed 13 01 2016].

- [18] Stratasys, "FDM 3D Printers," 2014. [Online]. Available: hfile:///C:/Users/user/Downloads/PSS_FDM_FDMSystemsOverview_1017a.pdf. [Accessed 12 01 2017].
- [19] Amazon, "CablesOnline," 2017. [Online]. Available: www.amazon.com. [Accessed 5 1 2017].
- [20] Pulak M. Pandey, MV Reddy, and Sanjay Govind Dhande, "Real Time Adaptive Slicing for Fused Deposition Modelling," *International Journal of Machine Tools and Manufacture*, vol. 43, no. 1, pp. 61-71, 2003.
- [21] "All 3D," [Online]. Available: <https://all3dp.com/1/best-free-3d-printing-software-3d-printer-program/>. [Accessed August 2017].
- [22] Gaoyan Zhonga, Mohammad Vaezi, Ping Liu, Lin Pan, and Shoufeng Yang, "Characterization Approach on the Extrusion Process of Bio Ceramics for the 3D Printing of Bone Tissue Engineering Scaffolds," *Ceramics International*, vol. 43, pp. 13860-13868, 2017.
- [23] Daniel L. Cohen, "Fostering Mainstream Adoption of Industrial 3D Printing: Understanding the Benefits and Promoting Organizational Readiness," *3D Printing and Additive Manufacturing*, vol. 1, no. 2, pp. 62-69, 2014.
- [24] Wohlers Associates Inc., "Wohlers Report," Wohlers Associates, 2017.
- [25] Vojislav Petrovic, Juan Vicente Haro Gonzalez, Olga Jordá Ferrando, Javier Delgado Gordillo, Jose Ramón Blasco Puchades, and Luis Portolés Griñan, "Additive Layered Manufacturing: Sectors of Industrial Application Shown Through Case Studies," *International Journal of Production Research*, vol. 49, no. 4, pp. 1061-1079, 2011.
- [26] Ian Wright, "Six 3D Printing Processes for Prototyping: Which is Right for You?," 04 05 2016. [Online]. Available: <http://www.engineering.com>. [Accessed 03 08 2017].
- [27] S. Guide, "Comparison between 3D Printing and Traditional Manufacturing Processes for Plastics," 2014. [Online]. Available: www.sculpteo.com. [Accessed 03 08 2017].

- [28] Sung-Hoon Ahn, Michael Montero, Dan Odell, Shad Roundy, and Paul K. Wright, "Anisotropic Material Properties of Fused Deposition Modeling ABS," *Rapid Prototyping Journal*, vol. 8, no. 4, pp. 248 - 257, 2002.
- [29] Ruth Jill Urbanic and L. DiCecco, "Development of Adaptable Light Weighting Methods for Material Extrusion Processes," in *Proceedings of the ASME 2015 International Mechanical Engineering Congress and Exposition*, 2015.
- [30] G.Q. Jin, W. Li, C.F. Tsai, and L. Wang, "Adaptive Tool-path Generation of Rapid Prototyping for Complex Product Models," *Journal of Manufacturing Systems*, vol. 30, no. 3, p. 154–164, 2011.
- [31] Yu-an Jin, Yong He, Guang-huai Xue, and Jian-zhong Fu, "A Parallel-based Path Generation Method for Fused Deposition Modeling," *Advanced Manufacturing Technology*, vol. 77, p. 927–937, 2015.
- [32] Debananda Misra, V.Sundararajan, and Paul K. Wright, "Zig-Zag Tool Path Generation for Sculptured Surface Finishing," *Dimacs Series in Discrete Mathematics and Theoretical Computer Science*, vol. 67, pp. 265-280, 2005.
- [33] Farzad Rayegani and Godfrey C. Onwubolu, "Fused Deposition Modelling (FDM) process parameter prediction and optimization using Group Method for Data Handling (GMDH) and Differential Evolution (DE)," *The International Journal of Advanced Manufacturing Technology*, vol. 73, no. 1, pp. 509-519, 2014.
- [34] Özgür Keles, Caleb Wayne Blevins, and Keith J. Bowman, "Effect of Build Orientation on the Mechanical Reliability of 3D Printed ABS," *Rapid Prototyping Journal*, vol. 23, no. 2, pp. 320-328, 2017.
- [35] Chad E. Duty, Vlastimil Kunc, Brett Compton, Brian Post, Donald Erdman, Rachel Smith, Randall Lind, Peter Lloyd, and Lonnie Love, "Structure and Mechanical Behavior of Big Area Additive Manufacturing (BAAM) Materials," *Rapid Prototyping Journal*, vol. 23, no. 1, pp. 181-189, 2017.

- [36] Vidya Kishore, Christine Ajinjeru, Andrzej Nycz, Brian Post, John Lindahl, Vlastimil Kunc, and Chad Duty, "Infrared Preheating to Improve Interlayer Strength of Big Area Additive Manufacturing (BAAM) Components," *Additive Manufacturing 1*, vol. 14, pp. 7-12, 2017.
- [37] Nectarios Vidakis, Markos Petousis, Savvakis Konstantinos, Achilles Vairis, Maniadi Athina, and Arapis Manolis, "Experimental Determination of Fused Deposition Modelling Parts Compressive Strength," in *9th International Conference "New Horizons in Industry, Business and Education*, Skiathos, 2015.
- [38] Venkatesh Vijayaraghavan, Akhil Garg, Jasmine Siu Lee Lam, B. Panda, and Siba Sankar Mahapatra, "Process Characterization of 3D-printed FDM Components Using Improved Evolutionary Computational Approach," *International Journal Advanced Manufacturing Technology*, vol. 78, no. 5–8, pp. 781-793, 2015.
- [39] Godfrey C. Onwubolu and Farzad Rayegani, "Characterization and Optimization of Mechanical Properties of ABS Parts Manufactured by the Fused Deposition Modelling Process," *International Journal of Manufacturing Engineering*, vol. 2014, pp. 1-13, 2014.
- [40] Olga S. Carneiro, A.F. Silva and R. Gomes, "Fused Deposition Modeling with Polypropylene," *Materials & Design*, vol. 83, pp. 768-776, 2015.
- [41] "Kyle Stetz," Makerbot Vs. Dimension SST 1200es, 20 08 2009. [Online]. Available: <https://kylestetzerp.wordpress.com/>. [Accessed 26 02 2018].
- [42] Anoop Kumar Sood, Vedansh Chaturvedi, Saurav Datta, and Siba Sankar Mahapatra, "Optimization of Process Parameters in Fused Deposition Modeling Using Weighted Principal Component Analysis," *Journal of Advanced Manufacturing Systems*, vol. 10, no. 2, pp. 241-259, 2011.
- [43] Sushanta Kumar Panda, Soumyakant Padhee, Anoop Kumar Sood, and Siba Sankar Mahapatra, "Optimization of Fused Deposition Modelling (FDM) Process Parameters Using Bacterial Foraging Technique," *Intelligent Information Management*, vol. 1, pp. 89-97, 2009.

- [44] Anoop Kumar Sood, Rajkumar Ohdar, and Siba Sankar Mahapatra, "Parametric Appraisal of Mechanical Property of Fused Deposition Modelling Processed Parts," *Materials and Design*, vol. 31, no. 1, pp. 287-295, 2010.
- [45] Anoop Kumar Sood , Asif Equbal, Vijay Toppo, R.K. Ohdar, and S.S. Mahapatra, "An Investigation on Sliding Wear of FDM Built Parts," *CIRP Journal of Manufacturing Science and Technology*, vol. 5, pp. 48-54, 2012.
- [46] Anoop Kumar Sood, Rajkumar Ohdar, and Siba Sankar Mahapatra, "Experimental Investigation and Empirical Modelling of FDM Process for Compressive Strength Improvement," *Journal of Advanced Research*, vol. 3, no. 1, pp. 81-90, 2012.
- [47] Mohammad Shojib Hossain, David Espalin, Jorge Ramos, Mireya Perez, and Ryan Wicker, "Improved Mechanical Properties of Fused Deposition Modeling-Manufactured Parts Through Build Parameter Modifications," *Manufacturing Science and Engineering*, vol. 136, no. 6, 2014.
- [48] Luigi Maria Galantucci, Ilo Bodi, Jorgaq Kacani, and Fulvio Lavecchia, "Analysis of Dimensional Performance for a 3D Open-source Printer Based on Fused Deposition Modeling Technique," *Procedia CIRP*, vol. 28, p. 82 – 87, 2015.
- [49] Omar S. Es-Said, J. Foyos, R. Noorani, M. Mendelson, and R. Marloth, "Effect of Layer Orientation on Mechanical Properties of Rapid Prototyped Samples," *Materials and Manufacturing Processes*, vol. 15, no. 1, pp. 107-122, 2000.
- [50] Byoung Hun Lee, J. Abdullah, and Zahid A. Khan, "Optimization of Rapid Prototyping Parameters for Production of Flexible ABS Object," *Journal of Materials Processing Technology*, vol. 169, no. 1, pp. 54-61, 2005.
- [51] Sophia Ziemian, Maryvivan Okwara, and Constance Wilkens Ziemian, "Tensile and Fatigue Behavior of Layered Acrylonitrile Butadiene Styrene," *Rapid Prototyping Journal*, vol. 21, no. 3, pp. 270-278, 2015.

- [52] Alberto Boschetto and Luana Bottini, "Design for Manufacturing of Surfaces to Improve Accuracy in Fused Deposition Modeling," *Robotics and Computer-Integrated Manufacturing*, vol. 37, pp. 103-114, 2016.
- [53] Hassan Rezayat, W. Zhao, Akawut Siriruk, and Sudarsanam S Babu, "Structure–Mechanical Property Relationship in Fused Deposition Modelling," *Materials Science and Technology*, vol. 31, no. 8, pp. 895-903, 2015.
- [54] Daekeon Ahn, Jin-Hwe Kweon, Soonman Kwon, Jungil Song, and Seokhee Lee, "Representation of Surface Roughness in Fused Deposition Modeling," *Journal of Materials Processing Technology*, vol. 209, no. 15-16, pp. 5593-5600, 2009.
- [55] Alberto Boschetto and Luana Bottini, "Accuracy Prediction in Fused Deposition Modeling," *The International Journal of Advanced Manufacturing Technology*, vol. 73, no. 5–8, pp. 913-928, 2014.
- [56] Walter Castro Smith and Richard W. Dean, "Structural Characteristics of Fused Deposition Modeling Polycarbonate Material," *Polymer Testing (Material properties)*, vol. 32, no. 8, pp. 1306-1312, December 2013.
- [57] Sandeep Raut, VijayKumar S. Jatti, Nitin K. Khedkar, and T.P. Singh, "Investigation of the Effect of Built Orientation on Mechanical Properties and Total Cost of FDM Parts," in *3rd International Conference on Materials Processing and Characterisation*, 2014.
- [58] Juraj Beniak, Peter Križan, Miloš Matúš, and Ľubomír Šooš, "Experiment on Production Time for Model Creation on Small Fused Deposition Modeling Device," *International Journal of Mechanics*, vol. 9, pp. 138-144, 2015.
- [59] Lennart Bochmann, Cindy Bayley, Moneer Helu, Robert Transchel, Konrad Wegener and David Dornfeld, "Understanding error generation in fused deposition modeling," *Surface Topography: Metrology and Properties*, vol. 3, no. 1, 2015.
- [60] Jean Hergel and Sylvain Lefebvre, "Clean Color: Improving Multi-filament 3D Prints," *Euro Graphics*, vol. 33, no. 2, 2014.

- [61] John C. Steuben, Athanasios P. Iliopoulos, and John G. Michopoulos, "Implicit Slicing for Functionally Tailored Additive Manufacturing," *Computer-Aided Design*, vol. 77, pp. 107-119, 2016.
- [62] Syed Masood, Wuttinut Rattanawong, and Pio Iovenitti, "Part Build Orientations Based on Volumetric Error in Fused Deposition Modelling," *International Journal of Advanced Manufacturing Technology*, vol. 16, no. 3, pp. 162-168, 2000.
- [63] Ronald Ian Campbell, Massimo Martorelli, and H.S. Lee, "Surface Roughness Visualization for Rapid Prototyping Models," *Computer-Aided Design*, vol. 34, no. 10, pp. 717-725, 2002.
- [64] Ivan Gajdoš and Jan Slota, "Influence of Printing Conditions on Structure in FDM Prototypes," *Tehnicki Vjesnik*, vol. 20, no. 2, p. 231–236, 2013.
- [65] Alberto Boschetto, V. Giordano, and Francesco Veniali, "Surface Roughness Prediction in Fused Deposition Modelling by Neural Networks," *International Journal Advanced Manufacturing Technology*, vol. 67, no. 9–12, p. 2727–2742, 2013.
- [66] R. Anitha, S. Arunachalam, and P. Radhakrishnan, "Critical Parameters Influencing the Quality of Prototypes in Fused Deposition Modelling," *Journal of Materials Processing Technology*, vol. 118, no. 1–3, p. 385–388, 2001.
- [67] Alberto Boschetto, V. Giordano, and Francesco Veniali, "Modelling Micro Geometrical Profiles in Fused Deposition Process," *The International Journal of Advanced Manufacturing Technology*, vol. 61, no. 9–12, p. 945–956, 2012.
- [68] P.M. Pandey, N. Venkata Reddy, and S.G. Dhande, "Improvement of Surface Finish by Staircase Machining in Fused Deposition Modeling," *Journal of Materials Processing Technology*, vol. 132, pp. 323-331, 2003.
- [69] Alberto Boschetto and Luana Bottini, "Surface Improvement of Fused Deposition Modeling Parts by Barrel Finishing," *Rapid Prototyping Journal*, vol. 21, no. 6, pp. 686-696, 2015.
- [70] Luigi Maria Galantucci, Fulvio Lavecchia, and Gianluca Percoco, "Experimental Study Aiming to Enhance the Surface Finish of Fused Deposition Modeled Parts," *CIRP Annals - Manufacturing Technology*, vol. 58, p. 189–192, 2009.

- [71] Ashu Garg, Anirban Bhattacharya, and Ajay Batish, "On Surface Finish and Dimensional Accuracy of FDM Parts After Cold Vapor Treatment," *Materials and Manufacturing Processes*, vol. 31, no. 4, pp. 522-529, 2016.
- [72] D. Ahn, H. Kim, and S. Lee, "Surface Roughness Prediction Using Measured Data and Interpolation in Layered Manufacturing," *Journal of Materials Processing Technology*, vol. 209, no. 2, p. 664-671, 2009.
- [73] C. J. L. Pérez, J. V. Calvet, and M. A. Sebastián Pérez, "Geometric Roughness Analysis in Solid Free-form Manufacturing Processes," *Journal of Materials Processing Technology*, vol. 119, no. 1-3, p. 52-57, 2001.
- [74] Brian N. Turner and Scott A. Gold, "A Review of Melt Extrusion Additive Manufacturing Processes: II. Materials, Dimensional Accuracy, and Surface Roughness," *Rapid Prototyping Journal*, vol. 21, no. 3, pp. 250-261, 2015.
- [75] Antonio Armillotta and Marco Cavallaro, "Edge Quality in Fused Deposition Modeling: I. Definition and Analysis," *Rapid Prototyping Journal*, vol. 23, no. 6, pp. 1079-1087, 2017.
- [76] Sanat Agrawal and Sanjay Govind Dhande, "Analysis of Mechanical Error in a Fused Deposition Process Using a Stochastic Approach," *International Journal of Production Research*, vol. 45, no. 17, pp. 3991-4012, 2007.
- [77] Kun Tong, Sanjay Joshi, and El-amine Lehtihet, "Error Compensation for Fused Deposition Modeling (FDM) Machine by Correcting Slice Files," *Rapid Prototyping Journal*, vol. 14, no. 1, pp. 4-14, 2008.
- [78] Jack Szu-Shen Chen and Hsi-Yung Feng, "Contour Generation for Layered Manufacturing with Reduced Part Distortion," *International Journal of Advanced Manufacturing Technology*, vol. 53, pp. 1103-1113, 2011.
- [79] Sarat Singamneni, Olaf Diegel, B. Huang, I. Gibson, and R. Chowdhury, "Curved Layer Fused Deposition Modeling," *Journal New General Science Engineering*, vol. 8, pp. 95-107, 2010.

- [80] Ibrahim T. Ozbolat and A. K. M. B. Khoda, "Design of a New Parametric Path Plan for Additive Manufacturing of Hollow Porous Structures With Functionally Graded Materials," 2014.
- [81] Pierre Muller, Jean-Yves Hascoet and Pascal Mognol, "Toolpaths for additive manufacturing of functionally graded materials (FGM) parts," *Rapid Prototyping Journal*, vol. 20, no. 6, pp. 511-522, 2014.
- [82] Brian N. Turner, Robert Strong, and Scott A. Gold, "A Review of Melt Extrusion Additive Manufacturing Processes: I. Process Design and Modeling," *Rapid Prototyping Journal*, vol. 20, no. 3, pp. 192-204, 2014.
- [83] Chil-Chyuan Kuo, Ci-Ming Chen, and Song-Xuan Chang, "Polishing Mechanism for ABS Parts Fabricated by Additive Manufacturing," *International Journal of Advanced Manufacturing Technology*, vol. 91, no. 5-8, pp. 1473-1479, 2017.
- [84] Jasgurpreet Singh Chohan, Rupinder Singh, Kamaljit Singh Boparai, Rosa Penna, and Fernando Fraternali, "Dimensional Accuracy Analysis of Coupled Fused Deposition Modeling and Vapour Smoothing Operations for Biomedical Applications," *Composites Part B*, vol. 117, pp. 138-149, 2017.
- [85] Anderson Vicente Borille, Jefferson De Oliveira Gomes, and Daniel Lopes, "Geometrical Analysis and Tensile Behavior of Parts Manufactured with Flame Retardant Polymers by Additive Manufacturing," *Rapid Prototyping Journal*, vol. 23, no. 1, pp. 169-180, 2017.
- [86] Daljinder Singh, Rupinder Singh, and Kamaljit Singh Boparai, "Development and Surface Improvement of FDM Pattern Based Investment Casting of Biomedical Implants: A State of Art," *Journal of Manufacturing Processes*, vol. 31, pp. 80-95, 2018.
- [87] Jasgurpreet Singh Chohan and Rupinder Singh, "Pre and Post Processing Techniques to Improve Surface Characteristics of FDM Parts: A state of Art Review and Future Applications," *Rapid Prototyping Journal*, vol. 23, no. 3, pp. 495-513, 2017.

- [88] Ladislav Morovič and Ján Milde, "Influence of Part Orientation on Geometrical and Dimensional Accuracy in FDM Method," *Academic Journal of Manufacturing Engineering*, vol. 15, no. 1, pp. 24-28, 2017.
- [89] Omar Ahmed Mohamed, Syed Hasan Masood, and Jahar Lal Bhowmik, "Experimental Investigation for Dynamic Stiffness and Dimensional Accuracy of FDM Manufactured Part Using IV-Optimal Response Surface Design," *Rapid Prototyping Journal*, vol. 23, no. 4, pp. 736-749, 2017.
- [90] Ian Gibson, David W. Rosen, and Brent Stucker, *Additive Manufacturing Technologies*, New York: Springer, 2010.
- [91] Siva Rama Krishna Ledalla, Balaji Tirupathi, and Venkatesh Sriram, "Performance Evaluation of Various STL File Mesh Refining Algorithms Applied for FDM-RP Process," *Journal of The Institution of Engineers*, pp. 1-8, 2016.
- [92] Hans Kellerer, Ulrich Pferschy, and David Pisinger, "The Bounded Knapsack Problem," in *Knapsack Problems*, Verlag Berlin Heidelberg, Springer, 2004, pp. 185-209.
- [93] Navid Nazemi and Ruth Jill Urbanic, "A Numerical Investigation for Alternative Toolpath Deposition Solutions for Surface Cladding of Stainless Steel P420 Powder on AISI 1018 Steel Substrate," *The International Journal of Advanced Manufacturing Technology*, pp. 1-21, 2018.
- [94] Jose F Rodriguez, James P. Thomas, and John E. Renaud, "Design of Fused-Deposition ABS Components for Stiffness and Strength," *Journal of Mechanical Design*, vol. 125, no. 3, pp. 545-551, 2003.
- [95] ASTM F2792 Standards, "7 Families of Additive Manufacturing," 7 November 2017. [Online]. Available: https://www.additivemanufacturing.media/cdn/cms/7_families_print_version.pdf.

APPENDICES

Appendix A

Published/submitted papers—Acceptance/Permission Letter from Publisher

Title: “**Using Genetic Algorithms to Optimize the Build Orientation for Fused Deposition Modeled Components Containing Internal Reinforcement Structures**” and
“**Minimizing Voids With Using an Optimal Raster Orientation and Bead Width for a Material Extrusion Based Process**”

Dear Ms. Eiliat,

It is our pleasure to grant you permission to use all or any part of the following ASME papers:

- Using Genetic Algorithms to Optimize the Build Orientation for Fused Deposition Modeled Components Containing Internal Reinforcement Structures, by Hasti Eiliat and Ruth Jill Urbanic, Paper No. IMECE2014-37683.
- Minimizing Voids With Using an Optimal Raster Orientation and Bead Width for a Material Extrusion Based Process, by Hasti Eiliat and Jill Urbanic, Paper No. IMECE2016-67708.

Cited in your letter for inclusion in a dissertation to be published by the University of Windsor Library. Permission is granted for the specific use as stated herein and does not permit further use of the materials without proper authorization (no future revisions and no editions of my dissertation without written permission). Proper attribution must be made to the author(s) of the materials. Please note: if any or all of the figures and/or Tables are of another source, permission should be granted from that outside source or include the reference to the original source. ASME does not grant permission for outside source material that may be referenced in the ASME works. As is customary, we request that you ensure full acknowledgment of this material, the author(s), source and ASME as the original publisher. The acknowledgment must be retained on all pages where the figure is printed and distributed.

Many thanks for your interest in ASME publications.

Sincerely,

Beth Darchi

Publishing Administrator ASME

2 Park Avenue, New York, NY 10016-5990

darchib@asme.org

Title: **Minimizing voids for a material extrusion based process**

Dear Hasti Eiliat,

This article is © Emerald Publishing and permission has been granted for this version to appear here (please insert the web address here). Emerald does not grant permission for this article to be further copied/distributed or hosted elsewhere without the express permission from Emerald Group Publishing Limited.

If the article will not be published prior to your dissertation being printed, we would request that you state the article is ‘forthcoming in the Rapid Prototyping Journal.’

If possible, we would request that the article is not deposited online prior to official publication by Emerald- if this is likely, please request an embargo period to ensure that Emerald has first publication.

In regards to granting others the right to reproduce the dissertation, we’re happy for others to reuse the dissertation in an academic context, however, if there are any other requests or you wish to republish in the future, please contact us again.

I hope this helps, please don’t hesitate to contact me should you require any further assistance.

Kind Regards,

Lauren Flintoft

Rights Executive| Emerald Group

T: +44 (0) 1274 785227

LFlintoft@emeraldgroup.com| www.emeraldinsight.com

Title: “An Optimization Approach for Components Built by Fused Deposition Modeling with Parametric Internal Structures”



RightsLink®

Home

Create Account

Help



ELSEVIER

Title: An Optimization Approach for Components Built by Fused Deposition Modeling with Parametric Internal Structures
Author: L. Villalpando, H. Elliat, R.J. Urbanic
Publication: Procedia CIRP
Publisher: Elsevier
Date: 2014

Copyright © 2014 Elsevier B.V.

LOGIN

If you're a [copyright.com](#) user, you can login to RightsLink using your [copyright.com](#) credentials. Already a [RightsLink user](#) or want to [learn more?](#)

Please note that, as the author of this Elsevier article, you retain the right to include it in a thesis or dissertation, provided it is not published commercially. Permission is not required, but please ensure that you reference the journal as the original source. For more information on this and on your other retained rights, please visit: <https://www.elsevier.com/about/our-business/policies/copyright#Author-rights>

BACK

CLOSE WINDOW

Copyright © 2018 Copyright Clearance Center, Inc. All Rights Reserved. [Privacy statement](#). [Terms and Conditions](#). Comments? We would like to hear from you. E-mail us at customercare@copyright.com

Title: “Visualizing, analyzing, and managing voids in the material extrusion process.”



RightsLink®

Home

Create Account

Help



SPRINGER NATURE

Title: Visualizing, analyzing, and managing voids in the material extrusion process
Author: Hasti Eiliat, Jill Urbanic
Publication: The International Journal of Advanced Manufacturing Technology
Publisher: Springer Nature
Date: Jan 1, 2018
Copyright © 2018, Springer Nature

LOGIN
If you're a [copyright.com](#) user, you can login to RightsLink using your [copyright.com](#) credentials. Already a [RightsLink](#) user or want to [learn more?](#)

Author Use

Authors of Springer Nature content do not require permission to use content from their article in most cases as stated in the [author's guidelines](#).

Authors wishing to use their article for commercial purposes must request permission in the normal way.

For journal content questions, please contact Springer Nature's permissions department at journalpermissions@springernature.com

For book content questions, please contact Springer Nature's permissions department at bookpermissions@springernature.com

BACK

CLOSE WINDOW

Copyright © 2018 [Copyright Clearance Center, Inc.](#) All Rights Reserved. [Privacy statement](#). [Terms and Conditions](#). Comments? We would like to hear from you. E-mail us at customer-care@copyright.com

Appendix B

Additive Manufacturing Categories

As it was explained in chapter 1, AM process is categorized into seven main groups (Figure 1). Below, these processes are explained by details [95].

Material Extrusion (AM-ME): Alternative names for this process are Fused Filament Fabrication (FFF) and Fused Deposition Modeling (FDM™). In this process, material is extruded through a nozzle or orifice in tracks or beads, which are then combined into multi-layer models. Common varieties include heated thermoplastic extrusion (similar to a hot glue gun) and syringe dispensing. The typical materials for this process are thermoplastic filaments and pellets and liquids, and slurries (Syringe Types). Next section describes this process more.

Powder Bed Fusion (PBF): Alternative names are Selective Laser Sintering (SLS™), Direct Metal Laser Sintering (DMLS™), Selective Laser Melting (SLM™), Electron Beam Melting (EBM™), Selective Heat Sintering (SHS™), and Multi-Jet Fusion (MJF™). In this process, powdered materials is selectively consolidated by melting it together using a heat source such as a laser or electron beam. The powder surrounding the consolidated part acts as support material for overhanging features. The typical materials are plastics, metal and ceramic powders, and sand.

Vat Photopolymerization: Alternative names are Stereolithography Apparatus (SLA™), Digital Light Processing (DLP™), Scan, Spin, and Selectively Photo cure (3SP™), and Continuous Liquid Interface Production (CLIP™). In this process, a vat of liquid photopolymer resin is cured through selective exposure to light (via a laser or projector) which then initiates polymerization and converts the exposed areas to a solid part. The typical material is UV-Curable Photopolymer Resins.

Binder Jetting: Alternative Names are 3D Printing (3DP™), ExOne, and Voxel jet. In this process, liquid bonding agents are selectively applied onto thin layers of powdered material to build up parts layer by layer. The binders include organic and inorganic materials. Metal or ceramic powdered parts are typically fired in a furnace after they are printed. The typical materials are powdered plastic, metal, ceramics, glass, and sand.

Material Jetting: Alternative names are Polyjet™, Smooth Curvatures Printing (SCP™), Multi-Jet Modeling (MJM), and Projet™. In this process droplets of material are deposited layer by layer to make parts. Common varieties include jetting a photo curable resin and curing it with UV light, as well as jetting thermally molten materials that then solidify in ambient temperatures. The typical materials are photopolymers, polymers, and waxes.

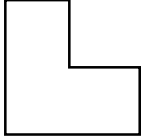
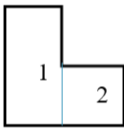
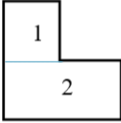
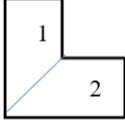
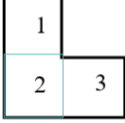
Sheet Lamination: Alternative names are Laminated Object Manufacture (LOM), Selective Deposition Lamination (SDL), and Ultrasonic Additive Manufacturing (UAM). In this process, sheets of material are stacked and laminated together to form an object. The lamination method can be adhesives or chemical (paper/ plastics), ultrasonic welding, or brazing (metals). Unneeded regions are cut out layer by layer and removed after the object is built. The typical materials are paper, plastic sheets, and metal foils/tapes.

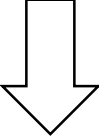
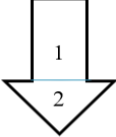
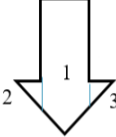
Directed Energy Deposition (DED): Alternative names are Laser Metal Deposition (LMD), Laser Engineered Net Shaping (LENS™), and Direct Metal Deposition (DM3D or DMD™). In this process, powder or wire is fed into a melt pool which has been generated on the surface of the part where it adheres to the underlying part or layers by using an energy source such as a laser or electron beam. This is essentially a form of automated build-up welding. The typical materials are metal wire and powder, with ceramics.

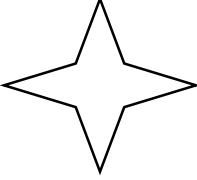
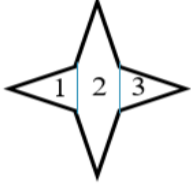
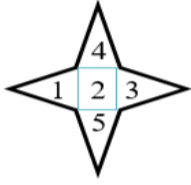
Appendix C

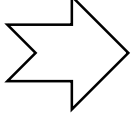
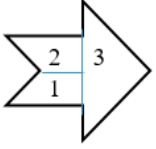
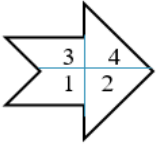
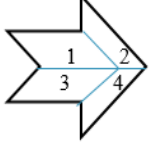
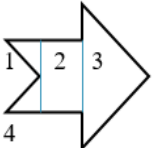
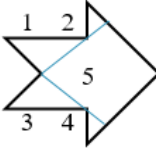
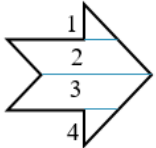
Voids Possibility Matrix

Table 50. (a to e) examples of dividing different concave shapes

(a)											
											
# Profile $f \in F$	1	2	1	2	1	2	3				
	3.93	4.72	3.93	5.86	4.72	8.65	3.93	3.93	4.72		
Total Voids Area (mm²)	8.65		10.79		13.36		12.58				
	8		8		8	8	10	10	8	8	8
Total Voids Possibility	16		16		20		24				
	0 1 0 1 1 0 1 0 0 1 0 1 1 0 1 0		0 1 0 1 1 0 1 0 0 1 0 1 1 0 1 0		0 1 0 1 1 0 1 0 0 1 0 1 1 0 1 0		0 1 1 1 1 0 1 0 1 1 0 1 1 0 1 0		0 1 0 1 1 0 1 0 0 1 0 1 1 0 1 0		0 1 0 1 1 0 1 0 0 1 0 1 1 0 1 0

(b)					
# Profile $f \in F$					
	1	2	1	2	3
Total Voids Area (mm ²)	3.14	5.72	10.65	2.34	2.34
	8.86		15.33		
Total Voids Possibility	0 1 0 1 1 0 1 0 0 1 0 1 1 0 1 0	0 1 1 1 0 1 1 1 0	0 1 0 1 1 0 1 0 0 1 0 1 1 0 1 0	0 1 1 1 0 1 1 1 0	0 1 1 1 0 1 1 1 0
	8	6	8	6	6
	14		20		

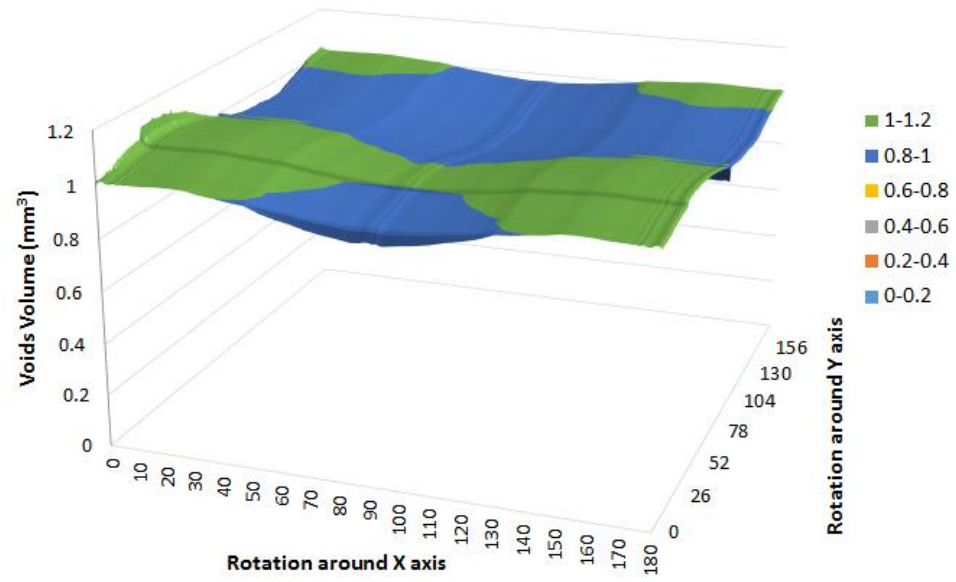
(c)								
# Profile $f \in F$								
	1	2	3	1	2	3	4	5
Total Voids Area (mm ²)	9.54	22.57	9.54	9.54	3.06	9.54	9.54	9.54
	41.65			41.22				
Total Voids Possibility	<pre> 0 1 1 1 0 1 1 1 0 </pre>	<pre> 0 1 1 0 1 1 1 0 1 1 0 1 1 1 0 1 1 0 0 1 1 0 1 1 1 0 1 1 0 1 1 1 0 1 1 0 </pre>	<pre> 0 1 1 1 0 1 1 1 0 </pre>	<pre> 0 1 1 1 0 1 1 1 0 </pre>	<pre> 0 1 0 1 1 0 1 0 0 1 0 1 1 0 1 0 </pre>	<pre> 0 1 1 1 0 1 1 1 0 </pre>	<pre> 0 1 1 1 0 1 1 1 0 </pre>	<pre> 0 1 1 1 0 1 1 1 0 </pre>
	6	24	6	6	8	6	6	6
	36			32				

(d)													
# Profile $f \in F$													
	1	2	3	1	2	3	4	1	2	3	4		
Total Voids Area (mm ²)	3.61	3.61	8.53	3.61	4.32	3.61	4.32	5.09	3.98	5.09	3.98		
	15.75			15.86				18.14					
Total Voids Possibility	10	10	6	10	6	10	6	8	10	8	10		
	26			32				36					
# Profile $f \in F$													
	1	2	3	4	1	2	3	4	5	1	2	3	4
Total Voids Area (mm ²)	1.23	4.33	8.53	1.23	3.8	0.91	3.8	0.91	6.55	2.48	5.41	5.41	2.48
	15.32				15.97					15.78			
Total Voids Possibility	6	8	6	6	6	6	6	6	8	6	8	8	6
	26				32					28			

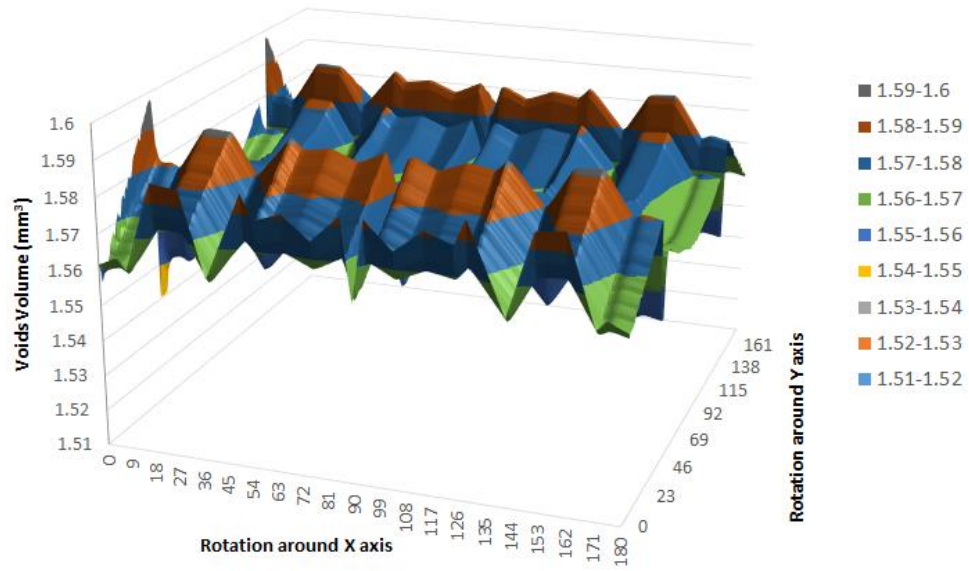
(e)																					
# Profile $f \in F$																					
	1	2	3	4	5	6	1	2	3	4	1	2	3	4	5	6	1	2	3	4	5
Area mm ²	2.4	2.4	2.4	2.4	2.4	10.4	2.47	6.69	2.47	2.47	2.47	2.47	2.47	2.34	2.47	8.31	2.47	6.54	2.47	4.7	4.7
	22.81						14.1				20.53						20.88				
Possibility	6	6	6	6	6	20	6	6	6	6	6	6	6	6	6	10	6	6	6	12	12
	50						24				40						42				
# Profile $f \in F$																					
	1	2	3	4	1	2	3	4	5	1	2	3	4	5							
Area mm ²	2.47	7.94	4.7	4.7	9.05	2.47	2.47	2.47	2.47	6.45	2.47	2.67	2.67	2.47							
	19.81				18.93					16.73											
Possibility	6	10	12	12	12	6	6	6	6	6	6	6	6	6							
	40				36					30											

Appendix D

Total Voids per Build Rotation

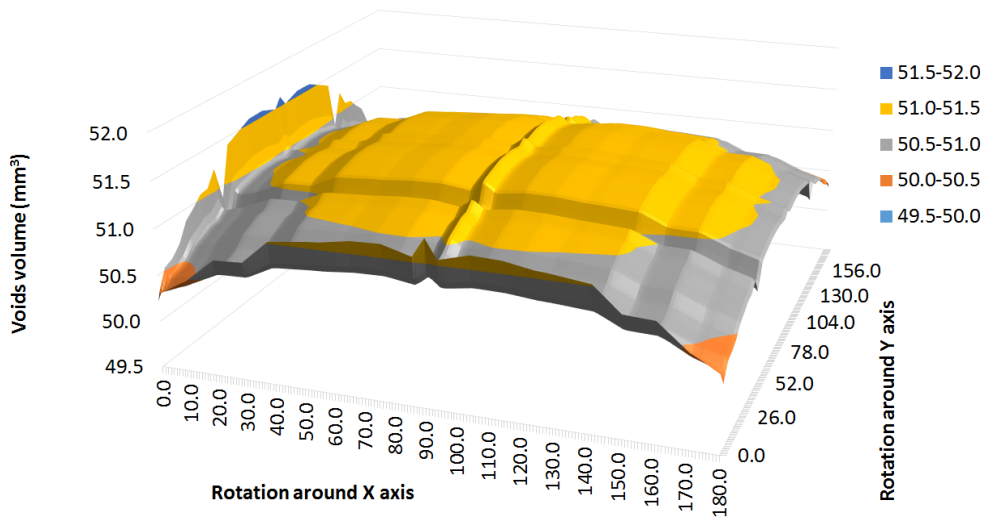


(a)

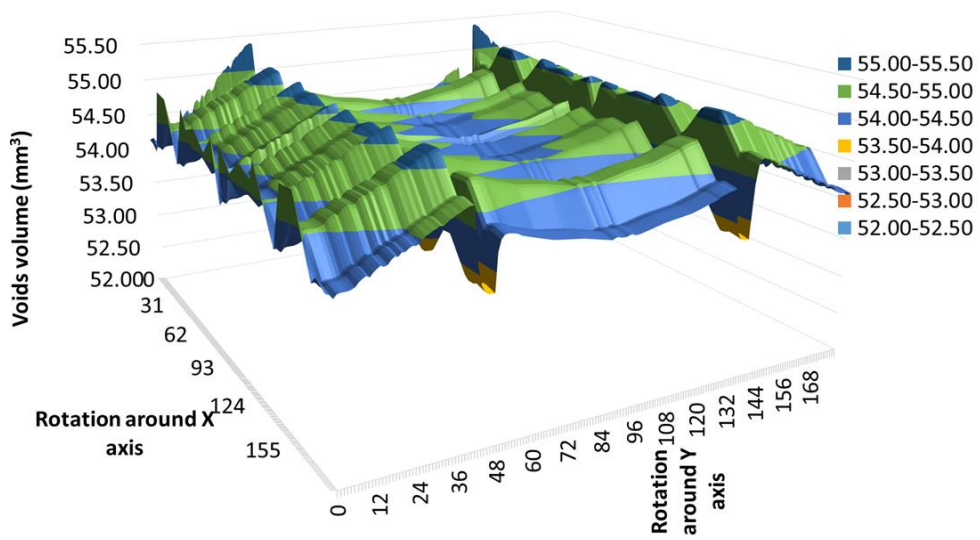


(b)

Figure 114. Voids volume (mm³) per rotation around X and Y axes for a Car seat with allowable overlaps (a) 50% and (b) 0%



(a)



(b)

Figure 115. Voids volume (mm^3) per rotation around X and Y axes for Valve cover I with allowable overlaps (a) 50% and (b) 0%

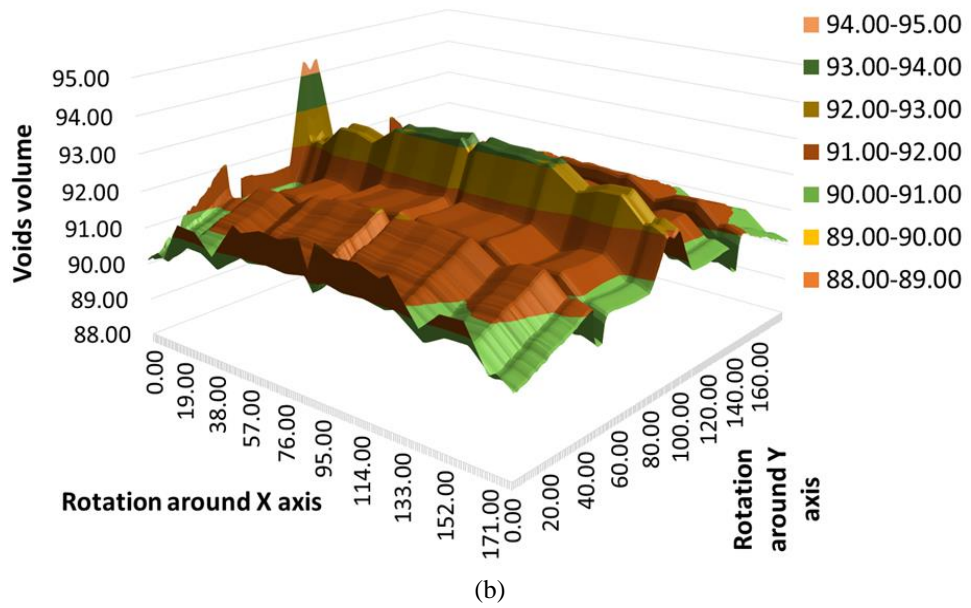
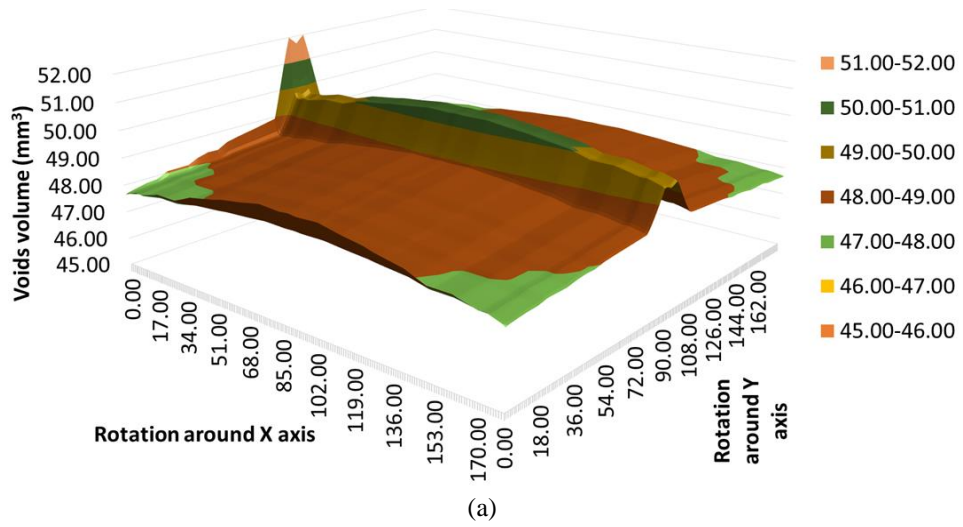


Figure 116. Voids volume (mm^3) per rotation around X and Y axes for Valve cover II with allowable overlaps (a) 50% and (b) 0%

Appendix E

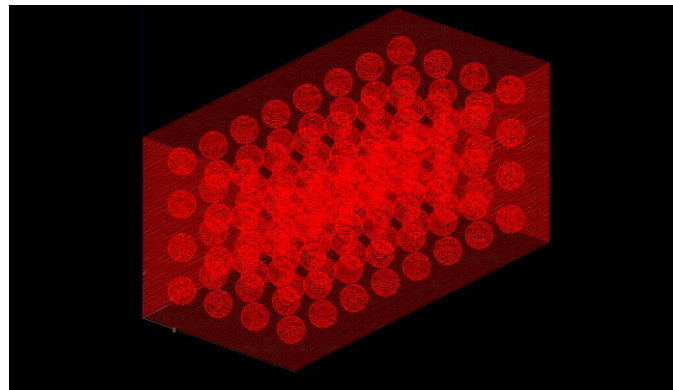
Mathematical Model Steps

1. Optimizing the bead height S_j for the part from Equation 1.
2. Slice a part with an optimal S_j to $T(N_j)$ layers.
3. For the layer $q \in Q$ with an optimal bead height S_j .
4. Finding the allowable range of bead width, w_i^j (from Table 17).
5. For one allowable raster angle $r = \{ 0^\circ \text{ to } 179^\circ \}$ find W_r for the layer q from Equation 3.
6. Calculate allowable overlap, O_i ; for each bead width, w_i^j from Equation 4.
7. For each bead width, w_i^j , and overlap, O_i , calculate total voids area from Equation 6, 7, and 8.
8. Finding minimum total voids area to find one optimal bead width and one optimal overlap for each raster angle, r .
9. Repeat step 5 to 8 for all allowable raster angles.
10. Find the minimum total voids area to find optimal raster angle with optimal bead width and overlap.
11. Repeat all processes for the next layers.

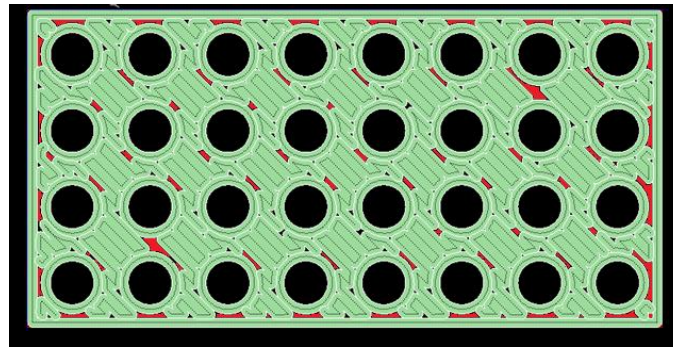
Appendix F

Future Work

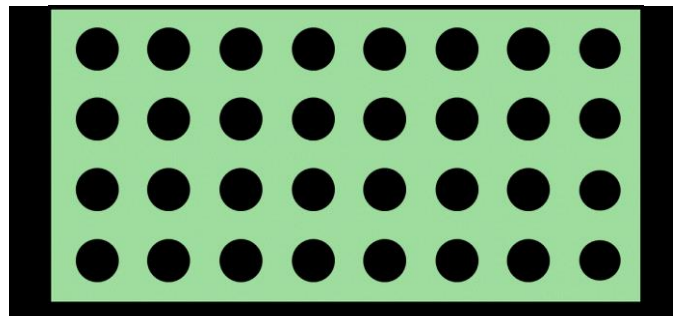
As it was discussed in Figure 113, the relationship between strength and the new toolpath needs to be examined. Figure 117 (a) shows the 3D model with sponge internal structure and Figure 117 (b) shows one layer of the part with the default toolpath of OEM software. As it is shown with red regions in Figure 117 (b), there are unwanted and uncovered voids during the OEM software toolpath. It would be expected that all voids (red regions) will be covered with the new model as same as Figure 117 (c) and the strength of the part will be increased.



(a)



(b)



(c)

Figure 117. (a) 3D model, (b) Voids in the OEM software toolpath, (c) Expectation of the new model toolpath

For experimenting the tensile strength, the comparison between the new model and the best orientation of the dog bone specimen which is shown in Figure 118 needs to be done.

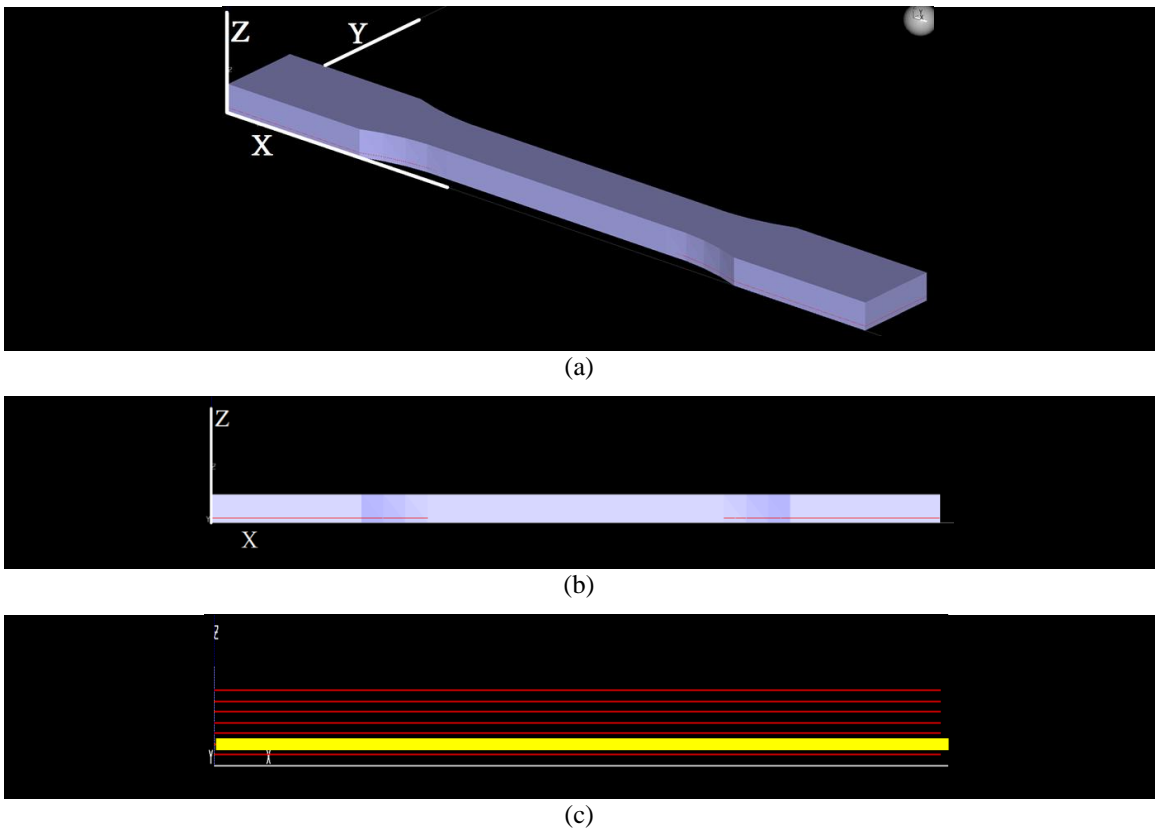


Figure 118. (a) 3D model of tensile strength sample, (b) the view of 3D model from Z and X axis, and (c) Layers of the sample

The last experimental test is for testing permeability. Figure 119 shows some suggestions for testing permeability with the new model.

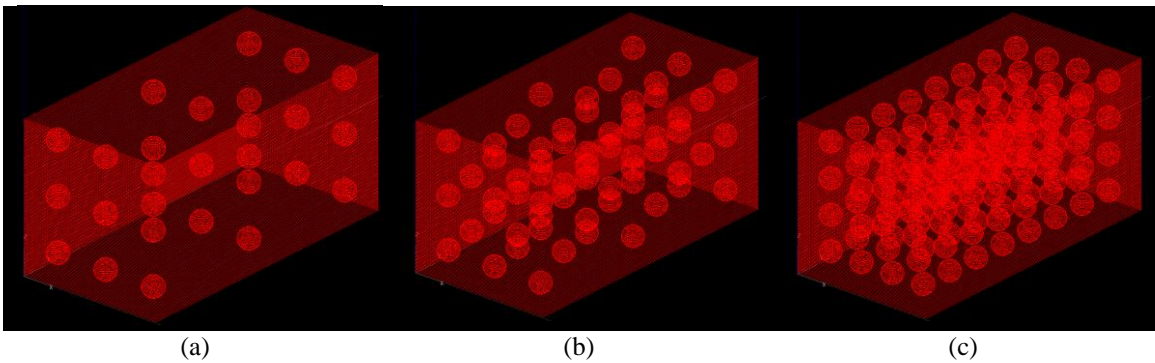


Figure 119. Three examples with different internal structures

VITA AUCTORIS

NAME: Hasti Eiliat

PLACE OF BIRTH: Tehran, Iran

YEAR OF BIRTH: 1988

EDUCATION: University of Windsor, Windsor, Ontario, 2013
M.A.Sc., Industrial and Manufacturing Systems
Engineering

Azad University of Tehran, Tehran, Iran, 2010
B.A.Sc., Industrial Engineering